Microscopic Analysis of the Nonlinear Optical Properties of Semiconductor Quantum Well Structures: Excitonic Anomalous Currents and Many-Body Correlations of Charge-Transfer Excitons

Dissertation

zur
Erlangung des Doktorgrades
der Naturwissenschaften
(Dr. rer. nat.)

der

Fakultät für Naturwissenschaften
der Universität Paderborn
vorgelegt von

Cong Thanh Ngo

Paderborn, 2024

Erklärung der Selbstständigkeit

Hiermit versichere ich, die vorliegende Arbeit selbstständig verfasst und keine anderen als die angegebenen Quellen und Hilfsmittel benutzt sowie die Zitate deutlich kenntlich gemacht zu haben.

Ort, Datum	Unterschrift

Vorsitzender der Prüfungskommission:	Prof. Dr. Tim Bartley
Erstgutachter:	Prof. Dr. Torsten Meier
Zweitgutachter:	Dr. Xuekai Ma
Weiteres Mitglied:	Prof. Dr. Jan Sperling
Datum der Abgabe:	20. Dezember 2024

Zusammenfassung

In dieser Dissertation werden exzitonische Effekte in der nichtlinearen optischen Antwort von Halbleiter-Quantenfilmen mithilfe der Mehrband-Halbleiter-Bloch-Gleichungen in der Längen-Eichung untersucht. Im ersten Ergebnisteil wird die Coulomb-Wechselwirkung in der zeitabhängigen Hartree-Fock-Näherung berücksichtigt, um exzitonische Effekte zu beschreiben. Streuprozesse von Ladungsträgern mit longitudinal-optischen und longitudinal-akustischen Phononen werden in der Born-Markov-Näherung in zweiter Ordnung einbezogen, um die Zerfallsdynamik präzise zu modellieren. Eine Herausforderung bei der Lösung der Bloch-Gleichungen, die durch die zufälligen k-abhängigen Phasenfaktoren der numerisch berechneten Wellenfunktionen entsteht, wird durch die Anwendung der Paralleltransport- und der verdrehten Paralleltransport-Eichungen gelöst. Diese gewährleisten glatte Phasen der Bloch-Eigenfunktionen und erleichtern die Berücksichtigung von Vielteilcheneffekten. Unsere numerischen Ergebnisse, die gut mit experimentellen Daten übereinstimmen, zeigen, dass Terahertz-induzierte anomale Ströme nach resonanter optischer Anregung durch exzitonische Effekte verstärkt werden. Zeitliche Oszillationen dieser Ströme korrelieren mit der Dynamik exzitonischer Wellenpakete. Im zweiten Ergebnisteil wird die Cluster-Entwicklungsmethode verwendet, um den Einfluß von Coulomb-Korrelationen auf die nichtlineare optische Dynamik von Typ-I- und Typ-II-Quantenfilmen zu untersuchen. In Typ-II-Systemen ist die Coulomb-Anziehung zwischen Elektronen und Löchern schwächer als die Coulomb-Abstoßung zwischen gleichartig geladenen Teilchen, was zu speziellen Beiträgen zur nichtlinearen optischen Antwort führt. Diese Ergebnisse liefern eine physikalische Erklärung für experimentelle Daten aus optischen Pump-Probe-Experimenten an Typ-I- und Typ-II-Halbleiter-Quantenfilmen.

Summary

In this thesis excitonic effects in the nonlinear optical response of semiconductor quantum wells are studied using the multiband semiconductor Bloch equations in the length gauge. In the first results part, the Coulomb interaction is included in the time-dependent Hartree-Fock approximation to describe excitonic effects. Carrier scatterings with longitudinal-optical and longitudinal-acoustic phonons are included in the second-order Born-Markov approximation to accurately model the decay dynamics. One challenge in solving the Bloch equations stemming from the random k-dependent phase factors of the numerically obtained wave functions is resolved by applying the parallel transport and the twisted parallel transport gauges. These ensure smooth phases of the Bloch eigenfunctions while facilitating the incorporation of many-body effects. Our numerical results, which align well with experiments, reveal that Terahertz-induced anomalous currents after resonant optical excitation are enhanced by excitonic effects. Temporal oscillations of these currents correlate with the dynamics of excitonic wave packets. In the second results part, the cluster expansion method is used to study Coulomb correlation effects in the nonlinear optical dynamics of type-I and type-II quantum wells. In type-II systems, the Coulomb attraction between electrons and holes is weaker than the Coulomb repulsion between carriers of the same charge, leading to unique contributions to the nonlinear optical response. These findings provide a physical explanation for experimental optical-pump optical-probe data obtained on type-I and type-II quantum well structures.

List of Abbreviations

CTX	**C**harge-**t**ransfer e**x**citons
DCT	**D**ynamics-**c**ontrolled **t**runcation
EOM	**E**quations **o**f **m**otion
LA	**L**ongitudinal-**a**coustic
LG	**L**ength **g**auge
LO	**L**ongitudinal-**o**ptical
OPOP	**O**ptical-**p**ump **o**ptical-**p**robe
PTG	**P**arallel **t**ransport **g**auge
QW	**Q**uantum **w**ell
SBE	**S**emiconductor **B**loch **e**quations
TDHF	**T**ime-**d**ependent **H**artree-**F**ock
TPTG	**T**wisted **p**arallel **t**ransport **g**auge
VG	**V**elocity **g**auge
PB	**P**auli **b**locking
CI_{1st}	Fir**st**-order **C**oulomb **i**nteraction
CI_{corr}	Higher-order **C**oulomb **corr**elations

List of Scientific Contributions

Doctorate-Related Publications

Peer-Reviewed Publications

1. L. H. Thong, **C. Ngo**, H. T. Duc, X. Song, and T. Meier, Microscopic analysis of high harmonic generation in semiconductors with degenerate bands, Phys. Rev. B **103**, 085201 (2021).
2. F. Schäfer, M. Stein, J. Lorenz, F. Dobener, **C. Ngo**, J. T. Steiner, C. Fuchs, W. Stolz, K. Volz, T. Meier, J. Hader, J. V. Moloney, S. W. Koch, and S. Chatterjee, Gain recovery dynamics in active type-II semiconductor heterostructures, Appl. Phys. Lett. **122**, 082104 (2023).
3. **C. Ngo**, S. Priyadarshi, H.T. Duc, M. Bieler, and T. Meier, Excitonic anomalous currents in semiconductor quantum wells, Phys. Rev. B **108**, 165302 (2023).
4. F. Schäfer, A. Trautmann, **C. Ngo**, J. T. Steiner, C. Fuchs, K. Volz, F. Dobener, M. Stein, T. Meier, and S. Chatterjee, Optical Stark effect in type-II semiconductor heterostructures, Phys. Rev. B **109**, 075301 (2024).
5. J. Röder, M. Gerhard, C. Fuchs, W. Stolz, W. Heimbrodt, M. Koch, **C. Ngo**, J. T. Steiner, and T. Meier, Charge-transfer magnetoexcitons in magneto absorption spectra of asymmetric type-II double quantum wells, Phys. Rev. B. **110**, 195306 (2024).

Conference Proceedings

1. A. Trautmann, R. Zuo, G. Wang, W.-R. Hannes, S. Yang, L.H. Thong, **C. Ngo**, J. T. Steiner, M. Ciappina, M. Reichelt, H. T. Duc, X. Song, W. Yang, and T. Meier, Microscopic simulations of high harmonic generation from semiconductors, Proc. SPIE **11999**, 1199909 (2022).
2. **C. Ngo**, S. Priyadarshi, H. T. Duc, M. Bieler, and T. Meier, Terahertz-induced anomalous currents following the optical excitation of excitons in semiconductor quantum wells, Proc. SPIE **12419**, 124190G (2023).

3. A. Trautmann, M. Stein, F. Schäfer, D. Anders, **C. Ngo**, J. T. Steiner, S. Chatterjee, and T. Meier, Analysis of the nonlinear optical response of excitons in type-I and type-II quantum wells inluding many-body correlations, Proc. SPIE **12419**, 124190A (2023).
4. M. Stein, F. Schäfer, D. Anders, J. Littman, M. Fey, A. Trautmann, **C. Ngo**, J. T. Steiner, M. Reichelt, C. Fuchs, K. Volz, T. Meier, and S. Chatterjee, Experimental studies of the excitonic nonlinear response of GaAs-based type-I and type-II quantum well structures interacting with optical and terahertz fields, Proc. SPIE **12419**, 1241909 (2023).

My Contributions

This study was carried out at Paderborn University from August 2020 until December 2024 under the supervision of Prof. Dr. Torsten Meier. All theoretical and numerical results presented in this thesis were obtained by myself. In Chapter 4, the experiments on anomalous currents were conducted by the group of Dr. Mark Bieler (Physikalisch-Technische Bundesanstalt, Braunschweig). The optical-pump optical-probe experiments presented in Chapter 5 were performed by the group of Prof. Dr. Sangam Chatterjee (Justus-Liebig-Universität Gießen).

The theoretical approach in Chapter 3 of this thesis is partially based on Papers 1 and 3 from the list of peer-reviewed publications. The results presented in Chapter 4 of this thesis are primarily based on the findings presented in Paper 3 from the list of peer-reviewed publications and Paper 2 from the conference proceedings.

Contents

Introduction 1

The miniaturization of semiconductor devices, specifically through advancements in low-dimensional nanostructures such as quantum wells, quantum wires, and quantum dots, has brought about a revolution in the field of electronics and photonics. Unlike quantum wires, which possess a one-dimensional structure allowing for linear electron flow, and quantum dots, which are zero-dimensional and display discrete energy levels that depend on size, quantum wells are notable for their two-dimensional structure [1]. This structure consists of a thin semiconductor layer confined between barriers with larger band gaps. Each of these nanostructures exhibits unique electronic and optical properties. One of the key factors that significantly influence these properties is the Coulomb interaction, which often governs the behavior of charge carriers within these confined structures. In bulk semiconductors, Coulomb interactions between electrons and holes play a crucial role but are often moderated by the three-dimensional nature of the material and dielectric screening effects. However, in quantum wells, the spatial confinement of charge carriers enhances the effective Coulomb interaction, leading to phenomena that are more pronounced and easier to observe than in bulk materials. This enhanced interaction is a direct consequence of the reduced dimensionality, which increases the overlap between electron and hole wave functions and diminishes the screening [2–4]. The impact of Coulomb interactions in quantum wells is multifaceted. One of the most prominent manifestations is the formation of excitons, bound states of electrons and holes. The increased binding energy of excitons in quantum wells compared to bulk semiconductors results from the stronger effective electron-hole attraction in these confined structures. This, in turn, affects the optical absorption and emission spectra of quantum wells, leading to discrete excitonic peaks below the band gap that are vital for various optoelectronic applications, such as light-emitting diodes, and laser diodes, as well as in absorbers and photodetectors [5–9]. Furthermore, Coulomb interactions influence the carrier dynamics in quantum wells. These interactions can lead to phenomena such as band gap renormalization, carrier-carrier scattering, and the formation of complex many-body states. Understanding these interactions is crucial for optimizing the performance of quantum well-based optical devices, as they affect key parameters like nonlinear optical responses, carrier mobility, recombination rates, and relaxation and dephasing.

The motion of charge carriers in crystalline solids has fundamentally different properties compared to their motion in vacuum. One very unusual property is the so-called anomalous movement of charge carriers where the charge carriers move perpendicular to an electric field even in the absence of a magnetic field. The velocity of this motion is called anomalous velocity. It is the source of several physical phenomena, such as the spin Hall effect and the anomalous Hall effect, directly impacting fields like spintronics, topological insulators, and quantum computing [10–13]. Currently, it is known that there are several different

microscopic mechanisms contributing to the anomalous velocity of charge carriers. These contributions can be divided into two main types: intrinsic and extrinsic. Intrinsic contributions were first studied in Refs. [14–18]. However, it was only rather recently discovered that they are related to the Berry curvature [19–21] of the material and depend solely on the band structure [22–24]. Extrinsic contributions are caused by scattering processes of charge carriers with impurities or phonons [25–27]. These contributions can be subdivided into three processes: side-jump scattering, anomalous distribution, and skew scattering. Recently, effects induced by the Berry curvature in semiconductors have attracted more focus [28–34]. In this thesis, we focus solely on the intrinsic contribution to the anomalous current in semiconductors quantum wells.

The pump-probe experiment is a powerful and widely used nonlinear optical technique for investigating the ultrafast dynamics of various materials, including semiconductors and their nanostructures [35, 36]. In this experiment, a short laser pulse (the pump) excites the system, creating a non-equilibrium state by promoting electrons from the valence band to the conduction band. After a controlled delay, a second laser pulse (the probe) is used to monitor the system's response, allowing one to track the evolution of excited states, the carrier dynamics, and relaxation processes on ultrafast time scales. By adjusting the time delay between the pump and probe pulses, the transient properties of the material, such as absorption, reflectivity, or transmission, can be measured as a function of time. This provides detailed insight into various physical processes, including carrier recombination, exciton dynamics, and many-body Coulomb correlations.

The objective of this thesis is to microscopically investigate excitonic effects in semiconductor quantum well (QW) structures. The first part of the thesis focuses on the influence of excitonic effects on the anomalous current induced by the Berry curvature, while the second part extends the investigation to examine the impact of higher-order Coulomb correlations on the excitonic nonlinear optical response of semiconductor QW structures, using an optical-pump optical-probe (OPOP) experiment.

This thesis is organized as follows. We start in Chapter 2 by presenting the theoretical approach and describe the interaction between classical light and the electronic system of semiconductor QWs. The extended Kane method (also referred to as the 14-band $\mathbf{k}\cdot\mathbf{p}$ method) within the envelope function approximation is used to obtain the energy band structure of gallium arsenide based (GaAs) semiconductor QWs. Next, we introduce the multiband semiconductor Bloch equations (SBE) in the length gauge (LG) to study the system's dynamics. This includes interband excitations, intraband acceleration, and the many-body Coulomb interaction, which is considered here within the time-dependent Hartree-Fock (TDHF) approximation, as well as carrier longitudinal-optical (LO) and carrier longitudinal-acoustic (LA) phonon-scattering processes which are included on the second-order Born-Markov level. The results section of this thesis is divided into two parts. In part one, we focus on excitonic anomalous currents of GaAs QWs resulting from optical interband excitation with circularly polarized light followed by the interaction with a Terahertz (THz) field. The general gauging procedure for numerically solving the SBE in the LG is presented in Chapter 3. Specifically, we construct gauge transformations

to smoothen the phase of the numerically computed Bloch functions as a function of the wave vector. The validity of the procedure is examined by comparing results obtained in the LG with those in the velocity gauge (VG) for injection currents and shift currents. In Chapter 4, we present numerical results and discussions of excitonic anomalous currents in semiconductor QWs. Our simulation results reveal the appearance of a strong anomalous current under resonant excitation at the exciton frequency. Oscillations occurring as a function of the time delay between the optical exciton pulse and the THz pulse are observed, which are due to the dynamics of excitonic wave packets when simultaneously exciting the 1s and 2s exciton states. Remarkably, these results align well with experimental data. In part two of the results section of this thesis, we extend the treatment of the many-body terms beyond the TDHF approximation and consider many-body Coulomb correlations in the perturbative and coherent regime by including correlations between polarizations and charge carriers and biexcitonic correlations. By employing the cluster expansion approach, we deal with the hierarchy problem and obtain a closed system of equations of motion (EOM) on the singlet-doublet level. A comparison is made of the excitonic nonlinear response between spatially-homogeneous type-I QW structures, where transitions are direct in space (spatially-direct), and spatially-inhomogeneous type-II QW structures, where transitions are spatially-indirect. Our theoretical analysis along with numerical results shows that the spatial inhomogeneity of type-II structures leads to an additional contribution to the excitonic nonlinear optical response already within the TDHF approximation. For strong spatial inhomogeneity this TDHF contribution may dominate over the terms that originate from many-body correlations. Finally, we summarize the results achieved in this thesis and provide a brief outlook.

Theoretical Basics 2

This chapter presents the theoretical basics which are used in the following chapters of this thesis. The detailed microscopic description of light-matter interactions in semiconductor nanostructures is constructed by combining the $\mathbf{k}\cdot\mathbf{p}$ model with the SBE. The $\mathbf{k}\cdot\mathbf{p}$ perturbation theory is a well-established method for calculating the band structure of bulk semiconductors, as well as semiconductor QW and wire systems within the envelope function approximation [37–43]. Over the decades, various $\mathbf{k}\cdot\mathbf{p}$ models have been developed, starting from 6-band and 8-band models focused on calculations around the Γ point to 14-band models that account for spin-orbit coupling, as well as QW models that incorporate strain effects [44–46]. Recently, the 30-band model and even higher-order models have been introduced, allowing for calculations over the entire Brillouin zone [47]. Once the energy band structure of semiconductor nanostructures is established, the dynamics of the photoexcited system is described by the SBE, which consists of nonlinear differential equations that characterize optical excitations within the semiconductor while accounting for many-body interactions. In this study, the many-body interactions examined include Coulomb interactions among charge carriers and the interactions between carriers and both LO and LA phonons. The cluster expansion approach is applied to deal with the hierarchy problem of many-body Coulomb interactions to obtain closed sets of EOM. The general method for solving the SBE in the LG is presented in Chapter 3. This method is applied to investigate the anomalous current in which the Coulomb interactions are restricted on the TDHF approximation. We go beyond the Hartree-Fock approximation in Chapter 5 by accounting for many-body Coulomb correlation effects to analyze the nonlinear excitonic contribution to OPOP experiments.

2.1 Extended Kane Model

2.1.1 Bulk Semiconductors

The extended Kane model (also referred to as the 14-band $\mathbf{k}\cdot\mathbf{p}$ model) is constructed based on $\mathbf{k}\cdot\mathbf{p}$ perturbation theory, which is a method that involves solving the Schrödinger equation in order to find the eigenfunctions and eigenvalues of electrons in a crystal. The Schrödinger equation describing electrons in a crystal has the following form

$$\left[\frac{p^2}{2m_0} + V_0(\mathbf{r}) + H_{\mathrm{SO}}\right]\psi_{m\mathbf{k}}(\mathbf{r}) = \varepsilon_{m\mathbf{k}}\psi_{m\mathbf{k}}(\mathbf{r}), \tag{2.1}$$

where m_0 is the electron rest mass, $V_0(\mathbf{r})$ is the periodic potential of the crystal, m is the band index, and $\mathrm{H_{SO}}$ is the term describing the spin-orbit interaction, given by

$$\mathrm{H_{SO}} = \frac{\hbar}{4m_0^2c^2}\boldsymbol{\sigma}\cdot(\boldsymbol{\nabla}V_0\times\mathbf{p})\,. \tag{2.2}$$

Here, $\boldsymbol{\sigma} = \left(\sigma_x, \sigma_y, \sigma_z\right)$ is the vector whose components are the Pauli matrices. The wave function of the electron in the periodic crystal satisfies Bloch's theorem and thus can be written as

$$\psi_{m\mathbf{k}} = e^{i\mathbf{k}\cdot\mathbf{r}}u_{m\mathbf{k}}(\mathbf{r}), \tag{2.3}$$

with $u_{n\mathbf{k}}(\mathbf{r})$ being a periodic function with the crystal lattice. The Bloch functions satisfy the orthonormality relation

$$\langle\psi_{n\mathbf{k}}|\psi_{m\mathbf{k}'}\rangle = \delta_{nm}.\delta_{\mathbf{k}\mathbf{k}'}. \tag{2.4}$$

When substituting the Bloch function from the above expression into Eq. (2.1), we obtain the following equation

$$\left[\frac{p^2}{2m_0} + V_0(\mathbf{r}) + \frac{\hbar^2k^2}{2m_0} + \frac{\hbar}{m_0}\mathbf{k}\cdot\left(\mathbf{p} + \frac{\hbar}{4m_0c^2}\sigma\times\boldsymbol{\nabla}V_0\right) + \frac{\hbar}{4m_0^2c^2}\sigma\,(\boldsymbol{\nabla}V_0\times\mathbf{p})\right]u_{m\mathbf{k}}(\mathbf{r}) = \varepsilon_{m\mathbf{k}}u_{m\mathbf{k}}(\mathbf{r}). \tag{2.5}$$

Next, we assume that the eigenfunctions and eigenvalues of the system at the Γ point ($\mathbf{k} = 0$) in the Brillouin zone are fully known. Because the eigenfunctions at the Γ point are complete, we can expand the eigenfunctions at nearby wave vectors $\mathbf{k}$ in terms of the eigenfunctions at the Γ point. We thus can write

$$u_{m\mathbf{k}}(\mathbf{r}) = \sum_n a^n_{m\mathbf{k}}u_n(\mathbf{r}), \tag{2.6}$$

where, $u_n(\mathbf{r})$ are the eigenfunctions of the system at the Γ point, satisfying the equation

$$\left[\frac{p^2}{2m_0} + V_0(\mathbf{r})\right] = \varepsilon^0_n u_n(\mathbf{r}). \tag{2.7}$$

Substituting the expression (2.6) into Eq. (2.5), we obtain the following system of equations

$$\sum_{n'}\mathrm{H}^{\mathbf{k}\cdot\mathbf{p}}_{\mathrm{nn'}}a^{n'}_{m\mathbf{k}} = \varepsilon_{m\mathbf{k}}a^n_{m\mathbf{k}}. \tag{2.8}$$

Here, $H_{nn'}$ is given by

$$H_{nn'}^{\mathbf{k}\cdot\mathbf{p}}(\mathbf{k}) = \left(\varepsilon_n^0 + \frac{\hbar^2 k^2}{2m_0}\right)\delta_{nn'} + \frac{\hbar}{m_0}\mathbf{k}\cdot\left(\langle u_n|\mathbf{p}|u_{n'}\rangle + \frac{\hbar}{4m_0c^2}\langle u_n|\boldsymbol{\sigma}\times\boldsymbol{\nabla}V_0|u_{n'}\rangle\right) + \frac{\hbar}{4m_0^2c^2}\langle u_n|\boldsymbol{\sigma}\cdot(\boldsymbol{\nabla}V_0\times\mathbf{p})|u_{n'}\rangle\,. \tag{2.9}$$

In the above expression, the first term is the diagonal component of the Hamiltonian matrix describing free electrons. The second term is the off-diagonal component describing the $\mathbf{k}\cdot\mathbf{p}$ interaction. The last term is the off-diagonal component describing the spin-orbit interaction.

In the 14-band $\mathbf{k}\cdot\mathbf{p}$ model, which is known to describe III-V semiconductors like GaAs well, the Hamiltonian consists of six bonding p-like valance bands states, two split-off band states $|7v\rangle$ ($\left|SO^{\uparrow}\right\rangle$, $\left|SO^{\downarrow}\right\rangle$) and four heavy- and light-hole band states $|8v\rangle$ ($\left|HH^{\uparrow}\right\rangle$, $\left|LH^{\uparrow}\right\rangle$, $\left|LH^{\downarrow}\right\rangle$, $\left|HH^{\downarrow}\right\rangle$), two anti-bonding s-like conduction band states $|6c\rangle$ ($\left|S^{\uparrow}\right\rangle$, $\left|S^{\downarrow}\right\rangle$), and six p-like anti-bonding conduction band states $|7c\rangle$ and $|8c\rangle$. The schematic band structure at the Γ point and related parameters for 14-band $\mathbf{k}\cdot\mathbf{p}$ model are illustrated in Fig. 2.1.

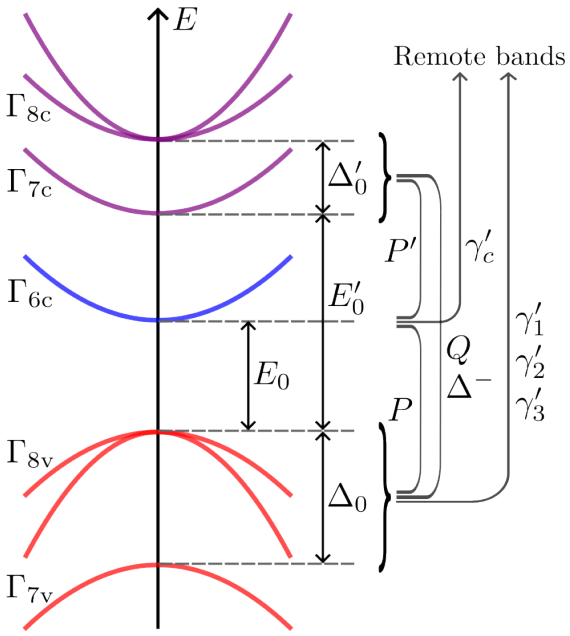

Figure 2.1: Schematic band structure at the Γ point for the 14-band $\mathbf{k}\cdot\mathbf{p}$ model. The parameters E_0, E_0', Δ_0, and Δ_0' represent the energy separation of the bands at the Γ point. The parameters P, P', Q, and Δ^- represent the couplings between the bands. The modified Luttinger parameters γ_1', γ_2', and γ_3' take into account the contributions of the remote band to the effective mass of the valance bands.

The basis functions are defined as common angular momentum eigenfunctions $|j, j_z\rangle$, that

is the s-symmetry and p-symmetry bands defined by the $j = 1/2$ and $j = 3/2$ angular momentum eigenfunctions, respectively. Using the above-mentioned basis of the 14-band $\mathbf{k}\cdot\mathbf{p}$ model, the Hamiltonian can be expressed in the form of a block matrix

$$\mathrm{H}_{14\times14} = \begin{pmatrix} \mathrm{H}_{8c8c} & \mathrm{H}_{8c7c} & \mathrm{H}_{8c6c} & \mathrm{H}_{8c8v} & \mathrm{H}_{8c7v} \\ \mathrm{H}_{7c8c} & \mathrm{H}_{7c7c} & \mathrm{H}_{7c6c} & \mathrm{H}_{7c8v} & \mathrm{H}_{7c7v} \\ \mathrm{H}_{6c8c} & \mathrm{H}_{6c7c} & \mathrm{H}_{6c6c} & \mathrm{H}_{6c8v} & \mathrm{H}_{6c7v} \\ \mathrm{H}_{8v8c} & \mathrm{H}_{8v7c} & \mathrm{H}_{8v6c} & \mathrm{H}_{8v8v} & \mathrm{H}_{8v7v} \\ \mathrm{H}_{7v8c} & \mathrm{H}_{7v7c} & \mathrm{H}_{7v6c} & \mathrm{H}_{7v8c} & \mathrm{H}_{7v7v} \end{pmatrix}. \tag{2.10}$$

It should be noted that, due to the Hermitian property, we only need to calculate the blocks in the upper or lower triangular part of the Hamiltonian matrix; the remaining blocks can be obtained by taking the transpose and complex conjugate. For the coordinate system where the wave vector k_x, k_y, and k_z correspond to the principal crystallographic direction $[1\,0\,0]$, $[0\,1\,0]$ and $[0\,0\,1]$, respectively, the block matrices of the 14-band $\mathbf{k}\cdot\mathbf{p}$ Hamiltonian are given by

$$\begin{aligned}
\mathrm{H}^{\mathbf{k}\cdot\mathbf{p}}_{8c8c} &= E_0' + \Delta_0', \\
\mathrm{H}^{\mathbf{k}\cdot\mathbf{p}}_{7c7c} &= E_0', \\
\mathrm{H}^{\mathbf{k}\cdot\mathbf{p}}_{6c6c} &= E_0 + \frac{\hbar^2 k^2}{2m'}, \\
\mathrm{H}^{\mathbf{k}\cdot\mathbf{p}}_{8v8v} &= -\frac{\hbar^2}{2m_0}\Bigg\{\gamma_1' k^2 - 2\gamma_2'\left[\left(J_x^2 - \frac{1}{3}J^2\right)k_x^2 + \text{c.p.}\right] - 4\gamma_3'\left[\{J_x, J_y\}\{k_x, ky\} + \text{c.p.}\right] \\
&\qquad + \frac{2}{\sqrt{3}}C_k\left[\{J_x, J_y^2 - J_z^2\}k_x + \text{c.p.}\right]\Bigg\}, \\
\mathrm{H}^{\mathbf{k}\cdot\mathbf{p}}_{7v7v} &= -\Delta_0 - \frac{\hbar^2}{2m_0}\gamma_1' k^2, \\
\mathrm{H}^{\mathbf{k}\cdot\mathbf{p}}_{8c7c} &= 0, \\
\mathrm{H}^{\mathbf{k}\cdot\mathbf{p}}_{8c6c} &= -\sqrt{3}P'(U_x k_x + \text{c.p.}), \\
\mathrm{H}^{\mathbf{k}\cdot\mathbf{p}}_{8c8v} &= -\frac{2}{3}Q\big(\{J_y, J_z\}k_x + \text{c.p.}\big) + \frac{1}{3}\Delta^-, \\
\mathrm{H}^{\mathbf{k}\cdot\mathbf{p}}_{8c7v} &= -2Q\big(U_{yz}k_x + \text{c.p.}\big), \\
\mathrm{H}^{\mathbf{k}\cdot\mathbf{p}}_{7c6c} &= \frac{1}{\sqrt{3}}P'(\sigma_x k_x + \text{c.p.}), \\
\mathrm{H}^{\mathbf{k}\cdot\mathbf{p}}_{6c8v} &= -2Q\big(T_{yz}k_x + \text{c.p.}\big), \\
\mathrm{H}^{\mathbf{k}\cdot\mathbf{p}}_{7c7v} &= -\frac{2}{3}\Delta^-, \\
\mathrm{H}^{\mathbf{k}\cdot\mathbf{p}}_{6c8v} &= \sqrt{3}P\mathbf{T}\cdot\mathbf{k}, \\
\mathrm{H}^{\mathbf{k}\cdot\mathbf{p}}_{6c7v} &= -\frac{1}{\sqrt{3}}P\boldsymbol{\sigma}\cdot\mathbf{k},
\end{aligned}$$

$$\mathrm{H}_{8\mathrm{v}7\mathrm{v}}^{\mathbf{k}\cdot\mathbf{p}} = -\frac{\hbar^2}{2m_0}\left[-6\gamma_2'\left(U_{xx}k_x^2 + \text{c.p.}\right) - 12\gamma_3'\left(U_{xy}\{k_x, k_y\} + \text{c.p.}\right)\right] - i\sqrt{3}C_k\left(U_{yz}k_x + \text{c.p.}\right). \tag{2.11}$$

Here, $\{A, B\} = 1/2(AB + BA)$ denotes the anticommutator, and c.p. stands for cyclic permutations. The matrices $\mathbf{J} = \left(J_x, J_y, J_z\right)$ represent the angular momentum for $j = 3/2$. The matrices $\mathbf{T} = \left(T_x, T_y, T_z\right)$ describe the coupling between the conduction and valence bands and transform as the components of a Cartesian tensor, denoted by T_{ij}, where i and j correspond to x, y and z. The matrices $\mathbf{U} = \left(U_x, U_y, U_z\right)$ represent the coupling between valance and split-off bands and are given by $U_i = T_i^\dagger$. All of these matrices are provided in Appendix A.1 and are also described in Ref. [48]. For different orientations of wave vectors k_x, k_y, k_z, the corresponding Hamiltonian can be obtained using Euler rotations (see Appendix A.3 for more details).

In the presence of strain effects, an additional term is present in the total Hamiltonian $\mathrm{H} = \mathrm{H}^{\mathbf{k}\cdot\mathbf{p}} + \mathrm{H}^{\varepsilon}$, with H^{ε} being the Bir-Pikus Hamiltonian [43]. The strain effect is considered only for the p-like valance bands and s-like conduction bands, i.e., ignoring the p-like conduction bands as the parameters for these bands are unknown. The block matrices of the strain Hamiltonian in the first order of the strain tensor components ε_{ij} are given by

$$\begin{aligned}
\mathrm{H}_{6\mathrm{c}6\mathrm{c}}^{\varepsilon} &= a_{\mathrm{c}}\,\mathrm{Tr}\,\varepsilon, \\
\mathrm{H}_{8\mathrm{v}8\mathrm{v}}^{\varepsilon} &= a_{\mathrm{v}}\,\mathrm{Tr}\,\varepsilon - b_{\mathrm{v}}\left[\left(J_x^2 - \frac{1}{3}J^2\right)\varepsilon_{xx} + \text{c.p.}\right] - \frac{d_{\mathrm{v}}}{\sqrt{3}}\left(2\{J_x, J_y\}\varepsilon_{xy} + \text{c.p.}\right), \\
\mathrm{H}_{7\mathrm{v}7\mathrm{v}}^{\varepsilon} &= a_{\mathrm{v}}\,\mathrm{Tr}\,\varepsilon, \\
\mathrm{H}_{6\mathrm{c}8\mathrm{v}}^{\varepsilon} &= i\sqrt{3}C_2\left(T_x\varepsilon_{yz} + \text{c.p.}\right), \\
\mathrm{H}_{6\mathrm{c}7\mathrm{v}}^{\varepsilon} &= -\frac{i}{\sqrt{3}}C_2\left(\sigma_x\varepsilon_{yz} + \text{c.p.}\right), \\
\mathrm{H}_{8\mathrm{v}7\mathrm{v}}^{\varepsilon} &= -3b_{\mathrm{v}}(U_{xx}\varepsilon_{xx} + \text{c.p.}) - \sqrt{3}d_{\mathrm{v}}\left(2U_{xy}\varepsilon_{xy} + \text{c.p.}\right),
\end{aligned} \tag{2.12}$$

where $\mathrm{Tr}\,\varepsilon = \varepsilon_{xx} + \varepsilon_{yy} + \varepsilon_{zz}$ and a_{c}, a_{v}, b_{v}, d_{v} are the deformation potentials. The term proportional to the C_2 parameter results from the inversion asymmetry. For the strained layer of a semiconductor QW grown on a [0 0 1]-oriented substrate, the components of the strain tensors are [49]

$$\varepsilon_{\parallel} = \frac{a_{\mathrm{S}}}{a_{\mathrm{L}}} - 1,, \quad \varepsilon_{xx} = \varepsilon_{yy} = \varepsilon_{\parallel},, \quad \varepsilon_{zz} = -2\frac{C_{12}}{C_{11}}\varepsilon_{\parallel},, \quad \varepsilon_{xy} = \varepsilon_{yz} = \varepsilon_{zx} = 0, \tag{2.13}$$

where $\varepsilon_{\parallel}$ is the in-plane strain, a_{S} and a_L denote the lattice constants of the substrate and the layer material, respectively. C_{ij} represent the elastic stiffness constants. The negative value of the in-plane strain corresponds to compressive strain, whereas the positive value corresponds to tensile strain in the layer material.

2.1.2 Semiconductor Quantum Wells

In the framework of the 14-band $\mathbf{k}\cdot\mathbf{p}$ model, within the envelope function approximation, the wave function of an electron in a semiconductor QW grown along the z axis is written as

$$\psi_{\lambda\mathbf{k}_\parallel}(\mathbf{r}) = \frac{1}{L^{3/2}} e^{i\mathbf{k}_\parallel\cdot\mathbf{r}_\parallel} \sum_{n=1}^{14} f^{\lambda}_{n\mathbf{k}_\parallel}(z) u_{n\mathbf{0}}(\mathbf{r}), \tag{2.14}$$

where λ denotes the band index, $\mathbf{k}_\parallel \equiv \mathbf{k} = (k_x, k_y)$ is the in-plane wave vector, and $u_{n\mathbf{0}}(\mathbf{r})$ are the basis functions of the 14-band $\mathbf{k}\cdot\mathbf{p}$ model. $f^{\lambda}_{n\mathbf{k}}(z)$ is a slowly varying envelope function that satisfies the effective mass equation

$$\sum_{n=1}^{14}\left[\mathrm{H}^{\mathbf{k}\cdot\mathbf{p}}_{nm}\left(\mathbf{k}, -i\frac{\partial}{\partial z}\right) + V^{\mathrm{conf}}(z)\delta_{nm}\right] f^{\lambda}_{m\mathbf{k}}(z) = \varepsilon^{\lambda}_{\mathbf{k}} f^{\lambda}_{n\mathbf{k}}(z). \tag{2.15}$$

Here, $\varepsilon^{\lambda}_{\mathbf{k}}$ is the band energy, and $\mathrm{H}_{nn'}$ are the Hamiltonian matrix elements of the bulk semiconductor, where the operator $\hat{k}_z$ is replaced by $-i\,\partial k/\partial z$. $V^{\mathrm{conf}}(z)$ is the band-offset potentials of the QW, which is introduced to describe the band discontinuity at the interfaces of materials that form the QW, as illustrated in Fig. 2.2.

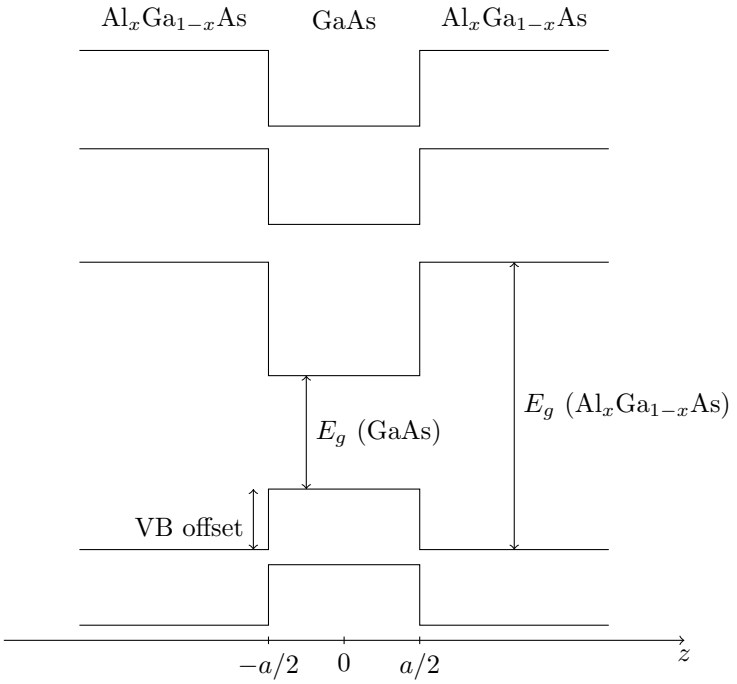

Figure 2.2: Cross-sectional diagram of a GaAs semiconductor QW within the 14-band $\mathbf{k}\cdot\mathbf{p}$ model.

Note that replacing the operator $\hat{k}_z$ can result in non-Hermitian terms in the Hamiltonian.

To ensure the Hamiltonian remains Hermitian, we write these terms in a symmetrized form as follows

$$h(z)\hat{k}_z \rightarrow -\frac{i}{2}\left(\frac{\partial}{\partial z}h(z) + h(z)\frac{\partial}{\partial z}\right),$$
$$h(z)\hat{k}_z^2 \rightarrow -\frac{\partial}{\partial z}h(z)\frac{\partial}{\partial z}.$$

To solve Eq. (2.15), the envelope function is expanded in terms of plane waves as

$$f_{n\mathbf{k}}^{\lambda}(z) = \sum_{m=1}^{N} c_{nm\mathbf{k}}^{\lambda}\phi_m(z), \tag{2.16}$$

where

$$\phi_m(z) = \begin{cases} \sqrt{\frac{2}{L_z}}\sin\left(\frac{m\pi}{L_z z}\right), & 0 \leq z \leq L_z, \\ 0, & \text{otherwise.} \end{cases} \tag{2.17}$$

In this case, L_z is a normalization constant chosen to be several times the thickness of the QW. Substituting expression (2.16) into Eq. (2.15) and multiplying both sides by $\phi_m^*(z)$, followed by integration with respect to z, we obtain the following $14N \times 14N$ matrix eigenvalue problem

$$\sum_{n'=1}^{14}\sum_{l=1}^{N} \langle\phi_l|\mathrm{H}_{nn'} + V_n\delta_{nn'}|\phi_{l'}\rangle\, c_{\mu\mathbf{k}}^{n'l'} = \varepsilon_{\mu\mathbf{k}}c_{\mu\mathbf{k}}^{nl}. \tag{2.18}$$

For given wave vectors $\mathbf{k}$, the eigenvalues $\varepsilon_{\mu\mathbf{k}}$, which represent the band structure, and the expansion coefficients of the envelope function, which determine the eigenstate, $|u_\lambda(\mathbf{k})\rangle$ can be obtained from numerically diagonalizing the above $14N \times 14N$ matrix. It is important to mention that the numerical diagonalization procedure introduces arbitrary phases in the eigenstates at each $\mathbf{k}$, causing phase discontinuities in $|u_\lambda(\mathbf{k})\rangle$ as $\mathbf{k}$ changes continuously. As a result, these eigenstates lack uniqueness and are only defined up to a phase factor. Additionally, such a procedure also imposes unitary gauge freedom within the degenerate subspace, leading to an arbitrary unitary mixing of degenerate states at each $\mathbf{k}$. Consequently, the numerically obtained eigenstates do not vary smoothly with respect to $\mathbf{k}$. To ensure that $|u_\lambda(\mathbf{k})\rangle$ are smooth and differentiable with respect to $\mathbf{k}$, a local gauge transformation is applied to the Bloch states, as detailed in Chapter 3.

2.2 Multiband Semiconductor Bloch Equations

2.2.1 Total Hamiltonian

In the single-particle basis formed by the Bloch states, the total many-body Hamiltonian of the photoexcited semiconductor QW system can be expressed in terms of five components as [4, 50]

$$\mathrm{H} = \mathrm{H}_0 + \mathrm{H}_{\mathrm{int}} + \mathrm{H}_{\mathrm{C}} + \mathrm{H}_{\mathrm{phon}} + \mathrm{H}_{\mathrm{P}}. \tag{2.19}$$

The first term H_0 represents non-interacting Bloch electrons and is given by

$$\mathrm{H}_0 = \sum_{\lambda,\mathbf{k}} \varepsilon^{\lambda}_{\mathbf{k}} a^{\dagger}_{\lambda,\mathbf{k}} a_{\lambda,\mathbf{k}}, \tag{2.20}$$

where $a^{\dagger}_{\lambda,\mathbf{k}}$ and $a_{\lambda,\mathbf{k}}$ are the creation and annihilation operators of an electron in band λ with wave vector $\mathbf{k}$ and $\varepsilon^{\lambda}_{\mathbf{k}}$ is the band energy obtained by diagonalization of band structure Hamiltonian. The second term of Eq. (2.19) describes the light-matter interaction that in the LG is written as

$$\mathrm{H}_{\mathrm{int}} = e\mathbf{E}(t) \cdot \sum_{\lambda,\lambda',\mathbf{k}} \mathbf{r}^{\lambda\lambda'}_{\mathbf{k}\mathbf{k}'} a^{\dagger}_{\lambda,\mathbf{k}} a_{\lambda',\mathbf{k}'}, \tag{2.21}$$

where $\mathbf{E}(t)$ denotes the electric field of the laser and $\mathbf{r}^{\lambda\lambda'}_{\mathbf{k}\mathbf{k}'}$ represents the matrix elements of the position operator and is given by [18, 51–53]

$$\mathbf{r}^{\lambda\lambda'}_{\mathbf{k}\mathbf{k}'} = \left[\boldsymbol{\xi}^{\lambda\lambda'}_{\mathbf{k}} + \Delta_{\lambda\lambda'}\left(\boldsymbol{\vartheta}^{\lambda\lambda'}_{\mathbf{k}} + i\boldsymbol{\nabla}_{\mathbf{k}}\right)\right]\delta(\mathbf{k}-\mathbf{k}'). \tag{2.22}$$

Here, for convenience, following Virk and Sipe [53], we split the position operator $\mathbf{r}^{\lambda\lambda'}_{\mathbf{k}\mathbf{k}'}$ into an interblock part $\boldsymbol{\xi}^{\lambda\lambda'}_{\mathbf{k}} = i\langle u_{\lambda\mathbf{k}}|\boldsymbol{\nabla}_{\mathbf{k}} u_{\lambda'\mathbf{k}}\rangle\,(1-\Delta_{\lambda\lambda'})$, and an intrablock part $\boldsymbol{\vartheta}^{\lambda\lambda'}_{\mathbf{k}} = i\langle u_{\lambda\mathbf{k}}|\boldsymbol{\nabla}_{\mathbf{k}} u_{\lambda'\mathbf{k}}\rangle\,\Delta_{\lambda\lambda'}$. The interblock part is also known as the transition interband dipole matrix element, while the intrablock part is called the non-Abelian Berry connection. The elements of the matrix Δ are set as unity within intrablock and zero otherwise. The intrablock is defined within single states or between degenerate states or near degenerate states where the corresponding eigenvalues have crossed or nearly crossed at some $\mathbf{k}$, while the interblock is defined between non-degenerate states. This scheme is demonstrated in Fig. 2.3.

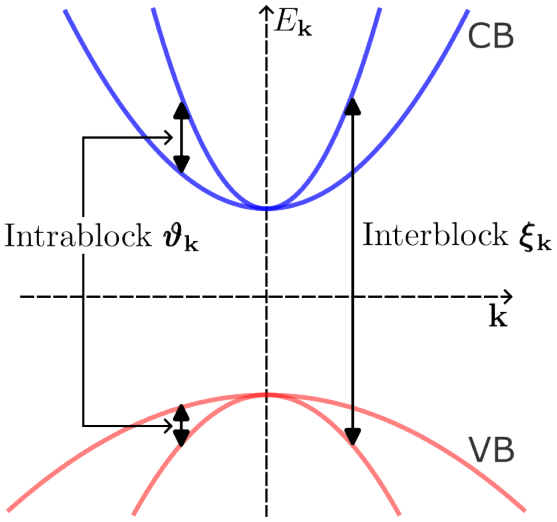

Figure 2.3: Schematic illustration of interblock and intrablock matrix elements.

Within the LG, it is possible to distinguish between interband transition processes, which are induced by the interband transition dipole matrix element and the intraband acceleration, which is determined by the gradient term in Eq. (2.22). According to the classical acceleration theorem, electrons are accelerated in their respective bands [32]. The interband dipole matrix element can be obtained from the velocity operator via the relation

$$\xi_{\mathbf{k}}^{\lambda\lambda'} = -i\hbar \frac{\mathbf{v}_{\mathbf{k}}^{\lambda\lambda'}}{\varepsilon_{\mathbf{k}}^{\lambda} - \varepsilon_{\mathbf{k}}^{\lambda'}}. \tag{2.23}$$

In turn, with the envelope function in Eq. (2.16) for the QW, the elements of the velocity matrix read

$$\mathbf{v}_{\mathbf{k}}^{\lambda\lambda'} = \int \mathrm{d}z \sum_{n,m=1}^{14} f_{n,\mathbf{k}}^{\lambda *}(z) \left(\frac{1}{\hbar} \boldsymbol{\nabla}_{\mathbf{k}} \mathrm{H}_{\mathbf{k}}^{\mathbf{k}\cdot\mathbf{p}} \right)_{nm} f_{m,\mathbf{k}}^{\lambda'}(z). \tag{2.24}$$

The many-body Coulomb interaction between electrons in bands λ_1, λ_2, λ_3, and λ_4, involving the exchange of momentum $\hbar\mathbf{q}$ is given by

$$\mathrm{H_C} = \frac{1}{2} \sum_{\substack{\lambda_1,\lambda_2,\lambda_3,\lambda_4 \\ \mathbf{k},\mathbf{k}',\mathbf{q}}} V_{\mathbf{k},\mathbf{k}',\mathbf{q}}^{\lambda_1\lambda_2\lambda_3\lambda_4} a_{\lambda_1,\mathbf{k}+\mathbf{q}}^{\dagger} a_{\lambda_2,\mathbf{k}'-\mathbf{q}}^{\dagger} a_{\lambda_3,\mathbf{k}'} a_{\lambda_4,\mathbf{k}}, \tag{2.25}$$

where, in the QW, the Coulomb matrix elements are given by [4, 50, 54]

$$V^{\lambda_1\lambda_2\lambda_3\lambda_4}_{\mathbf{k},\mathbf{k}',\mathbf{q}} = \frac{2\pi e^2}{\epsilon_\infty L^2}\frac{1}{|\mathbf{q}|}\iint \mathrm{d}z\,\mathrm{d}z'\, e^{-|\mathbf{q}||z-z'|}\sum_{n=1}^{14} f^{\lambda_1 *}_{n,\mathbf{k}+\mathbf{q}}(z) f^{\lambda_4}_{n,\mathbf{k}}(z)\sum_{n=1}^{14} f^{\lambda_2 *}_{n,\mathbf{k}'-\mathbf{q}}(z') f^{\lambda_3}_{n,\mathbf{k}'}(z'). \tag{2.26}$$

Here, e is the notation of the elementary charge, ε_0, ϵ_∞, and L^2 are the notations of the vacuum permittivity, relative permittivity at high frequencies of the unexcited QW, and QW area, respectively.

In addition to many-body Coulomb interactions, electrons-phonons interactions are also considered and represent an additional many-body contribution. These interactions lead to dephasing and relaxation processes in the material, as well as to the formation of quasi-particles (i.e., polarons which, however, are not considered here) [55]. The Hamiltonian of the noninteracting phonons is the fourth term in Eq. (2.19) and can be written as

$$\mathrm{H}_{\mathrm{phon}} = \sum_{\alpha,\mathbf{q},q_\perp} \hbar\omega^{\alpha}_{\mathbf{q},q_\perp}\left(b^{\dagger}_{\alpha,\mathbf{q},q_\perp} b_{\alpha,\mathbf{q},q_\perp} + \frac{1}{2}\right), \tag{2.27}$$

where $b^{\dagger}_{\alpha,\mathbf{q},q_\perp}$ and $b_{\alpha,\mathbf{q},q_\perp}$ are the creation and annihilation operators of phonons in branch α with wave vector $(\mathbf{q}, q_\perp)$ and energy $\hbar\omega^{\alpha}_{\mathbf{q},q_\perp}$.

The last term in Eq. (2.19) is the interaction between electrons and phonons and is described by

$$\mathrm{H}_{\mathrm{P}} = \sum_{\alpha,\lambda,\lambda',\mathbf{k},\mathbf{q},q_\perp} g^{\alpha,\lambda\lambda'}_{\mathbf{k}+\mathbf{q},\mathbf{k},q_\perp} a^{\dagger}_{\lambda,\mathbf{k}+\mathbf{q}} a_{\lambda',\mathbf{k}}\left(b_{\alpha,\mathbf{q},q_\perp} + b^{\dagger}_{\alpha,\mathbf{q},q_\perp}\right), \tag{2.28}$$

with

$$g^{\alpha,\lambda\lambda'}_{\mathbf{k}+\mathbf{q},\mathbf{k},q_\perp} = g^{\alpha}_{\mathbf{q},q_\perp}\gamma^{\lambda\lambda'}_{\mathbf{k}+\mathbf{q},\mathbf{k},q_\perp} \tag{2.29}$$

being the coupling matrix elements between electrons and longitudinal phonons [55–58], where the structure parameter reads

$$\gamma^{\lambda\lambda'}_{\mathbf{k}+\mathbf{q},\mathbf{k},q_\perp} = \int \mathrm{d}z\, e^{iq_\perp z}\sum_{n=1}^{14} f^{\lambda *}_{n,\mathbf{k}+\mathbf{q}}(z) f^{\lambda'}_{n,\mathbf{k}}(z). \tag{2.30}$$

In the case of electrons coupling to LO phonons, the coupling matrix elements g^{LO} are defined by the Fröhlich relation

$$\left(g^{\mathrm{LO}}_{\mathbf{q},q_\perp}\right)^2 = \frac{1}{2}\hbar\omega^{\mathrm{LO}}\frac{4\pi e^2}{L^2 L_z}\frac{1}{\mathbf{q}^2 + q_\perp^2}\left(\frac{1}{\epsilon_\infty} - \frac{1}{\epsilon_0}\right), \tag{2.31}$$

and for the case of the coupling to LA phonons, they are given by

$$\left(g^{\mathrm{LA}}_{\mathbf{q},q_\perp}\right)^2 = \frac{\hbar|D|^2\sqrt{\mathbf{q}^2+q_\perp^2}}{2c_{\mathrm{LA}}\rho_{\mathrm{M}}L^2L_z}. \tag{2.32}$$

Here, D represents the deformation constant, c_{LA} is the LA-velocity of sound, ρ_{M} denotes the mass density of the lattice, and ϵ_0 is the low-frequency (static) relative permittivity. L_z is the thickness of the QW, which is simplified when summing over the wave vectors. In cases of GaAs material, these parameters $\epsilon_0 = 12.9$, $\epsilon_\infty = 10.9$, $\hbar\omega^{\mathrm{LO}} = 36\,\mathrm{meV}$, and $D = 8.6\,\mathrm{eV}$ [50, 55, 59].

2.2.2 Cluster Expansion Approach

In the Heisenberg's picture, the time evolution of an operator O is obtained from the Heisenberg equation of motion as

$$i\hbar\frac{\partial}{\partial t}\langle O\rangle = \langle[O,\mathrm{H}]\rangle\,. \tag{2.33}$$

Here, H denotes the system's Hamiltonian (2.19), which was introduced in the previous section. In the photoexcited semiconductor, various phenomena can be analyzed through the single-particle expectation values defined as $\left\langle a^\dagger_{\lambda,\mathbf{k}}a_{\lambda',\mathbf{k}'}\right\rangle$. Under the homogeneous excitation conditions considered in this study, momentum is conserved in all physical quantities. As a result, only elements diagonal in $\mathbf{k}$ are generated, given by $P^{\lambda\lambda'}_{\mathbf{k}} = \left\langle a^\dagger_{\lambda,\mathbf{k}}a_{\lambda',\mathbf{k}}\right\rangle$. This quantity provides a comprehensive description of the occupations and coherences within the system. For $\lambda = \lambda'$, it describes the electron and hole occupations or distributions, expressed as

$$n^{\mathrm{e}}_{\mathbf{k}} = \left\langle a^\dagger_{\mathrm{c},\mathbf{k}}a_{\mathrm{c},\mathbf{k}}\right\rangle, \qquad n^{\mathrm{h}}_{\mathbf{k}} = 1 - \left\langle a^\dagger_{\mathrm{v},\mathbf{k}}a_{\mathrm{v},\mathbf{k}}\right\rangle. \tag{2.34}$$

For $\lambda = \mathrm{v}$ and $\lambda' = \mathrm{c}$, it describes the interband coherence (also referred to as microscopic polarization) between the valence and conduction bands

$$p_{\mathbf{k}} = \left\langle a^\dagger_{\mathrm{v},\mathbf{k}}a_{\mathrm{c},\mathbf{k}}\right\rangle. \tag{2.35}$$

For λ and λ' within the same band but different subbands, it represents the intersubband coherences between valence subbands and between conduction subbands

$$n^{\mathrm{vv}'}_{\mathbf{k}} = \left\langle a^\dagger_{\mathrm{v},\mathbf{k}}a_{\mathrm{v}',\mathbf{k}}\right\rangle, \qquad n^{\mathrm{cc}'}_{\mathbf{k}} = \left\langle a^\dagger_{\mathrm{c},\mathbf{k}}a_{\mathrm{c}',\mathbf{k}}\right\rangle. \tag{2.36}$$

It is widely known that for the many-body Coulomb and the electron-phonon interactions, the EOM for the single-particle quantities $P^{\lambda\lambda'}_{\mathbf{k}}$ are not a closed set of equations due to the many-body hierarchy. In particular, the commutator between $P^{\lambda\lambda'}_{\mathbf{k}}$ and the Coulomb

interaction produces the following terms

$$i\hbar\frac{\partial}{\partial t}\left\langle a^\dagger_{\lambda,\mathbf{k}}a_{\lambda',\mathbf{k}}\right\rangle\Big|_{\mathrm{C}} = \sum_{\lambda_2,\lambda_3,\lambda_4,\mathbf{k}',\mathbf{q}} V^{\lambda'\lambda_2,\lambda_3,\lambda_4}_{\mathbf{k}-\mathbf{q},\mathbf{k}',\mathbf{q}}\left\langle a^\dagger_{\lambda,\mathbf{k}}a^\dagger_{\lambda_2,\mathbf{k}'-\mathbf{q}}a_{\lambda_3,\mathbf{k}'}a_{\lambda_4,\mathbf{k}-\mathbf{q}}\right\rangle - \sum_{\lambda_1,\lambda_2,\lambda_3,\mathbf{k}',\mathbf{q}} V^{\lambda_1,\lambda_2,\lambda_3,\lambda}_{\mathbf{k},\mathbf{k}'+\mathbf{q},\mathbf{q}}\left\langle a^\dagger_{\lambda_1,\mathbf{k}+\mathbf{q}}a^\dagger_{\lambda_2,\mathbf{k}'}a_{\lambda_3,\mathbf{k}'+\mathbf{q}}a_{\lambda',\lambda',\mathbf{k}}\right\rangle. \tag{2.37}$$

This equation shows that the Coulomb interaction introduces correlations, i.e., the coupling of single-particle terms to two-particle terms. This pattern continues for equations of two-particle terms and higher-order terms, generating a hierarchy of equations that prevents a straightforward solution. Schematically, the hierarchy problem is described by the following expression

$$i\hbar\frac{\partial}{\partial t}\langle N\rangle = T[\langle N\rangle] + V[\langle N+1\rangle], \tag{2.38}$$

here, $\langle N\rangle$ is the expectation value of N-particles involving N fermion creation and N fermion annihilation operators

$$\langle N\rangle = \left\langle a^\dagger_{\lambda_1,\mathbf{k}_1}\dots a^\dagger_{\lambda_N,\mathbf{k}_N}a_{\lambda'_1,\mathbf{k}'_1}\dots a_{\lambda'_N,\mathbf{k}'_N}\right\rangle. \tag{2.39}$$

In the expression (2.38), the functional $T[\langle N\rangle]$ represents the non-interacting part of the Hamiltonian, e.g., the band structure, and $V[\langle N+1\rangle]$ represents many-body interactions which introduce a coupling to the next level of $(N+1)$-particle correlations, demonstrating the recursive nature of the hierarchy. This recursive structure can typically not be solved exactly but requires a decoupling to obtain a closed set of equations, which is achieved through approximation methods.

There are several well-established methods that can approximate this hierarchy problem, such as the dynamics-controlled truncation scheme (DCT) [4, 60–67], the second-order Born approximation [4, 57, 68–71], and the cluster expansion method [55, 58, 72–82]. Note that the two formers are subsets of the more general cluster expansion method [55]. For instance, the equations obtained from the DCT scheme in the $\chi^{(3)}$ limit are entirely encompassed within the singlet-doublet approximation of the cluster expansion. The cluster expansion offers the advantage of providing a more accurate description in scenarios involving a strong external field or a fully incoherent system.

In this thesis, we leverage the robustness of the cluster expansion approach to systematically truncate the hierarchy of many-body correlations. The main idea is to represent the correlations among N particles in terms of lower-order correlations called clusters, which refer to a subset of particles correlated with each other. By keeping clusters up to a specified order and factorizing, i.e., approximating high-order clusters, we realize a consistent approximation. At the lowest level, where the expectation value $\langle N\rangle$ is expressed as N

independent single-particle expectation $\langle 1 \rangle$ as

$$\langle N \rangle_{\mathrm{S}} = \langle N \rangle_{\mathrm{HF}} = \sum_{\sigma} (-1)^{\sigma} \prod_{i=1}^{N} \left\langle a^{\dagger}_{\lambda_i, \mathbf{k}_i} a_{\lambda'_{\sigma[i]}, \mathbf{k}'_{\sigma[i]}} \right\rangle, \tag{2.40}$$

where σ is a permutation of $\left(\lambda'_i, \mathbf{k}'_i\right)$ with sign $(-1)^{\sigma}$. The above factorial with the subscript HF is well-known as the Hartree-Fock approximation.

For higher levels, the N-particle correlation, $\langle N \rangle$, will be generalized by expressing it into possible lower-order clusters, i.e., $\langle 1 \rangle$, $\langle 2 \rangle$, ..., $\langle N \rangle$, which are denoted for independent single particles (singlets), correlated pairs (doublets), and correlated N-particle clusters, respectively. This procedure is accomplished recursively via

$$\langle 1 \rangle = \langle 1 \rangle_{\mathrm{S}}, \tag{2.41}$$

$$\langle 2 \rangle = \langle 2 \rangle_{\mathrm{S}} + \Delta \langle 2 \rangle, \tag{2.42}$$

$$\langle 3 \rangle = \langle 3 \rangle_{\mathrm{S}} + \langle 1 \rangle \Delta \langle 2 \rangle + \Delta \langle 3 \rangle, \tag{2.43}$$

$$\langle N \rangle = \langle N \rangle_{\mathrm{S}} + \langle N-4 \rangle \Delta \langle 2 \rangle \Delta \langle 2 \rangle + \ldots + \langle N-3 \rangle \Delta \langle 3 \rangle + \ldots + \Delta \langle N \rangle. \tag{2.44}$$

In this formulation, the term $\langle N \rangle$ encompasses all possible correlations among N particles, including the purely correlated component $\Delta \langle N \rangle$. Thus, $\Delta \langle N \rangle$ can be obtained by subtracting all lower-order components from the fully correlated expectation value $\langle N \rangle$.

This study limits the consideration of contributions up to doublet levels. The dynamics of the singlet and doublet quantities can be examined using the following general form

$$i\hbar \frac{\partial}{\partial t} \langle 1 \rangle = T_1[\langle 1 \rangle] + V_1[\langle 1 \rangle_{\mathrm{S}}] + V_1[\Delta \langle 2 \rangle], \tag{2.45}$$

$$i\hbar \frac{\partial}{\partial t} \Delta \langle 2 \rangle = T_2[\langle 2 \rangle] + V_2[\langle 3 \rangle_{\mathrm{SD}}] + V_2[\Delta \langle 3 \rangle], \tag{2.46}$$

where the singlet-doublet factorization $\langle 3 \rangle_{\mathrm{SD}} = \langle 3 \rangle_{\mathrm{S}} + \langle 1 \rangle \Delta \langle 2 \rangle$. Within the singlet-doublet approximation, pure triplet correlations $\Delta \langle 3 \rangle$ and higher-order correlations are omitted. This results in closed Eqs. (2.45) (2.46). In the singlet approximation, where correlations are disregarded, the two-particle correlations, $V_1[\Delta \langle 2 \rangle]$ in Eq. (2.45), are also neglected. It should be noted that sometimes $V_1[\Delta \langle 2 \rangle]$ as well as $\Delta \langle 3 \rangle$ are not simply set to zero; instead, they are often replaced by phenomenological models, such as a simple constant dephasing time or a more accurate diffusive dephasing model [58], which try to account approximate for higher-order effects. The schematic representation of the approximations behind Eqs. (2.45) and (2.46) are illustrated in Fig. 2.4

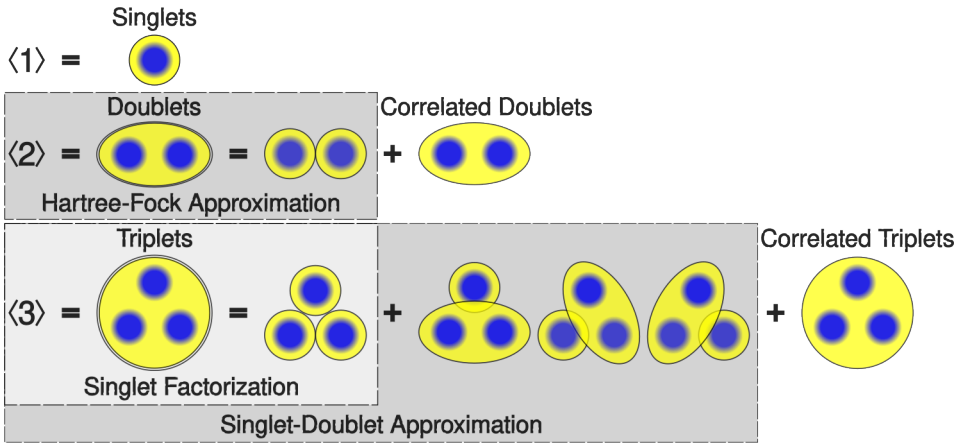

Figure 2.4: Schematic representation of the cluster expansion approach up to the singlet-doublet level. The singlets, full doublet correlations, and full triplet correlations are introduced in the first, second, and third rows, respectively. The second row illustrates the decomposition of doublets into their singlet components and the correlated part. The third row demonstrates the expansion of triplets into combinations of three singlets, correlated doublets paired with singlets, and correlated triplets.

Applying the cluster expansion approach at a singlet-doublet level, we can obtain the EOM for $P^{\lambda\lambda'}_{\mathbf{k}}$ as following

$$i\hbar\frac{\partial}{\partial t}P^{\lambda\lambda'}_{\mathbf{k}} = \left(\varepsilon^{\lambda'}_{\mathbf{k}} - \varepsilon^{\lambda}_{\mathbf{k}}\right)P^{\lambda\lambda'}_{\mathbf{k}} + \hbar\sum_{\mu}\left(\Omega^{\mu\lambda}_{\mathbf{k}}P^{\mu\lambda'}_{\mathbf{k}} - \Omega^{\lambda'\mu}_{\mathbf{k}}P^{\lambda\mu}_{\mathbf{k}}\right) + \sum_{\lambda'',\mu,\mu',\mathbf{k}',\mathbf{q}}\left[V^{\lambda'\mu\mu'\lambda''}_{\mathbf{k}-\mathbf{q},\mathbf{k}',\mathbf{q}}c^{\mathbf{q},\mathbf{k}',\mathbf{k}}_{\lambda\mu\mu'\lambda''} - \left(V^{\lambda\mu\mu'\lambda''}_{\mathbf{k}-\mathbf{q},\mathbf{k}',\mathbf{q}}c^{\mathbf{q},\mathbf{k}',\mathbf{k}}_{\lambda'\mu\mu'\lambda''}\right)^*\right]. \tag{2.47}$$

Here, the pure two-particle correlations have the form

$$c^{\mathbf{q},\mathbf{k}',\mathbf{k}}_{\lambda\mu\mu'\lambda'} = \Delta\left\langle a^{\dagger}_{\lambda,\mathbf{k}}a^{\dagger}_{\mu,\mathbf{k}'}a_{\mu',\mathbf{k}'+\mathbf{q}}a_{\lambda',\mathbf{k}-\mathbf{q}}\right\rangle, \tag{2.48}$$

and the generalized Rabi frequency is generally defined as

$$\Omega^{\lambda\lambda'}_{\mathbf{k}} = \frac{1}{\hbar}\left[\mathbf{E}(t)\cdot\mathbf{d}^{\lambda\lambda'}_{\mathbf{k}} + \sum_{\mu',\mu,\mathbf{k}'}\left(V^{\mu'\lambda\mu\lambda'}_{\mathbf{k},\mathbf{k}',\mathbf{k}'-\mathbf{k}} - V^{\lambda\mu'\mu\lambda'}_{\mathbf{k},\mathbf{k}',\mathbf{0}}\right)P^{\mu'\mu}_{\mathbf{k}'}\right]. \tag{2.49}$$

For more clarity, we rewrite the EOM (2.47) explicitly in terms of interband coherences, intersubband coherences, and the charge carrier occupations. The EOM for interband

coherences $p_{\mathbf{k}}^{h_i e_j} \equiv P_{\mathbf{k}}^{v_i c_j}$ between holes and electrons are given by

$$\begin{aligned} i\hbar\frac{\partial}{\partial t}p_{\mathbf{k}}^{h_i e_j} &= \left(\tilde{\varepsilon}_{\mathbf{k}}^{e_j} + \tilde{\varepsilon}_{\mathbf{k}}^{h_i}\right)p_{\mathbf{k}}^{h_i e_j} - \hbar\Omega_{\mathbf{k}}^{e_j h_i}\left(1 - n_{\mathbf{k}}^{e_j} - n_{\mathbf{k}}^{h_i}\right) \\ &\quad + \sum_{e_\lambda \neq e_j}\left(\hbar\Omega_{\mathbf{k}}^{e_\lambda h_i} n_{\mathbf{k}}^{e_\lambda e_j} - \hbar\Omega_{\mathbf{k}}^{e_j e_\lambda} p_{\mathbf{k}}^{h_i e_\lambda}\right) + \sum_{h_\lambda \neq h_i}\left(\hbar\Omega_{\mathbf{k}}^{h_\lambda h_i} p_{\mathbf{k}}^{h_\lambda e_j} - \hbar\Omega_{\mathbf{k}}^{e_j h_\lambda} n_{\mathbf{k}}^{h_i h_\lambda}\right) \\ &\quad - e\mathbf{E}(t)\cdot\left(\sum_{h_\lambda}\boldsymbol{\vartheta}_{\mathbf{k}}^{h_\lambda h_i} p_{\mathbf{k}}^{h_\lambda e_j} - \sum_{e_\lambda}\boldsymbol{\vartheta}_{\mathbf{k}}^{e_j e_\lambda} p_{\mathbf{k}}^{h_i e_\lambda} + i\boldsymbol{\nabla}_{\mathbf{k}} p_{\mathbf{k}}^{h_i e_j}\right) \\ &\quad + \Gamma_{\mathbf{k}}^{p,h_i e_j}. \end{aligned} \tag{2.50}$$

Here, $\Gamma_{\mathbf{k}}$ term encompasses all contributions from correlations and scattering processes. The EOM for intersubband coherences between electrons, $n_{\mathbf{k}}^{e_i e_j} \equiv P_{\mathbf{k}}^{c_i c_j}$, and between holes, $n_{\mathbf{k}}^{h_i h_j} \equiv P_{\mathbf{k}}^{v_i v_j}$, are given by

$$\begin{aligned} i\hbar\frac{\partial}{\partial t}n_{\mathbf{k}}^{e_i e_j} &= \left(\tilde{\varepsilon}_{\mathbf{k}}^{e_j} - \tilde{\varepsilon}_{\mathbf{k}}^{e_i}\right)n_{\mathbf{k}}^{e_i e_j} + \hbar\Omega_{\mathbf{k}}^{e_j e_i}\left(n_{\mathbf{k}}^{e_j} - n_{\mathbf{k}}^{e_i}\right) \\ &\quad + \sum_{e_\lambda \neq \{e_i, e_j\}}\left(\hbar\Omega_{\mathbf{k}}^{e_\lambda e_i} n_{\mathbf{k}}^{e_\lambda e_j} - \hbar\Omega_{\mathbf{k}}^{e_j e_\lambda} n_{\mathbf{k}}^{e_i e_\lambda}\right) + \sum_{h_\lambda}\left[\hbar\Omega_{\mathbf{k}}^{h_\lambda e_i} p_{\mathbf{k}}^{h_\lambda e_j} - \hbar\Omega_{\mathbf{k}}^{e_j h_\lambda}\left(p_{\mathbf{k}}^{h_\lambda e_i}\right)^*\right] \\ &\quad - e\mathbf{E}(t)\cdot\left[\boldsymbol{\vartheta}_{\mathbf{k}}^{e_j e_i}\left(n_{\mathbf{k}}^{e_j} - n_{\mathbf{k}}^{e_i}\right) + \sum_{e_\lambda \neq e_j}\boldsymbol{\vartheta}_{\mathbf{k}}^{e_\lambda e_i} n_{\mathbf{k}}^{e_\lambda e_j} - \sum_{e_\lambda \neq e_i}\boldsymbol{\vartheta}_{\mathbf{k}}^{e_j e_\lambda} n_{\mathbf{k}}^{e_i e_\lambda} + i\boldsymbol{\nabla}_{\mathbf{k}} n_{\mathbf{k}}^{e_i e_j}\right] \\ &\quad + \Gamma_{\mathbf{k}}^{n,e_i e_j}, \end{aligned} \tag{2.51}$$

$$\begin{aligned} i\hbar\frac{\partial}{\partial t}n_{\mathbf{k}}^{h_i h_j} &= \left(\tilde{\varepsilon}_{\mathbf{k}}^{h_i} - \tilde{\varepsilon}_{\mathbf{k}}^{h_i}\right)n_{\mathbf{k}}^{h_i h_j} + \hbar\Omega_{\mathbf{k}}^{h_j h_i}\left(n_{\mathbf{k}}^{h_i} - n_{\mathbf{k}}^{h_j}\right) \\ &\quad + \sum_{h_\lambda \neq \{h_i, h_j\}}\left(\hbar\Omega_{\mathbf{k}}^{h_\lambda h_i} n_{\mathbf{k}}^{h_\lambda h_j} - \hbar\Omega_{\mathbf{k}}^{h_j h_\lambda} n_{\mathbf{k}}^{h_i h_\lambda}\right) + \sum_{e_\lambda}\left[\hbar\Omega_{\mathbf{k}}^{e_\lambda h_i}\left(p_{\mathbf{k}}^{h_j e_\lambda}\right)^* - \hbar\Omega_{\mathbf{k}}^{h_j e_\lambda} p_{\mathbf{k}}^{h_i e_\lambda}\right] \\ &\quad - e\mathbf{E}(t)\cdot\left[\boldsymbol{\vartheta}_{\mathbf{k}}^{h_\lambda h_i}\left(n_{\mathbf{k}}^{h_j} - n_{\mathbf{k}}^{h_i}\right) + \sum_{h_\lambda \neq h_j}\boldsymbol{\vartheta}_{\mathbf{k}}^{h_\lambda h_i} n_{\mathbf{k}}^{h_\lambda h_j} - \sum_{h_\lambda \neq h_i}\boldsymbol{\vartheta}_{\mathbf{k}}^{h_j h_\lambda} n_{\mathbf{k}}^{h_i h_\lambda} + i\boldsymbol{\nabla}_{\mathbf{k}} n_{\mathbf{k}}^{h_i h_j}\right] \\ &\quad + \Gamma_{\mathbf{k}}^{n,h_i h_j}. \end{aligned} \tag{2.52}$$

The renormalized band structure due to the repulsive Coulomb interaction between charge carriers is given by

$$\tilde{\varepsilon}_{\mathbf{k}}^{\lambda} = \varepsilon_{\mathbf{k}}^{\lambda} - \sum_{\mathbf{k}'} V_{\mathbf{k},\mathbf{k}',\mathbf{k}'-\mathbf{k}}^{\lambda\lambda\lambda\lambda} n_{\mathbf{k}'}^{\lambda}, \tag{2.53}$$

where λ runs over all conduction and valence subbands. The renormalized Rabi frequency

between the valence and conduction subbands is

$$\Omega_{\mathbf{k}}^{\lambda\lambda'} = \frac{1}{\hbar}\left[e\mathbf{E}(t)\cdot\boldsymbol{\xi}_{\mathbf{k}}^{\lambda\lambda'} - \sum_{\mu,\mu',\mathbf{k}'} V_{\mathbf{k},\mathbf{k}',\mathbf{k}'-\mathbf{k}}^{\mu'\lambda\mu\lambda'} p_{\mathbf{k}'}^{\mu'\mu}\right], \tag{2.54}$$

and between subbands is

$$\Omega_{\mathbf{k}}^{\lambda\lambda'} = \frac{1}{\hbar}\left[e\mathbf{E}(t)\cdot\boldsymbol{\xi}_{\mathbf{k}}^{\lambda\lambda'} - \sum_{\mu,\mu'\neq\mu,\mathbf{k}'} V_{\mathbf{k},\mathbf{k}',\mathbf{k}'-\mathbf{k}}^{\mu'\lambda\mu\lambda'} n_{\mathbf{k}'}^{\mu'\mu}\right]. \tag{2.55}$$

The EOM for occupations of electrons $n_{\mathbf{k}}^{e_i} \equiv P_{\mathbf{k}}^{c_i c_i}$ and hole $n_{\mathbf{k}}^{h_i} \equiv 1 - P_{\mathbf{k}}^{v_i v_i}$ are given by

$$\begin{aligned}\hbar\frac{\mathrm{d}}{\mathrm{d}t}n_{\mathbf{k}}^{e_i} = &-2\,\mathrm{Im}\left[\sum_{e_\lambda\neq e_i}\hbar\Omega_{\mathbf{k}}^{e_i e_\lambda}\left(n_{\mathbf{k}}^{e_\lambda e_i}\right)^* + \sum_{h_\lambda}\hbar\Omega_{\mathbf{k}}^{e_i h_\lambda}\left(p_{\mathbf{k}}^{h_\lambda e_i}\right)^* + e\mathbf{E}(t)\cdot\sum_{e_\lambda\neq e_i}\boldsymbol{\vartheta}_{\mathbf{k}}^{e_i e_\lambda}\left(n_{\mathbf{k}}^{e_\lambda e_i}\right)^*\right] \\ &+ e\mathbf{E}(t)\cdot\boldsymbol{\nabla}_{\mathbf{k}} n_{\mathbf{k}}^{e_i} + \Gamma_{\mathbf{k}}^{n,e_i},\end{aligned} \tag{2.56}$$

$$\begin{aligned}\hbar\frac{\mathrm{d}}{\mathrm{d}t}n_{\mathbf{k}}^{h_i} = &-2\,\mathrm{Im}\left[\sum_{h_\lambda\neq h_i}\hbar\Omega_{\mathbf{k}}^{h_\lambda h_i}\left(n_{\mathbf{k}}^{h_i h_\lambda}\right)^* + \sum_{e_\lambda}\hbar\Omega_{\mathbf{k}}^{e_\lambda h_i}\left(p_{\mathbf{k}}^{h_i e_\lambda}\right)^* + e\mathbf{E}(t)\cdot\sum_{h_\lambda\neq h_i}\boldsymbol{\vartheta}_{\mathbf{k}}^{h_\lambda h_i}\left(n_{\mathbf{k}}^{h_i h_\lambda}\right)^*\right] \\ &+ e\mathbf{E}(t)\cdot\boldsymbol{\nabla}_{\mathbf{k}} n_{\mathbf{k}}^{h_i} + \Gamma_{\mathbf{k}}^{n,h_i}.\end{aligned} \tag{2.57}$$

It should be noted that with the excitation conditions and material systems considered in this study, the only relevant Coulomb matrix elements are $V^{\mathrm{v_1c_1c_2v_2}}$, $V^{\mathrm{c_1v_1v_2c_2}}$, $V^{\mathrm{v_1v_2v_3v_4}}$ and $V^{\mathrm{c_1c_2c_3c_4}}$. Here, $\mathrm{c_i}$ and $\mathrm{v_i}$ represent conduction and valence band indices, respectively. The terms $V^{\mathrm{v_1c_1c_2v_2}}$ and $V^{\mathrm{c_1v_1v_2c_2}}$ describe the Coulomb attraction of electron and hole, giving rise to excitonic effects. Meanwhile, $V^{\mathrm{v_1v_2v_3v_4}}$ and $V^{\mathrm{c_1c_2c_3c_4}}$ describe the Coulomb repulsion between electrons in the valence and in the conduction bands, respectively, leading to effects such as band energy renormalization. The remaining terms, particularly those describing interband Auger transitions, are neglected due to their negligible impact under the considered conditions.

Using the same procedure, the EOM for the pure correlations at a singlet-doublet level are as follows

$$\begin{aligned}i\hbar\frac{\partial}{\partial t}c_{\lambda\mu\mu'\lambda'}^{\mathbf{q},\mathbf{k}',\mathbf{k}} = &\left(\varepsilon_{\mathbf{k}-\mathbf{q}}^{\lambda'} + \varepsilon_{\mathbf{k}'+\mathbf{q}}^{\mu'} - \varepsilon_{\mathbf{k}'}^{\mu} - \varepsilon_{\mathbf{k}}^{\lambda}\right)c_{\lambda\mu\mu'\lambda'}^{\mathbf{q},\mathbf{k}',\mathbf{k}} \\ &+ \hbar\sum_{\nu}\left(\Omega_{\mathbf{k}}^{\nu\lambda}c_{\nu\mu\mu'\lambda'}^{\mathbf{q},\mathbf{k}',\mathbf{k}} + \Omega_{\mathbf{k}'}^{\nu\mu}c_{\lambda\nu\mu'\lambda'}^{\mathbf{q},\mathbf{k}',\mathbf{k}} - \Omega_{\mathbf{k}'+\mathbf{q}}^{\mu'\nu}c_{\lambda\mu\nu\lambda'}^{\mathbf{q},\mathbf{k}',\mathbf{k}} - \Omega_{\mathbf{k}-\mathbf{q}}^{\lambda'\nu}c_{\lambda\mu\mu'\nu}^{\mathbf{q},\mathbf{k}',\mathbf{k}}\right) \\ &+ S_{\lambda\mu\mu'\lambda'}^{\mathbf{q},\mathbf{k}',\mathbf{k}} + D_{\lambda\mu\mu'\lambda'}^{\mathbf{q},\mathbf{k}',\mathbf{k}},\end{aligned} \tag{2.58}$$

where $\Omega_{\mathbf{k}}^{\lambda,\lambda'}$ is the generalized Rabi frequency defined in Eq. (2.49), $S_{\lambda\mu\mu'\lambda'}^{\mathbf{q},\mathbf{k}',\mathbf{k}}$ contains all

terms that appear from the singlet factorization, and $D^{\mathbf{q},\mathbf{k}',\mathbf{k}}_{\lambda\mu\mu'\lambda'}$ is from doublet factorization. The full expression for these singlet and doublet terms are given in Appendix A.4. In this thesis, we restrict the analyzing of many-body correlations to the coherent regime, in which only the coherent doublets, i.e., the hole-polarization correlation $c_{\mathrm{ph}} \equiv c_{\mathrm{vvvc}}$, the electron-polarization correlation $c_{\mathrm{pe}} \equiv c_{\mathrm{vccc}}$, and the biexcitonic correlation $c_{\mathrm{BX}} \equiv c_{\mathrm{vvcc}}$ are the relevant remaining quantities. Contributions from many-body correlations to pump-probe spectroscopy will be investigated in detail in Chapter 5.

2.3 Berry Phase and Curvature

Band structures have successfully been used to describe various electronic properties of solid-state systems. However, recent advancements in the field have emerged from a deeper understanding of more subtle aspect of electrons in crystals: the Berry curvature of Bloch states. The concept of the Berry phase and curvature, first proposed by Michael Berry in 1984 [19], has proven to be highly useful across many areas of physics. Its detailed derivation is described in numerous works, e.g., Refs. [83–88].

Consider a quantum system that is described by a time-dependent Hamiltonian involving a real parameter $\boldsymbol{\mathcal{R}}(t) = (\mathcal{R}_1, \mathcal{R}_2, \ldots)$

$$\mathrm{H} = \mathrm{H}(\boldsymbol{\mathcal{R}}(t)). \tag{2.59}$$

The parameter $\boldsymbol{\mathcal{R}}$ can be regarded as the influence of the external environment on the system under consideration (such as an electric field, a magnetic field, etc.). The evolution of the system over time is governed by the time-dependent Schrödinger equation

$$\mathrm{H}(\boldsymbol{\mathcal{R}}(t))\,|\psi(t)\rangle = i\hbar\frac{\partial}{\partial t}\,|\psi(t)\rangle\,. \tag{2.60}$$

Here, we are interested in the adiabatic evolution of the system over time. Therefore, the parameter $\boldsymbol{\mathcal{R}}$ is considered to change very slowly over time along a path C in the parameter space $\boldsymbol{\mathcal{R}}$. As a result, the solution to the above equation can be expressed as a linear combination of the instantaneous eigenstates of the Hamiltonian $\mathrm{H}(\boldsymbol{\mathcal{R}})$ at the points $\boldsymbol{\mathcal{R}}$ as follows

$$|\psi(t)\rangle = \sum_m a_m(t) e^{i\theta_m(t)}\,|m(\boldsymbol{\mathcal{R}})\rangle\,. \tag{2.61}$$

Here, $\theta_m(t) = -\frac{i}{\hbar}\int_{t_0}^{t} \mathrm{d}t' \mathcal{E}_m((\boldsymbol{\mathcal{R}}(t'))$ is the dynamical phase and the instantaneous eigenstates $|m(\boldsymbol{\mathcal{R}})\rangle$ at each point $\boldsymbol{\mathcal{R}}$ is obtained by diagonalizing the Hamiltonian $\mathrm{H}(\boldsymbol{\mathcal{R}})$ at the points $\boldsymbol{\mathcal{R}}$, i.e.,

$$\mathrm{H}(\boldsymbol{\mathcal{R}})\,|m(\boldsymbol{\mathcal{R}})\rangle = \mathcal{E}_m(\boldsymbol{\mathcal{R}})\,|m(\boldsymbol{\mathcal{R}})\rangle\,. \tag{2.62}$$

It is important to note that the above equation is not sufficient to uniquely determine the eigenstates $|m(\boldsymbol{\mathcal{R}})\rangle$, as they may still include an arbitrary phase factor. Additionally, there is no connection between the eigenstates $|m(\boldsymbol{\mathcal{R}})\rangle$ at different points $\boldsymbol{\mathcal{R}}$. We can

choose phase factors at the points $\boldsymbol{\mathcal{R}}$ to eliminate this arbitrariness, under the condition that the eigenstates $|m(\boldsymbol{\mathcal{R}})\rangle$ vary smoothly and are single-valued along the cycle C in the parameter space. To determine an EOM for the expansion coefficients $a_m(t)$, we substitute the expression (2.61) into Eq. (2.60) then left multiply both sides by $\langle n(\boldsymbol{\mathcal{R}})|$. Using the normalized orthogonality of the eigenfunctions, we get

$$\begin{aligned}\frac{\mathrm{d}}{\mathrm{d}t}a_n(t) =& -\langle n(\boldsymbol{\mathcal{R}})|\frac{\mathrm{d}}{\mathrm{d}t}|n(\boldsymbol{\mathcal{R}})\rangle\, a_n(t) \\ &- \sum_{m\neq n}\langle n(\boldsymbol{\mathcal{R}})|\frac{\mathrm{d}}{\mathrm{d}t}|m(\boldsymbol{\mathcal{R}})\rangle\, e^{i[\theta_m(t)-\theta_n(t)]}a_m(t).\end{aligned} \tag{2.63}$$

The first term on the right-hand side of Eq. (2.64) is dependent solely on the n-th state., whereas the second term involves the couplings between adiabatic states, which causes transfer of population between these states. Next, we assume that at the initial moment, the system is in a specific eigenstate n, $|n(\boldsymbol{\mathcal{R}}(t_0))\rangle$, of the Hamiltonian $\mathrm{H}(\boldsymbol{\mathcal{R}}(t_0))$, which allows us to express $a_m(t_0) = \delta_{nm}$. In first-order perturbation theory, the wave function of the system can be expressed as

$$\left|\psi^{(1)}(t)\right\rangle = e^{i\theta_n(t)}e^{i\gamma_n(t)}\left[|n(\boldsymbol{\mathcal{R}})\rangle - i\hbar\sum_{m\neq n}\frac{\langle m(\boldsymbol{\mathcal{R}})|\,\mathrm{d}/\mathrm{d}t\,|n(\boldsymbol{\mathcal{R}})\rangle}{\mathcal{E}_m(\boldsymbol{\mathcal{R}})-\mathcal{E}_n(\boldsymbol{\mathcal{R}})}\,|m(\boldsymbol{\mathcal{R}})\rangle\right]. \tag{2.64}$$

The phase factor $\gamma_n(t)$ is referred to as the geometric phase factor of the system, which is also known as the Berry phase. Expression (2.64) indicates that in the zeroth-order approximation (the first term), the system is in a specific eigenstate $|n(\boldsymbol{\mathcal{R}}(t_0))\rangle$ of $\mathrm{H}(\boldsymbol{\mathcal{R}}(t_0))$ at the initial moment, and throughout the evolution of the adiabatic process, the system remains in the instantaneous eigenstates $|n(\boldsymbol{\mathcal{R}})\rangle$ of the Hamiltonian $\mathrm{H}(\boldsymbol{\mathcal{R}})$. This is known as the adiabatic theorem in quantum systems.

The second term on the right-hand side of Eq. (2.64) gives rise to the phenomenon known as the anomalous current, which will be examined in Chapter 4. This term, along with the Berry phase, has been pivotal in advancing the modern theory of polarization [88, 89]. To study this term further, we rewrite it as

$$\frac{\langle m(\boldsymbol{\mathcal{R}})|\,\mathrm{d}/\mathrm{d}t\,|n(\boldsymbol{\mathcal{R}})\rangle}{\mathcal{E}_m(\boldsymbol{\mathcal{R}})-\mathcal{E}_n(\boldsymbol{\mathcal{R}})} = \frac{i\hbar\,\langle n(\boldsymbol{\mathcal{R}})|(\,\mathrm{dH}(\boldsymbol{\mathcal{R}})/\mathrm{d}t\,)|m(\boldsymbol{\mathcal{R}})\rangle}{\left[\mathcal{E}_m(\boldsymbol{\mathcal{R}})-\mathcal{E}_n(\boldsymbol{\mathcal{R}})\right]^2}. \tag{2.65}$$

From this expression, one can see that if the Hamiltonian changes slowly enough, the non-adiabatic contribution to the wave function becomes insignificant.

The Berry phase γ_n in Eq. (2.64) can be rewritten as follows

$$\gamma_n(C) = \int_C \mathrm{d}\mathbf{R}\cdot\mathbf{A}_n(\boldsymbol{\mathcal{R}}), \tag{2.66}$$

where $\mathbf{A}_n(\boldsymbol{\mathcal{R}})$ is referred to as Berry connection or Berry vector potential

$$\mathbf{A}_n(\boldsymbol{\mathcal{R}}) = i \langle n(\boldsymbol{\mathcal{R}}) | \boldsymbol{\nabla}_{\boldsymbol{\mathcal{R}}} | n(\boldsymbol{\mathcal{R}}) \rangle . \tag{2.67}$$

It should be noted that the Berry phase, as defined in Eq. (2.66), is real-valued. From the expression (2.67), it can be seen that the geometric phase of the system depends only on the geometric shape of the path the system traverses in the parameter space $\boldsymbol{\mathcal{R}}$. It does not depend on the time variation of the parameter $\boldsymbol{\mathcal{R}}$ (i.e., it is independent of $\mathrm{d}\boldsymbol{\mathcal{R}}/\mathrm{d}t$).

For a closed loop, the Berry phase can be rewritten as a surface integral using Stokes' theorem as follows

$$\gamma_n(C) = \int_{\mathcal{S}} \mathrm{d}\boldsymbol{\mathcal{R}}_\mu \wedge \mathrm{d}\boldsymbol{\mathcal{R}}_\nu \Omega_n^{\mu\nu}(\boldsymbol{\mathcal{R}}), \tag{2.68}$$

here, μ and ν are the indices of the dimensions of the parameter space, $\mathcal{S}$ is the surface enclosed by the closed curve C, and $\mathrm{d}\boldsymbol{\mathcal{R}}_\mu \wedge \mathrm{d}\boldsymbol{\mathcal{R}}_\nu$ is the differential area element. $\Omega_n^{\mu\nu}(\boldsymbol{\mathcal{R}})$ is an antisymmetric second-rank tensor, called the Berry curvature, and has the form

$$\Omega_n^{\mu\nu}(\boldsymbol{\mathcal{R}}) = \frac{\partial}{\partial \boldsymbol{\mathcal{R}}_\mu} A_n^\nu(\boldsymbol{\mathcal{R}}) - \frac{\partial}{\partial \boldsymbol{\mathcal{R}}_\nu} A_n^\mu(\boldsymbol{\mathcal{R}}). \tag{2.69}$$

With the definitions of the Berry phase and Berry curvature given above, we can show that the Berry curvature is a gauge-invariant quantity, so it may alter observable physical effects. In contrast, the Berry connection is a gauge-dependent quantity and thus cannot be observed. To derive this, we consider a gauge transformation of the eigenstates of the system in the form $|\tilde{n}(\boldsymbol{\mathcal{R}})\rangle = e^{i\beta_n(\boldsymbol{\mathcal{R}})} |n(\boldsymbol{\mathcal{R}})\rangle$, where the phase factor $\beta_n(\boldsymbol{\mathcal{R}})$ is an arbitrary smooth function which guarantees the single valuedness of the wave function. Substituting this expression into Eq. (2.67), we obtain

$$\tilde{\mathbf{A}}_n(\boldsymbol{\mathcal{R}}) = \mathbf{A}_n(\boldsymbol{\mathcal{R}}) + \boldsymbol{\nabla}_{\boldsymbol{\mathcal{R}}} \beta(\boldsymbol{\mathcal{R}}). \tag{2.70}$$

This expression indicates that, through the gauge transformation, the Berry vector potential is altered by an amount $\boldsymbol{\nabla}_{\boldsymbol{\mathcal{R}}} \beta(\boldsymbol{\mathcal{R}})$. Thus, it depends on the arbitrarily chosen phase factor $\beta(\boldsymbol{\mathcal{R}})$. Next, by substituting expression (2.70) into expression (2.66), we obtain

$$\tilde{\gamma}_n(C) = \gamma_n(C) - \int_C \mathrm{d}\boldsymbol{\mathcal{R}}\, \boldsymbol{\nabla}_{\boldsymbol{\mathcal{R}}} \beta(\boldsymbol{\mathcal{R}}) = \gamma_n(C) + \beta(\boldsymbol{\mathcal{R}}(t_0)) - \beta(\boldsymbol{\mathcal{R}}). \tag{2.71}$$

In the expression above, $\beta(\boldsymbol{\mathcal{R}}(t_0))$ and $\beta(\boldsymbol{\mathcal{R}})$ are the phase factors at the initial and final points of the curve C in the parameter space. It shows that under the gauge transformation, the geometric phase changes by an amount $\beta(\boldsymbol{\mathcal{R}}(t_0)) - \beta(\boldsymbol{\mathcal{R}})$. At this point, we cannot yet conclude whether the geometric phase depends on the chosen gauge or not. If the system evolves over time along an open curve C in parameter space, the geometric phase will depend on the choice of the phase factor $\beta(\boldsymbol{\mathcal{R}})$, making it gauge-dependent. In such cases, we can choose a gauge that eliminates the geometric phase, leaving only the dynamic

phase. This gauge is chosen such that the eigenstates of the system satisfy

$$\langle \tilde{n}(\boldsymbol{\mathcal{R}})|\frac{\mathrm{d}}{\mathrm{d}t}|\tilde{n}(\boldsymbol{\mathcal{R}})\rangle = \langle \tilde{n}(\boldsymbol{\mathcal{R}})|\boldsymbol{\nabla}_{\boldsymbol{\mathcal{R}}}|\tilde{n}(\boldsymbol{\mathcal{R}})\rangle \frac{\mathrm{d}\boldsymbol{\mathcal{R}}}{\mathrm{d}t} = 0. \tag{2.72}$$

The above condition for the wave function is also known as the parallel transport condition, and states that satisfy this condition are referred to as parallel states. For these states, the geometric phase of the system cancels, leaving only the dynamic phase. However, when the system evolves over time along a closed curve in the parameter space, Berry realized that the geometric phase of the system is not canceled. In this case, the initial and final points of the closed curve C coincide, i.e., $\boldsymbol{\mathcal{R}}(t_0) = \boldsymbol{\mathcal{R}}(t)$. Consequently, the initial and final states must be identical, i.e., $|n(\boldsymbol{\mathcal{R}}(t))\rangle = |n(\boldsymbol{\mathcal{R}}(t_0))\rangle$. This property must hold under gauge transformation. Additionally, due to the single valuedness of the wave function, we have

$$\beta(\boldsymbol{\mathcal{R}}(t)) - \beta(\boldsymbol{\mathcal{R}}(t_0)) = 2\pi n, \quad \text{with } n \in \mathbb{Z}. \tag{2.73}$$

From the above expression, we can see that for any chosen phase factors $\beta(\boldsymbol{\mathcal{R}})$ the geometric phase of the system can only change by an integer multiple of 2π. Therefore, it cannot be eliminated, making the geometric phase a gauge-invariant quantity in this case.

In practical numerical calculations, the previously defined expression for the Berry curvature is often not used. This is because the eigenstates of the Hamiltonian at different points $\boldsymbol{\mathcal{R}}$ in parameter space are obtained by diagonalizing the Hamiltonian independently, which results in no phase relation between the eigenstates at different points $\boldsymbol{\mathcal{R}}$. This lack of phase continuity complicates the calculation of derivatives of the eigenstates. To avoid this, the formula for the Berry curvature can be reformulated in a way that depends only on the eigenstates at a single point $\boldsymbol{\mathcal{R}}$ in parameter space as

$$\Omega_n^{\mu\nu}(\boldsymbol{\mathcal{R}}) = i \sum_{m\neq n} \frac{\langle n(\boldsymbol{\mathcal{R}})|\left(\partial \mathrm{H}(\boldsymbol{\mathcal{R}})/\partial \boldsymbol{\mathcal{R}}_\mu\right)|m(\boldsymbol{\mathcal{R}})\rangle \langle m(\boldsymbol{\mathcal{R}})|\partial \mathrm{H}(\boldsymbol{\mathcal{R}})/\partial \boldsymbol{\mathcal{R}}_\nu|n(\boldsymbol{\mathcal{R}})\rangle - (\mu \leftrightarrow \nu)}{(\mathcal{E}_m - \mathcal{E}_n)^2}. \tag{2.74}$$

This formula is also known as the Kubo-like formula for the Berry curvature. It indicates that the Berry curvature depends only on the eigenstates, the eigenvalues of the Hamiltonian, and derivatives of the Hamiltonian at a specific point $\boldsymbol{\mathcal{R}}$. Therefore, if having an analytical expression of the system's Hamiltonian, we can calculate the Berry curvature using the Kubo-like formula.

In this section, we only considered the case of a non-degenerate system. Degenerate systems were first discussed in the work of Wilczek and Zee [20]. In first-order perturbation theory, the wave function of the non-degenerate system is

$$\left|\psi^{(1)}(t)\right\rangle = e^{i\theta_n(t)} \sum_{m\in\Delta} g_{mn}\left[|m(\boldsymbol{\mathcal{R}})\rangle - i\hbar \sum_{l\notin\Delta} \frac{\langle l(\boldsymbol{\mathcal{R}})|\,\mathrm{d}/\mathrm{d}t\,|m(\boldsymbol{\mathcal{R}})\rangle}{\mathcal{E}_l(\boldsymbol{\mathcal{R}}) - \mathcal{E}_m(\boldsymbol{\mathcal{R}})}\,|l(\boldsymbol{\mathcal{R}})\rangle\right]. \tag{2.75}$$

Here, Δ represents all indices corresponding to the subspaces of the degenerate states. The non-Abelian phase factor g is the unitary matrix that accounts for the geometric phase

$$g = \exp\left(i \int_C \mathrm{d}\boldsymbol{\mathcal{R}} \cdot \mathbf{A}\right). \tag{2.76}$$

Here, the non-Abelian Berry vector potential is a matrix-valued vector quantity, defined as

$$\mathbf{A}_{mn}(\boldsymbol{\mathcal{R}}) = i \left\langle m(\boldsymbol{\mathcal{R}}) | \boldsymbol{\nabla}_{\boldsymbol{\mathcal{R}}} | n(\boldsymbol{\mathcal{R}}) \right\rangle, \quad \text{with } m, n \in \Delta. \tag{2.77}$$

The non-Abelian Berry curvature is expressed as a matrix quantity in the form

$$\boldsymbol{\Omega}(\boldsymbol{\mathcal{R}}) = \boldsymbol{\nabla}_{\boldsymbol{\mathcal{R}}} \times \mathbf{A}(\boldsymbol{\mathcal{R}}) - i\mathbf{A}(\boldsymbol{\mathcal{R}}) \times \mathbf{A}(\boldsymbol{\mathcal{R}}). \tag{2.78}$$

As with the non-degenerate case, we can also derive a Kubo-like formula for calculating the Berry curvature in the presence of degeneracy. The formula takes the following form [90]

$$\Omega^{\mu\nu}_{mn}(\boldsymbol{\mathcal{R}}) = i \sum_{l \notin \Delta} \frac{\langle m(\boldsymbol{\mathcal{R}}) | \partial \mathrm{H}(\boldsymbol{\mathcal{R}}) / \partial \boldsymbol{\mathcal{R}}_\mu | l(\boldsymbol{\mathcal{R}}) \rangle \, \langle l(\boldsymbol{\mathcal{R}}) | \partial \mathrm{H}(\boldsymbol{\mathcal{R}}) / \partial \boldsymbol{\mathcal{R}}_\nu | n(\boldsymbol{\mathcal{R}}) \rangle - (\mu \leftrightarrow \nu)}{(\mathcal{E}_l - \mathcal{E}_m)(\mathcal{E}_l - \mathcal{E}_n)}. \tag{2.79}$$

In the context of periodic systems, the reciprocal lattice serves as the parameter space, situating our system within the closed manifold known as the Brillouin zone. For the case of non-degeneracy, the Berry connection and Berry curvature can be defined in this framework as

$$\boldsymbol{\vartheta}^n_{\mathbf{k}} = i \left\langle u_{n\mathbf{k}} | \boldsymbol{\nabla}_{\mathbf{k}} | u_{n\mathbf{k}} \right\rangle, \tag{2.80}$$

$$\boldsymbol{\Omega}^n_{\mathbf{k}} = \boldsymbol{\nabla}_{\mathbf{k}} \times \boldsymbol{\vartheta}^n_{\mathbf{k}} = i \left\langle \boldsymbol{\nabla}_{\mathbf{k}} u_{n\mathbf{k}} | \times | \boldsymbol{\nabla}_{\mathbf{k}} u_{n\mathbf{k}} \right\rangle, \tag{2.81}$$

and Berry berry phase

$$\gamma_n(C) = \int_C \mathrm{d}\mathbf{k} \cdot \mathbf{A}_n(\mathbf{k}) = \int_{\mathcal{S}} \mathrm{d}\boldsymbol{\mathcal{S}} \cdot \boldsymbol{\Omega}_n(\mathbf{k}). \tag{2.82}$$

If taking this integral over the closed surface $\boldsymbol{\mathcal{S}}$, we will obtain a value that is an integer multiple of 2π

$$\oint_{\mathcal{S}} \mathrm{d}\boldsymbol{\mathcal{S}} \cdot \boldsymbol{\Omega}^n_{\mathbf{k}} = 2\pi C_m, \quad \text{with } C_m \in \mathbb{Z}. \tag{2.83}$$

This integer C_m is also known as the Chern number or the topological invariant, and it depends solely on the solid crystal's structure.

In the case of degeneracy or near-degeneracy, typically involving the spin degeneracy of energy bands, we need to modify the above definition and work with a non-Abelian gauge

field within each subspace. The non-Abelian Berry curvature has form [90, 91]

$$\Omega_{\mathbf{k}} = \boldsymbol{\nabla}_{\mathbf{k}} \times \boldsymbol{\vartheta}_{\mathbf{k}} - i\boldsymbol{\vartheta}_{\mathbf{k}} \times \boldsymbol{\vartheta}_{\mathbf{k}}, \tag{2.84}$$

with $\boldsymbol{\vartheta}^{nm}_{\mathbf{k}}$ being the Berry connection in the degenerate case, it takes the form

$$\boldsymbol{\vartheta}^{nm}_{\mathbf{k}} = i \langle u_{n\mathbf{k}} | \boldsymbol{\nabla}_{\mathbf{k}} | u_{m\mathbf{k}} \rangle , \quad \text{with } n, m \in \Delta, \tag{2.85}$$

where Δ is the set containing the indices of the degenerate states. We can express the Berry curvature in terms of the periodic components of the Bloch function as follows

$$\Omega^{nm}_{\mathbf{k}} = i \langle \boldsymbol{\nabla}_{\mathbf{k}} u_n(\mathbf{k}) | \times | \boldsymbol{\nabla}_{\mathbf{k}} u_m(\mathbf{k}) \rangle - i \sum_{l \in \Delta} \langle u_n(\mathbf{k}) | \boldsymbol{\nabla}_{\mathbf{k}} u_l \rangle \times \langle u_l(\mathbf{k}) | \boldsymbol{\nabla}_{\mathbf{k}} u_m(\mathbf{k}) \rangle . \tag{2.86}$$

In the representation of the eigenfunctions of the band structure, $\boldsymbol{\Omega}_{\mathbf{k}}$ can be expressed in terms of velocity matrix elements as

$$\Omega^{nm}_{\mathbf{k}} = i\hbar^2 \sum_{l \notin \Delta} \frac{\mathbf{v}^{nl}_{\mathbf{k}} \times \mathbf{v}^{lm}_{\mathbf{k}}}{\left(\varepsilon^{l}_{\mathbf{k}} - \varepsilon^{n}_{\mathbf{k}}\right)\left(\varepsilon^{l}_{\mathbf{k}} - \varepsilon^{m}_{\mathbf{k}}\right)}, \tag{2.87}$$

where n and m are in the same degenerate or near-degenerate subspace. This expression will be applied in Chapter 4 to evaluate the Berry curvature for semiconductor QWs, specifically for investigating the anomalous current induced by the Berry curvature.

Finally, we discuss the effect of the symmetricity of the solid crystal structure on its Berry curvature. For crystals with spatial inversion symmetry, the periodic components of the Bloch function exhibit the symmetry

$$u_{n,\sigma,-\mathbf{k}}(-\mathbf{r}) = u_{n,\sigma,\mathbf{k}}(\mathbf{r}), \tag{2.88}$$

where σ is the spin index for band n. Using the relation in this expression and the expression (2.81), we obtain the following symmetry expression for the Berry curvature

$$\Omega^{nn}_{\sigma\sigma,-\mathbf{k}} = \Omega^{nn}_{\sigma\sigma,\mathbf{k}}. \tag{2.89}$$

If the crystal structure also possesses time-reversal symmetry, then the periodic components of the Bloch function satisfy the symmetry

$$u^{*}_{n,\sigma,-\mathbf{k}}(\mathbf{r}) = u_{n,\bar{\sigma},\mathbf{k}}(\mathbf{r}), \tag{2.90}$$

in which $\bar{\sigma}$ denotes the spin state opposite to that of σ. Similarly to the previous case, we obtain the following symmetry relation for the Berry curvature in this case

$$\Omega^{nn}_{\sigma\sigma,-\mathbf{k}} = -\Omega^{nn}_{\bar{\sigma}\bar{\sigma},\mathbf{k}}. \tag{2.91}$$

In the case where the crystal structure possesses both symmetries, combining the Berry curvature symmetry relations (2.89) and (2.91) results in the Berry curvature of the system

canceling out, eliminating any net effect from the Berry curvature. In the case of broken spatial inversion symmetry, the system still exhibits microscopic Berry curvature as governed by Eq. (2.91). However, the macroscopic Berry curvature, obtained by integrating the microscopic Berry curvature over the entire Brillouin zone, will vanish. As a result, we do not observe a macroscopic Berry curvature effect in this case. However, if we can break time-reversal symmetry in the system, for example, by exciting the system with circularly polarized light pulses to induce spin polarization–a transient macroscopic Berry curvature effect can be observed during the system's spin relaxation time. This transient effect will be the focus of the study in Chapter 4.

General Numerical Approach for Solving the Semiconductor Bloch Equations in the Length Gauge

3

The interaction between electrons in a semiconductor and an electric laser field has been widely studied in the VG through the coupling term $\mathbf{A}(t) \cdot \mathbf{v}$ between the vector potential of the laser field, $\mathbf{A}(t)$, and the velocity of the electrons, $\mathbf{v}$. Using this gauge has advantages due to the independence of this coupling term on the wave vector $\mathbf{k}$. However, it has also some disadvantages. The vector potential $\mathbf{A}(t)$ is gauge-dependent, whereas the electric field $\mathbf{E}(t)$ is not. The relation between the vector potential and a uniform electric field in frequency space is expressed as $\mathbf{A}(\omega) = -i\mathbf{E}(\omega)/\omega$. This expression implies that when the frequency ω approaches zero, the vector potential becomes infinite while the electric field remains finite. Moreover, this can magnify round-off errors at low frequencies, potentially leading to unphysical effects if the basis set is incomplete [32, 52]. These issues do not arise in the LG, which involves the electric field $\mathbf{E}(t)$ with the position operator $\mathbf{r}$, $\mathbf{E}(t) \cdot \mathbf{r}$. From a computational perspective, however, solving the SBE in the LG is more challenging than in the VG due to the presence of $\mathbf{k}$ derivatives, which require the Bloch states to be smooth, differentiable functions with respect to $\mathbf{k}$. Since Bloch states are often determined at each $\mathbf{k}$ point through independent numerical diagonalizations, they acquire arbitrary $\mathbf{k}$-dependent phases. To solve this issue, we apply the method proposed by Virk and Sipe [53] and construct the parallel transport gauge (PTG) to transform the original eigenstates into parallel transport states aligned with the external field direction. Additionally, we utilize the twisted parallel transport gauge (TPTG) transformation [85, 92, 93], which was introduced for Cartesian coordinates, here, we adapt it specifically for polar coordinates to properly solve the problem. This chapter will provide a detailed description of the construction of the PTG and TPTG transformations and their application when numerically solving the SBE in the LG. In order to validate our gauging procedure, we use this approach to calculate both the injection current and shift current in a GaAs semiconductor QW. We then compare the results from the LG with those obtained from the VG.

The dynamics of the photoexcited semiconductor system is obtained by solving the EOM in the LG (2.47) for the single-particle expectation value. They can be rewritten in the

matrix form using the reduced density matrix $\rho_{\mathbf{k}}$ as

$$\frac{\mathrm{d}}{\mathrm{d}t}\rho_{\mathbf{k}} = -\frac{i}{\hbar}\left[\mathrm{H}_{0,\mathbf{k}} - \hbar\Omega_{\mathbf{k}}, \rho_{\mathbf{k}}\right] + \frac{i}{\hbar}[e\mathbf{E}(t)\cdot(\boldsymbol{\vartheta}_{\mathbf{k}} + i\boldsymbol{\nabla}_{\mathbf{k}}), \rho_{\mathbf{k}}] + \Gamma_{\mathbf{k}}. \tag{3.1}$$

Here, the band structure $\mathrm{H}^{\lambda\lambda'}_{0,\mathbf{k}} = \varepsilon^{\lambda}_{\mathbf{k}}\delta_{\lambda\lambda'}$, and the generalized Rabi frequency $\Omega_{\mathbf{k}}$ given by Eq. (2.49). $\Gamma_{\mathbf{k}}$ represents all contributions from scattering and correlations. In the VG, the equation of motion for reduced density matrix reads as [94]

$$\frac{\partial}{\partial t}\rho_{\mathbf{k}}(t) = -\frac{i}{\hbar}[\mathrm{H}_{0\mathbf{k}}, \rho_{\mathbf{k}}(t)] - \frac{ie}{\hbar}[\mathbf{A}(t)\cdot\mathbf{v}_{\mathbf{k}}, \rho_{\mathbf{k}}(t)] + \Gamma_{\mathbf{k}}, \tag{3.2}$$

where the vector potential $\mathbf{A}(t)$ is obtained from the electric laser field $\mathbf{E}(t)$ by the relation $\mathbf{A}(t) = -\int_{-\infty}^{t}\mathbf{E}(t')\,\mathrm{d}t'$. In principle, using the unitary operator $Q = e^{ie\mathbf{A}(t)\cdot\mathbf{r}/\hbar}$ [93, 95], the equations of motion in the LG and VG can be transformed into one another. In practice, unlike Eq. (3.1) in the LG, the equations for the reduced density matrix in the VG, as presented in Eq. (3.2), are independent of each other for different $\mathbf{k}$ vectors. Thus, there is no need for a gauge choice that ensures the smoothness of the wave function in k-space. As demonstrated in the following section, where we compare numerical results from both gauges, the final results are identical. However, the LG is shown to be more efficient since it requires fewer bands to achieve convergence, and an intuitive interpretation in terms of interband and intraband contributions is possible.

3.1 The Parallel Transport Gauge

To construct the PTG, we start with the relation of Bloch functions between two different $\mathbf{k}$ points. In perturbation theory, these functions can be expressed to first order of $\Delta\mathbf{k}$ as [51]

$$\left|u_{\lambda,\mathbf{k}+\Delta\mathbf{k}}\right\rangle = \sum_{\mu\nu}\left|u_{\lambda,\mathbf{k}}\right\rangle\left(\delta_{\mu\nu} - i\Delta\mathbf{k}\cdot\boldsymbol{\xi}^{\mu\nu}_{\mathbf{k}}\right)g_{\mu\nu}(\mathbf{k},\mathbf{k}+\Delta\mathbf{k}) + O(\Delta\mathbf{k}^2), \tag{3.3}$$

where the unitary matrix $g(\mathbf{k},\mathbf{k}+\Delta\mathbf{k}) = \exp\left(-i\Delta\mathbf{k}\cdot\boldsymbol{\vartheta}_{\mathbf{k}}\right)$ accounts for arbitrary phase factors and the arbitrary mixing of degenerate states originating from numerical band structure calculations. $\boldsymbol{\xi}_{\mathbf{k}}$ and $\boldsymbol{\vartheta}_{\mathbf{k}}$ are, respectively, the transition dipole matrix elements between connected and disconnected states

$$\begin{aligned}\boldsymbol{\xi}^{\lambda\lambda'}_{\mathbf{k}} &= i\left\langle u_{\lambda,\mathbf{k}}\middle|\boldsymbol{\nabla}_{\mathbf{k}}u_{\lambda',\mathbf{k}}\right\rangle\Delta_{\lambda\lambda'},\\ \boldsymbol{\vartheta}^{\lambda\lambda'}_{\mathbf{k}} &= i\left\langle u_{\lambda,\mathbf{k}}\middle|\boldsymbol{\nabla}_{\mathbf{k}}u_{\lambda',\mathbf{k}}\right\rangle\bar{\Delta}_{\lambda\lambda'},\end{aligned} \tag{3.4}$$

where $\Delta_{\lambda\lambda'} = 1$ if the two bands have the same energy at least at one $\mathbf{k}$ point in the Brillouin zone, otherwise $\Delta_{\lambda\lambda'} = 1$ and $\bar{\Delta}_{\lambda\lambda'} = 1 - \Delta_{\lambda\lambda'}$. To calculate the matrix $g(\mathbf{k},\mathbf{k}+\Delta\mathbf{k})$, one needs the overlap matrix which is defined as $S_{\lambda\lambda'}(\mathbf{k},\mathbf{k}+\Delta\mathbf{k}) = \left\langle u_{\lambda,\mathbf{k}}\middle|u_{\lambda',\mathbf{k}+\Delta\mathbf{k}}\right\rangle$ between

two neighboring $\mathbf{k}$ points. With the perturbative relation (3.3), one can obtain

$$g(\mathbf{k}, \mathbf{k} + \Delta\mathbf{k}) = S_{\lambda\lambda'}(\mathbf{k}, \mathbf{k} + \Delta\mathbf{k})\Delta, \tag{3.5}$$

and

$$\xi(\mathbf{k}) = \frac{i}{2|\Delta\mathbf{k}|}\left[\bar{S}(\mathbf{k}, \mathbf{k} + \Delta\mathbf{k})g^{\dagger}(\mathbf{k}, \mathbf{k} + \Delta\mathbf{k}) - g(\mathbf{k}, \mathbf{k} + \Delta\mathbf{k})\bar{S}^{\dagger}(\mathbf{k}, \mathbf{k} + \Delta\mathbf{k})\right]. \tag{3.6}$$

Here, $\bar{S}(\mathbf{k}, \mathbf{k} + \Delta\mathbf{k}) = S(\mathbf{k}, \mathbf{k} + \Delta\mathbf{k})\bar{\Delta}$. Equation (3.6) is symmetrized to enforce exact hermiticity. This equation allows one to calculate the transition dipole matrix elements from the overlap matrices, which are determined by the wave functions obtained from the band structure calculations. This is useful in case an analytical expression for the Hamiltonian is not available.

In practice, $g(\mathbf{k}, \mathbf{k} + \Delta\mathbf{k})$ obtained from Eq. (3.5) is not exactly unitary, but it can be made unitary by performing a singular value decomposition as

$$S(\mathbf{k}, \mathbf{k} + \Delta\mathbf{k})\Delta = U(\mathbf{k})\Sigma(\mathbf{k})V^{\dagger}(\mathbf{k}). \tag{3.7}$$

Finally, $g(\mathbf{k}, \mathbf{k} + \Delta\mathbf{k})$ is obtained from the product of two unitary matrices as

$$g(\mathbf{k}, \mathbf{k} + \Delta\mathbf{k}) = U(\mathbf{k})V^{\dagger}(\mathbf{k}). \tag{3.8}$$

It should be noted that when writing the overlap matrix in polar decomposition form as $S(\mathbf{k})\Delta = g(\mathbf{k})M(\mathbf{k})$, one can see that $g(\mathbf{k})$ plays the role of the angle of a complex number and $M(\mathbf{k})$ is its magnitude.

To eliminate the relative phase and unitary mixing of Bloch states between two neighboring $\mathbf{k}$ points, from the relation (3.3), one performs the gauge transformation

$$\left|\tilde{u}_{\lambda,\mathbf{k}+\Delta\mathbf{k}}\right\rangle = \sum_{\mu} g^{*}_{\lambda\mu}(\mathbf{k}, \mathbf{k} + \Delta\mathbf{k})\left|u_{\mu,\mathbf{k}+\Delta\mathbf{k}}\right\rangle. \tag{3.9}$$

To make the Bloch functions smooth as a function of $\mathbf{k}$ in the j direction, one can construct the gauge transformation matrix W^j by extending to a series of $\mathbf{k}$ points on a straight line in the j direction, with the unit vector $\mathbf{e}_j$, starting from the first point $\mathbf{k}_0$, one has

$$W^j(\mathbf{k}_0, \mathbf{k}) = g(\mathbf{k}_0, \mathbf{k}_0 + \mathbf{e}_j\Delta k)g(\mathbf{k}_0 + \mathbf{e}_j\Delta k, \mathbf{k}_0 + 2\mathbf{e}_j\Delta k)\ldots g(\mathbf{k} - \mathbf{e}_j\Delta k, \mathbf{k}). \tag{3.10}$$

With the W^j matrix, one can obtain the new Bloch functions as

$$\left|\tilde{u}_{\lambda,\mathbf{k}}\right\rangle = \sum_{\mu} W^{j*}_{\lambda\mu}(\mathbf{k}_0, \mathbf{k})\left|u_{\mu,\mathbf{k}}\right\rangle. \tag{3.11}$$

In the new basis, the transition dipole matrix $\xi(\mathbf{k})$ is transformed as

$$\tilde{\xi}(\mathbf{k}) = W^j(\mathbf{k}_0, \mathbf{k})\xi(\mathbf{k})W^{j\dagger}(\mathbf{k}_0, \mathbf{k}), \tag{3.12}$$

which is a smooth function of $\mathbf{k}$. It should be noted that the matrix $g(\mathbf{k}, \mathbf{k} + \Delta\mathbf{k})$ in the new basis becomes an identity matrix, which leads to the vanishing of the non-Abelian Berry connection $\boldsymbol{\vartheta}_{\mathbf{k}}$ and the new gauge is so-called the parallel transport gauge.

3.2 The Twisted Parallel Transport Gauge

In the case of periodicity, the phase difference when we move the $\mathbf{k}$ point from the beginning to itself after that is the Berry phase, which represents the total phase accumulated during the final transition. Since the Berry phase is gauge invariant, there is no gauge transformation that can eliminate this phase difference. A possible way to overcome this discontinuous problem is that we spread out the phase difference uniformly to the basis at $\mathbf{k}$ points along the path [85, 92, 93]. Supposed we distribute $(N + 1)$ $\mathbf{k}$ points along the $\mathbf{k}$ path starting at $\mathbf{k}_0$, and the path is a closed loop such that the states at $\mathbf{k}_0$ and at $\mathbf{k}_N$ represented by the same Hamiltonian. In the case of non-degenerate bands, the periodicity can be restored by applying the graded phase twist as

$$\left|\bar{u}_{\lambda,\mathbf{k}_j}\right\rangle = e^{-i\phi_\lambda k_j / L_C} \left|\tilde{u}_{\lambda,\mathbf{k}_j}\right\rangle, \tag{3.13}$$

where k_j is the length of k-path between $\mathbf{k}_0$ and $\mathbf{k}_j$, L_C is the length of the closed path in k-space, and ϕ_λ is the Berry phase associated with band λ along the closed path, whose the discrete formulation are

$$\phi_\lambda = -\operatorname{Im} \ln \left\langle \tilde{u}_{\lambda,\mathbf{k}_N} \middle| e^{-i\mathbf{b}_n \cdot \mathbf{r}} \middle| \tilde{u}_{\lambda,\mathbf{k}_0} \right\rangle. \tag{3.14}$$

Here, the factor $e^{-i\mathbf{b}_n \cdot \mathbf{r}}$ is inserted only if the path involves a winding by a reciprocal lattice vector $\mathbf{b}_n$. The phase twists in Eq. (3.13) are known as twisted parallel-transport gauge. The situation is more complex in the case of degenerate bands. Because of the unitary mixing of states in the degenerate subspace, one cannot treat each band separately. In that case, one must consider the non-Abelian Berry phase (also called multiband Berry phase), which is given by

$$\phi_{\text{tot}} = -\operatorname{Im} \ln \det \tilde{g}(\mathbf{k}_N, \mathbf{k}_0). \tag{3.15}$$

Here, $\tilde{g}$ is obtained by Eq. (3.5) but in the PTG basis. It is noted that the PTG states at $\mathbf{k}_0$ and $\mathbf{k}_N$ are related by the unitary transformation as

$$\left|\tilde{u}_{\lambda,\mathbf{k}_0}\right\rangle = e^{i\mathbf{b}_n \cdot \mathbf{r}} \sum_\mu \tilde{g}_{\lambda\mu}(\mathbf{k}_N, \mathbf{k}_0) \left|\tilde{u}_{\mu,\mathbf{k}_N}\right\rangle. \tag{3.16}$$

To extract the set of individual phases ϕ_m (non-Abelian Berry phases), we must diagonalize the matrix $\tilde{g}(\mathbf{k}_N, \mathbf{k}_0)$. Because $\tilde{g}$ is unitary, its eigenvalues have the form $\lambda_m = e^{-i\phi_m}$. The

total Berry phase can be written as the sum of the individual phase ϕ_m

$$\phi_{\text{tot}} = -\sum_m \text{Im} \ln \lambda_m = \sum_m \phi_m. \tag{3.17}$$

With the unitary matrix V, which diagonalizes $\tilde{g}(\mathbf{k}_N, \mathbf{k}_0)$, one rotates all states at all $\mathbf{k}_j$ to the new states which correspond to the eigenstates of the individual multiband Berry phase as

$$\left|\bar{u}_{\lambda,\mathbf{k}_j}\right\rangle = \sum_\mu V_{\mu\lambda} \left|\tilde{u}_{\mu,\mathbf{k}_j}\right\rangle. \tag{3.18}$$

In the basis defined by these new states, the matrix $\tilde{g}(\mathbf{k}_N, \mathbf{k}_0)$ becomes diagonal with the diagonal elements being $\lambda_m = e^{-i\phi_m}$. This means that each state $\left|\bar{u}_{\lambda,\mathbf{k}_j}\right\rangle$ will return to itself at the end of the loop, but has acquired the Berry phase ϕ_m. Now, it is straightforward to obtain periodicity by applying the graded phase twists (3.13) to the new states (3.18). In these new states, the new gauge transformation matrices W are

$$\bar{W}(\mathbf{k}_0, \mathbf{k}_j) = D^\dagger(\mathbf{k}_j) V^\dagger W(\mathbf{k}_0, \mathbf{k}_j), \tag{3.19}$$

where $D_m(\mathbf{k}_j) = e^{-i\phi_m k_j / L_C}$ is diagonal matrix and the new transition dipole matrix is

$$\bar{\boldsymbol{\xi}}(\mathbf{k}_j) = \bar{W}(\mathbf{k}_0, \mathbf{k}_j) \boldsymbol{\xi}(\mathbf{k}_j) \bar{W}^\dagger(\mathbf{k}_0, \mathbf{k}_j). \tag{3.20}$$

The new gauge is now smooth and periodic along the $\mathbf{k}$ path. It is noted that, in the new TPTG basis, the matrix $g(\mathbf{k}, \mathbf{k} + \Delta\mathbf{k})$ is not an identity matrix anymore, we can see that in the transformation

$$\begin{aligned} \bar{g}_{\lambda\lambda'}(\mathbf{k}_j, \mathbf{k}_{j+1}) &= \left[D^\dagger(\mathbf{k}_j) V^\dagger \tilde{g}(\mathbf{k}_j, \mathbf{k}_{j+1}) V D(\mathbf{k}_{j+1})\right]_{\lambda\lambda'} = \left[D^\dagger(\mathbf{k}_j) D(\mathbf{k}_{j+1})\right]_{\lambda\lambda'} \\ &= e^{-i\phi_\lambda \Delta k / L_C} \delta_{\lambda\lambda'}. \end{aligned} \tag{3.21}$$

Now, the new non-Abelian Berry connection does not vanish and becomes

$$\bar{\boldsymbol{\vartheta}}_{\lambda\lambda'}(\mathbf{k}) = \frac{\phi_\lambda}{L_C} \delta_{\lambda\lambda'}. \tag{3.22}$$

In the above expression, we see that this new Berry connection in the TPTG is independent of $\mathbf{k}$.

3.3 The Gauging Procedure in Polar Coordinates

The Coulomb matrix in the generalized Rabi frequency (2.49) not only involves four band indices but also couples all two-dimensional wave vectors $\mathbf{k}$ and $\mathbf{k}'$, making the evaluation of the Hartree-Fock terms when solving the SBE the most computationally demanding aspect. If using a Cartesian grid for the wave vectors, the computational effort

scales as N^4, where N represents the number of k-points in one direction. Since the band structure is approximately parabolic near the Γ point, the Cartesian grid is not an optimal choice, leading to large N and requiring significant memory and computing time to obtain convergent results. In contrast, if using a polar grid – a more natural choice for the near-circular symmetry of the band structure at the Γ point – despite the computational scaling of $N_k^2\, N_\phi^2$, where N_k and N_ϕ are the number of radial k-points and the number of angles, respectively. Both N_k and N_ϕ can be significantly smaller than N while still achieving convergent results. Therefore, a polar grid is more effective for accurately describing excitonic effects within reasonable numerical effort.

In this section, we will apply the PTG and TPTG to transform the interband term of the SBE (3.1) in polar coordinates.

First, the interband term can be split into two independent components in the polar coordinates as

$$\frac{\partial}{\partial t}\rho_{\mathbf{k}}\Big|_{\text{intra}} = \frac{\partial}{\partial t}\rho_{\mathbf{k}}\Big|^{k}_{\text{intra}} + \frac{\partial}{\partial t}\rho_{\mathbf{k}}\Big|^{\varphi_k}_{\text{intra}}, \tag{3.23}$$

in which

$$\frac{\partial}{\partial t}\rho_{\mathbf{k}}\Big|^{k}_{\text{intra}} = \frac{i}{\hbar}\left[eE^{k}_{\mathbf{k}}(t)\vartheta^{k}_{\mathbf{k}}, \rho_{\mathbf{k}}\right] - \frac{1}{\hbar}eE^{k}_{\mathbf{k}}(t)\frac{\partial}{\partial k}\rho_{\mathbf{k}}, \tag{3.24}$$

$$\frac{\partial}{\partial t}\rho_{\mathbf{k}}\Big|^{\varphi_k}_{\text{intra}} = \frac{i}{\hbar}\left[eE^{\varphi_k}_{\mathbf{k}}(t)\vartheta^{\varphi_k}_{\mathbf{k}}, \rho_{\mathbf{k}}\right] - \frac{1}{\hbar}eE^{\varphi_k}_{\mathbf{k}}(t)\frac{\partial}{\partial \varphi_k}\rho_{\mathbf{k}}. \tag{3.25}$$

Here, the superscripts k and φ_k denote the components in polar coordinate. The relations between the polar and Cartesian components for the Berry connection are

$$\vartheta^{k,\lambda\lambda'}_{\mathbf{k}} = i\left\langle u_{\lambda,\mathbf{k}}\middle|\frac{\partial}{\partial\hat{\mathbf{k}}}\middle|u_{\lambda'\mathbf{k}}\right\rangle = \cos\varphi_k\vartheta^{x,\lambda\lambda'}_{\mathbf{k}} + \sin\varphi_k\vartheta^{y,\lambda\lambda'}_{\mathbf{k}}, \tag{3.26}$$

$$\vartheta^{\varphi_k,\lambda\lambda'}_{\mathbf{k}} = i\left\langle u_{\lambda,\mathbf{k}}\middle|\frac{\partial}{\partial\hat{\boldsymbol{\varphi}}_{\boldsymbol{k}}}\middle|u_{\lambda'\mathbf{k}}\right\rangle = k\Big(-\sin\varphi_k\vartheta^{x,\lambda\lambda'}_{\mathbf{k}} + \cos\varphi_k\vartheta^{y,\lambda\lambda'}_{\mathbf{k}}\Big), \tag{3.27}$$

where $\hat{\mathbf{k}}$ and $\hat{\boldsymbol{\varphi}}_{\boldsymbol{k}}$ are unit vectors in polar coordinates. That these unit vectors are not the same for any k-points leads to the k-dependence of the electric field, with its components given by

$$E^{k}_{\mathbf{k}}(t) = \cos\varphi_k E^{x}(t) + \sin\varphi_k E^{y}(t), \tag{3.28}$$

$$E^{\varphi_k}_{\mathbf{k}}(t) = \frac{1}{k}[-\sin\varphi_k E^{x}(t) + \cos\varphi_k E^{y}(t)]. \tag{3.29}$$

Next, we will build the gauge transformation matrix $W(\mathbf{k}_0, \mathbf{k})$ by using Eq. (3.10) for each component of the polar coordinates as illustrated in Fig. 3.1. For the k-component, we choose the k-path as the straight lines starting at $(0, 0)$ whose k-points have the same angular coordinate. For the φ-component, the k-path is chosen as a concentric part of a circle starting at $\mathbf{k}_{\varphi_0} = (k, 0)$ whose k-points have the same radial coordinate.

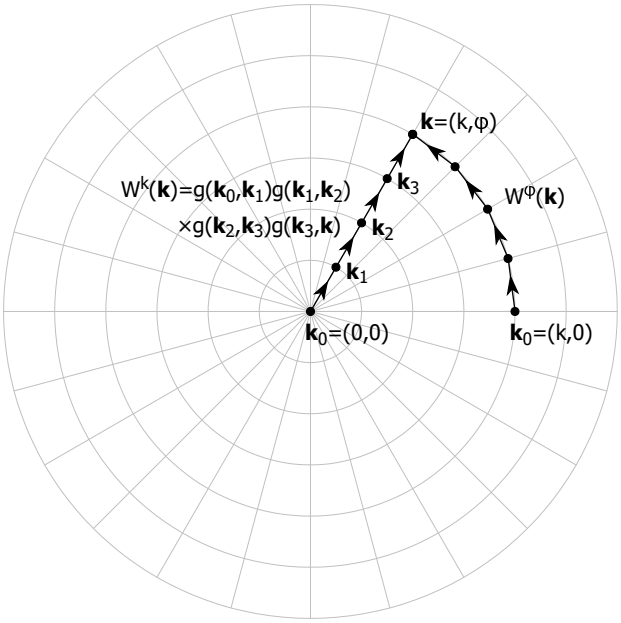

Figure 3.1: Diagrammatic illustration of the operators W^k and W^φ on a polar grid, where these operators establish connections between the basis point $\mathbf{k}$ and the starting points $\mathbf{k}_0$ located on their respective grid lines. This schematic is reproduced with permission from Ref. [96].

Applying the PTG transform for the k-component part in Eq. (3.23) and performing some algebraic manipulation via the relation

$$\frac{\partial}{\partial k} W^k(\mathbf{0},\mathbf{k}) = -iW^k(\mathbf{0},\mathbf{k})\vartheta^k_{\mathbf{k}}, \tag{3.30}$$

we can obtain

$$W^k(\mathbf{0},\mathbf{k})\left(\frac{\partial}{\partial t}\rho_{\mathbf{k}}\Big|^k_{\text{intra}}\right)\left[W^k(\mathbf{0},\mathbf{k})\right]^\dagger = -\frac{1}{\hbar}eE^k(t)\frac{\partial}{\partial k}\tilde{\rho}_{\mathbf{k}}. \tag{3.31}$$

Now, we can take the numerical derivative in the expression above and transform it back to the original Bloch basis

$$\frac{\partial}{\partial t}\rho_{\mathbf{k}}\Big|^k_{\text{intra}} = \left[W^k(\mathbf{0},\mathbf{k})\right]^\dagger\left(-\frac{1}{\hbar}eE^k_{\mathbf{k}}(t)\frac{\partial}{\partial k}\tilde{\rho}_{\mathbf{k}}\right)W^k(\mathbf{0},\mathbf{k}). \tag{3.32}$$

For the φ_k-component part in Eq. (3.23), to reserve the periodicity in this dimension, we

apply the TPTG transformation by using Eq. (3.19). With the relation

$$\frac{\partial}{\partial\varphi_k}\bar{W}^{\varphi_k}(\mathbf{k}_{\varphi_0},\mathbf{k}) = -iD(\mathbf{k})\bar{\vartheta}^{\varphi_k}_{\mathbf{k}} - i\bar{W}^{\varphi_k}(\mathbf{k}_{\varphi_0},\mathbf{k})\vartheta^{\varphi_k}_{\mathbf{k}}, \tag{3.33}$$

and after some algebraic manipulation, we obtain

$$\bar{W}^{\varphi_k}(\mathbf{k}_{\varphi_0},\mathbf{k})\left(\frac{\partial}{\partial t}\rho_{\mathbf{k}}\Big|^{\varphi_k}_{\text{intra}}\right)\left[\bar{W}^{\varphi_k}(\mathbf{k}_{\varphi_0},\mathbf{k})\right]^{\dagger} = \frac{i}{\hbar}\left[eE^{\varphi_k}_{\mathbf{k}}(t)\bar{\vartheta}^{\varphi_k}_{\mathbf{k}},\bar{\rho}_{\mathbf{k}}\right] - \frac{1}{\hbar}eE^{\varphi_k}_{\mathbf{k}}(t)\frac{\partial}{\partial\varphi_k}\bar{\rho}_{\mathbf{k}}. \tag{3.34}$$

Again, taking the numerical derivative and subsequently transforming it back to the original Bloch basis leads to

$$\frac{\partial}{\partial t}\rho_{\mathbf{k}}\Big|^{\varphi_k}_{\text{intra}} = \left[\bar{W}^{\varphi_k}(\mathbf{k}_{\varphi_0},\mathbf{k})\right]^{\dagger}\left\{\frac{i}{\hbar}\left[eE^{\varphi_k}_{\mathbf{k}}(t)\bar{\vartheta}^{\varphi_k}_{\mathbf{k}},\bar{\rho}_{\mathbf{k}}\right] - \frac{1}{\hbar}eE^{\varphi_k}_{\mathbf{k}}(t)\frac{\partial}{\partial\varphi_k}\bar{\rho}_{\mathbf{k}}\right\}\bar{W}^{\varphi_k}(\mathbf{k}_{\varphi_0},\mathbf{k}). \tag{3.35}$$

Here, the density matrix and Berry connection are transformed with the TPTG as

$$\bar{\rho}_{\mathbf{k}} = \bar{W}^{\varphi_k}(\mathbf{k}_{\varphi_0},\mathbf{k})\rho_{\mathbf{k}}\left[\bar{W}^{\varphi_k}(\mathbf{k}_{\varphi_0},\mathbf{k})\right]^{\dagger}, \tag{3.36}$$

$$\bar{\vartheta}^{\varphi_k}_{\mathbf{k}} = \bar{W}^{\varphi_k}(\mathbf{k}_{\varphi_0},\mathbf{k})\vartheta^{\varphi_k}_{\mathbf{k}}\left[\bar{W}^{\varphi_k}(\mathbf{k}_{\varphi_0},\mathbf{k})\right]^{\dagger}. \tag{3.37}$$

The new Berry connection is just a diagonal matrix which has the elements

$$\bar{\vartheta}^{\varphi_k,\lambda\lambda'}_{\mathbf{k}} = \frac{\phi^{\lambda}_k}{2\pi}\delta_{\lambda\lambda'}, \tag{3.38}$$

where ϕ^{λ}_k are the non-Abelian Berry phases.

3.4 Photocurrents

In semiconductor systems lacking inversion symmetry, a nonzero second-order optical susceptibility, $\chi^{(2)}$, allows photocurrents to be generated using a single optical pulse [26, 28, 40, 54, 94, 97–110]. These photocurrents arise from three main mechanisms: injection, shift, and rectification currents. This section focuses on the first two contributions. Injection currents result from an asymmetric momentum distribution of photoexcited carriers induced by circularly polarized light, while shift currents are caused by real-space displacements of electrons during excitation from the valence to the conduction band under linearly polarized light. After numerical integrating the SBE in the LG (3.1), the density of the charge current induced by the optical excitation is given by

$$\mathbf{j}(t) = \frac{e}{L^2}\sum_{\lambda,\mu,\mathbf{k}}\mathbf{v}^{\lambda\mu}_{\mathbf{k}}\rho^{\mu\lambda}_{\mathbf{k}}(t), \tag{3.39}$$

whereas in the VG, we have

$$\mathbf{j}(t) = \frac{e}{L^2} \sum_{\lambda,\mu,\mathbf{k}} \left(\mathbf{v}_{\mathbf{k}}^{\lambda\mu} - \frac{e}{m} \mathbf{A}(t) \right) \rho_{\mathbf{k}}^{\mu\lambda}(t). \tag{3.40}$$

The injection and shift currents are defined as the zero-frequency contributions of the diagonal

$$\mathbf{j}_d(t) = \frac{e}{L^2} \sum_{\lambda,\mathbf{k}} \mathbf{v}_{\mathbf{k}}^{\lambda\lambda} \rho_{\mathbf{k}}^{\lambda\lambda}(t) \tag{3.41}$$

and off-diagonal

$$\mathbf{j}_{od}(t) = \frac{e}{L^2} \sum_{\lambda,\mu\neq\lambda,\mathbf{k}} \mathbf{v}_{\mathbf{k}}^{\lambda\mu} \rho_{\mathbf{k}}^{\lambda\mu}(t) \tag{3.42}$$

contributions to the total current $\mathbf{j}(t)$, respectively [54, 94].

Additionally, in the term $\Gamma_{\lambda,\mathbf{k}}$ in the EOM (3.1) for the LG and the EOM (3.2) for the VG, we consider the contributions from scattering processes by accounting for the scattering between LO and LA phonons and carriers in the second-order Born-Markov approximations. The resulting contributions for occupations are given by [4, 50, 69]

$$\begin{aligned}\left(\frac{\partial}{\partial t}\rho_{\mathbf{k}}\Big|_{\text{scatt}}\right)_{\lambda\lambda} = \frac{2\pi}{\hbar^2} \sum_{\alpha,\mu,\mathbf{q},q_\perp} \left|g^{\alpha,\mu\lambda}_{\mathbf{k}+\mathbf{q},\mathbf{k},q_\perp}\right|^2 \Big\{ & \\ \left[\delta\left(\omega^{\alpha,\mu\lambda-}_{\mathbf{k}+\mathbf{q},\mathbf{k},q_\perp}\right)\left(N^{\alpha}_{\mathbf{q},q_\perp}+1\right) + \delta\left(\omega^{\alpha,\mu\lambda+}_{\mathbf{k}+\mathbf{q},\mathbf{k},q_\perp}\right) N^{\alpha}_{\mathbf{q},q_\perp}\right] \rho^{\mu\mu}_{\mathbf{k}+\mathbf{q}}\left(1-\rho^{\lambda\lambda}_{\mathbf{k}}\right) & \\ - \left[\delta\left(\omega^{\alpha,\mu\lambda-}_{\mathbf{k}+\mathbf{q},\mathbf{k},q_\perp}\right) N^{\alpha}_{\mathbf{q},q_\perp} + \delta\left(\omega^{\alpha,\mu\lambda+}_{\mathbf{k}+\mathbf{q},\mathbf{k},q_\perp}\right)\left(N^{\alpha}_{\mathbf{q},q_\perp}+1\right)\right]\left(1-\rho^{\mu\mu}_{\mathbf{k}+\mathbf{q}}\right)\rho^{\lambda\lambda}_{\mathbf{k}} \Big\}, & \end{aligned} \tag{3.43}$$

and for the coherences ($\lambda \neq \lambda'$) by

$$\begin{aligned}\left(\frac{\partial}{\partial t}\rho_{\mathbf{k}}\Big|_{\text{scatt}}\right)_{\lambda\lambda'} = -\frac{1}{\hbar^2}\rho^{\lambda\lambda'}_{\mathbf{k}} \sum_{\alpha,\mu,\mathbf{q},q_\perp} \Bigg\{ & \left|g^{\alpha,\mu\lambda'}_{\mathbf{k}+\mathbf{q},\mathbf{k},q_\perp}\right|^2 \Bigg[\mathcal{D}\left(\omega^{\alpha,\mu\lambda'-}_{\mathbf{k}+\mathbf{q},\mathbf{k},q_\perp}\right)\left(N^{\alpha}_{\mathbf{q},q_\perp} + \rho^{\mu\mu}_{\mathbf{k}+\mathbf{q}}\right) \\ & \qquad + \mathcal{D}\left(\omega^{\alpha,\mu\lambda'+}_{\mathbf{k}+\mathbf{q},\mathbf{k},q_\perp}\right)\left(N^{\alpha}_{\mathbf{q},q_\perp}+1-\rho^{\mu\mu}_{\mathbf{k}+\mathbf{q}}\right)\Bigg] \\ & + \left|g^{\alpha,\lambda\mu}_{\mathbf{k},\mathbf{k}+\mathbf{q},q_\perp}\right|^2 \Bigg[\mathcal{D}\left(\omega^{\alpha,\lambda\mu+}_{\mathbf{k},\mathbf{k}+\mathbf{q},q_\perp}\right)\left(N^{\alpha}_{\mathbf{q},q_\perp} + \rho^{\mu\mu}_{\mathbf{k}+\mathbf{q}}\right) \\ & \qquad + \mathcal{D}\left(\omega^{\alpha,\lambda\mu-}_{\mathbf{k},\mathbf{k}+\mathbf{q},q_\perp}\right)\left(N^{\alpha}_{\mathbf{q},q_\perp}+1-\rho^{\mu\mu}_{\mathbf{k}+\mathbf{q}}\right)\Bigg]\Bigg\}, \end{aligned} \tag{3.44}$$

in which the phonon distribution is $N^{\alpha}_{\mathbf{q},q_\perp} = \left[\exp\left\{\hbar\omega^{\alpha}_{\mathbf{q},q_\perp}/k_{\mathrm{B}}T\right\}-1\right]^{-1}$, $\mathcal{D}(\omega) = i\mathcal{P}(1/\omega) + \pi\delta(\omega)$, and $\omega^{\alpha,\lambda\mu\pm}_{\mathbf{k},\mathbf{k}',q_\perp} = \varepsilon^{\lambda}_{\mathbf{k}}/\hbar - \varepsilon^{\mu}_{\mathbf{k}'}/\hbar \pm \omega^{\alpha}_{\mathbf{q},q_\perp}$.

Below, we present results obtained from numerically integrating the SBE in the LG (3.1),

including the scattering between carriers and LO phonons. These results will be compared to those obtained from solving the SBE in the VG (3.2). The material used for our simulation is a [1 1 0]-oriented GaAs/$Al_{0.35}Ga_{0.65}As$ QW of 10 nm wide with the crystallographic directions [0 0 $\bar{1}$], [$\bar{1}$ 1 0], [1 1 0] taken as the x, y, z directions, respectively. The calculations are carried out for temperatures of $T = 10\,\mathrm{K}$ and $T = 300\,\mathrm{K}$ (room temperature). The parameters of bulk GaAs are taken from the work of Winkler [46]. Figure 3.2 is the result of the band structure of the GaAs QW at room temperature. The band gap energy is 1.46 eV. The spin splitting is quite large in the direction [$\bar{1}$ 1 0] and vanishes in the direction [0 0 1].

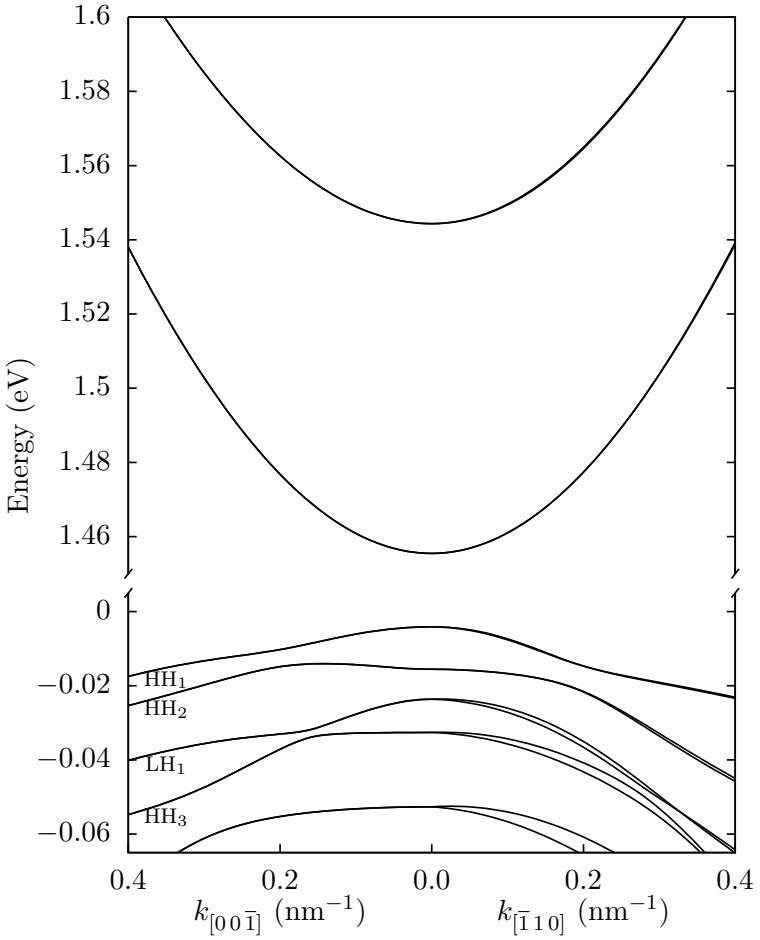

Figure 3.2: Band structure of a 10 nm wide [1 1 0]-oriented GaAs/$Al_{0.35}Ga_{0.65}As$ QW at room temperature. The band gap energy is 1.46 eV.

After obtaining the eigenstates by diagonalization, we do construct the matrix $\mathbf{g}(\mathbf{k})$ by the procedure described above. To verify the validity, we compare the matrix elements for $\xi(\mathbf{k})$ that were calculated by two different expressions (3.6) and (2.23).

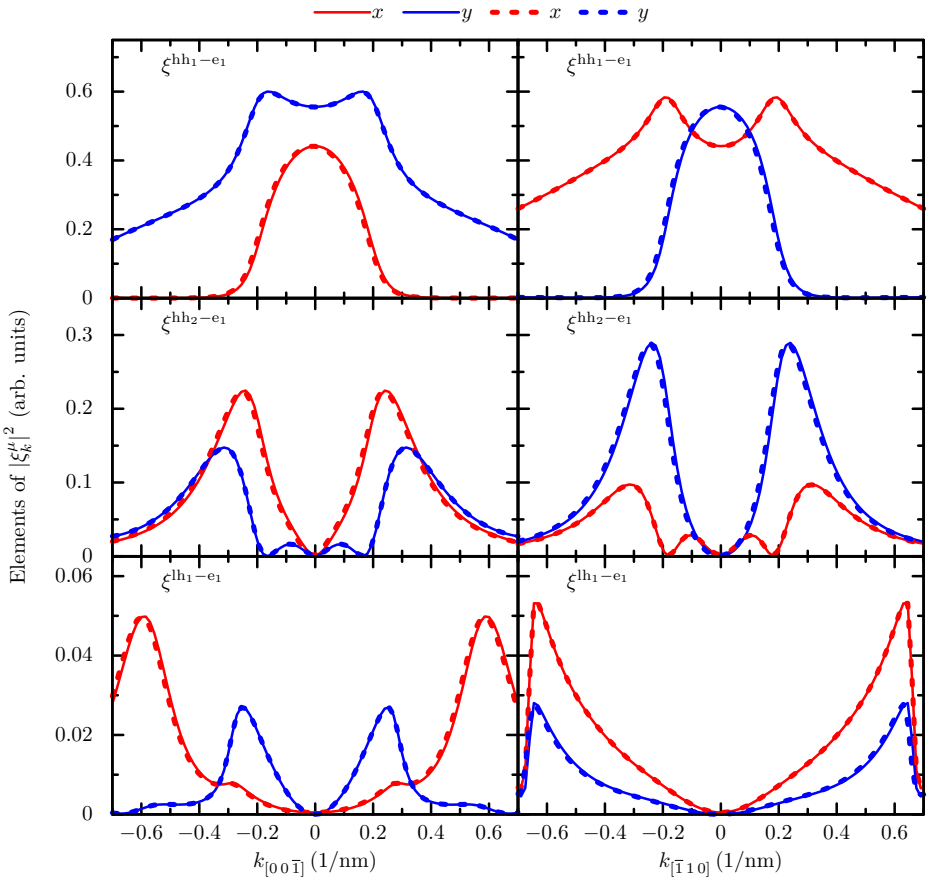

Figure 3.3: Matrix elements $|\boldsymbol{\xi}(\mathbf{k})|^2$ calculated by two different formulas Eq. (2.23) (dashed line) and Eq. (3.6) (solid line). The left figures show the $[0\,0\,\bar{1}]$ direction, while the right figures show the $[\bar{1}\,1\,0]$ direction. The red and blue lines display, respectively, x and y components of $\boldsymbol{\xi}_{\mathbf{k}}$. It should be noted that the matrix elements are taken as the sum of all spin states.

Figure 3.3 shows results of the squared amplitude of the $\boldsymbol{\xi}_{\mathbf{k}}$ matrix elements between the energetically highest heavy-hole bands (HH_1 and HH_2) and the energetically highest light-hole bands (LH_1) and the energetically lowest conduction state (e1). The results obtained by the two different formulas coincide with each other.

To solve the SBE, we take into account the eight energetically highest valance bands and the four energetically lowest s-like conduction bands. For the calculation of shift currents, we also include twelve energetically lowest p-like conduction bands to obtain converged results in the VG.

The excitation pulse propagates in the z direction, which is the growth direction of the QW, resulting in the electric polarization lying in the xy plane of the QW and taking the

time dependence

$$\mathbf{E}(t) = \mathbf{E}_\omega(t)e^{i\omega t} + \text{c.c.}, \tag{3.45}$$

where ω denotes the central frequency of the laser pulse, and $\mathbf{E}_\omega(t)$ represents the envelope function. In our study, it is a Gaussian-shaped form and varies slowly in time as

$$\mathbf{E}_\omega(t) = E_0 e^{-\frac{t^2}{2\tau_L^2}} \left(\cos\theta, \sin\theta e^{i\varphi}, 0\right). \tag{3.46}$$

Here, the notations of E_0 and τ_L denote respectively the peak amplitude and the Gaussian pulse duration. The angle θ represents the polarization angle relative to the x axis, and φ is the phase difference between the x and y components of the laser electric polarization. In the case of a circularly polarized pulse, we set $\varphi = \pm\pi/2$ and $\theta = \pi/4$, whereas for a linearly polarized pulse, $\varphi = 0$ is used.

3.4.1 Injection Currents

The circularly polarized excitation pulse used in this section has $\hbar\omega = 1.54\,\text{eV}$, $\tau_L = 150\,\text{fs}$, and $E_0 = 1 \times 10^4\,\text{V/cm}$. The system is excited by left and right circularly polarized pulses, which are denoted as σ^- and σ^+ in Fig. 3.4, respectively.

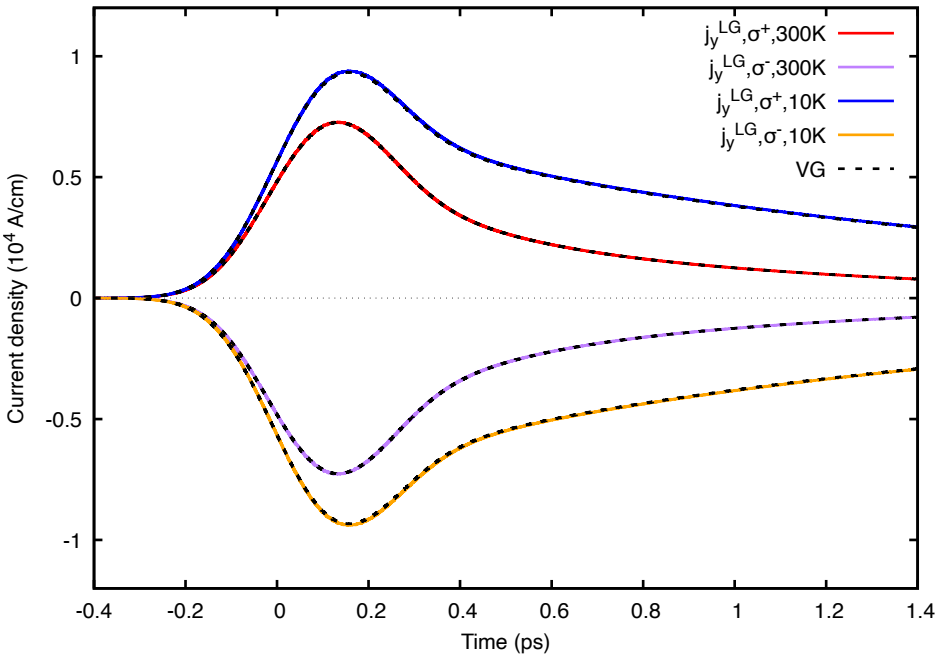

Figure 3.4: Time-dependent injection current densities calculated using the LG (solid lines) and the VG (dashed lines) for different helicities of the circularly polarized excitation pulse as well as for two different temperatures.

Figure 3.4 shows the numerical results of the injection current densities calculated in the LG (solid lines) and in the VG (dashed lines) with different helicities (red and blue lines represent the right circular polarization while purple and yellow lines are for the left one) and different temperatures (red and purple lines are calculated at 300 K while the blue and orange lines are at 10 K). Figure 3.4 reveals three main findings. Firstly, we can see that the results obtained by using the two gauges, i.e., LG and VG, are, as it should be, identical; secondly, the injection currents of two opposite helicities show a mirror symmetry with respect to the zero axis, i.e., the helicity defines the current direction; finally, the influence of temperature: the current decays faster at elevated temperatures. Since at higher temperatures, more phonons exist, they interact with the carriers and lead to a more rapid decay than at low temperatures. To explore this in more detail, we examine how the peak values of the injection currents change when varying the number of bands used in the calculations, see Fig. 3.5.

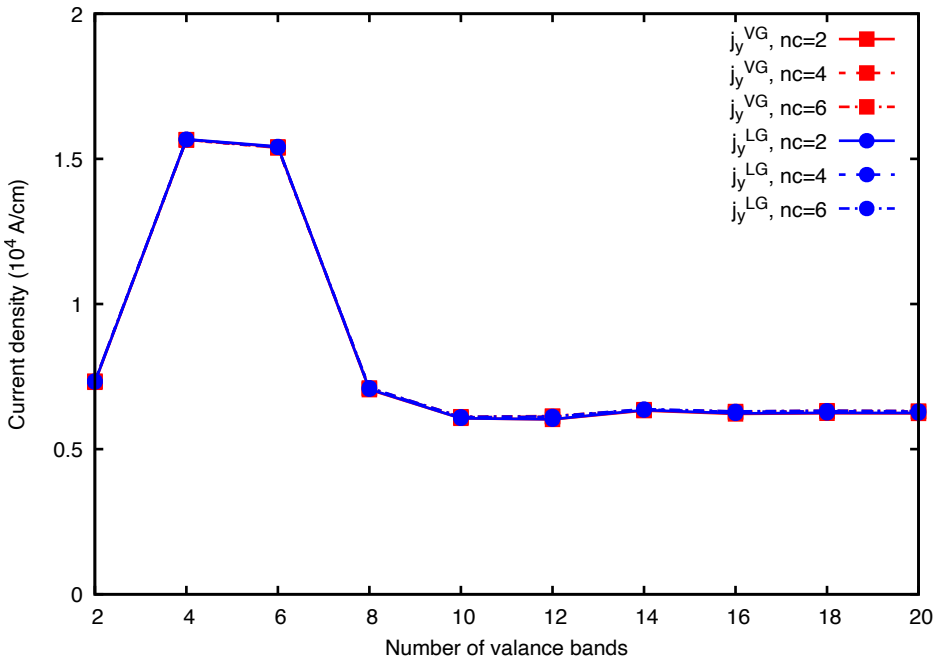

Figure 3.5: Peak values of the injection current densities as a function of the number of valance bands for different numbers of considered conduction bands. The results obtained in the LG and in the VG are depicted by the blue and red lines, respectively.

Obviously, we can see that the injection currents in the two different gauges are identical and converge at about eight valance bands. In principle, because the injection currents only involve resonant near or above band gap excitation, there is no difference between the LG and the VG when varying the number of bands considered in the calculation.

3.4.2 Shift Currents

Next, we present results on shift currents in which the LG reveals an advantage in comparison to the VG. Figure 3.6 displays the x component of the shift current densities calculated in the LG and in the VG. The excitation pulse is linearly polarized along the y direction and has $\hbar\omega = 1.54\,\text{eV}$, $\tau_L = 150\,\text{fs}$, and $E_0 = 1 \times 10^4\,\text{V/cm}$. The temperature is assumed to be 300 K.

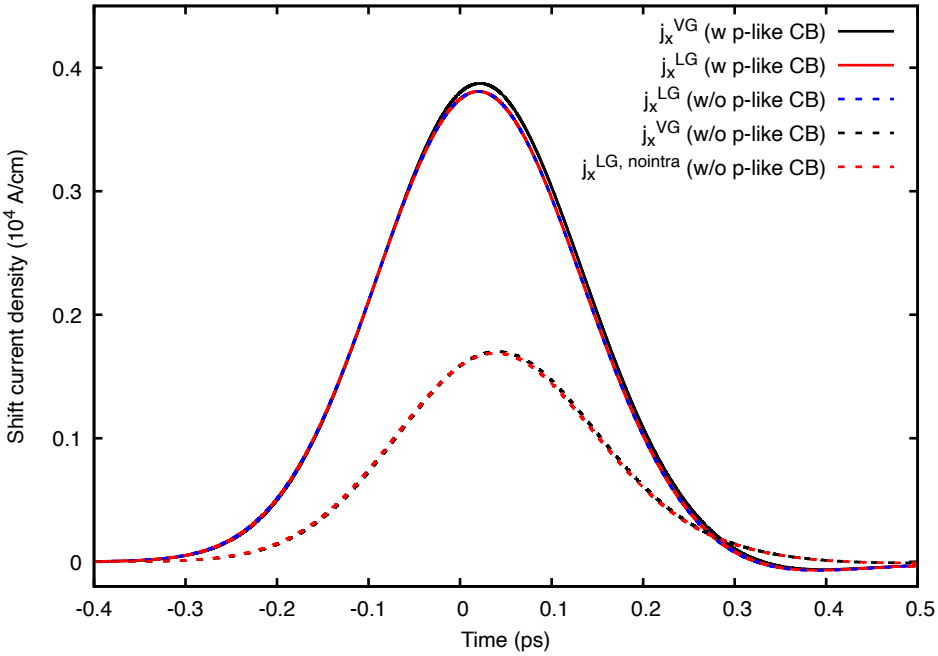

Figure 3.6: x component of the time-dependent shift current densities calculated in the LG with and without p-like conduction bands (solid red and dashed blue lines) and without intraband term (dashed red line). Those of the VG with and without p-like conduction bands are in solid and dashed black lines, respectively. The incident pulse is linearly polarized along the y direction.

Firstly, we can see in Fig. 3.6 that the shape of the shift currents is identical to the envelope of the excitation pulse. Then, there are two noticeable points that we want to discuss here. The first one is the agreement of the results in the LG and in the VG, which indicates that one can use either the LG or the VG to get the correct results. However, a remarkable aspect lies in the fact that if using the VG, we have to take into account the contribution of higher off-resonant bands, i.e., the p-like conduction bands, to obtain the converged result. In contrast, there is no such contribution from these bands in the LG.

To analyze some features of the shift currents, we now study the change of the peak values of the shift currents transients as a function of the number of p-like conduction bands.

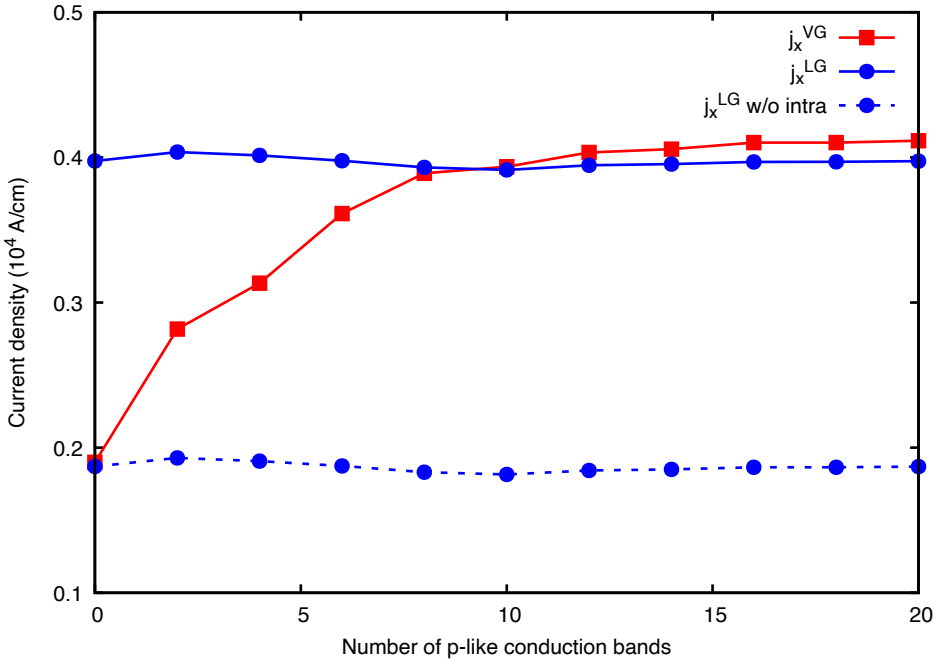

Figure 3.7: Peak values of the x components of shift current densities as a function of the number of p-like conduction bands. The blue lines are calculated using the LG, whereas the red line is for the VG. The dotted line is calculated without intraband terms. The incident pulse is linearly polarized in the y direction.

The result is shown in Fig. 3.7, where the red line is calculated in the VG and the blue lines are in the LG, in which the dotted line is calculated without intraband terms. We can see that when the convergence is obtained, the results from the two gauges approach each other. However, it should be noted that based on this figure, one can learn about the contribution of each term. On the one hand, in the LG, the p-like conduction band does not contribute to the shift current, while it does in the VG. On the other hand, when ignoring intraband terms, the current in the LG will be suppressed. In other words, it reveals two different mechanisms for the two gauges.

3.5 Conclusions

To sum up, we have described a general numerical approach for solving the SBE in the LG. In particular, the implementation of the PTG and TPTG for degenerate bands has been elaborated in detail, enabling the integration of many-body effects in the process of integrating the dynamical equations. Notably, the gauging procedures are validated through their application in calculating ultrafast photocurrents, with results compared against those obtained using the VG. The numerical results demonstrate very good agreement between the two gauges. Furthermore, for the case of shift currents, it should be

emphasized that in the LG, we do not have to include higher off-resonant conduction bands to obtain convergence, which, however, contributes to the VG. This considerably reduces the computational efforts, including time and resource consumption in the LG compared to the VG.

Excitonic Anomalous Currents of Semiconductor Quantum Wells

4

It is well-known that Berry curvature can induce an unconventional motion of charged particles in a direction perpendicular to a slowly varying applied electric field. This phenomenon is called the anomalous velocity or the anomalous current [14–17, 86]. Recently, this anomalous current has been observed in GaAs QWs with appropriate designs both in theory [111] and experiment [112].

Due to the spatial inversion asymmetry in the lattice structure of GaAs, the Berry curvature of the system can exhibit non-zero values at various $\mathbf{k}$ points within the Brillouin zone. However, since the Chern number of the material is zero [111], the macroscopic Berry curvature in equilibrium remains zero. As a result, macroscopic Berry curvature effects cannot be observed in the ground state. So, to break time-reversal symmetry, Virk and Sipe [111] proposed using a circularly polarized laser pulse to excite electrons and induce a spin polarization in the system, thereby generating a macroscopic Berry curvature. This approach and considered setup is illustrated in Fig. 4.1.

Nevertheless, the model used in Ref. [111] is relatively simplified due to the circularly symmetric band structure and the neglecting of many-body interactions, which include Coulomb interactions between carriers and carrier-phonon scattering. To improve this situation, the study presented in this chapter examines the influence of many-body interactions, with a focus on excitonic resonances and phonon scattering processes, in the generation of anomalous currents. We also use a more realistic band-structure model which, e.g., includes anisotropies. For more accurate results, the multiband SBE in the LG, incorporating both Coulomb interaction between carriers and interactions between carriers and phonons, are employed. Specifically, the Coulomb interaction is treated within the TDHF approximation. At this level, the exciton effect arises from the Coulomb attraction term between electrons and holes. The scattering processes between carriers and LO and LA phonons are handled within the framework of the second-order Born-Markov approximation. It is worth noting that carrier-phonon scattering plays a significant role in describing the decay of carrier spin polarization, which in turn alters the decay of the macroscopic Berry curvature caused by circularly polarized light. Here, we focus on the weak excitation regime, where the Coulomb scattering between carriers becomes insignificant and can be disregarded.

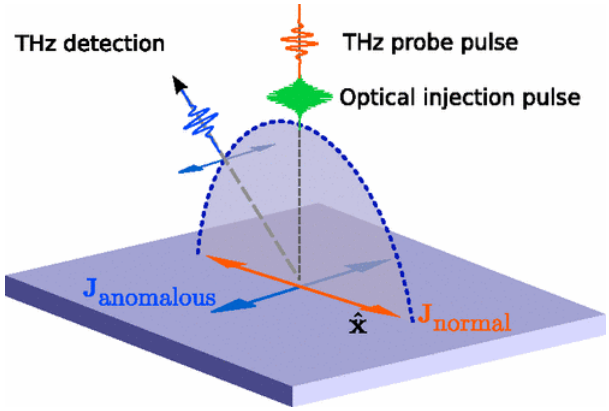

Figure 4.1: Schematic for investigating anomalous currents in GaAs QWs. The green laser pulse (optical injection pulse) is a circularly polarized optical excitation pulse used to initially break the time-reversal symmetry of the system, thereby inducing a macroscopic Berry curvature. The orange laser pulse (THz probe pulse) is a linearly polarized THz pulse (with frequency on the order of THz) whose electric field component is oriented along the x direction, which is used to accelerate the charge carriers. The orange current (J_{normal}) represents the normal current along the direction of the THz electric field, which is generated by carriers accelerated in that direction. The blue current ($J_{\text{anomalous}}$) is the anomalous current perpendicular to the THz pulse, which results from the presence of the macroscopic transient Berry curvature in the system. The blue THz detection pulse is the electromagnetic radiation emitted due to the anomalous current. The figure is reproduced with permission from Ref. [111].

Experimentally, to detect the anomalous current [112] based on the theoretical framework proposed by [111], two distinct pulses are used. First, a circularly polarized optical pulse is applied to generate charged carriers in the material and break time-reversal symmetry, inducing a finite macroscopic Berry curvature, as described in Eq. (4.5). Then, a linearly polarized THz pulse is used to accelerate the carriers excited by the optical pulse within their respective bands, potentially generating an anomalous current in the presence of the finite macroscopic Berry curvature. This acceleration causes the carriers to emit THz radiation with two polarization components: one parallel to the polarization of the THz pulse, corresponding to the normal current, and one perpendicular, corresponding to the anomalous current. The strength of the emitted radiation is proportional to the acceleration of the charged carriers, i.e., the time derivative of both the normal and anomalous THz-induced currents. The anomalous component of the THz radiation measured by the experiment will be compared with the time derivative of the anomalous current obtained from our numerical calculations. The experimental arrangement is illustrated in Fig. 4.2 and will be described in detail in the following section.

4.1 Experimental Setup to Detect Anomalous Currents

This section details the experimental setup employed by the group of Dr. Mark Bieler at Physikalisch-Technische Bundesanstalt [113] with the schematic representation shown in Fig. 4.2. The experiments were conducted on (110)-oriented, undoped, nominally symmetric GaAs/$Al_{0.3}Ga_{0.7}As$ QWs. These samples were chosen for their well-characterized band structure, long relaxation times, and high-quality availability. The (1 1 0)-orientation is particularly advantageous, as it induces significant spin splitting along the [1-10] direction, which results in a large Berry curvature and, thereby, a substantial anomalous current. The investigated QWs have thicknesses of 15 nm and 28 nm, with the crystallographic axes [0 0 1], [1 $\bar{1}$ 0], and [1 1 0] aligned along the x, y, and z directions, respectively [113].

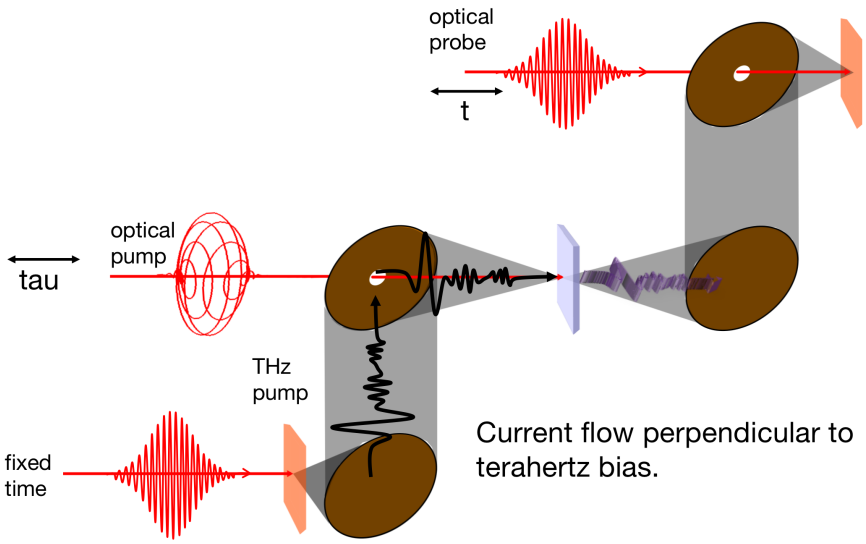

Figure 4.2: Schematic diagram of the experimental setup for measuring anomalous currents in GaAs QWs. These measurements were conducted by the group of Dr. Mark Bieler (Physikalisch-Technische Bundesanstalt, Braunschweig).

Initially, the output from a femtosecond laser (150-fs duration pulses, tunable energy between 1.51 eV and 1.55 eV to excite heavy-hole excitons) was split into three beams.

The first beam, a circularly polarized optical pump beam with 2 nJ pulse energy, was focused to a spot size of 200 µm, creating a carrier density of $1 \times 10^{11}\,\mathrm{cm}^{-2}$ in the QWs. This excitation breaks time-inversion symmetry, which is a key condition for observing anomalous currents in GaAs.

The second beam, a linearly polarized THz pulse, $\mathbf{E}_{\mathrm{THz}}$, is generated via optical rectification in a 2 mm thick (110)-oriented zinc telluride (ZnTe) crystal. This THz pulse, with polarization parallel to the x axis, acts as a time-dependent electric bias, generating a peak electric field of 10 V/cm in the sample that is aligned with the optical pump. The

combined optical/THz excitation induces an anomalous current in the QW plane along the y direction. This ultrafast-induced anomalous current emits THz radiation, which corresponds to an electric field that is proportional to the time derivative of the anomalous current and orthogonal to E_{THz}.

The third beam, a linearly polarized probe, detects the THz radiation using electro-optic sampling in a 1 mm thick, (1 1 0)-oriented ZnTe crystal [98]. To isolate the THz radiation and suppress E_{THz}, the detection crystal was oriented accordingly and two THz polarizers were employed.

The measurement process is conducted as follows. The delay of the probe beam is set to capture a specific time instant t of the time derivative of the anomalous current, denoted as $\mathrm{d}\mathbf{J}^{\mathrm{a}}(t)/\mathrm{d}t$, and its strength is assessed in relation to the delay between the optical pump and the THz pulses. This procedure is referred to as a delay scan. To generate the contour plots, the probe beam delay is incremented from t to $t + \Delta t$, and a new delay scan is performed for the updated time instant of $\mathrm{d}\mathbf{J}^{\mathrm{a}}(t)/\mathrm{d}t$. The starting point of the delay scan is adjusted to $\tau \longrightarrow \tau - \Delta t$. This process is repeated to cover the entire shape of $\mathrm{d}\mathbf{J}^{\mathrm{a}}(t)/\mathrm{d}t$, with each delay scan forming a column in the contour plot. A consistent optically-induced momentum-space distribution is ensured across all time instances of the emitted THz radiation by varying the starting point of the delay scans according to the sampled time instant of $\mathrm{d}\mathbf{J}^{\mathrm{a}}(t)/\mathrm{d}t$.

It is important to note that the total current may also include other components, such as shift currents. To isolate the anomalous current and eliminate these extraneous contributions, one subtracts the measurements taken with left and right circularly polarized pump pulses [112]. This method works because reversing the helicity of the circular optical pulse reverses the sign of the anomalous current while shift currents remain unchanged.

4.2 Theoretical Model

To obtain the anomalous current generated according to the scheme in Fig. 4.1, we use the SBE in the LG as presented in Chapter 3, Eq. (3.1), within the TDHF approximation. Also, the electrons scattering with LA and LO phonons are incorporated as described by Eqs. (3.43) and (3.44). Once the SBE solutions have been computed, the charge current density induced by the light-matter interaction is determined by

$$\mathbf{J}(t) = \mathbf{J}^{\mathrm{intra}}(t) + \mathbf{J}^{\mathrm{inter}}(t). \tag{4.1}$$

The first term on the right-hand side of Eq. (4.1) is the current contributed from carrier occupations, given by

$$\mathbf{J}^{\mathrm{intra}}(t) = \frac{e}{L^2}\sum_{e_i,\mathbf{k}} \mathbf{v}_{\mathbf{k}}^{e_i e_i} n_{\mathbf{k}}^{e_i} + \frac{e}{L^2}\sum_{h_i,\mathbf{k}} \mathbf{v}_{\mathbf{k}}^{h_i h_i} n_{\mathbf{k}}^{h_i}. \tag{4.2}$$

The above current is defined by the derivative of the band energy dispersion, $\mathbf{v}_{\mathbf{k}}^{\lambda\lambda} = 1/\hbar\boldsymbol{\nabla}_{\mathbf{k}}\varepsilon_{\mathbf{k}}^{\lambda}$. In centrosymmetric material, this current will vanish, whereas in centrosymmetric material, this current will exist for non-symmetric carrier occupations. When a THz field is applied, it accelerates the charged carriers within the material, causing a shift in their distribution in k-space. This shift results in a non-symmetric carrier distribution, which in turn generates a current aligned with the polarization direction of the THz pulse. This current is referred to as the normal current. The second term on the right-hand side of Eq. (4.1) is the current contributed from interband and intersubband coherences, given by

$$\mathbf{J}^{\text{inter}}(t) = \frac{e}{L^2}\sum_{h_i\neq h_j,\mathbf{k}} \mathbf{v}_{\mathbf{k}}^{h_ih_j} n_{\mathbf{k}}^{h_ih_j} + \frac{e}{L^2}\sum_{e_i\neq e_j,\mathbf{k}} \mathbf{v}_{\mathbf{k}}^{e_ie_j} n_{\mathbf{k}}^{e_ie_j} + \frac{e}{L^2}\sum_{h_i,e_j,\mathbf{k}} \left(\mathbf{v}_{\mathbf{k}}^{h_ie_j} p_{\mathbf{k}}^{h_ie_j} + \text{c.c}\right). \quad (4.3)$$

From the interband current $\mathbf{J}^{\text{inter}}(t)$, the anomalous current $\mathbf{J}^{\text{a}}(t)$ can be extracted by filtering the appropriate direction and frequency. In the first-order adiabatic perturbation with respect to the THz pulse, the anomalous currents can be approximated as [32, 86, 111]

$$\mathbf{J}^{\text{a}}(t) = -\frac{e^2}{\hbar}\mathbf{E}_{\text{THz}}(t)\times\mathbf{e}_z\left\langle\Omega^z\right\rangle(t), \quad (4.4)$$

with $\left\langle\Omega^z\right\rangle(t)$ being the macroscopic Berry curvature, given by

$$\begin{aligned}\left\langle\Omega^z\right\rangle(t) = &\frac{1}{L^2}\sum_{e_i,\mathbf{k}}\Omega_{\mathbf{k}}^{z,e_ie_i} n_{\mathbf{k}}^{e_i} + \frac{1}{L^2}\sum_{h_i,\mathbf{k}}\Omega_{\mathbf{k}}^{z,h_ih_i} n_{\mathbf{k}}^{h_i} \\ &+ \frac{1}{L^2}\sum_{e_i\neq e_j,\mathbf{k}}\Omega_{\mathbf{k}}^{z,e_ie_j} n_{\mathbf{k}}^{e_ie_j} + \frac{1}{L^2}\sum_{h_i\neq h_j,\mathbf{k}}\Omega_{\mathbf{k}}^{z,h_ih_j} n_{\mathbf{k}}^{h_ih_j}.\end{aligned} \quad (4.5)$$

Here, $\Omega_{\mathbf{k}}^{z,\lambda\lambda'}$ are the matrix elements of the non-Abelian microscopic Berry curvature defined within a single band and between two degenerate or near-degenerate bands. Their matrix elements can be evaluated using the Kubo-like formula [90, 91] in terms of velocity matrix elements as

$$\Omega_{\mathbf{k}}^{z,\lambda\lambda'} = i\hbar^2\sum_{\mu\notin\Delta}\frac{v_{\mathbf{k}}^{x,\lambda\mu}v_{\mathbf{k}}^{y,\mu\lambda'} - v_{\mathbf{k}}^{y,\lambda\mu}v_{\mathbf{k}}^{x,\mu\lambda'}}{\left(\varepsilon_{\mathbf{k}}^{\lambda} - \varepsilon_{\mathbf{k}}^{\mu}\right)\left(\varepsilon_{\mathbf{k}}^{\lambda'} - \varepsilon_{\mathbf{k}}^{\mu}\right)}, \quad (4.6)$$

where λ and λ' lie within the same degenerate or near-degenerate subspaces.

It is important to mention that the experimentally measured anomalous current is a third-order nonlinear process involving a second-order excitation induced by the optical field and a linear interaction with the THz field. In second order in the optical field, three types of currents can arise: injection, shift, and rectification currents [54, 94, 101], with the first two discussed in Chapter 3. To isolate the anomalous current, we expand the SBE to third order by calculating $\rho^{(i)}(\mathbf{k})$ for $i = 1, 2, 3$, and $\rho_{\mathbf{k}}^{(3)} \propto |\mathbf{E}_{\text{opt}}|^2\mathbf{E}_{\text{THz}}$. We realize that $\rho_{\mathbf{k}}^{(3)}$ can result from two different excitation pathways: (i) Opt-Opt-THz where $\rho_{\mathbf{k}}^{(1)}$ and $\rho_{\mathbf{k}}^{(2)}$

are generated by $\mathbf{E}_{\text{opt}}$ and then $\rho_{\mathbf{k}}^{(3)}$ is generated by $\mathbf{E}_{\text{THz}}$ from $\rho_{\mathbf{k}}^{(2)}$; and (ii) Opt-THz-Opt where $\rho_{\mathbf{k}}^{(1)}$ is generated by $\mathbf{E}_{\text{opt}}$, then $\rho_{\mathbf{k}}^{(2)}$ by $\mathbf{E}_{\text{THz}}$ from $\rho_{\mathbf{k}}^{(1)}$, and finally $\rho_{\mathbf{k}}^{(3)}$ by $\mathbf{E}_{\text{opt}}$ from $\rho_{\mathbf{k}}^{(2)}$. Upon implementing both pathways and analyzing the results, we find that pathway (i) vastly dominates under the conditions considered in this study.

4.3 Band Structure of GaAs Quantum Wells and their Berry Curvatures

In the simulation, GaAs/$Al_{0.3}Ga_{0.7}$As QWs grown in the direction [1 1 0] with widths of 15 nm and 28 nm are considered. The dependence of the band gap on temperature is modeled using the Varshni relation [114], expressed as $E_g(T) = E_g(0) - \alpha T^2/(T+\beta)$, where α and β are material-specific parameters. Furthermore, the band parameters are given in Appendix A.2 and were taken from Ref. [46]. For comparison with experimental data [112], the calculations are performed at 4 K for the 28 nm wide QW and at 77 K for the 15 nm wide QW.

The valence band structures and their microscopic Berry curvatures along the $[\bar{1}\,1\,0]$ direction are displayed in Fig. 4.3. The Berry curvatures shown in this figure are summed over the spin subbands. In the $[\bar{1}\,1\,0]$ direction, one can see that the band structure reveals a slight spin splitting, which arises from the inversion asymmetry of the lattice structure and quite strong spin-orbit coupling of the GaAs material. The Berry curvatures, on the other hand, exhibit large amplitudes near the avoided crossings of the valence bands. Additionally, due to the material's time-reversal symmetry, the Berry curvature summed over spin subbands behaves as an odd function of $\mathbf{k}$, resulting in a vanishing macroscopic Berry curvature in equilibrium.

Before delving into the dynamics of the anomalous currents, it is worth examining the characteristics of the linear absorption spectra of the QWs under consideration. These spectra are defined by the imaginary part of optical response, $\alpha(\omega) \propto \text{Im}[\mathbf{e} \cdot \mathbf{P}(\omega)]$, where $\mathbf{e}$ represents the polarization direction of the optical pulse and $\mathbf{P}(t)$ represents the macroscopic optical polarization. This polarization is determined by the interband coherence p_{vc} via

$$\mathbf{P}(t) = \sum_{\text{vc}} \xi_{\mathbf{k}}^{\text{cv}} p_{\mathbf{k}}^{\text{vc}} + \text{c.c.}, \tag{4.7}$$

here, $p_{\text{vc}}(\mathbf{k})$ is the interband coherence. In the linear optical regime, $p_{\text{vc}}(\mathbf{k})$ is obtained from the SBE solution as follows

$$i\hbar \frac{\partial}{\partial t} p_{\mathbf{k}}^{\text{vc}} = \left(\varepsilon_{\mathbf{k}}^{\text{v}} - \varepsilon_{\mathbf{k}}^{\text{c}} - \frac{i\hbar}{T_2} \right) p_{\mathbf{k}}^{\text{vc}} - e\mathbf{E}(t) \cdot \xi_{\mathbf{k}}^{\text{vc}} - \sum_{\text{c}',\text{v}',\mathbf{k}'} V_{\mathbf{k},\mathbf{k}',\mathbf{k}'-\mathbf{k}}^{\text{v}'\text{cc}'\text{v}} p_{\mathbf{k}'}^{\text{v}'\text{c}'}. \tag{4.8}$$

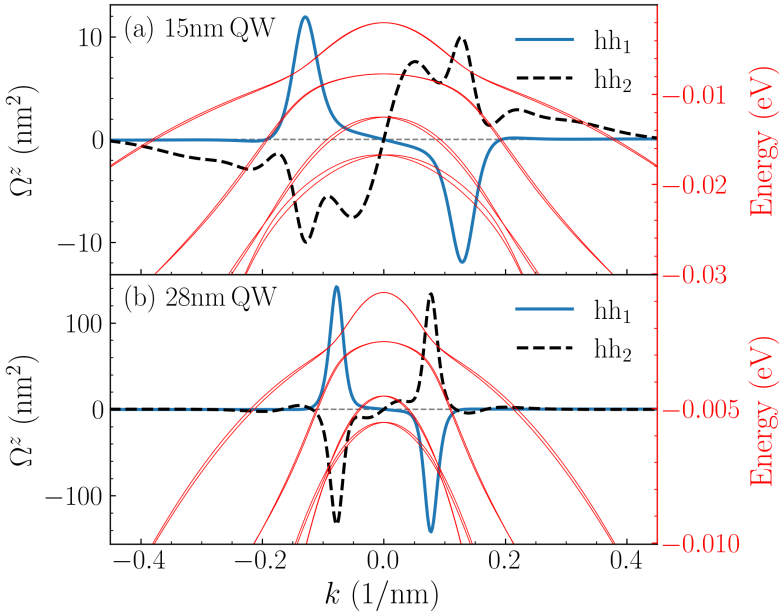

Figure 4.3: The microscopic Berry curvatures as a function of k calculated using Eq. (4.6) are presented for (1 1 0)-oriented GaAs/$Al_{0.3}Ga_{0}$.7As QWs along the $[\bar{1}\,1\,0]$ direction. These results are obtained by summing over the spin subbands for the two highest heavy-hole bands: hh_1 (solid blue lines) and hh_2 (dashed black lines), and are shown for QW widths of 15 nm at 77 K (a) and 28 nm at 4 K (b). To enhance clarity, the valence band structures obtained by the 14-band $\mathbf{k}\cdot\mathbf{p}$ model within the envelope function approximation are overlaid with the red curves. For the 15 nm well, the band gap energy is 1.526 eV and 1.525 eV for the 28 nm well. The figure is reproduced with permission from Ref. [96].

The ultrashort pulse $\mathbf{E}(t)$ in Eq. (4.8) used to calculate the linear absorption spectrum is modeled as a delta-function-like pulse. The scattering with phonons is phenomenologically modeled by a constant dephasing time T_2. By choosing a dephasing time $T_2 = 2$ ps, multiple excitonic resonances can be well resolved.

When solving the multiband SBE (3.2), we account for sixteen bands: the twelve highest-energy levels of the valence band and the four lowest-energy levels of the conduction band. The numerical integration is performed using the fourth-order Runge-Kutta algorithm [115]. These simulation tools and parameters are consistently applied throughout the study.

The results of the linear absorption spectra for different light polarization directions for widths of 15 nm and the 28 nm are shown in Figs. 4.4(a) and 4.4(b), respectively. In both QW widths and for both light polarization directions, the spectra reveal the resonances from excitons. Specifically, the higher peaks are from the 1s heavy-hole excitons corresponding to the e_1-hh_1, e_1-hh_2, and e_2-hh_2 interband transitions. Additionally, smaller peaks associated with the weakly absorbing 2s excitons are also observed. However, the linear absorption spectra for the two polarization directions, [0 0 1] and $[1\,\bar{1}\,0]$, show minor differences in

magnitude, reflecting the anisotropy inherent in the QWs, which is encapsulated in the electronic band structure and wave functions [50].

In the interest of comparison, Fig. 4.4 also includes the interband absorption calculated without accounting for the electron-hole attraction. It is clear that the single-particle absorption is noticeably weaker than the excitonic absorption and displays a step-like rise at the band gap, which reflects the two-dimensional density of states in QWs.

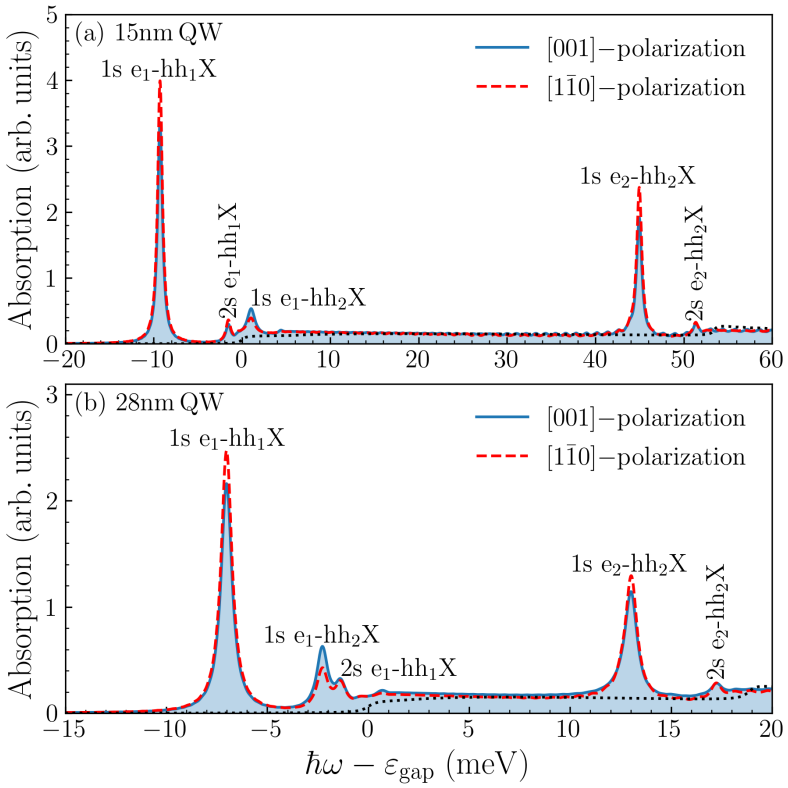

Figure 4.4: The linear absorption spectra for (1 1 0)-oriented GaAs/$Al_{0.3}Ga_{0.7}As$ QWs illustrated for light polarized along the [0 0 1] (solid blue lines) and [1 $\bar{1}$ 0] (dashed red lines) with widths of 15 nm (a) and 28 nm (b). The spectra show peaks at the 1s and 2s heavy-hole exciton resonances (e_1-hh_1 and e_2-hh_2) at −9.2 meV, −1.4 meV, 45 meV, and 51.4 meV for the 15 nm QW, and at −6.9 meV, −1.3 meV, 13.0 meV, and 17.3 meV for the 28 nm QW. In support of comparison, the absorption spectra in the case without Coulomb interaction for light polarized in the [0 0 1] direction are also provided by the dotted black lines. The figure is reproduced with permission from Ref. [96].

4.4 Dynamics of the Berry Curvature

Since the Berry curvature induces anomalous currents, it is insightful to examine its dynamics first before addressing the dynamics of anomalous currents in the next section. It is worth recalling that to simulate anomalous currents, we employ the method described in Refs. [111, 112], as outlined in Sec. 4.1. This approach utilizes two pulses, $\mathbf{E}(t) = \mathbf{E}_{\mathrm{opt}}(t) + \mathbf{E}_{\mathrm{THz}}(t+\tau)$, where τ represents the time delay between them. Both pulses are Gaussian shaped and propagate along the z direction as defined in Eqs. (3.45) and (3.46). The THz pulse is linearly polarized in the x direction with a central frequency of 2 THz, an electric field amplitude of $E_0 = 10\,\mathrm{V/cm}$ and a duration of $\tau_L = 150\,\mathrm{ps}$. The optical excitation pulse has a tunable frequency with an amplitude of $E_0 = 2\,\mathrm{kV/cm}$ and a duration of $\tau_L = 150\,\mathrm{fs}$. As previously noted, we restrict the analysis to the perturbative limit, where the anomalous currents scale linearly with the THz field amplitude and quadratically with the optical field amplitude (i.e., are proportional to the optical field intensity). This scaling remains valid for THz field amplitudes up to approximately 1 kV/cm and optical field amplitudes up to around 10 kV/cm. Beyond these thresholds, additional non-perturbative intensity-dependent effects, such as exciton ionization for stronger THz fields and phase-space filling along with many-body Coulomb correlations (e.g., carrier-carrier scattering) for stronger optical fields, come into play. These effects can weaken the coherent oscillatory dynamics of excitonic wave packets and possibly alter some of the results presented here.

Now, we analyze the macroscopic Berry curvature caused by the circularly polarized optical pulse in the two considered GaAs QWs, as shown in Fig. 4.5. Regarding the temporal evolution, for both QW widths, neglecting the Coulomb interaction results in a monotonic decay of the macroscopic Berry curvature over time, see Figs. 4.5(b) and 4.5(d). In contrast, when the Coulomb interaction is considered, see Figs. 4.5(a) and 4.5(c), the macroscopic Berry curvature exhibits oscillations, which suggest the emergence of oscillations in the transients of anomalous currents, as predicted by Eq. (4.4). The oscillation frequency corresponds to the energy difference between the 1s and 2s exciton resonances, indicating the origin of an excitonic wave packet in the optical excitation [116]. Additionally, the primary contribution of the Coulomb interaction arises due to the hole-electron attraction, which leads to exciton resonances in the absorption. This is reasonable since, in the low-density regime, the repulsive interactions between carriers (electrons and holes) mainly cause a minor renormalization of the band energy, leading to only small changes in the oscillation frequency.

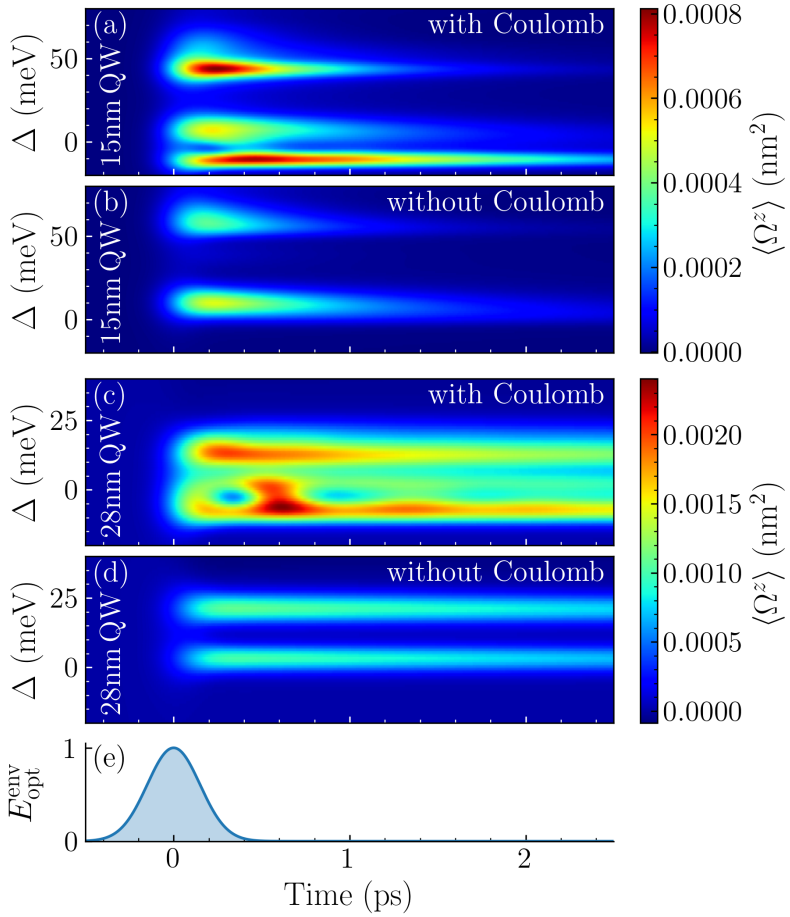

Figure 4.5: The dynamics of the macroscopic Berry curvature [Eq. (4.5)] as a function of time and the detuning $\Delta = \hbar\omega_{\mathrm{L}} - \varepsilon_{\mathrm{gap}}$, i.e., the difference between the optical excitation photon energy ω_{L} and the band gap $\varepsilon_{\mathrm{gap}}$. The results are displayed for (11 0)-oriented GaAs QWs with widths of 15 nm [(a) and (b)], and 28 nm [(c) and (d)] in the two cases: with Coulomb interaction [(a) and (c)] and without Coulomb interaction [(b) and (d)]. The normalized envelope of the circularly polarized excitation pulse is plotted in panel (e). The figure is reproduced with permission from Ref. [96].

Regarding the temporal decay of $\langle\Omega^z\rangle$, the decay is slower for both QW widths when the excitation is below the band gap than when it is above the band gap. This difference is because only scattering with LA phonons is relevant for excitation below the band gap. Meanwhile, both LA and LO phonon scatterings contribute to the decay for excitation above the band gap. Regarding the decay rate, $\langle\Omega^z\rangle$ of the 28 nm QW, see Figs. 4.5(c) and 4.5(d), decays more slowly than for the 15 nm QW, see Figs. 4.5(a) and 4.5(b). This can be attributed to the considered very low temperature (4K for the 28 nm QW), where phonon occupation is very small, which leads to reduced scattering and, thus, a slower decay rate.

To examine the dependence on the detuning more closely, we present a slice of the macroscopic Berry curvature from Fig. 4.5 at $t = 0.6$ ps. For both QW widths, as shown in Fig. 4.6, one can observe that $\langle \Omega^z \rangle$ reaches its maximum when the 1s excitons, namely 1s e_1-hh_1X and 1s e_2-hh_1X, see Fig. 4.4, are excited resonantly. In addition, Fig. 4.6 indicates that the shifts in energy and increase in magnitude are due to the electron-hole attraction. Indeed, when the Coulomb interaction is neglected and excitation occurs below the band gap, no absorption is possible, which results in no induced macroscopic Berry curvature. Above the band gap, the macroscopic Berry curvature peaks at values of photon energies corresponding to avoided crossings in the valence bands shown in Fig. 4.3. Finally, compared to the results that include excitonic effects, the maximum macroscopic Berry curvature is significantly lower.

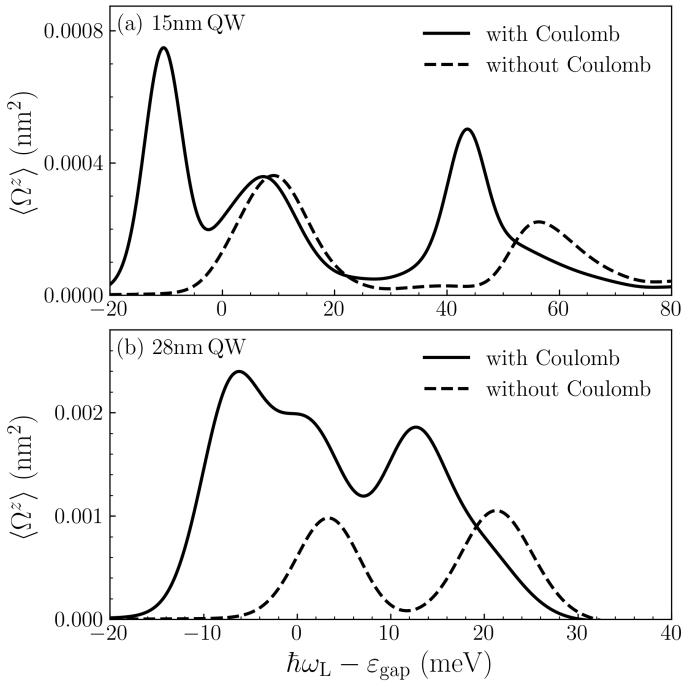

Figure 4.6: The dependence of the macroscopic Berry curvature on the detuning $\hbar\omega_L - \varepsilon_{gap}$, presented for (110)-oriented GaAs/$Al_{0.3}Ga_{0.7}$As QWs with widths of 15 nm (a) and 28 nm (b) at $t = 0.6$ ps. The excitonic enhancement of the macroscopic Berry curvature is clearly illustrated by the difference between the calculations with (solid lines) and without (dashed lines) Coulomb interaction. The figure is reproduced with permission from Ref. [96].

To qualitatively explain the emergence of a macroscopic Berry curvature upon excitonic resonant excitation, we employ a simple model based on ideal, isotropic two-dimensional 1s excitons. In k-space, the exciton ground state is described by the hydrogenic wave

function [4]

$$\psi_{1s}^{X,2D}(k) = \frac{\sqrt{2\pi}a_0}{\left(1+\frac{a_0^2k^2}{4}\right)^{3/2}}, \tag{4.9}$$

where a_0 is the exciton Bohr radius, which is related to the exciton Rydberg energy E_X via

$$E_X = \frac{E_{1s}^{X,2D}}{4} = \frac{\hbar^2}{2m_r a_0^2}. \tag{4.10}$$

We choose E_X to match the numerically calculated exciton binding energies, see Fig. 4.4.

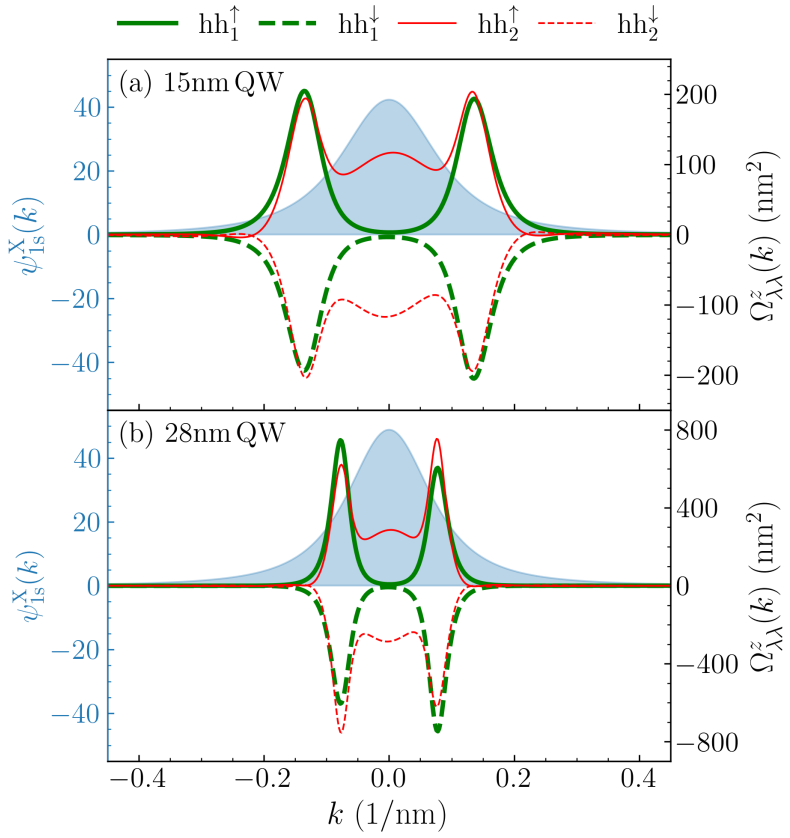

Figure 4.7: The wave functions of 1s excitons in the $[\bar{1}10]$ direction in k-space from the ideal two-dimensional model, represented by cyan areas for (110)-oriented GaAs QWs of 15 nm wide (a) and 28 nm wide (b). The binding energy for the 15 nm QW is $E_{1s}^X = 9.2$ meV with a Bohr radius of $a_0 = 16.9$ nm, while for the 28 nm QW, we use $E_{1s}^X = 6.9$ meV and $a_0 = 19.5$ nm. For the analysis, the Berry curvatures of the bands with a specific spin are shown for the two highest heavy-hole bands: hh_1 (thick green lines) and hh_2 (thin red lines). The figure is reproduced with permission from Ref. [96].

Figure 4.7 illustrates that in k-space, the exciton wave function covers the region with a significant Berry curvature. It indicates that the excitation of excitonic resonances can lead to a large macroscopic Berry curvature. Additionally, Fig. 4.7 shows that for a particular spin, the Berry curvatures of the bands are nearly even functions of k. Under excitation with a circularly polarized optical pulse, only the Berry curvature with spin up (or, depending on the helicity, spin down) is generated, which results in a finite macroscopic Berry curvature. These findings support the experimental arguments presented in Ref. [112].

4.5 Dynamics of the Anomalous Currents

This section focuses on studying the dynamics of anomalous currents, which are proportional to the emitted electromagnetic field, by analyzing their time derivatives. Figure 4.8 shows contour plots of $\mathrm{d}J^{\mathrm{a}}(t)/\mathrm{d}t$ as a function of time and the delay τ between the two laser pulses, i.e., the optical and the THz pulses.

Firstly, as predicted from the macroscopic Berry curvature presented in Fig. 4.5, the presence of the Coulomb interaction induces oscillations in $\mathrm{d}J^{\mathrm{a}}(t)/\mathrm{d}t$ with respect to the time delay τ. These oscillations occur at frequencies corresponding to the energy difference between the 1s and 2s exciton resonances of e_1-hh_1, see Fig. 4.4). This frequency originates from the time-dependent evolution of macroscopic excitonic Berry curvature [117, 118].

Moreover, Fig. 4.8 demonstrates that the Coulomb interaction considerably enhances anomalous currents for both QW widths, peaking around 0.5 ps and persisting over long delays, even after the THz and the optical pulses no longer overlap. Contrarily, to the case without the Coulomb interaction, when the excitation is off-resonant, the current essentially vanishes when the two pulses do not overlap.

Based on the theoretical analysis, we conclude that circularly polarized optical interband excitations generate spin-polarized carriers in the QW's conduction and valence bands. The THz pulse then accelerates these carriers within their respective bands, producing a current. This current can be detected by measuring the emitted THz radiation with the appropriate polarization direction. Notably, when optical excitations occur in regions where the bands exhibit a nonvanishing Berry curvature, an anomalous current component perpendicular to the THz pulse direction is generated. When the excitation frequency approaches excitonic resonances, the strong oscillator strength of the generated excitons enhances the anomalous current. Furthermore, utilizing sufficiently short optical pulses, one can excite coherent superpositions of 1s and 2s excitonic wave packets, leading to 4.4 oscillations in the anomalous current. Finally, phonon scattering causes the currents to decay through processes of relaxation and dephasing, dissipating energy from the electronic systems.

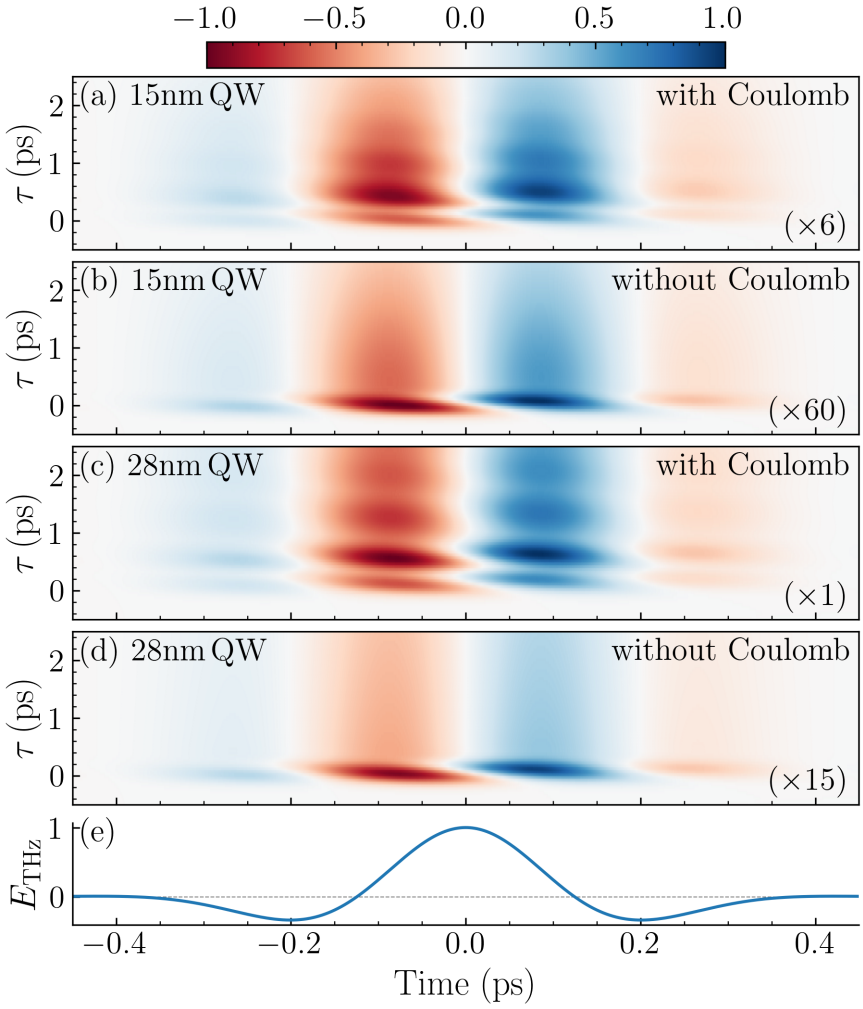

Figure 4.8: The contour plots of the time derivative of the anomalous currents, i.e., $\mathrm{d}J^{\mathrm{a}}(t)/\mathrm{d}t$, as functions of time and the time delay τ between the optical and the THz pulses. For visibility, the results are normalized to the same value and the respective multiplied factors are stated in each panel. The (1 1 0)-oriented GaAs QWs are excited optically 5 meV below the band gap. The results are for QWs of 15 nm thickness [(a)-(b)] and 28 nm thickness [(c)-(d)] in the two cases: with [(a) and (c)] and without Coulomb interaction [(b) and (d)]. Additionally, the normalized incident THz pulse is provided in panel (e). The figure is reproduced with permission from Ref. [96].

It should be emphasized that comparing our simulation results to experimental data reveals very good agreement. The simulations, which examine $\mathrm{d}J^{\mathrm{a}}(t)/\mathrm{d}t$ at $t = 0.1\,\mathrm{ps}$ (derived from Figure 4.8), align well with experimental data representing THz radiation measured under the same conditions [112]. Figure 4.9 highlights this consistency, strengthening the conclusions drawn from our theoretical analysis.

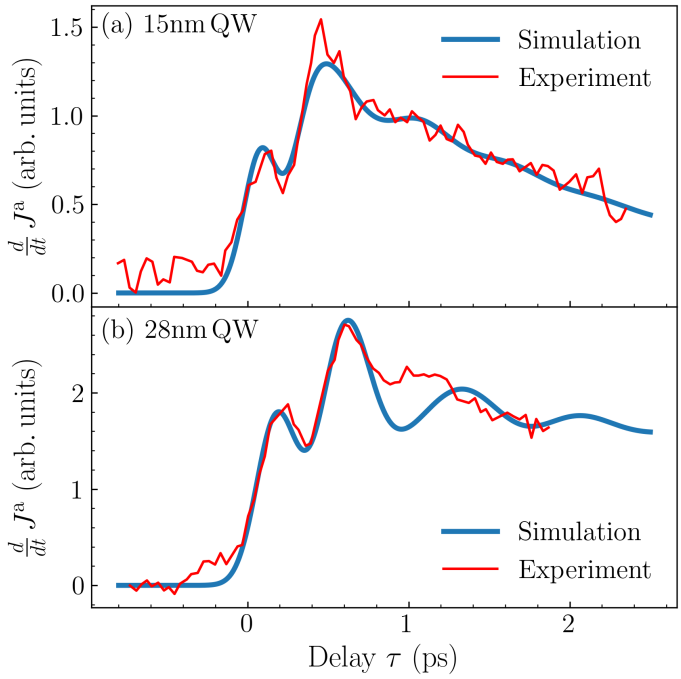

Figure 4.9: The comparison between the time derivatives of the anomalous currents obtained from the simulation results (the thick blue lines) and the measured THz emission from the experimental data (the thin red lines) at $t = 0.1$ ps. The results are presented for (1 1 0)-oriented GaAs QWs of 15 nm width at 77 K (a) and of 28 nm width at 4 K (b). The figure is reproduced with permission from Ref. [96].

4.6 Dynamics of the Normal Currents

To complete the analysis of THz pulse-induced currents, we now discuss the dynamics of the normal currents resulting from the carrier acceleration within their bands (intraband acceleration) induced by the THz field after the optical excitation. This intraband acceleration is determined by the gradient term, $(e/\hbar)\mathbf{E}_{\mathrm{THz}}(t)\boldsymbol{\nabla}_{\mathbf{k}}\rho(\mathbf{k})$, in the SBE (3.1). If transforming into a time-dependent k-space, where the quasi-momentum follows the acceleration theorem [119–122],

$$\frac{d\mathbf{k}}{dt} = -\frac{e}{\hbar}\mathbf{E}_{\mathrm{THz}}(t), \tag{4.11}$$

one can eliminate this term from the SBE. Then, integrating this theorem, the time-dependent wave vector is

$$\mathbf{k}(t) = -\int_{-\infty}^{t} \frac{e}{\hbar}\mathbf{E}_{\mathrm{THz}}(t')\,\mathrm{d}t' \,. \tag{4.12}$$

In the perturbative regime, the normal currents are proportional to $|\mathbf{E}_{\mathrm{opt}}|^2\mathbf{E}_{\mathrm{THz}}$. Numerically, the normal current is calculated by projecting the vectorial current Eq. (4.1) onto a unit vector aligned with the polarization direction of the THz electric field. Under the conditions examined in this study, our calculations show that the magnitude of the normal current is approximately three times larger than that of the anomalous current.

Following a similar approach to the analysis of the anomalous currents, we first examine how the time derivative of the normal currents, $\mathrm{d}J^{\mathrm{normal}}(t)/\mathrm{d}t$, depends on time and the time delay between the optical and the THz pulses, as shown in Fig. 4.10.

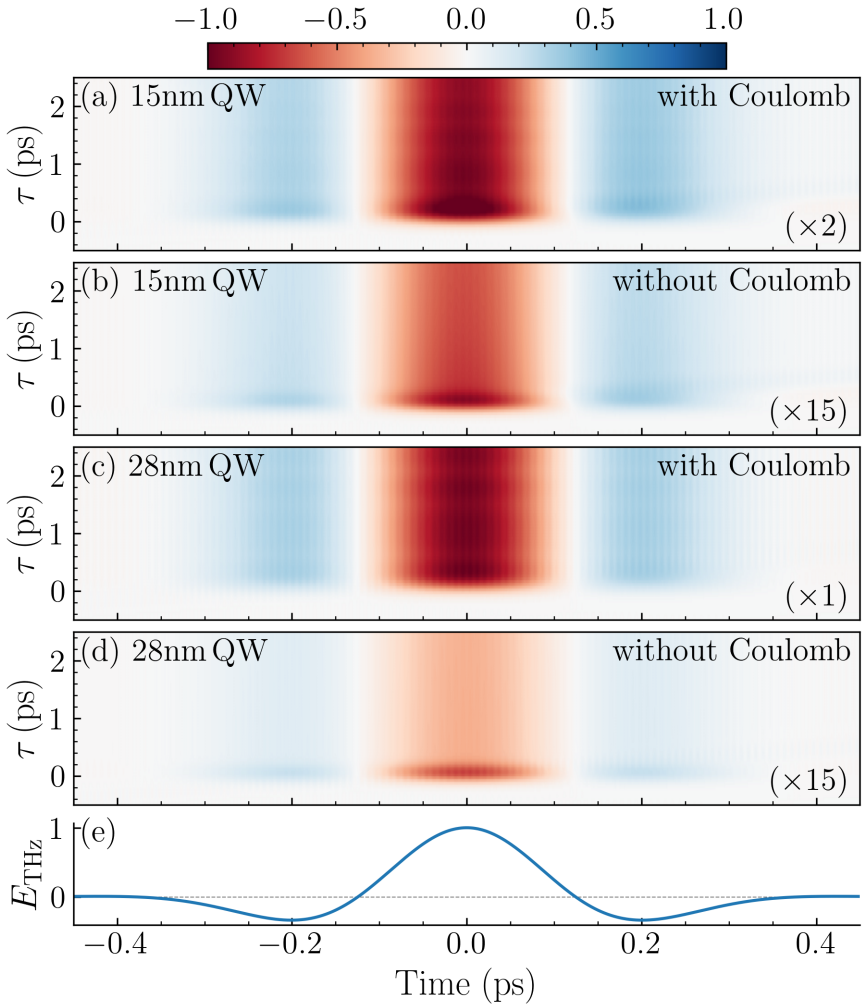

Figure 4.10: The same as Fig. 4.8 but for the time derivative of the normal currents, i.e., $\mathrm{d}J^{\mathrm{normal}}(t)/\mathrm{d}t$, for (1 1 0)-oriented GaAs QWs of 15 nm width [(a)-(b)] and 28 nm width [(c)-(d)] in two cases: with Coulomb interaction [(a) and (c)] and without Coulomb interaction [(b) and (d)]. The QWs are optically excited 5 meV. The figure is reproduced with permission from Ref. [96].

The fact that the derivative $\mathrm{d}J^{\mathrm{normal}}(t)/\mathrm{d}t$ is in phase with the THz electric field, as shown in Fig 4.10, indicates that the phase of the normal currents has a $\pi/2$ shift relative to the THz field, $\mathbf{E}_{\mathrm{THz}}$. This phase shift arises from, as implied by Eq. (4.12), the time-dependent $\mathbf{k}(t)$ responsible for generating the normal current is proportional to the time integral of the THz field. With regards to time modulation, the normal current decays more slowly than the anomalous current. This is because scattering processes that alter the electron spin suppress the anomalous current but do not affect the normal current. As for the variation with the time delay τ, small oscillations in the normal current also originate from the excitation of excitonic wave packets. For a more detailed view, specific time slices of $\mathrm{d}J^{\mathrm{normal}}(t)/\mathrm{d}t$ are depicted in Fig. 4.11.

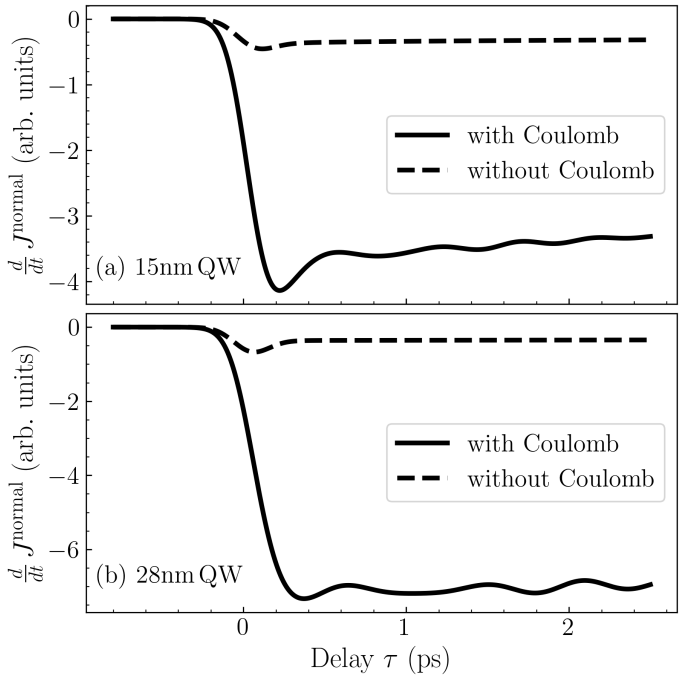

Figure 4.11: A slice of the time derivative of the normal currents shown in Fig. 4.10, specifically at the instant of $t = 0$ ps. The results are presented for (1 1 0)-oriented GaAs QWs with thicknesses of 15 nm (a) and 28 nm (b) in two cases: with and without Coulomb interaction by solid and dashed lines, respectively. The figure is reproduced with permission from Ref. [96].

4.7 Conclusions

In summary, we investigated the dynamics of the Berry curvature and of anomalous currents in GaAs QWs by utilizing the SBE in the LG within the TDHF approximation, incorporating both the scattering of electrons with LA and LO phonons. By successfully implementing the PTG and TPTG transformations for degenerate bands, we were able to

solve the dynamical equations while simultaneously considering many-body effects. Our simulation results, which agree very well with experimental data, emphasize the crucial role of the Coulomb interactions in describing anomalous currents induced by THz pulses after optical excitation near the band gap.

Furthermore, we found that the inclusion of the Coulomb interaction causes the anomalous current to peak at the exciton resonances. We also observed oscillations in the anomalous current as a function of the time delay between the optical and the THz pulses, which is attributed to the excitation of 1s-2s exciton wave packets. To provide a detailed microscopic description of the temporal decay of the macroscopic excitonic Berry curvature and the anomalous current, it is essential to account for carrier-phonon scattering.

Our findings offer in-depth insights into the generation of anomalous currents in many-body systems, revealing novel features that emerge from the intrinsic structure of excitonic eigenstates.

Analysis of Many-Body Coulomb Correlations of Charge-Transfer Excitons

5

Excitons are well-known to play a crucial role in the optical response near the band gap, particularly in low-dimensional materials, notably in two-dimensional materials such as QWs and transition-metal dichalcogenide (TMDC) monolayers and heterostructures [123–126]. Over the decades, the nonlinear response of excitons in spatially-homogeneous type-I QW nanostructures has been thoroughly studied [60, 63, 64, 68, 127–130]. With advancements in experimental techniques, the quality of semiconductor nanostructure samples has improved significantly, alongside with progress in theoretical methods for describing many-body Coulomb correlation effects at the microscopic level. The substantial impact of higher-order Coulomb correlations on the nonlinear optical response has been observed, particularly in ultrafast spectroscopy experiments conducted at low intensities with specific polarization orientations of laser pulses. This includes effects such as excitation-induced dephasing [129, 131–133] and the presence of bound biexciton resonances [66, 134–142]. Recently, type-II heterostructure QWs have been a focus of recent research [67, 143, 144], exhibit charge-transfer excitons (CTX) as the energetically lowest optical resonances in these structures. Remarkably, OPOP experiments on type-II QWs were successfully explained using the DCT scheme [67]. In this chapter, we employ the cluster expansion method, a more general framework than DCT approach, to investigate the nonlinear optical response of excitons in QW structures through OPOP experiments. To account for the effects of higher-order Coulomb correlations, the cluster expansion approach is utilized to treat the hierarchy problem. This study limits higher-order Coulomb correlations to those appearing up to third order in the optical laser field. This is the minimum order required for analyzing nonlinear optical responses of pump-probe experiments. In the coherent limit, higher-order Coulomb correlations include interactions between polarizations and carriers, as well as biexcitonic correlations. Performing numerical calculations that include many-body Coulomb correlations is computationally highly demanding. Therefore, we use a one-dimensional model in this study. Compared to two-dimensional QW models, one-dimensional models can achieve qualitatively similar results when excitation near the exciton resonance is considered [135, 145]. Use this approach, we describe the excitonic response of spatially-direct type-I QW structures and extend it to investigate spatially-indirect type-II QW structures.

5.1 Optical-Pump Optical-Probe Experiments on Type-I and Type-II Quantum Well Structures

In the following, we describe the OPOP experiments conducted on spatially-direct type-I and spatially-indirect type-II QW structures. Figure 5.1 illustrates the type-I and type-II QWs schematically. The type-I QW structure is composed of multiple stacked gallium indium arsenide [(GaIn)As] QW layers, each encapsulated by GaAs barrier layers, as depicted in Fig. 5.1(a). In contrast, the type-II QW structure has an indirect spatial design and consists of asymmetric double QW layers, as shown in Fig. 5.1(b). Each layer of the type-II QW includes two different QWs: one (GaIn)As well and one gallium arsenide antimonide [Ga(AsSb)] well, which are separated by a thin GaAs layer.

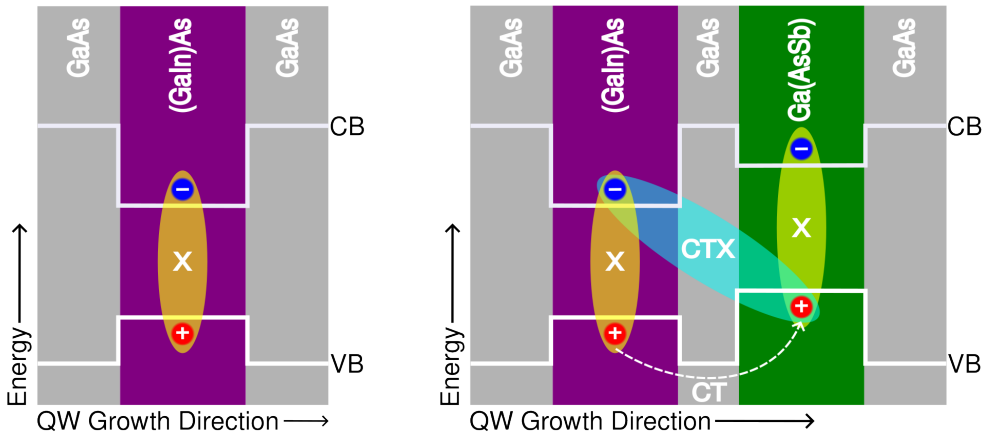

(a) Type-I QW structure.

(b) Type-II QW structure.

Figure 5.1: Schematic band profiles for the type-I QW heterostructure (a) and the type-II QW heterostructure (b). In these diagrams, blue circles represent electrons in the conduction band, while red circles represent holes in the valence band. The type-I heterostructure consists of a (GaIn)As QW surrounded by GaAs barriers. In this configuration, a spatially-direct transition occurs within the (GaIn)As layer. Conversely, the type-II heterostructure comprises two distinct QWs, made of (GaIn)As and Ga(AsSb), which are separated by thin layers of GaAs. In this arrangement, the lowest energy transition available within this heterostructure is a spatially-indirect transition between a hole in the Ga(AsSb) layer and an electron in the (GaIn)As layer.

QWs are typically fabricated using epitaxy, which enables the precise growth of thin semiconductor layers on a crystalline substrate, ensuring structural lattice uniformity. During epitaxial growth, thin layers of different semiconductors, such as (GaIn)As, Ga(AsSb), or GaAs, are sequentially deposited to create the QW structure. Differences in lattice constants between the constituent materials in QWs generate strain, which causes energy shifts in the valence and conduction bands. These changes affect the electronic band structure, the effective mass, and the binding energy of excitons [146–148]. To compensate the strain

within the QW structure, additional gallium arsenide phosphide [Ga(AsP)] barrier layers are often introduced. In type-I QW structures, both the valence band maximum and the conduction band minimum are located within the same well, resulting in a spatially-direct exciton. In contrast, type-II QW structures have a double-well design in which the valence band maximum and the conduction band minimum occur in different QWs. This spatial separation makes the lowest energy transition, which forms a CTX state, spatially-indirect [67, 143, 149]. In a type-II QW structure, the spatial distance between the wells leads to reduced wave function overlap between the electrons and the holes, unlike in type-I QWs where they are both confined in the same well. Consequently, the Coulomb attraction in type-II QWs is weaker and the exciton binding energy is lower than that of excitons in type-I QWs. In a type-I QW the exciton wave function is localized within a single well, while in the CTX state of a type-II QW the exciton wave function extends across both QWs due to the separation of the electrons and holes. This separation leads to distinct properties of excitons in type-II QWs compared to the spatially-direct excitons in type-I QWs.

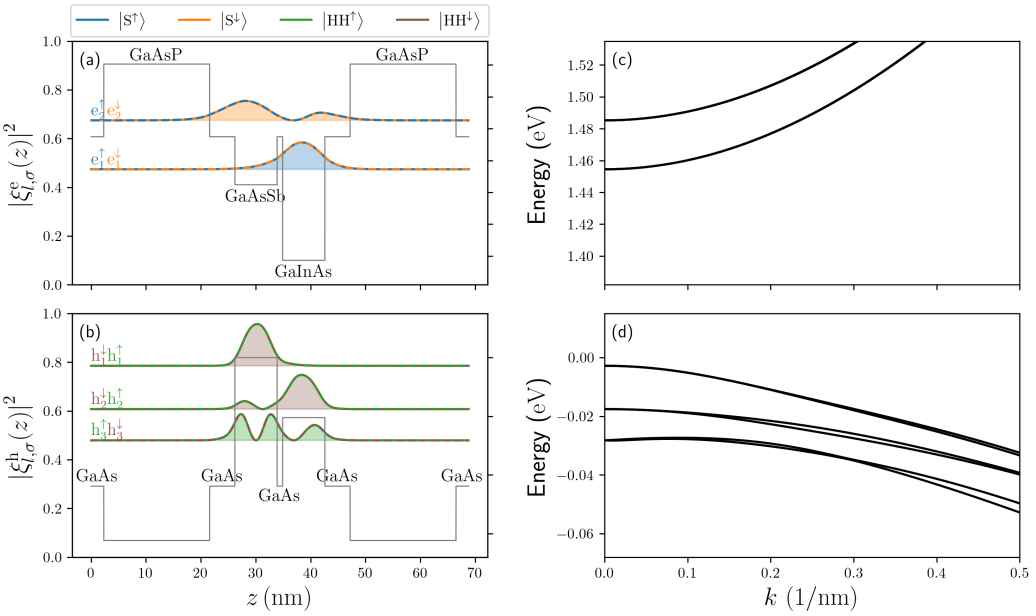

Figure 5.2: Confinement functions of the two-lowest electron states (a), three-highest heavy-hole states (b), and their corresponding in-plane band structure (c)-(d) for a type-II $Ga_{0.942}In_{0.058}As/GaAs/GaAs_{0.967}Sb_{0.033}$ asymmetric double QW.

To illustrate the band structure and electron-hole confinements in a type-II QW, the 14-band $\mathbf{k}\cdot\mathbf{p}$ method within the envelope function approximation is employed to obtain the band structure for type-II (GaIn)As/GaAs/Ga(AsSb) double QWs. The calculations are performed in two-dimensional k-space, and the results are displayed in Fig. 5.2. Figure 5.2(a) shows the electron and hole confinement functions, while Fig. 5.2(b) illustrates the in-plane band structure. The confinement function $\xi^{\lambda}_{l,\sigma}(z)$ is obtained from the envelope functions at the

Γ point, i.e., at $k = 0$. The type-II QW layers have thicknesses of 7.7 nm for $Ga_{0.942}In_{0.058}As$ and $GaAs_{0.967}Sb_{0.033}$, with In and Sb concentrations of 5.8% and 3.3%, respectively. The thin GaAs interlayer has a thickness of only 1 nm. The effective masses of the electron and hole are obtained by fitting the band structure. The effective mass for the first electron band is $0.07m_0$, while the effective masses for the first and second heavy-hole bands are $0.357m_0$ and $0.457m_0$, respectively. These values are very close to those of bulk GaAs. In Fig. 5.2(a), we show the overlap between the first confinement function of the electron in the conduction band located in the (GaIn)As layer and the first confinement function of the hole in the valence band located in the Ga(AsSb) layer. The transition between these two states generates a CTX. Meanwhile, two spatially-direct exciton states can be excited by transitions between the second hole and the first electron band in the (GaIn)As layer and the first hole and the second electron band in the Ga(AsSb) layer. They can be seen in the linear absorption spectrum of the type-II QW, as presented in Fig. 5.3.

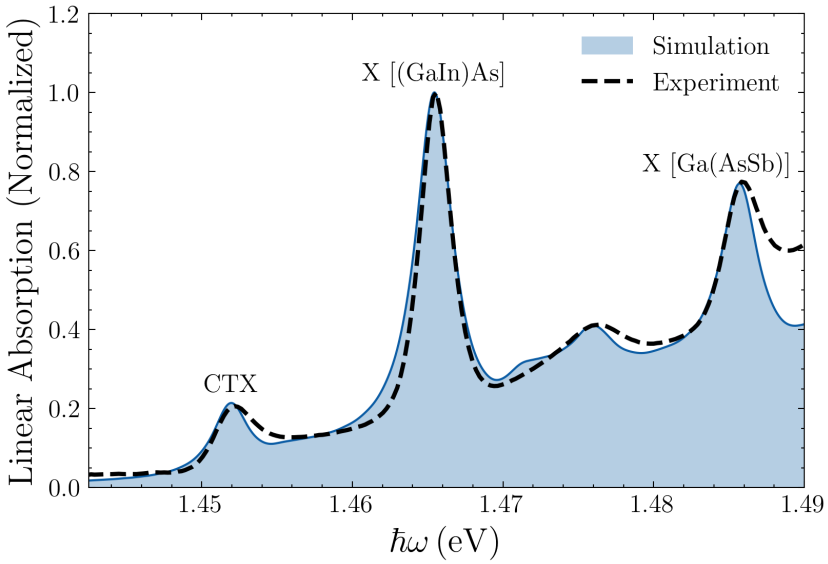

Figure 5.3: The linear absorption spectrum of the type-II (GaIn)As/GaAs/Ga(AsSb) double QW. The spectrum shows the CTX at 1.452 eV, and direct excitons at 1.466 eV and 1.486 eV for the type-I QWs in (GaIn)As and Ga(AsSb), respectively. The peak around 1.476 eV corresponds to the transition from the third heavy-hole band to the first electron band in the (GaIn)As QW layers. The experimental data is taken from Ref. [143].

Figure 5.3 presents the linear absorption spectrum of the type-II QW, derived from numerical calculations and compared with experimental data. The numerical results are obtained by solving the SBE in two-dimensional k-space in the linear regime and show good agreement with experiment. The linear absorption spectrum reveals three distinct peaks at 1.452 eV, 1.466 eV, and 1.486 eV. The lowest-energy peak corresponds to the CTX transition, while the other two peaks are attributed to type-I heavy-hole excitons in the (GaIn)As and Ga(AsSb) layers, respectively. Additionally, a peak at 1.476 eV represents the

transition from the third heavy-hole band to the first electron band within the (GaIn)As QW. The CTX has a binding energy of 4.8 meV, while the direct excitons in the (GaIn)As QW exhibit a binding energy of 7 meV.

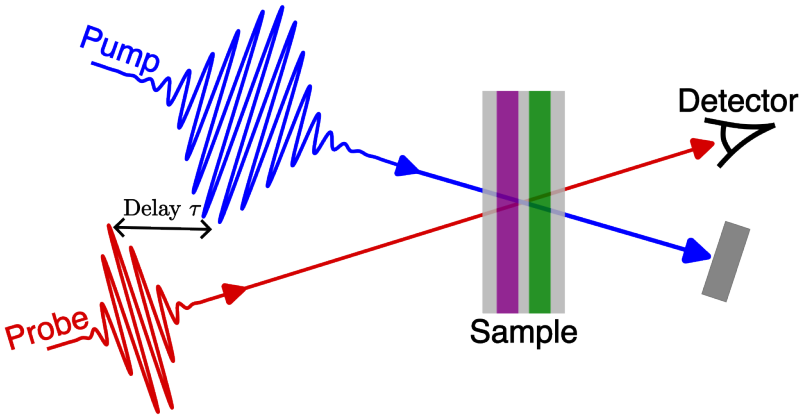

Figure 5.4: Schematic illustration of an OPOP experiment, which is performed by two laser pulses: a pump pulse and a probe pulse, with a time delay τ between them. The differential absorption is measured along the direction of the probe pulse and represents the difference in absorption with and without the presence of the pump pulse.

The nonlinear optical experiments investigated in this chapter, as depicted in Fig. 5.4, utilize a pump-probe configuration involving two excitation pulses: the pump pulse and the probe pulse. In the OPOP measurement, the system is excited by both pulses, with the differential absorption measured in the direction of the probe. The pump pulse induces carrier occupations, microscopic interband polarization, and correlations. In the coherent regime considered in this study, we focus solely on coherent correlations, which encompass the correlations between microscopic polarization and carrier occupations, as well as biexcitonic correlations. The probe pulse induces a small change in the carrier distributions, interband polarization, and coherent correlations. With the probe-induced polarization, we can determine the differential absorption as $\Delta\alpha(\omega) = \alpha(\omega) - \alpha_0(\omega)$, where $\alpha(\omega)$ and $\alpha_0(\omega)$ represent the probe absorption with and without the pump, respectively. This probe-induced absorption is proportional to the imaginary part of the susceptibility, expressed as $\delta\chi(\omega) = \delta P(\omega)/E_{\text{probe}}(\omega)$, where the probe-induced macroscopic polarization $\delta P(\omega)$ is obtained through a Fourier transform of

$$\delta P(t) = \frac{1}{\mathcal{S}} \sum_{\sigma,\mathbf{k}} \left(\mathbf{e}_{\text{probe}} \cdot \mathbf{d}^{\text{cv}}_{\sigma,\mathbf{k}} \right) \delta p^{\text{vc}}_{\sigma,\mathbf{k}} + \text{c.c.} \tag{5.1}$$

Here, $\mathbf{d}^{\text{cv}}_{\sigma,\mathbf{k}}$ denotes the dipole matrix elements and $\mathbf{e}_{\text{probe}}$ indicates the polarization direction of the probe pulse. The temporal envelopes of the electric fields, $E_{\text{pump}}(t)$ and $E_{\text{probe}}(t)$, are described using Gaussian functions and the time delay between the two pulses is denoted by τ. A positive time delay occurs when the pump pulse excites the system prior to the

probe pulse, while a negative time delay represents the situation when the probe pulse precedes the pump pulse.

5.2 Theoretical Approach

Computing many-body Coulomb correlation effects for two-dimensional QW structures is numerically very demanding. Therefore, in this thesis, we use only a one-dimensional two-band model, which includes the energetically lowest conduction and the energetically highest valence bands and accounts for spin degeneracy. Such a one-dimensional model is still able to provide results that are in good qualitative agreement with several experimental observations on QW systems [129, 135, 150]. The energy band structure near the Γ point is approximated by a parabolic form as

$$\varepsilon^{\lambda}_{\sigma,\mathbf{k}} = \frac{\hbar k^2}{2m_\lambda}, \tag{5.2}$$

with $\lambda = \mathrm{e}$ for the conduction band and $\lambda = \mathrm{h}$ for the heavy-hole valance band. The excitation pulses used to investigate the nonlinear response of excitons in this study are circularly polarized. For convenience, we use the spherical basis vectors that are defined as

$$\mathbf{e}_+ = \frac{1}{\sqrt{2}}\begin{pmatrix}1\\ i\end{pmatrix}, \quad \mathbf{e}_- = \frac{1}{\sqrt{2}}\begin{pmatrix}1\\ -i\end{pmatrix}. \tag{5.3}$$

Because of the well-known selection rules in zinc blende materials, specifically in semiconductor nanostructures based on GaAs, only specific pairs of electron and hole states couple optically [42]. The dipole matrix elements at the Γ point can be expressed using the spherical basis vectors as follows

$$\mathbf{d}^{\mathrm{cv}}_{\uparrow\uparrow,\mathbf{0}} = d^{\mathrm{cv}}_0 \mathbf{e}_+, \quad \mathbf{d}^{\mathrm{cv}}_{\downarrow\downarrow,\mathbf{0}} = d^{\mathrm{cv}}_0 \mathbf{e}_-, \quad \mathbf{d}^{\mathrm{cv}}_{\uparrow\downarrow,\mathbf{0}} = \mathbf{d}^{\mathrm{cv}}_{\downarrow\uparrow,\mathbf{0}} = \mathbf{0}. \tag{5.4}$$

The k-dependence of the dipole matrix elements can be obtained by a simple relation from their values at the Γ point as [4]

$$\mathbf{d}^{\mathrm{cv}}_{\sigma\sigma,\mathbf{k}} = \mathbf{d}^{\mathrm{cv}}_{\sigma\sigma,\mathbf{0}} \frac{\varepsilon^{\mathrm{e}}_{\sigma,\mathbf{0}} + \varepsilon^{\mathrm{h}}_{\sigma,\mathbf{0}}}{\varepsilon^{\mathrm{e}}_{\sigma,\mathbf{k}} + \varepsilon^{\mathrm{h}}_{\sigma,\mathbf{k}}}. \tag{5.5}$$

In the framework of the $\mathbf{k}\cdot\mathbf{p}$ model, within the envelope function approximation, the Coulomb matrix elements of the one-dimensional model are given by [151–153]

$$\begin{aligned} V^{\lambda\lambda'}_{\sigma\sigma',q} = \frac{e^2}{2\pi\epsilon_0\epsilon_{\mathrm{BG}}L_z} \iiiint \mathrm{d}x_1\,\mathrm{d}x_2\,\mathrm{d}y_1\,\mathrm{d}y_2\, K_0\left(|q|\sqrt{(x_2-x_1)^2+(y_2-y_1)^2}\right) \\ \times \left[\xi^{\lambda}_{\sigma}(x_1,y_1)\right]^* \xi^{\lambda}_{\sigma}(x_1,y_1) \left[\xi^{\lambda'}_{\sigma'}(x_2,y_2)\right]^* \xi^{\lambda'}_{\sigma'}(x_2,y_2)\,. \end{aligned} \tag{5.6}$$

Here, K_0 is the modified Bessel function of the second kind and $\xi_\sigma^\lambda(x,y)$ is the confinement function at the Γ point. In the spatially-inhomogeneous type-II QW structure, the spatial charge separation results in the Coulomb attraction between electrons and holes being weaker than the intrawell Coulomb repulsion between equally charged carriers. To account for this effect in our simplified model, we multiply the attractive Coulomb matrix elements by a constant factor to reduce their strength. Based on the multiband SBE presented in Chapter 2, specifically Eq. (2.47), we can obtain the EOM for describing the OPOP experiment within a two-band model including spin. The EOM for the occupations of the system are given by

$$\hbar\frac{\partial}{\partial t}n_{\sigma,\mathbf{k}} = -i\left[\left(\mathbf{E}_{\text{pump}}(t)\cdot\mathbf{d}^{\text{cv}}_{\sigma,\mathbf{k}} + \sum_{\mathbf{k}'}V^{\text{vc}}_{\sigma\sigma,\mathbf{k}'-\mathbf{k}}p_{\sigma,\mathbf{k}'}\right)^* p_{\sigma,\mathbf{k}} - \text{c.c.}\right] - \gamma_1 n_{\sigma,\mathbf{k}} \tag{5.7}$$

and the EOM for the microscopic polarization are given by

$$\begin{aligned} i\hbar\frac{\partial}{\partial t}p_{\sigma,\mathbf{k}} = {} & \left(\varepsilon^{\text{e}}_{\sigma,\mathbf{k}} + \varepsilon^{\text{h}}_{\sigma,\mathbf{k}} - i\gamma_2\right)p_{\sigma,\mathbf{k}} - \sum_{\mathbf{k}'}V^{\text{vc}}_{\sigma\sigma,\mathbf{k}'-\mathbf{k}}p_{\sigma,\mathbf{k}'} - \mathbf{E}(t)\cdot\mathbf{d}^{\text{cv}}_{\sigma,\mathbf{k}} \\ & + 2n_{\sigma,\mathbf{k}}\mathbf{E}(t)\cdot\mathbf{d}^{\text{cv}}_{\sigma,\mathbf{k}} + \sum_{\mathbf{k}'}\left[2V^{\text{vc}}_{\sigma\sigma,\mathbf{k}'-\mathbf{k}}p_{\sigma,\mathbf{k}'}n_{\sigma,\mathbf{k}} - \left(V^{\text{vv}}_{\sigma\sigma,\mathbf{k}'-\mathbf{k}} + V^{\text{cc}}_{\sigma\sigma,\mathbf{k}'-\mathbf{k}}\right)n_{\sigma,\mathbf{k}'}p_{\sigma,\mathbf{k}}\right] \\ & - \sum_{\sigma'}\left(2V^{\text{vc}}_{\sigma\sigma',\mathbf{0}} - V^{\text{vv}}_{\sigma\sigma',\mathbf{0}} - V^{\text{cc}}_{\sigma\sigma',\mathbf{0}}\right)\sum_{\mathbf{k}'}n_{\sigma',\mathbf{k}'}p_{\sigma,\mathbf{k}} \\ & + \Gamma_{\sigma,\mathbf{k}}. \end{aligned} \tag{5.8}$$

In the above equation, the first line represents the linear optical equation, comprising the homogeneous terms and the linear source term (the last term) associated with the electric laser field. The homogeneous terms describe the exciton, which is formed by an electron-hole pair through the attractive Coulomb interaction. This homogeneous equation is referred to as the Waniner equation. In the second line, the first term represents the nonlinear Pauli-blocking (PB) contribution. The second and third terms contain first-order Coulomb interactions, resulting from the Hartree-Fock factorization, describing the exchange Coulomb interaction. This includes attractive interactions between electrons and holes and repulsive interactions between electrons or between holes. These terms couple singlets with identical spin states. The third line contains first-order Coulomb interactions resulting from Hartree-Fock factorization, which describes direct Coulomb interactions. Unlike the Coulomb exchange terms, these direct terms couple the spin subspaces, as seen in the sum over spins. This term vanishes in spatially-homogeneous systems [62, 67] and is finite only in spatially-inhomogeneous systems, where there is a difference in the strength of the attractive and repulsive Coulomb interactions. This is described by the prefactor, which contains the difference between the sum of the two attractive interactions and the two repulsive interactions. The final term $\Gamma_{\sigma,\mathbf{k}}$ includes contributions from higher-order Coulomb correlations. In the cluster expansion approach, this involves on the coherent singlet-doublet level the correlations between microscopic polarizations and electrons

$c^{\mathbf{q},\mathbf{k}',\mathbf{k}}_{\mathrm{pe};\sigma\sigma'\sigma'\sigma}$ or holes $c^{\mathbf{q},\mathbf{k}',\mathbf{k}}_{\mathrm{ph};\sigma\sigma'\sigma'\sigma}$,

$$\Gamma_{\sigma,\mathbf{k}} = \sum_{\sigma',\mathbf{k}',\mathbf{q}} \left[V^{\mathrm{cv}}_{\sigma\sigma',\mathbf{q}} c^{\mathbf{q},\mathbf{k}',\mathbf{k}}_{\mathrm{ph};\sigma\sigma'\sigma'\sigma} + V^{\mathrm{cc}}_{\sigma\sigma',\mathbf{q}} c^{\mathbf{q},\mathbf{k}',\mathbf{k}}_{\mathrm{pe};\sigma\sigma'\sigma'\sigma} - V^{\mathrm{vv}}_{\sigma\sigma',\mathbf{q}} c^{-\mathbf{q},\mathbf{k}'+\mathbf{q},\mathbf{k}-\mathbf{q}}_{\mathrm{ph};\sigma\sigma'\sigma'\sigma} - V^{\mathrm{vc}}_{\sigma\sigma',\mathbf{q}} c^{-\mathbf{q},\mathbf{k}'+\mathbf{q},\mathbf{k}-\mathbf{q}}_{\mathrm{pe};\sigma\sigma'\sigma'\sigma} \right]. \tag{5.9}$$

The EOM for the polarization-hole correlations $c^{\mathbf{q},\mathbf{k}',\mathbf{k}}_{\mathrm{ph};\sigma\sigma'\sigma'\sigma}$ are

$$\begin{aligned}
i\hbar\frac{\partial}{\partial t} c^{\mathbf{q},\mathbf{k}',\mathbf{k}}_{\mathrm{ph};\sigma\sigma'\sigma'\sigma} &= \left(\varepsilon^{\mathrm{e}}_{\sigma,\mathbf{k}-\mathbf{q}} - \varepsilon^{\mathrm{h}}_{\sigma',\mathbf{k}'+\mathbf{q}} + \varepsilon^{\mathrm{h}}_{\sigma',\mathbf{k}'} + \varepsilon^{\mathrm{h}}_{\sigma,\mathbf{k}} - i\gamma_T\right) c^{\mathbf{q},\mathbf{k}',\mathbf{k}}_{\mathrm{ph};\sigma\sigma'\sigma'\sigma} \\
&\quad + \sum_{\mathbf{k}''} \Bigg(V^{\mathrm{vv}}_{\sigma'\sigma,\mathbf{k}''-\mathbf{q}} c^{\mathbf{k}'',\mathbf{k}'+\mathbf{q}-\mathbf{k}'',\mathbf{k}-\mathbf{q}+\mathbf{k}''}_{\mathrm{ph};\sigma\sigma'\sigma'\sigma} - V^{\mathrm{vc}}_{\sigma\sigma,\mathbf{k}''-\mathbf{k}} c^{\mathbf{q},\mathbf{k}',\mathbf{k}''}_{\mathrm{ph};\sigma\sigma'\sigma'\sigma} \\
&\qquad - V^{\mathrm{vc}}_{\sigma'\sigma,\mathbf{k}''-\mathbf{k}'} c^{\mathbf{k}'+\mathbf{q}-\mathbf{k}'',\mathbf{k}'',\mathbf{k}}_{\mathrm{ph};\sigma\sigma'\sigma'\sigma} \Bigg) \\
&\quad + \left(V^{\mathrm{vc}}_{\sigma'\sigma,\mathbf{q}} p_{\sigma,\mathbf{k}} - V^{\mathrm{vv}}_{\sigma'\sigma,\mathbf{q}} p_{\sigma,\mathbf{k}-\mathbf{q}}\right) n_{\sigma',\mathbf{k}'+\mathbf{q}} \\
&\quad - \left(V^{\mathrm{cc}}_{\sigma'\sigma,\mathbf{q}} p_{\sigma,\mathbf{k}} - V^{\mathrm{cv}}_{\sigma'\sigma,\mathbf{q}} p_{\sigma,\mathbf{k}-\mathbf{q}}\right) \left(p_{\sigma',\mathbf{k}'+\mathbf{q}}\right)^* p_{\sigma',\mathbf{k}'} \\
&\quad + \delta_{\sigma\sigma'} \Bigg[\left(V^{\mathrm{vv}}_{\sigma\sigma,\mathbf{j}} p_{\sigma,\mathbf{k}-\mathbf{q}} - V^{\mathrm{vc}}_{\sigma\sigma,\mathbf{j}} p_{\sigma,\mathbf{k}'}\right) n_{\sigma,\mathbf{k}'+\mathbf{q}} \\
&\qquad - \left(V^{\mathrm{cv}}_{\sigma\sigma,\mathbf{j}} p_{\sigma,\mathbf{k}-\mathbf{q}} - V^{\mathrm{cc}}_{\sigma\sigma,\mathbf{j}} p_{\sigma,\mathbf{k}'}\right) \left(p_{\sigma,\mathbf{k}'+\mathbf{q}}\right)^* p_{\sigma,\mathbf{k}} \Bigg] \\
&\quad - \left(\mathbf{E}(t)\cdot\mathbf{d}^{\mathrm{cv}}_{\sigma',\mathbf{k}'+\mathbf{q}} + \sum_{\mathbf{k}''} V^{\mathrm{vc}}_{\sigma'\sigma',\mathbf{k}''-\mathbf{k}'-\mathbf{q}} p_{\sigma',\mathbf{k}''}\right)^* c^{\mathbf{q},\mathbf{k}',\mathbf{k}}_{\mathrm{BX};\sigma\sigma'\sigma'\sigma} \\
&\quad + \left(p_{\sigma',\mathbf{k}'+\mathbf{q}}\right)^* \sum_{\mathbf{k}''} \Bigg(V^{\mathrm{vc}}_{\sigma'\sigma',\mathbf{k}''-\mathbf{k}'} c^{\mathbf{q},\mathbf{k}'',\mathbf{k}}_{\mathrm{BX};\sigma\sigma'\sigma'\sigma} - V^{\mathrm{cc}}_{\sigma\sigma',\mathbf{k}''-\mathbf{q}} c^{\mathbf{k}'',\mathbf{k}',\mathbf{k}}_{\mathrm{BX};\sigma\sigma'\sigma'\sigma} \\
&\qquad + V^{\mathrm{vc}}_{\sigma\sigma',\mathbf{k}''-\mathbf{k}} c^{\mathbf{k}''+\mathbf{q}-\mathbf{k},\mathbf{k}',\mathbf{k}''}_{\mathrm{BX};\sigma\sigma'\sigma'\sigma} \Bigg).
\end{aligned} \tag{5.10}$$

In this equation, the first three lines include the homogeneous terms describing the eigenstates of $c^{\mathbf{q},\mathbf{k}',\mathbf{k}}_{\mathrm{ph};\sigma\sigma'\sigma'\sigma}$. The subsequent four lines result from the singlet factorization of the three-particle correlations involving singlet quantities, such as microscopic polarizations and hole occupations. Specifically, the 4th and 5th lines involve $V^{\lambda\lambda'}_{\sigma\sigma',\mathbf{q}}$, which describes the direct Coulomb interaction between electrons and holes. In contrast, the 6th and 7th lines contain the Coulomb term $V^{\lambda\lambda'}_{\sigma\sigma',\mathbf{j}}$, which describes the Coulomb exchange interaction. Notably, due to the factor $\delta_{\sigma\sigma'}$ these exchange terms appear only for co-circular excitation. In the case of counter-circular excitation, only the direct interaction terms contribute. The final three lines result from the doublet factorization of the three-particle correlations, which describes biexcitonic contributions. A similar structure is observed in the EOM for

the polarization-hole correlation $c^{\mathbf{q},\mathbf{k}',\mathbf{k}}_{\mathrm{pe};\sigma\sigma'\sigma'\sigma}$ as

$$
\begin{aligned}
i\hbar\frac{\partial}{\partial t}c^{\mathbf{q},\mathbf{k}',\mathbf{k}}_{\mathrm{pe};\sigma\sigma'\sigma'\sigma} &= \left(\varepsilon^{\mathrm{e}}_{\sigma,\mathbf{k}-\mathbf{q}} + \varepsilon^{\mathrm{e}}_{\sigma',\mathbf{k}'+\mathbf{q}} - \varepsilon^{\mathrm{e}}_{\sigma',\mathbf{k}'} + \varepsilon^{\mathrm{h}}_{\sigma,\mathbf{k}} - i\gamma_T\right)c^{\mathbf{q},\mathbf{k}',\mathbf{k}}_{\mathrm{pe};\sigma\sigma'\sigma'\sigma} \\
&\quad + \sum_{\mathbf{k}''}\Bigg(V^{\mathrm{cc}}_{\sigma\sigma',\mathbf{k}''-\mathbf{q}}c^{\mathbf{k}'',\mathbf{k}',\mathbf{k}}_{\mathrm{pe};\sigma\sigma'\sigma'\sigma} - V^{\mathrm{vc}}_{\sigma\sigma',\mathbf{k}''-\mathbf{k}}c^{\mathbf{k}''+\mathbf{q}-\mathbf{k},\mathbf{k}',\mathbf{k}''}_{\mathrm{pe};\sigma\sigma'\sigma'\sigma} \\
&\qquad - V^{\mathrm{vc}}_{\sigma\sigma,\mathbf{k}''-\mathbf{k}}c^{\mathbf{q},\mathbf{k}',\mathbf{k}''}_{\mathrm{pe};\sigma\sigma'\sigma'\sigma}\Bigg) \\
&\quad + \left(V^{\mathrm{cc}}_{\sigma'\sigma,\mathbf{q}}p_{\sigma,\mathbf{k}} - V^{\mathrm{cv}}_{\sigma'\sigma,\mathbf{q}}p_{\sigma,\mathbf{k}-\mathbf{q}}\right)n_{\sigma',\mathbf{k}'} \\
&\quad - \left(V^{\mathrm{vc}}_{\sigma'\sigma,\mathbf{q}}p_{\sigma,\mathbf{k}} - V^{\mathrm{vv}}_{\sigma'\sigma,\mathbf{q}}p_{\sigma,\mathbf{k}-\mathbf{q}}\right)\left(p_{\sigma',\mathbf{k}'}\right)^*p_{\sigma',\mathbf{k}'+\mathbf{q}} \\
&\quad + \delta_{\sigma\sigma'}\Bigg[\left(V^{\mathrm{vc}}_{\sigma\sigma,\mathbf{j}}p_{\sigma,\mathbf{k}'+\mathbf{q}} - V^{\mathrm{cc}}_{\sigma\sigma,\mathbf{j}}p_{\sigma,\mathbf{k}}\right)n_{\sigma,\mathbf{k}'} \\
&\qquad - \left(V^{\mathrm{vv}}_{\sigma\sigma,\mathbf{j}}p_{\sigma,\mathbf{k}'+\mathbf{q}} - V^{\mathrm{cv}}_{\sigma\sigma,\mathbf{j}}p_{\sigma,\mathbf{k}}\right)\left(p_{\sigma,\mathbf{k}'}\right)^*p_{\sigma,\mathbf{k}-\mathbf{q}}\Bigg] \\
&\quad + \left(\mathbf{E}(t)\cdot\mathbf{d}^{\mathrm{cv}}_{\sigma',\mathbf{k}'} + \sum_{\mathbf{k}''}V^{\mathrm{vc}}_{\sigma'\sigma',\mathbf{k}''-\mathbf{k}'}p_{\sigma',\mathbf{k}''}\right)^*c^{\mathbf{q},\mathbf{k}',\mathbf{k}}_{\mathrm{BX};\sigma\sigma'\sigma'\sigma} \\
&\quad - \left(p_{\sigma',\mathbf{k}'}\right)^*\sum_{\mathbf{k}''}\Bigg(V^{\mathrm{vc}}_{\sigma'\sigma',\mathbf{k}''-\mathbf{k}'}c^{\mathbf{q},\mathbf{k}'',\mathbf{k}}_{\mathrm{BX};\sigma\sigma'\sigma'\sigma} + V^{\mathrm{vc}}_{\sigma'\sigma,\mathbf{k}''-\mathbf{k}'}c^{\mathbf{k}'+\mathbf{q}-\mathbf{k}'',\mathbf{k}'',\mathbf{k}}_{\mathrm{BX};\sigma\sigma'\sigma'\sigma} \\
&\qquad - V^{\mathrm{vv}}_{\sigma'\sigma,\mathbf{k}''-\mathbf{q}}c^{\mathbf{k}'',\mathbf{k}'+\mathbf{q}-\mathbf{k}'',\mathbf{k}-\mathbf{q}+\mathbf{k}''}_{\mathrm{BX};\sigma\sigma'\sigma'\sigma}\Bigg).
\end{aligned}
\tag{5.11}
$$

Both EOMs for the polarization-carrier correlations include biexcitonic correlations, indicating an indirect contribution of biexcitons to the microscopic polarization through the polarization-carrier correlations. This is unlike in the coherent DCT scheme where biexcitonic contributions directly enter the microscopic polarization via Γ [4, 154] as

$$
\begin{aligned}
\Gamma_{\sigma,\mathbf{k}} &= \sum_{\sigma',\mathbf{k}',\mathbf{q}}\left(p_{\sigma',\mathbf{k}'}\right)^*\Bigg[-V^{\mathrm{vc}}_{\sigma\sigma',\mathbf{q}}\left(c^{-\mathbf{q},\mathbf{k}',\mathbf{k}-\mathbf{q}}_{\mathrm{BX};\sigma\sigma'\sigma'\sigma} + c^{-\mathbf{q},\mathbf{k}'+\mathbf{q},\mathbf{k}}_{\mathrm{BX};\sigma\sigma'\sigma'\sigma}\right) \\
&\qquad + V^{\mathrm{cc}}_{\sigma\sigma',\mathbf{q}}c^{\mathbf{q},\mathbf{k}',\mathbf{k}}_{\mathrm{BX};\sigma\sigma'\sigma'\sigma} + V^{\mathrm{vv}}_{\sigma\sigma',\mathbf{q}}c^{-\mathbf{q},\mathbf{k}'+\mathbf{q},\mathbf{k}-\mathbf{q}}_{\mathrm{BX};\sigma\sigma'\sigma'\sigma}\Bigg].
\end{aligned}
\tag{5.12}
$$

The EOM for the biexcitonic correlations are given by

$$
\begin{aligned}
i\hbar\frac{\partial}{\partial t}c^{\mathbf{q},\mathbf{k}',\mathbf{k}}_{\mathrm{BX};\sigma\sigma'\sigma'\sigma} &= \left(\varepsilon^{\mathrm{e}}_{\sigma,\mathbf{k}-\mathbf{q}} + \varepsilon^{\mathrm{e}}_{\sigma',\mathbf{k}'+\mathbf{q}} + \varepsilon^{\mathrm{h}}_{\sigma',\mathbf{k}'} + \varepsilon^{\mathrm{h}}_{\sigma,\mathbf{k}} - i\gamma_{\mathrm{BX}}\right)c^{\mathbf{q},\mathbf{k}',\mathbf{k}}_{\mathrm{BX};\sigma\sigma'\sigma'\sigma} \\
&\quad + \sum_{\mathbf{k}''}\Bigg(V^{\mathrm{vv}}_{\sigma'\sigma,\mathbf{k}''-\mathbf{q}}c^{\mathbf{k}'',\mathbf{k}'+\mathbf{q}-\mathbf{k}'',\mathbf{k}-\mathbf{q}+\mathbf{k}''}_{\mathrm{BX};\sigma\sigma'\sigma'\sigma} + V^{\mathrm{cc}}_{\sigma\sigma',\mathbf{k}''-\mathbf{q}}c^{\mathbf{k}'',\mathbf{k}',\mathbf{k}}_{\mathrm{BX};\sigma\sigma'\sigma'\sigma} \\
&\qquad - V^{\mathrm{vc}}_{\sigma\sigma,\mathbf{k}''-\mathbf{k}}c^{\mathbf{q},\mathbf{k}',\mathbf{k}''}_{\mathrm{BX};\sigma\sigma'\sigma'\sigma} - V^{\mathrm{vc}}_{\sigma\sigma',\mathbf{k}''-\mathbf{k}}c^{\mathbf{k}''+\mathbf{q}-\mathbf{k},\mathbf{k}',\mathbf{k}''}_{\mathrm{BX};\sigma\sigma'\sigma'\sigma} \\
&\qquad - V^{\mathrm{vc}}_{\sigma'\sigma',\mathbf{k}''-\mathbf{k}'}c^{\mathbf{q},\mathbf{k}'',\mathbf{k}}_{\mathrm{BX};\sigma\sigma'\sigma'\sigma} - V^{\mathrm{vc}}_{\sigma'\sigma,\mathbf{k}''-\mathbf{k}'}c^{\mathbf{k}'+\mathbf{q}-\mathbf{k}'',\mathbf{k}'',\mathbf{k}}_{\mathrm{BX};\sigma\sigma'\sigma'\sigma}\Bigg) \\
&\quad + \left(V^{\mathrm{cc}}_{\sigma'\sigma,\mathbf{q}}p_{\sigma',\mathbf{k}'} - V^{\mathrm{vc}}_{\sigma'\sigma,\mathbf{q}}p_{\sigma',\mathbf{k}'+\mathbf{q}}\right)p_{\sigma,\mathbf{k}} - \left(V^{\mathrm{cv}}_{\sigma'\sigma,\mathbf{q}}p_{\sigma',\mathbf{k}'} - V^{\mathrm{vv}}_{\sigma'\sigma,\mathbf{q}}p_{\sigma',\mathbf{k}'+\mathbf{q}}\right)p_{\sigma,\mathbf{k}-\mathbf{q}} \\
&\quad + \delta_{\sigma\sigma'}\left[\left(V^{\mathrm{vc}}_{\sigma\sigma,\mathbf{j}}p_{\sigma,\mathbf{k}'} - V^{\mathrm{vv}}_{\sigma\sigma,\mathbf{j}}p_{\sigma,\mathbf{k}-\mathbf{q}}\right)p_{\sigma,\mathbf{k}'+\mathbf{q}} - \left(V^{\mathrm{cc}}_{\sigma\sigma,\mathbf{j}}p_{\sigma,\mathbf{k}'} - V^{\mathrm{cv}}_{\sigma\sigma,\mathbf{j}}p_{\sigma,\mathbf{k}-\mathbf{q}}\right)p_{\sigma,\mathbf{k}}\right].
\end{aligned}
\tag{5.13}
$$

In the above equation, the first four lines describe the eigenstate of the biexciton, including bound and unbound states. A biexciton is a state formed by two excitons, each consisting of one electron and one hole, totaling two electrons and two holes. In this state, there are two repulsive Coulomb interactions between the two holes and between the two electrons, as represented by the two terms in the second line. Meanwhile, the four attractive Coulomb interactions between the two electrons and the two holes are represented by the four terms in the third and fourth lines. Note that the contributions from attractive and repulsive interactions are of opposite sign. The last two lines describe nonlinear source terms resulting from the singlet factorization of three-particle correlations involving only microscopic polarizations. The terms in the second-to-last line with $V_{\mathbf{q}}$ describe the direct Coulomb interaction and can couple the spin subspaces. The final line's terms, with $V_{\mathbf{j}}$, describe the exchange interaction and only couple the singlet terms with the same spin.

The calculations in this chapter are conducted within the coherent $\chi^{(3)}$ limit. In first order, the pump and probe pulses induce the interband coherences $p^{(1)}_{\sigma,\mathbf{k}}$ and $\delta p^{(1)}_{\sigma,\mathbf{k}}$, respectively. In second order, three key quantities are generated: the pump-induced occupations $n^{(2)}_{\sigma,\mathbf{k}}$, the pump-probe induced occupations $\delta n^{(2)}_{\sigma,\mathbf{k}}$, and the biexcitonic correlations $\delta c^{\mathbf{q},\mathbf{k}',\mathbf{k},(2)}_{\mathrm{BX},\sigma\sigma'\sigma'\sigma}$. The contributions from biexcitonic states, both bound and unbound, can be tuned by adjusting the helicity of the pump and probe pulses, as illustrated in Fig. 5.5. Under co-circularly polarized excitation, only unbound continuum states are generated, while bound biexcitons become significant in the case of counter-circularly polarized excitation. In third order, the probe-induced coherence $\delta p^{(3)}_{\sigma,\mathbf{k}}$ is generated along with polarization–occupation correlations, $\delta c^{\mathbf{q},\mathbf{k}',\mathbf{k},(3)}_{\mathrm{ph},\sigma\sigma'\sigma'\sigma}$ (polarization–hole) and $\delta c^{\mathbf{q},\mathbf{k}',\mathbf{k},(3)}_{\mathrm{pe},\sigma\sigma'\sigma'\sigma}$ (polarization–electron). The differential absorption is determined by the third-order probe-induced coherence, $\delta p^{(3)}_{\sigma,\mathbf{k}}$, by Eq. (5.1). The EOM for all these quantities are provided in detail in Appendix A.6.

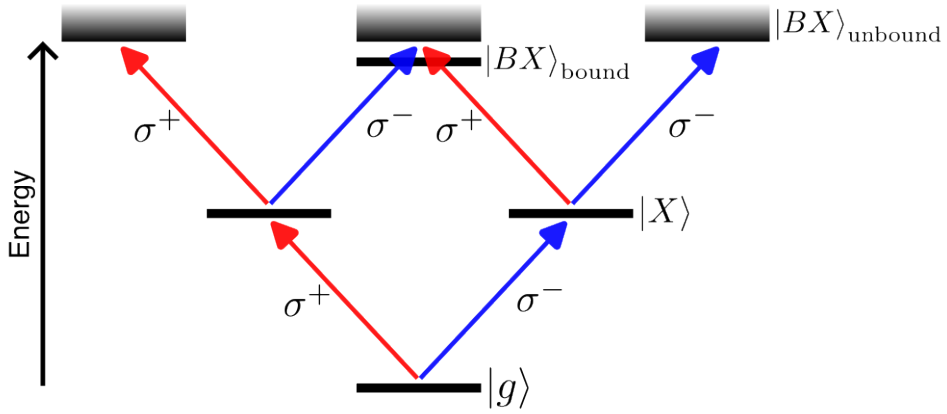

Figure 5.5: Schematic illustration of the optical transitions with circularly polarized excitation and selection rules for excitons and biexciton states. $|g\rangle$ denotes the ground state, $|X\rangle$ the exciton states, $|BX\rangle_{\text{bound}}$ and $|BX\rangle_{\text{unbound}}$ denote the bound and unbound biexciton states, respectively.

5.3 Numerical Results

In this section, we present numerical results of OPOP simulations for spatially-homogeneous type-I and spatially-inhomogeneous type-II QW structures. The pump pulse excites both resonantly and off-resonantly, either at or below the direct exciton or the CTX. The probe pulse has a duration of $\tau = 10$ fs to test a broad frequency range, while the pump pulse has a duration of $\tau = 1$ ps to excite a well-defined spectral region. In the coherent limit, the phenomenological relaxation times are chosen as $T_1 = T_2/2$ for the occupations, $T_{\text{BX}} = T_2/2$ for the biexcitonic correlations, and $T_{\text{c}} = T_2/3$ for the polarization-carrier correlations.

First, we investigate the excitonic nonlinear response of the spatially-homogeneous type-I QW structure. Figure 5.6 shows the pump-induced differential absorption $\Delta\alpha(\omega)$ for co-circularly polarized pump and probe pulses in panels (a) and (b), and for counter-circularly polarized pulses in panels (c) and (d). The optical pump pulse excites the direct exciton resonantly. The exciton binding energy is 7 meV. In Fig. 5.6(a), the total response near the direct exciton originates from pump-induced exciton bleaching and induced absorption above the exciton due to transitions from the exciton to unbound biexcitons. Figure 5.6(b) shows the individual contributions to the nonlinearity originating from PB, the first-order Coulomb interactions (CI_{1st}), and the higher-order Coulomb correlations (CI_{corr}).

Under resonant exciton excitation, the PB contribution is relatively weak compared to the Coulomb-induced contributions. PB causes pure bleaching at the exciton resonance. The CI_{1st} and CI_{corr} contributions have dispersive lineshapes, CI_{1st} causes a blueshift, while CI_{corr} results in a redshift. These two contributions mostly cancel each other, such that the total signal primarily reflects exciton bleaching. If we only consider the theoretical

framework up to the TDHF approximation, CI_{1st} would dominate and result in an overall blueshift. This highlights the importance of including higher-order Coulomb correlation effects when investigating excitonic nonlinear responses [64, 135].

Additionally, the CI_{corr} contribution causes weak excited-state absorption above the exciton, corresponding to the transition from the exciton to unbound biexciton states. This contribution cannot be canceled by CI_{1st} and is visible in the total signal.

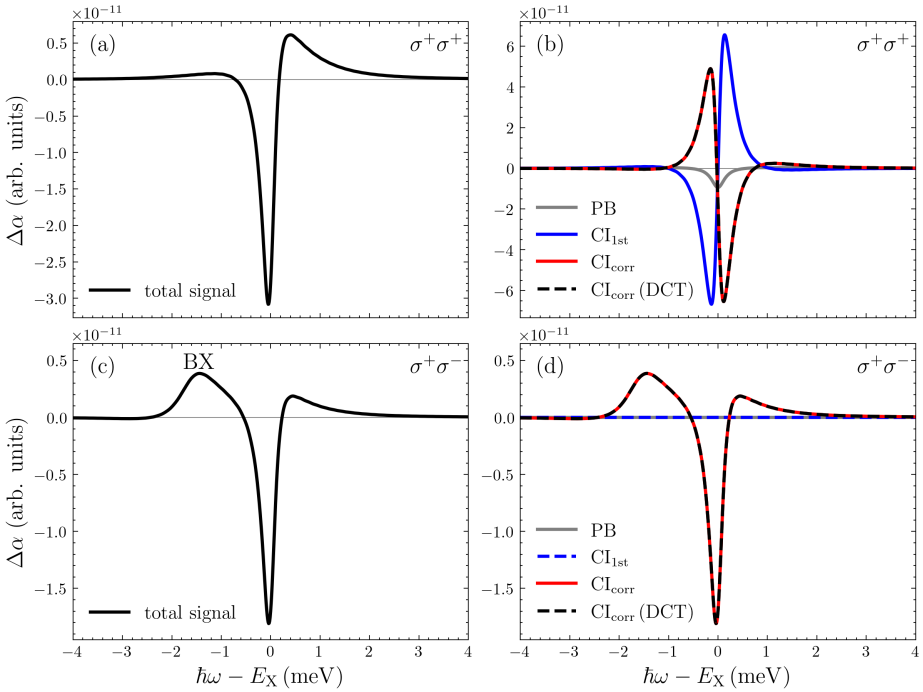

Figure 5.6: Differential absorption signals of the spatially-homogeneous type-I QW structure are shown, where the spatially-direct exciton is resonantly excited with no time delay between the pump and probe pulses. Panels (a) and (c) display the total differential absorption for co-circular ($\sigma^+\sigma^+$) and counter-circular ($\sigma^+\sigma^-$) excitations, respectively. The corresponding individual contributions to nonlinearity are shown in panels (b) and (d), with the Pauli-blocking term indicated by gray lines, the first-order Coulomb interaction (CI_{1st}) by blue lines, and the higher-order Coulomb correlations (CI_{corr}) by red lines. The dashed black lines represent CI_{corr} as calculated via the DCT approach. The exciton binding energy is 7 meV and the biexciton binding energy is 1.44 meV. The dephasing time is set to $T_2 = 4$ ps.

Next, we examine the case of counter-circularly polarized excitation for the type-I QW structure. The total differential absorption is shown in Fig. 5.6(c) and the individual nonlinearity contributions are shown in Fig. 5.6(d). In this case, we see that only the CI_{corr} contribution contributes to the total signal, meaning the response arises purely from higher-order Coulomb correlations. Examining the EOM reveals that only the terms that couple different spin states give a finite contribution. For this reason, the PB contribution

vanishes due to the selection rules. In the case of Coulomb-induced nonlinear contribution, there are two types of terms: one that couples the same spin states and the other one that couples the spin subspaces. For $\mathrm{CI}_{\mathrm{1st}}$, these terms are described by the second and third lines of Eq. (5.8), respectively. Under counter-circular excitation conditions and depending on the system's structure, only the terms that couple the spin subspaces can contribute. This contribution has the following form

$$i\hbar\frac{\partial}{\partial t}p_{\sigma,\mathbf{k}} \propto -\sum_{\sigma'}\left(2V^{\mathrm{vc}}_{\sigma\sigma',\mathbf{0}} - V^{\mathrm{vv}}_{\sigma\sigma',\mathbf{0}} - V^{\mathrm{cc}}_{\sigma\sigma',\mathbf{0}}\right)\sum_{\mathbf{k}'} n_{\sigma',\mathbf{k}'}p_{\sigma,\mathbf{k}}. \tag{5.14}$$

In the expression above, the prefactor contains the difference between the Coulomb attraction and the Coulomb repulsion. This demonstrates that the contribution is finite only in spatially-inhomogeneous systems, where the Coulomb repulsion and the Coulomb attraction between alike-charged and oppositely charged carriers, respectively, do not cancel each other. In the case of spatially-inhomogeneous type-II QWs, due to the spatial separation, the attractive interaction between electrons and holes across different layers of the QW is weaker than the repulsive interaction between alike-charged carriers within the same QW layer. Due to this imbalance, the repulsive interaction is not completely canceled by the attractive interaction. This results in a finite residual repulsion, which introduces an additional contribution and can, therefore, influence the system's physical response under excitation conditions. For $\mathrm{CI}_{\mathrm{corr}}$, in contrast to $\mathrm{CI}_{\mathrm{1st}}$, the terms that couple different spin states are still finite for both spatially-homogeneous and spatially-inhomogeneous systems.

In summary, for counter-circularly polarized excitation in spatially-homogeneous systems the nonlinear response is determined purely by higher-order Coulomb correlations. This includes excited-state absorption above the exciton resonance, as seen in the case of co-circular excitation due to transitions from excitons to unbound biexciton states. In the counter-circular case, the $\mathrm{CI}_{\mathrm{corr}}$ term also includes induced absorption due to transitions to bound biexcitons that appear below the exciton resonance at -1.44 meV meV, which is visible in Figs. 5.6(c) and (d). This energy difference is the binding energy of the bound biexciton. It should be noted that in all the results presented in this section, the correlation contributions align completely with the DCT approach [64, 67, 135], as represented by the dashed black lines, highlighting our successful implementation of the cluster expansion method.

Next, we examine the nonlinear response for a spatially-inhomogeneous type-II QW, as shown in Fig. 5.7. For ease of comparison, we keep the excitation conditions the same but switch to a type-II QW structure by reducing the Coulomb attraction between electrons and holes by a constant factor while keeping the repulsive interaction between alike-charged carriers unchanged. This constant factor is tuned to match the binding energy of 4.8 meV for the CTX observed in experiments [67].

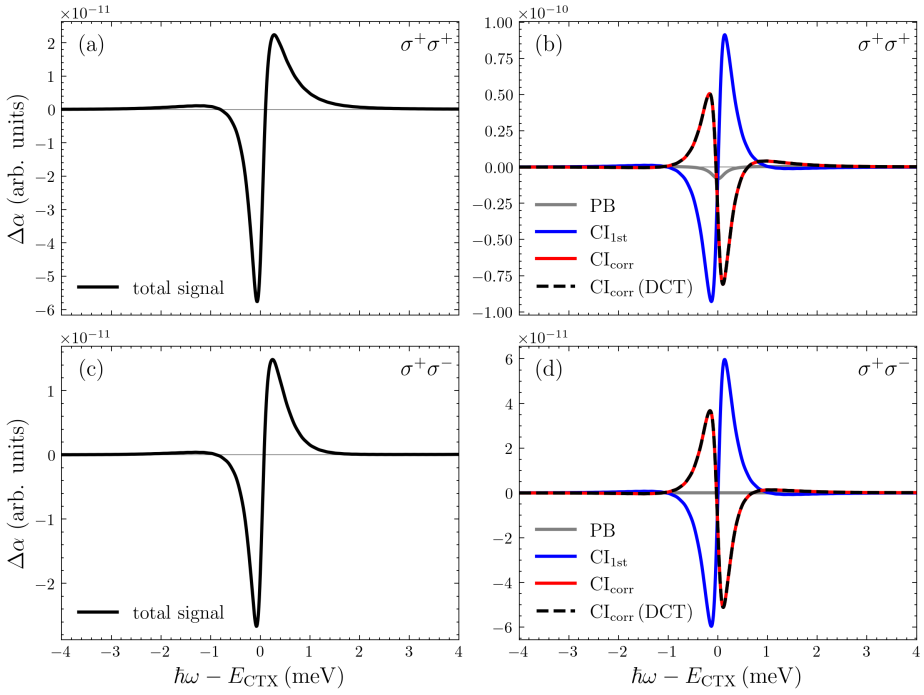

Figure 5.7: Differential absorption signals of the spatially-homogeneous type-II QW structure are shown, where the CTX is resonantly excited with no time delay between the pump and probe pulses. Panels (a) and (c) display the total differential absorption for co-circular ($\sigma^+\sigma^+$) and counter-circular ($\sigma^+\sigma^-$) excitations, respectively. The corresponding individual contributions to nonlinearity are shown in panels (b) and (d), with the Pauli-blocking term indicated by gray lines, the first-order Coulomb interaction (CI_{1st}) by blue lines, and the higher-order Coulomb correlations (CI_{corr}) by red lines. The dashed black lines represent CI_{corr} as calculated via coherent DCT scheme. The CTX binding energy is 4.7 meV. The dephasing time is set to $T_2 = 4$ ps.

For the case of co-circularly polarized excitation, the features observed near the CTX in the type-II QW structure [Fig. 5.7(b)] and the spatially-direct exciton in the type-I QW structure [Fig. 5.6(b)] exhibit almost similar nonlinear contributions to the differential absorption. However, under counter-circularly polarized excitation, the differential absorption spectrum displays significant differences compared to the results observed for the spatially-homogeneous type-I QW structure. As discussed above, the terms coupling between excitons with different spins of CI_{1st} in Eq. (5.14) lead to a finite contribution to the optical response of inhomogeneous systems. This phenomenon is not present in spatially-homogeneous systems, such as type-I QW structures. Regarding the CI_{corr} contribution to the differential absorption spectrum under counter-circular excitation [Fig. 5.7(d)], we observe only minor absorption of unbound biexcitons, with no bound biexciton-induced absorption as seen in the type-I QW structure; instead, a redshift occurs. This is because, in CTX, the attractive Coulomb interaction between the electron and hole in different QW layers is weaker than the repulsive Coulomb interaction between electrons and between

holes within the same QW layer. Consequently, when the spatial separation between electron and hole in CTX is large enough, the weak Coulomb attraction can no longer lead to the formation of a bound two-exciton state, leaving only unbound two-exciton states.

To gain a better understanding of the contributions of the TDHF to the nonlinear optical response from type-II QW structures, we examine a simple model which can be solved analytically. Similar models have been successfully applied to explain the behavior of type-I QW structures [66, 155]. However, in the case of type-II QWs, an additional term must be included to account for the system's inhomogeneity. For the resonant excitation at the 1s exciton, we can expand the coherent $p_{\sigma,\mathbf{k}}$ in the exciton basis, i.e., the solutions of the Wannier equation, as

$$p_{\sigma,\mathbf{k}} = \sum_n \psi^n_{\sigma,\mathbf{k}} p^n_\sigma \approx \psi^{1\mathrm{s}}_{\sigma,\mathbf{k}} p^{1s}_\sigma. \tag{5.15}$$

In the coherent limit, by replacing $n_{\sigma,\mathbf{k}} = p^*_{\sigma,\mathbf{k}} p_{\sigma,\mathbf{k}}$ and inserting Eq. (5.15) into Eq. (5.8), then left-multiplying by $\left(\psi^{1s}_{\sigma,\mathbf{k}}\right)^*$ and summing over $\mathbf{k}$, we obtain

$$\begin{aligned} i\hbar\frac{\partial}{\partial t}p_\sigma = &\left(E^{\mathrm{X}}_{1\mathrm{s}} - i\frac{\hbar}{T_2}\right)p_\sigma - \mathbf{E}(t)\cdot\mathbf{d}_\sigma\tilde{\psi}^{1s*}_\sigma(\mathbf{r}=0) + \mathbf{E}(t)\cdot\mathbf{d}_\sigma b_\sigma|p_\sigma|^2 \\ &+ \sum_{\sigma'} V_{\sigma\sigma'}|p_{\sigma'}|^2 p_\sigma. \end{aligned} \tag{5.16}$$

Here, $\tilde{\psi}^{1s}_\sigma(\mathbf{r})$ is the Fourier transform of $\psi^{1\mathrm{s}}_{\sigma,\mathbf{k}}$, $\mathbf{d}_\sigma = \mathbf{d}^{\mathrm{cv}}_{\sigma\sigma,\mathbf{0}}$ is the constant dipole matrix element, and $T_2 = \hbar/\gamma_2$ is dephasing time. The first term describes the 1s exciton, the second term represents the linear source term, and the third and fourth terms account for contributions from nonlinear PB and $\mathrm{CI}_{1\mathrm{st}}$. The terms b_σ and $V_{\sigma\sigma'}$ are defined as

$$b_\sigma = 2\sum_{\mathbf{k}}\left(\psi^{1\mathrm{s}}_{\sigma,\mathbf{k}}\right)^*\left|\psi^{1\mathrm{s}}_{\sigma,\mathbf{k}}\right|^2, \tag{5.17}$$

$$\begin{aligned} V_{\sigma\sigma'} = &\delta_{\sigma\sigma'}\sum_{\mathbf{k},\mathbf{k}'}\left[2V^{\mathrm{vc}}_{\sigma\sigma,\mathbf{k}'-\mathbf{k}}\psi^{1\mathrm{s}}_{\sigma,\mathbf{k}'}\left(\psi^{1\mathrm{s}}_{\sigma,\mathbf{k}}\right)^* - \left(V^{\mathrm{vv}}_{\sigma\sigma,\mathbf{k}'-\mathbf{k}} + V^{\mathrm{cc}}_{\sigma\sigma,\mathbf{k}'-\mathbf{k}}\right)\left|\psi^{1\mathrm{s}}_{\sigma,\mathbf{k}'}\right|^2\right]\left|\psi^{1\mathrm{s}}_{\sigma,\mathbf{k}}\right|^2 \\ &- \left(2V^{\mathrm{vc}}_{\sigma\sigma',\mathbf{0}} - V^{\mathrm{vv}}_{\sigma\sigma',\mathbf{0}} - V^{\mathrm{cc}}_{\sigma\sigma',\mathbf{0}}\right)\sum_{\mathbf{k}'}\left|\psi^{1\mathrm{s}}_{\sigma',\mathbf{k}'}\right|^2\sum_{\mathbf{k}}\left|\psi^{1\mathrm{s}}_{\sigma,\mathbf{k}}\right|^2. \end{aligned} \tag{5.18}$$

By using delta-function ultrashort pulses for the pump pulse $\mathbf{E}_{\mathrm{pump}} = \mathbf{e}_{\mathrm{pump}}E^0_{\mathrm{pump}}\delta(t+\tau)$, and the probe pulse $\mathbf{E}_{\mathrm{probe}} = \mathbf{e}_{\mathrm{probe}}E^0_{\mathrm{probe}}\delta(t)$, where τ is the time delay between them, we obtain the solutions at third order for the nonlinear PB contribution as

$$\begin{aligned} \delta p^{\mathrm{PB},(3)}_\sigma = &\left(\frac{i}{\hbar}\right)^3 b_\sigma\left(\mathbf{e}_{\mathrm{pump}}\cdot\mathbf{d}_\sigma\right)^2\left(\mathbf{e}_{\mathrm{probe}}\cdot\mathbf{d}_\sigma\right)\left|E^0_{\mathrm{pump}}\right|^2 E^0_{\mathrm{probe}}e^{-i(\omega_{1\mathrm{s}}-i/T_2)t} \\ &\times\left[\theta(t)\theta(\tau)e^{-\frac{\tau}{T_2/2}} + \theta(t+\tau)\theta(-\tau)\right], \end{aligned} \tag{5.19}$$

and for nonlinear $\mathrm{CI}_{1\mathrm{st}}$ contribution as

$$\delta p_{\sigma}^{\mathrm{CI}_{1\mathrm{st}},(3)} = \sum_{\sigma'} 2\left(\frac{i}{\hbar}\right)^4 V_{\sigma\sigma'}\left(\mathbf{e}_{\mathrm{pump}}\cdot\mathbf{d}_{\sigma'}\right)^2\left(\mathbf{e}_{\mathrm{probe}}\cdot\mathbf{d}_{\sigma}\right)\left|E^0_{\mathrm{pump}}\right|^2 E^0_{\mathrm{probe}}\frac{T_2}{2}e^{-i(\omega_{1\mathrm{s}}-i/T_2)t} \times\left[\theta(t)\theta(\tau)\left(1-e^{-\frac{t}{\tau/2}}\right)e^{-\frac{\tau}{T_2/2}}+\theta(t+\tau)\theta(-\tau)\left(1-e^{-\frac{t+\tau}{T_2/2}}\right)\right]. \tag{5.20}$$

Here, $\theta(t)$ is the step function. From the above solutions for δp_σ, Eqs. (5.19) and (5.20), we obtain the probe-induced change of the macroscopic polarization in the direction of probe pulse by $\delta P(t) = \sum_\sigma \left(\mathbf{e}_{\mathrm{probe}}\cdot\mathbf{d}_\sigma\right)\delta p_\sigma$. By taking the Fourier transformation of $\delta P(t)$ and then getting their imaginary part, we obtain the differential absorption $\Delta\alpha$ for the case of $\tau > 0$, i.e., the pump before the probe pulse, as

$$\Delta\alpha_{\mathrm{PB}} = -\sum_{\sigma}\frac{1}{\hbar^3}b_\sigma\left|\mathbf{e}_{\mathrm{pump}}\cdot\mathbf{d}_\sigma\right|^2\left(\mathbf{e}_{\mathrm{probe}}\cdot\mathbf{d}_\sigma\right)^2\left|E^0_{\mathrm{pump}}\right|^2 E^0_{\mathrm{probe}}\frac{1}{T_2}\frac{e^{-\frac{\tau}{T_2/2}}}{(\omega_{1\mathrm{s}}-\omega)^2+\left(\frac{1}{T_2}\right)^2}. \tag{5.21}$$

$$\Delta\alpha_{\mathrm{CI}_{1\mathrm{st}}} = \sum_{\sigma,\sigma'}\frac{2}{\hbar^4}V_{\sigma\sigma'}\left|\mathbf{e}_{\mathrm{pump}}\cdot\mathbf{d}_{\sigma'}\right|^2\left(\mathbf{e}_{\mathrm{probe}}\cdot\mathbf{d}_\sigma\right)^2\left|E^0_{\mathrm{pump}}\right|^2 E^0_{\mathrm{probe}}\frac{T_2}{2}e^{-\frac{\tau}{T_2/2}} \times(\omega-\omega_{1\mathrm{s}})\left[\frac{1}{(\omega_{1\mathrm{s}}-\omega)^2+\left(\frac{1}{T_2}\right)^2}-\frac{1}{(\omega_{1\mathrm{s}}-\omega)^2+\left(\frac{1}{T_2/3}\right)^2}\right]. \tag{5.22}$$

The expression (5.21) for $\Delta\alpha_{\mathrm{PB}}$ describes exciton bleaching under co-circularly excitation and vanishes for counter-circularly excitation. For $\mathrm{CI}_{1\mathrm{st}}$ contribution, given by expressions (5.22), the Coulomb term $V_{\sigma\sigma'}$ affects $\Delta\alpha_{\mathrm{CI}_{1\mathrm{st}}}$, which is influenced when the Coulomb interaction strength is suppressed. Furthermore, $\Delta\alpha_{\mathrm{CI}_{1\mathrm{st}}}$ will result in a blueshift if $V_{\sigma\sigma'} > 0$ and a redshift if $V_{\sigma\sigma'} < 0$. Assumed that $V^{vc} = V/\alpha$ ($\alpha > 0$), $V^{vv} = V^{cc} = V$, Eq. (5.18) can be rewritten as

$$V_{\sigma\sigma'} = \delta_{\sigma\sigma'}\sum_{\mathbf{k},\mathbf{k}'}\left[\frac{1}{\alpha}\psi^{1\mathrm{s}}_{\sigma,\mathbf{k}'}\left(\psi^{1\mathrm{s}}_{\sigma,\mathbf{k}}\right)^* - \left|\psi^{1\mathrm{s}}_{\sigma,\mathbf{k}'}\right|^2\right]2V_{\sigma\sigma,\mathbf{k}'-\mathbf{k}}\left|\psi^{1\mathrm{s}}_{\sigma,\mathbf{k}}\right|^2 + (1-1/\alpha)2V_{\sigma\sigma',\mathbf{0}}\sum_{\mathbf{k}'}\left|\psi^{1\mathrm{s}}_{\sigma',\mathbf{k}'}\right|^2\sum_{\mathbf{k}}\left|\psi^{1\mathrm{s}}_{\sigma,\mathbf{k}}\right|^2. \tag{5.23}$$

For the case of spatially-homogeneous type-I QW structures ($\alpha = 1$), the second term vanishes. The first term is finite only under co-circular excitation, as indicated by the $\delta_{\sigma\sigma'}$ factor in the first line. In this scenario, $V_{\sigma\sigma'} > 0$ and leads to the well-known blueshift induced by the first-order Coulomb interaction. In the case of spatially-inhomogeneous type-II QW structures ($\alpha > 0$) under co-circular excitation, the value of the first term gradually decreases as α increases and can become negative with further increases in α. This reduction leads to a transition of the first term's contribution from a blueshift to a redshift. Meanwhile, the second term's value under co-circular excitation is positive and increases with α, resulting in an overall blueshift. Under counter-circular excitation, only

the second term remains and its contribution increases steadily as α increases.

Now, we study the effect of gradually reducing the attractive Coulomb interaction and examine the optical response. The results are shown in Fig. 5.8 for both co-circularly and counter-circularly polarized excitations, with an exciton binding energy obtained as 7 meV for the type-I QW structure and lower exciton binding energies for the type-II QW structures.

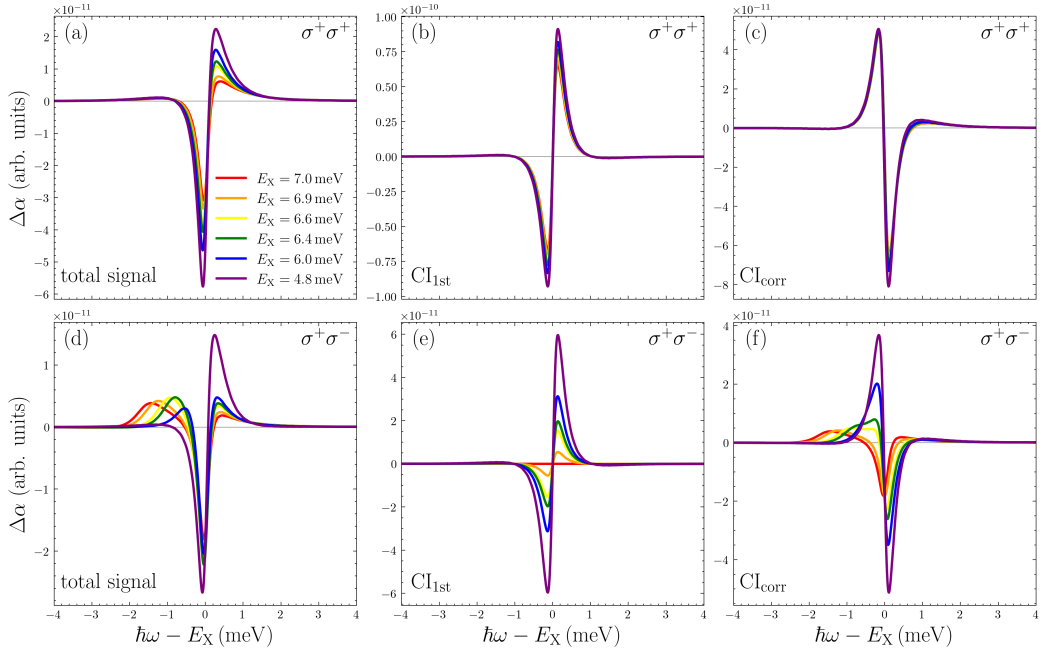

Figure 5.8: Differential absorption spectra when gradually reducing the exciton binding energy by reducing the electron-hole attraction for the case of resonant optical excitation with no time delay between the pump and probe pulses. Panels (a) and (d) display the total differential absorption for co-circular ($\sigma^+\sigma^+$) and counter-circular ($\sigma^+\sigma^-$) excitations, respectively. The corresponding individual contributions to nonlinearity are shown in panels (b) and (e) for the first-order Coulomb interaction (CI_{1st}), and panels (c) and (f) for the higher-order Coulomb correlations (CI_{corr}). The exciton binding energy of 7 meV corresponds to the case of a type-I QW. The dephasing time is set to $T_2 = 4$ ps.

The total signal for co-circularly polarized excitation, shown in Fig. 5.8(a), reveals the modulation of the differential absorption spectrum when gradually reducing the exciton binding energy from 7 meV (corresponding to type-I QW structure) to 4.8 meV (corresponding to type-II QW structure). The nonlinear contributions caused by Coulomb terms CI_{1st} and CI_{corr} are shown in Figs. 5.8(a) and 5.8(b), respectively. The results indicate that the enhancement of the differential absorption spectrum primarily originates from CI_{1st}, while CI_{corr} remains nearly unchanged as the Coulomb attraction is reduced. Theoretical analysis shows that the increased blueshift in CI_{1st} stems from the term in Eq. (5.14), which describes the contribution from the system's inhomogeneity.

For the case of counter-circularly polarized excitation, the total differential absorption signal is shown in Fig. 5.8(d), with the contributions from CI_{1st} and CI_{corr} displayed in Figs. 5.8(e) and 5.8(f), respectively. Here, the CI_{1st} contribution shows the same characteristics as for the co-circularly polarized excitation case, with the only difference that this contribution vanishes for type-I QWs, as there is no spin-subspace coupling term. Regarding the CI_{corr} contribution, we observe a gradual reduction in the biexciton binding energy as the Coulomb attraction weakens, resulting in a gradual change to a redshift. This reduction in biexciton binding energy, as discussed earlier, is due to the weaker Coulomb attraction between oppositely charged particles compared to the repulsive Coulomb interaction between alike-charged particles.

By the results presented above, we analyze the nonlinear excitonic response under resonant excitation conditions. For off-resonant excitation with direct excitons and CTX with optical detunings, $\Delta = \hbar\omega_{\text{pump}} - E_X$, the results for both co-circularly and counter-circularly polarized excitations are shown in Fig. 5.9 for type-I QW structures and in Fig. 5.10 for type-II QW structures. In all cases, the differential absorption signal decreases significantly as the excitation becomes more off-resonantly.

First, examining the signal in the type-I QW case as illustrated in Fig. 5.9(a), we see that the primary response is a blueshift at an optical detuning of $\Delta = -2$ meV, while exciton bleaching remains weak. For larger optical detunings, the blueshift becomes the dominant effect. The detailed contributions of nonlinear components at $\Delta = -8$ meV are shown in Fig. 5.9(b). Here, we see that the blueshift in the total signal primarily originates from contributions by PB and CI_{1st}, while the CI_{corr} contribution introduces a slight redshift. Among these contributions, PB is more dominant than the other components.

For the case of counter-circularly polarized excitation, the results are presented in Fig. 5.9(c). The signal at $\Delta = -2$ meV shows exciton bleaching, along with induced absorption caused by transitions to both bound and unbound biexcitons appearing below and above the exciton resonance, which is similar to the resonant excitation case. For larger detunings, the total signal gradually changes to a redshift and the biexciton-induced absorption disappears. The results for the contributing components at $\Delta = -8$ meV are shown in Fig. 5.9(d), indicating that the redshift in this case purely arises from the CI_{corr} contribution.

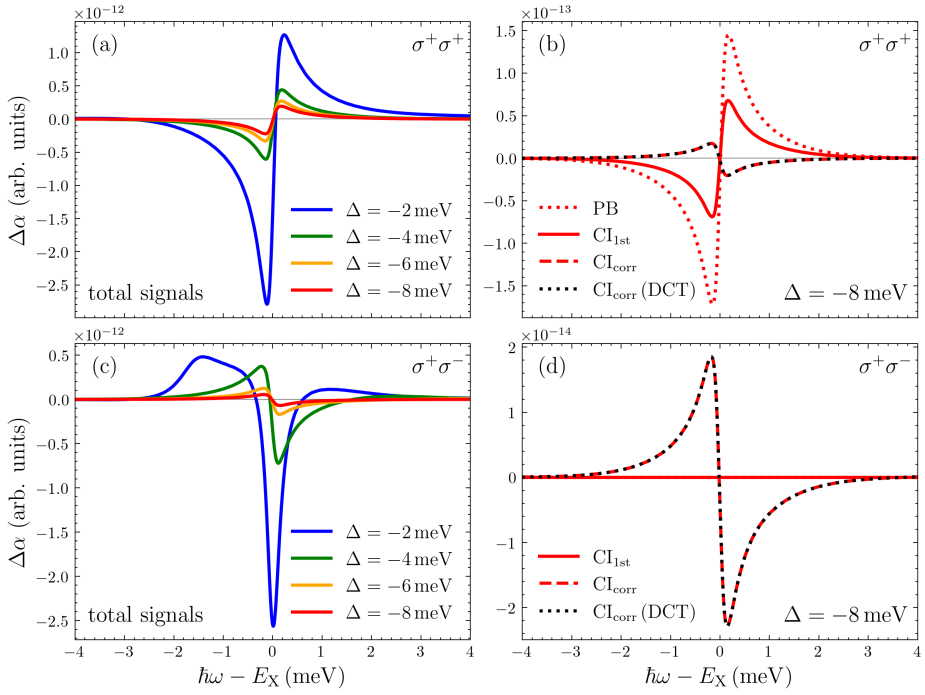

Figure 5.9: Differential absorption signals of the spatially-homogeneous type-I QW structure for different detuned pumping to exciton, i.e., $\Delta = \hbar\omega_{\mathrm{pump}} - E_X$. The spatially-direct exciton is excited off-resonantly with zero time delay between pump and probe pulses. (a) and (c) show the total differential absorptions with different detuning to exciton for co-circular excitation ($\sigma^+\sigma^+$) and counter-circular excitation ($\sigma^+\sigma^-$), respectively. Note that in panel (c), for better visibility, the signals for $\Delta = -4$ meV, -6 meV, and -8 meV are multiplied by a factor of 3. The corresponding individual nonlinearity contributions for $\Delta = -8$ meV are shown in (b) and (d). The PB contributions are in dotted red lines, the first-order Coulomb ($\mathrm{CI_{1st}}$) contribution in solid red lines, and higher-order Coulomb correlations ($\mathrm{CI_{corr}}$) contribution in dashed red lines. The dotted black lines show the $\mathrm{CI_{corr}}$ contribution obtained by coherent DCT scheme. The exciton binding energy is 7 meV and the binding energy of the bound biexciton is 1.44 meV. The dephasing time is set to $T_2 = 4$ ps.

For the case of the type-II QW shown in Fig. 5.10, the total signal under both co-circularly and counter-circularly polarized off-resonance excitation exhibits a blueshift. The contributing components are similar to those for the case of the type-I QW under far-off-resonant pumping but with one notable difference: under counter-circular excitation, a blueshift occurs because of the predominant contribution from $\mathrm{CI_{1st}}$.

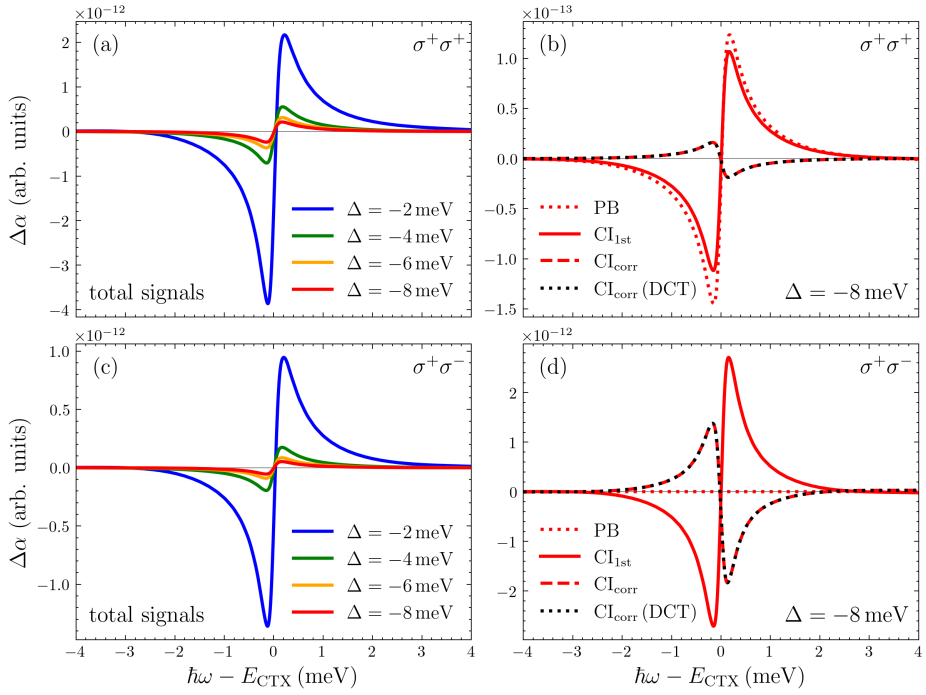

Figure 5.10: Differential absorption signals of the spatially-inhomogeneous type-II QW structure for different detuned pumping to exciton, i.e., $\Delta = \hbar\omega_{\text{pump}} - E_X$. The CTX is excited off-resonantly with zero time delay between pump and probe pulses. (a) and (c) show the total differential absorptions with different detuning to exciton for co-circular excitation ($\sigma^+\sigma^+$) and counter-circular excitation ($\sigma^+\sigma^-$), respectively. The corresponding individual nonlinearity contributions for $\Delta = -8$ meV are shown in (b) and (d). The PB contributions are in dotted red lines, the first-order Coulomb (CI_{1st}) contribution in solid red lines, and higher-order Coulomb correlations (CI_{corr}) contribution in dashed red lines. The dotted black lines show the CI_{corr} contribution obtained by coherent DCT scheme. The exciton binding energy is 4.7 meV. The dephasing time is set to $T_2 = 4$ ps.

Figure 5.11 illustrates the modulation of the differential absorption spectra when the exciton binding energy is reduced gradually for the case of detuned excitation below 6 meV of the exciton resonance. For co-circular excitation, the total signal shows a blueshift. In contrast, for counter-circular excitation, the total signal gradually changes from a redshift to a blueshift. An analysis of the Coulomb-induced nonlinearity reveals that the primary contribution to this change arises from CI_{1st}. This blueshift is further enhanced by the decreased Coulomb attraction, which originates from the system's inhomogeneity.

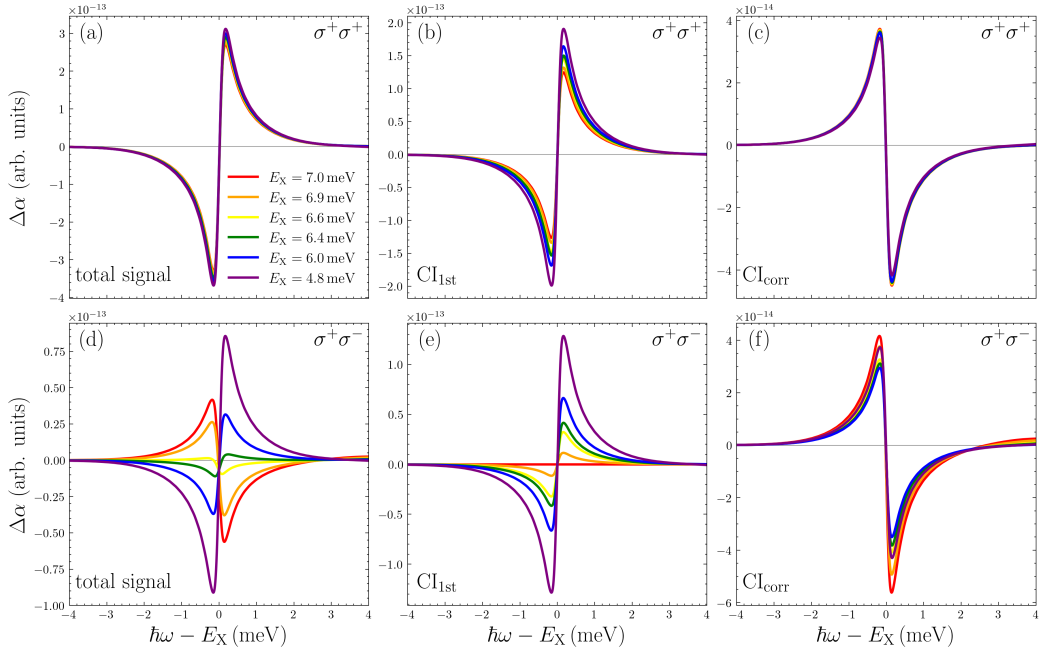

Figure 5.11: Differential absorption spectra when gradually reducing exciton binding energy for the case of excitation at 6 meV below the exciton, with no time delay between the pump and probe pulses. Panels (a) and (d) display the total differential absorption for co-circular ($\sigma^+\sigma^+$) and counter-circular ($\sigma^+\sigma^-$) excitations, respectively. The corresponding individual contributions to nonlinearity are shown in panels (b) and (e) for the first-order Coulomb interaction (CI_{1st}), and panels (c) and (f) for the higher-order Coulomb correlations (CI_{corr}). The exciton binding energy of 7 meV corresponds to the case of a type-I QW, and the dephasing time is set to $T_2 = 4$ ps.

5.4 Conclusions

In this chapter, we develop a theoretical model and implement numerical calculations to analyze the nonlinear optical response of excitons in spatially-homogeneous type-I QW structure and CTXs in spatially-inhomogeneous type-II QW structure through OPOP experiments. To achieve a deeper and more comprehensive understanding of the nonlinear excitonic response, we expand our analysis of the Coulomb interaction beyond the TDHF approximation. Through the application of the cluster expansion method, we obtain the EOM that accurately represent many-body correlation effects. In the coherent third-order limit, the relevant contributions to correlations include correlations between polarizations and electrons in the conduction band or holes in the valence band, as well as biexciton correlations.

Our numerical calculations and theoretical analysis uncover distinctive features in OPOP experiments when exciting CTXs in spatially-inhomogeneous type-II QWs, as well as

variations in the differential absorption spectrum with different polarizations of the excitation pulses. Significantly, we identify additional contributions already at the Hartree-Fock level in type-II QWs. The analysis of the EOM clearly demonstrates this finite contribution, highlighting its role in coupling spin subspaces and its occurrence exclusively in spatially-inhomogeneous systems.

Furthermore, in the limit of the coherent $\chi^{(3)}$ approximation, the results obtained from the cluster expansion method are practically identical to those within the DCT method. This is because the DCT method is fully encompassed within the cluster expansion, which confirms the successful implementation of our approach.

Conclusions and Outlook 6

In this thesis, we develop microscopic descriptions to theoretically and numerically investigate many-body Coulomb interactions in optically-excited semiconductor quantum well structures. The interaction between light and the quantum wells is modeled using a combination of the 14-band $\mathbf{k} \cdot \mathbf{p}$ approach within the envelope function approximation and the semiconductor Bloch equations in the length gauge. The first results part of this study focuses on exploring the influence of excitonic effects on the anomalous current generated by the Berry curvature in type-I semiconductor quantum wells. In the second results part, we expand the simulations to examine not only the impact of excitonic effects but also of many-body Coulomb correlations on the nonlinear optical response of spatially-homogeneous type-I and spatially-inhomogeneous type-II quantum well structures, which are analyzed through optical-pump optical-probe experiments.

To carry out simulations, we develop a general method for numerically solving the semiconductor Bloch equations in the length gauge. When numerically diagonalizing the Hamiltonian of the band structure, phase discontinuities appear at different $\mathbf{k}$ points in the Bloch states. We address this by constructing parallel transport gauge transformations of the Bloch states. As a result, we obtain smooth eigenfunctions as a function of $\mathbf{k}$. To ensure wave function periodicity, we employ twisted parallel transport gauge transformations to distribute the Berry phase uniformly along the k-path. These transformations are performed in each time step of the numerical integration, which simplifies the incorporation of many-body interactions. We validate this approach by calculating optical injection and shift photocurrents and by comparing these results with those obtained from the semiconductor Bloch equations in the velocity gauge. The agreement between the two approaches confirms the correctness and accuracy of our method.

Next, we apply this method to study the influence of excitonic effects on anomalous currents generated by the Berry curvature in semiconductor quantum wells which are excited by a THz pulse following excitation by a circularly polarized optical pulse. The calculations show that the anomalous current is significantly enhanced when the excitation is resonant with the exciton, demonstrating a significant excitonic Berry curvature in the system. Additionally, both the anomalous and normal currents display oscillations that depend on the time delay between the optical and the THz pulses, with oscillation frequencies matching the energy difference between the 1s and 2s exciton states. This suggests that the oscillations arise from wave packet dynamics when both 1s and 2s excitons are simultaneously excited. The damping dynamics of the system are microscopically described through interactions of electrons and holes with longitudinal optical and longitudinal acoustic phonons. The results show that the current's dynamics and decay align well with experimental observations. These theoretical findings highlight the crucial role of

excitonic effects on the anomalous currents that are generated by the Berry curvature in nanostructures and affirm the presence of an excitonic Berry curvature. This study can be extended in the future to additionally investigate extrinsic contributions to anomalous currents, such as side-jump and skew-scattering effects, which depend on scattering processes between carriers and phonons.

Finally, we extend the theory to study many-body Coulomb interactions beyond the time-dependent Hartree-Fock approximation. To deal with the hierarchy problem, we apply the cluster expansion method to account for many-body correlations on the singlet-doublet level. In the perturbative and coherent regime, these correlations include correlations between polarizations and conduction-band electrons or valence-band holes, as well as biexcitonic correlations. Using this approach, we develop a theoretical model to simulate optical-pump optical-probe experiments and investigate the nonlinear optical response of excitons in spatially-homogeneous type-I quantum well structures and of charge-transfer excitons in spatially-inhomogeneous type-II quantum well structures. The numerical results reveal the substantial influence of many-body Coulomb correlations on the nonlinear excitonic response of semiconductor nanostructures and highlight fundamental differences between type-I and type-II quantum wells. Notably, in type-II structures, both numerical simulations and the analysis of the equations of motion identify additional contributions at the Hartree-Fock level arising from the coupling between spin subspaces. This effect is unique to spatially-inhomogeneous systems and may dominate over the the contributions from many-body correlations.

This thesis primarily examines theoretical models within the weak excitation regime, considering correlation effects only within a framework limited to the third-order susceptibility, $\chi^{(3)}$ and the coherent regime. Nowadays, interest has grown in investigating effects induced by stronger fields. Expanding the equations of motion to incorporate higher-order correlation contributions, enabling comparison with experimental results at high intensities, represents a promising direction for future research development.

Appendix

A.1 Block Matrices of the Extended Kane Model

The following is the list of Pauli spin-1/2 matrices, the J spin-3/4 matrices, matrices $\mathbf{T}$, and the matrices $\mathbf{U}$ are given by $\mathbf{U} = \mathbf{T}^{\dagger}$

$$\sigma_x = \begin{pmatrix} 0 & 1 \\ 1 & 0 \end{pmatrix}, \qquad \sigma_y = \begin{pmatrix} 0 & -\mathrm{i} \\ \mathrm{i} & 0 \end{pmatrix},$$

$$\sigma_z = \begin{pmatrix} 1 & 0 \\ 0 & -1 \end{pmatrix},$$

$$J_x = \begin{pmatrix} 0 & \sqrt{3} & 0 & 0 \\ \sqrt{3} & 0 & 2 & 0 \\ 0 & 2 & 0 & \sqrt{3} \\ 0 & 0 & \sqrt{3} & 0 \end{pmatrix}, \qquad J_y = \begin{pmatrix} 0 & -\sqrt{3} & 0 & 0 \\ \sqrt{3} & 0 & -2 & 0 \\ 0 & 2 & 0 & -\sqrt{3} \\ 0 & 0 & \sqrt{3} & 0 \end{pmatrix},$$

$$J_z = \begin{pmatrix} 3 & 0 & 0 & 0 \\ 0 & 1 & 0 & 0 \\ 0 & 0 & -1 & 0 \\ 0 & 0 & 0 & -3 \end{pmatrix}$$

$$T_x = \frac{1}{3\sqrt{2}} \begin{pmatrix} -\sqrt{3} & 0 & 1 & 0 \\ 0 & -1 & 0 & \sqrt{3} \end{pmatrix}, \qquad T_y = \frac{-\mathrm{i}}{3\sqrt{2}} \begin{pmatrix} \sqrt{3} & 0 & 1 & 0 \\ 0 & 1 & 0 & \sqrt{3} \end{pmatrix},$$

$$T_z = \frac{\sqrt{3}}{3\sqrt{2}} \begin{pmatrix} 0 & 1 & 0 & 0 \\ 0 & 0 & 1 & 0 \end{pmatrix},$$

$$T_{xx} = \frac{1}{3\sqrt{2}} \begin{pmatrix} 0 & -1 & 0 & \sqrt{3} \\ -\sqrt{3} & 0 & 1 & 0 \end{pmatrix}, \qquad T_{yy} = \frac{1}{3\sqrt{2}} \begin{pmatrix} 0 & -1 & 0 & -\sqrt{3} \\ \sqrt{3} & 0 & 1 & 0 \end{pmatrix},$$

$$T_{zz} = \frac{\sqrt{3}}{3\sqrt{2}} \begin{pmatrix} 0 & 1 & 0 & 0 \\ 0 & 0 & -1 & 0 \end{pmatrix},$$

$$T_{yz} = \frac{\mathrm{i}}{2\sqrt{6}} \begin{pmatrix} -1 & 0 & -\sqrt{3} & 0 \\ 0 & \sqrt{3} & 0 & 1 \end{pmatrix}, \qquad T_{zx} = \frac{1}{2\sqrt{6}} \begin{pmatrix} -1 & 0 & \sqrt{3} & 0 \\ 0 & \sqrt{3} & 0 & -1 \end{pmatrix},$$

$$T_{xy} = \frac{\mathrm{i}}{\sqrt{6}} \begin{pmatrix} 0 & 0 & 0 & -1 \\ -1 & 0 & 0 & 0 \end{pmatrix}.$$

A.2 Model Parameters for the Extended Kane Model

Table A.1: The table of parameters for the extended Kane model taken from [37, 46, 156].

	GaAs	$Al_{0.3}Ga_{0.7}As$
E_0 (eV)	1.519	1.884
E_0' (eV)	4.488	4.504
Δ_0 (eV)	0.341	0.329
Δ_0' (eV)	0.171	0.165
Δ^- (eV)	−0.05	−0.05
P (eV nm)	1.0493	1.004
P' (eV nm)	0.478	0.478
Q (eV nm)	0.8165	0.817
C_k (eV nm)	−0.00034	−0.00018
γ_1	6.85	5.77
γ_2	2.1	1.67
γ_3	2.9	2.4
m^*/m_0	0.067	0.091

The relationship between the effective masses m^* and the Luttinger parameters γ_1, γ_2, γ_3 obtained from experiments, and the modified parameters m', γ_1', γ_2', γ_3' used in the 14-band $\mathbf{k}\cdot\mathbf{p}$ model is determined through the third-order Löwdin perturbation theory as [46]

$$\frac{m_0}{m^*} = \frac{m_0}{m'} + \frac{2m_0}{3\hbar^2}\left[P^2\left(\frac{2}{E_0} + \frac{1}{E_0+\Delta_0}\right) + P'^2\left(\frac{1}{E_0 - E_0'} + \frac{2}{E_0 - E_0' - \Delta_0'}\right) + \frac{4}{3}PP'\Delta^-\left(\frac{1}{(E_0+\Delta_0)(E_0-E_0')} - \frac{1}{E_0(E_0-E_0'-\Delta_0')}\right)\right], \tag{A.1}$$

$$\gamma_1 = \gamma_1' + \frac{2m_0}{3\hbar^2}\left(\frac{P^2}{E_0} + \frac{Q^2}{E_0'} + \frac{Q^2}{E_0'+\Delta_0'} + \frac{2}{3}\frac{PP'\Delta^-}{E_0(E_0'+\Delta_0')}\right), \tag{A.2}$$

$$\gamma_2 = \gamma_2' + \frac{2m_0}{3\hbar^2}\left(\frac{1}{2}\frac{P^2}{E_0} - \frac{1}{2}\frac{Q^2}{E_0'} + \frac{1}{3}\frac{PP'\Delta^-}{E_0(E_0'+\Delta_0')}\right), \tag{A.3}$$

$$\gamma_3 = \gamma_3' + \frac{2m_0}{3\hbar^2}\left(\frac{1}{2}\frac{P^2}{E_0} + \frac{1}{2}\frac{Q^2}{E_0'} + \frac{1}{3}\frac{PP'\Delta^-}{E_0(E_0'+\Delta_0')}\right). \tag{A.4}$$

A.3 Rotation of the Coordinate System

In the 14-band $\mathbf{k} \cdot \mathbf{p}$ model presented in Chapter 2, the x, y, and z coordinates of the system align with the crystal axes [1 0 0], [0 1 0], and [0 0 1], respectively. To transform the coordinate system, we use Euler rotations [84]. With this transformation, we rotate the coordinate system around the $z-y-z$ axes by angles $\alpha-\beta-\gamma$. The rotation operator for the wave vector $\mathbf{k}$ is a matrix that is given by

$$\begin{aligned} R &= R_z(\alpha)\, R_y(\beta)\, R_z(\gamma) \\ &= \begin{pmatrix} \cos(\alpha) & -\sin(\alpha) & 0 \\ \sin(\alpha) & \cos(\alpha) & 0 \\ 0 & 0 & 1 \end{pmatrix} \begin{pmatrix} \cos(\beta) & 0 & \sin(\beta) \\ 0 & 1 & 0 \\ -\sin(\beta) & 0 & \cos(\beta) \end{pmatrix} \begin{pmatrix} \cos(\gamma) & -\sin(\gamma) & 0 \\ \sin(\gamma) & \cos(\gamma) & 0 \\ 0 & 0 & 1 \end{pmatrix}. \end{aligned} \tag{A.5}$$

With the above operator, the wave vector $\mathbf{k}$ transforms as follows

$$\begin{pmatrix} k_x \\ k_y \\ k_z \end{pmatrix} = R \begin{pmatrix} k_x^{'} \\ k_y^{'} \\ k_z^{'} \end{pmatrix}. \tag{A.6}$$

The rotation operator for the momentum vectors with $j = 1/2$ and $j = 3/2$ is a matrix given by

$$\begin{aligned} D_{1/2} &= D^x_{1/2}(\alpha)\, D^y_{1/2}(\beta)\, D^z_{1/2}(\gamma) \\ &= \begin{pmatrix} \exp\{-i\frac{\alpha}{2}\} & 0 \\ 0 & \exp\{i\frac{\alpha}{2}\} \end{pmatrix} \begin{pmatrix} \cos\left(\frac{\beta}{2}\right) & -\sin\left(\frac{\beta}{2}\right) \\ \sin\left(\frac{\beta}{2}\right) & \cos\left(\frac{\beta}{2}\right) \end{pmatrix} \begin{pmatrix} \exp\{-i\frac{\gamma}{2}\} & 0 \\ 0 & \exp\{i\frac{\gamma}{2}\} \end{pmatrix} \end{aligned} \tag{A.7}$$

and

$$\begin{aligned} D_{3/2} &= D^z_{3/2}(\alpha)\, D^y_{3/2}(\beta)\, D^z_{3/2}(\gamma) \\ &= \begin{pmatrix} \exp\{-i\frac{3}{2}\alpha\} & 0 & 0 & 0 \\ 0 & \exp\{-i\frac{1}{2}\alpha\} & 0 & 0 \\ 0 & 0 & \exp\{i\frac{1}{2}\alpha\} & 0 \\ 0 & 0 & 0 & \exp\{i\frac{3}{2}\alpha\} \end{pmatrix} \end{aligned}$$

$$\times \begin{pmatrix} \cos^3\left(\frac{\beta}{2}\right) & -\sqrt{3}\cos^2\left(\frac{\beta}{2}\right)\sin\left(\frac{\beta}{2}\right) & \sqrt{3}\cos\left(\frac{\beta}{2}\right)\sin^2\left(\frac{\beta}{2}\right) & -\sin^3\left(\frac{\beta}{2}\right) \\ \sqrt{3}\cos^2\left(\frac{\beta}{2}\right)\sin\left(\frac{\beta}{2}\right) & \cos^3\left(\frac{\beta}{2}\right) & -2\cos^2\left(\frac{\beta}{2}\right)\sin\left(\frac{\beta}{2}\right) & \sqrt{3}\cos\left(\frac{\beta}{2}\right)\sin^2\left(\frac{\beta}{2}\right) \\ & -2\cos\left(\frac{\beta}{2}\right)\sin\left(\frac{\beta}{2}\right) & +\sin^3\left(\frac{\beta}{2}\right) & \\ \sqrt{3}\cos\left(\frac{\beta}{2}\right)\sin^2\left(\frac{\beta}{2}\right) & 2\cos\left(\frac{\beta}{2}\right)\sin\left(\frac{\beta}{2}\right) & -\sqrt{3}\cos^2\left(\frac{\beta}{2}\right)\sin\left(\frac{\beta}{2}\right) & -\sqrt{3}\cos\left(\frac{\beta}{2}\right)\sin^2\left(\frac{\beta}{2}\right) \\ & -\sin^3\left(\frac{\beta}{2}\right) & & \\ \sin^3\left(\frac{\beta}{2}\right) & \sqrt{3}\cos\left(\frac{\beta}{2}\right)\sin^2\left(\frac{\beta}{2}\right) & \sqrt{3}\cos^2\left(\frac{\beta}{2}\right)\sin\left(\frac{\beta}{2}\right) & \cos^3\left(\frac{\beta}{2}\right) \end{pmatrix}$$

$$\times \begin{pmatrix} \exp\left\{-i\frac{3}{2}\gamma\right\} & 0 & 0 & 0 \\ 0 & \exp\left\{-i\frac{1}{2}\gamma\right\} & 0 & 0 \\ 0 & 0 & \exp\left\{i\frac{1}{2}\gamma\right\} & 0 \\ 0 & 0 & 0 & \exp\left\{i\frac{3}{2}\gamma\right\} \end{pmatrix}. \tag{A.8}$$

A.4 Singlet and Doublet Terms in the Equations of Motion for Many-Body Correlations

The following are lists of singlet and doublet terms in the EOM for the many-body correlations Eq. (2.58). The singlet term is

$$
\begin{aligned}
S^{\mathbf{q},\mathbf{k}',\mathbf{k}}_{\lambda\mu\mu'\lambda'} = &\sum_{\nu,\nu'}\left(\sum_{\lambda''} V^{\nu'\lambda'\lambda''\nu}_{\mathbf{k},\mathbf{k}',\mathbf{j}} P^{\mu,\lambda''}_{\mathbf{k}'} - \sum_{\mu''} V^{\nu'\mu''\mu\nu}_{\mathbf{k},\mathbf{k}',\mathbf{j}} P^{\mu'',\lambda'}_{\mathbf{k}-\mathbf{q}}\right)\left(P^{\nu',\mu'}_{\mathbf{k}'+\mathbf{q}} - \delta_{\nu'\mu'}\right)P^{\lambda,\nu}_{\mathbf{k}} \\
&- \sum_{\nu,\nu'}\left(\sum_{\lambda''} V^{\lambda''\nu'\nu\lambda}_{\mathbf{k},\mathbf{k}',\mathbf{j}} P^{\lambda'',\mu'}_{\mathbf{k}'+\mathbf{q}} - \sum_{\mu''} V^{\mu'\nu'\nu\mu''}_{\mathbf{k},\mathbf{k}',\mathbf{j}} P^{\lambda,\mu''}_{\mathbf{k}}\right)\left(P^{\mu,\nu}_{\mathbf{k}'} - \delta_{\nu\mu}\right)P^{\nu',\lambda'}_{\mathbf{k}-\mathbf{q}} \\
&+ \sum_{\nu,\nu'}\left(\sum_{\mu''} V^{\mu''\nu'\nu\mu}_{\mathbf{k}',\mathbf{k},\mathbf{q}} P^{\mu'',\mu'}_{\mathbf{k}'+\mathbf{q}} - \sum_{\mu''} V^{\mu'\nu'\nu\mu''}_{\mathbf{k}',\mathbf{k},\mathbf{q}} P^{\mu,\mu''}_{\mathbf{k}'}\right)\left(P^{\nu',\lambda'}_{\mathbf{k}-\mathbf{q}} - \delta_{\nu'\lambda'}\right)P^{\lambda,\nu}_{\mathbf{k}} \\
&- \sum_{\nu,\nu'}\left(\sum_{\lambda''} V^{\nu'\lambda'\lambda''\nu}_{\mathbf{k}',\mathbf{k},\mathbf{q}} P^{\lambda,\lambda''}_{\mathbf{k}} - \sum_{\lambda''} V^{\nu'\lambda''\lambda\nu}_{\mathbf{k}',\mathbf{k},\mathbf{q}} P^{\lambda'',\lambda'}_{\mathbf{k}-\mathbf{q}}\right)\left(P^{\mu,\nu}_{\mathbf{k}'} - \delta_{\nu\mu}\right)P^{\nu',\mu'}_{\mathbf{k}'+\mathbf{q}},
\end{aligned}
\tag{A.9}
$$

and the doublet term is

$$
\begin{aligned}
D^{\mathbf{q},\mathbf{k}',\mathbf{k}}_{\lambda\mu\mu'\lambda'} = &\sum_{\nu,\nu',\mathbf{k}''}\left(\sum_{\lambda''} V^{\nu'\lambda'\lambda''\nu}_{\mathbf{k}''-\mathbf{q},\mathbf{k},\mathbf{q}} P^{\lambda,\lambda''}_{\mathbf{k}} - \sum_{\lambda''} V^{\nu'\lambda''\lambda\nu}_{\mathbf{k}''-\mathbf{q},\mathbf{k},\mathbf{q}} P^{\lambda'',\lambda'}_{\mathbf{k}-\mathbf{q}}\right) c^{\mathbf{q},\mathbf{k}',\mathbf{k}''}_{\nu',\mu;\mu',\nu} \\
&- \sum_{\nu,\nu',\mathbf{k}''}\left(\sum_{\mu''} V^{\mu''\nu'\nu\mu}_{\mathbf{k}',\mathbf{k}''+\mathbf{q},\mathbf{q}} P^{\mu'',\mu'}_{\mathbf{k}'+\mathbf{q}} - \sum_{\mu''} V^{\mu'\nu'\nu\mu''}_{\mathbf{k}',\mathbf{k}''+\mathbf{q},\mathbf{q}} P^{\mu,\mu''}_{\mathbf{k}'}\right) c^{\mathbf{q},\mathbf{k}'',\mathbf{k}}_{\lambda,\nu';\nu,\lambda'} \\
&+ \sum_{\nu,\nu',\mathbf{k}''}\left(\sum_{\lambda''} V^{\lambda''\nu'\nu\lambda}_{\mathbf{k},\mathbf{k}''+\mathbf{j},\mathbf{j}} P^{\lambda'',\mu'}_{\mathbf{k}'+\mathbf{q}} - \sum_{\mu''} V^{\mu'\nu'\nu\mu''}_{\mathbf{k},\mathbf{k}''+\mathbf{j},\mathbf{j}} P^{\lambda,\mu''}_{\mathbf{k}}\right) c^{-\mathbf{j},\mathbf{k}',\mathbf{k}''}_{\nu',\mu;\lambda',\nu} \\
&- \sum_{\nu,\nu',\mathbf{k}''}\left(\sum_{\lambda''} V^{\nu'\lambda'\lambda''\nu}_{\mathbf{k}''-\mathbf{j},\mathbf{k}',\mathbf{j}} P^{\mu,\lambda''}_{\mathbf{k}'} - \sum_{\mu''} V^{\nu'\mu''\mu\nu}_{\mathbf{k}''-\mathbf{j},\mathbf{k}',\mathbf{j}} P^{\mu'',\lambda'}_{\mathbf{k}-\mathbf{q}}\right) c^{-\mathbf{j},\mathbf{k}'',\mathbf{k}}_{\lambda,\nu';\nu,\mu'} \\
&+ \sum_{\nu,\nu'} P^{\lambda,\nu}_{\mathbf{k}} \sum_{\mathbf{q}'}\left[\sum_{\mu''} V^{\mu''\nu'\nu\mu}_{\mathbf{k}',\mathbf{k},\mathbf{q}'+\mathbf{q}}\left(c^{\mathbf{q}',\mathbf{k}'+\mathbf{q},\mathbf{k}-\mathbf{q}}_{\lambda',\mu';\mu'',\nu'}\right)^*\right] \\
&+ \sum_{\nu,\nu'}\left(P^{\mu,\nu}_{\mathbf{k}'} - \delta_{\nu\mu}\right)\sum_{\mathbf{q}'}\left[\sum_{\lambda''} V^{\nu'\lambda''\lambda\nu}_{\mathbf{k}',\mathbf{k},\mathbf{q}'+\mathbf{q}}\left(c^{\mathbf{q}',\mathbf{k}'+\mathbf{q},\mathbf{k}-\mathbf{q}}_{\lambda',\mu';\nu',\lambda''}\right)^*\right] \\
&- \sum_{\nu,\nu'} P^{\nu',\lambda'}_{\mathbf{k}-\mathbf{q}} \sum_{\mathbf{q}'}\left(\sum_{\mu''} V^{\nu'\mu'\mu''\nu}_{\mathbf{k}-\mathbf{q}',\mathbf{k}'+\mathbf{q}',\mathbf{q}'-\mathbf{q}} c^{\mathbf{q}',\mathbf{k}',\mathbf{k}}_{\lambda,\mu;\mu'',\nu}\right) \\
&- \sum_{\nu,\nu'}\left(P^{\nu',\mu'}_{\mathbf{k}'+\mathbf{q}} - \delta_{\nu'\mu'}\right)\sum_{\mathbf{q}'}\left(\sum_{\lambda''} V^{\lambda'\nu'\nu\lambda''}_{\mathbf{k}-\mathbf{q}',\mathbf{k}'+\mathbf{q}',\mathbf{q}'-\mathbf{q}} c^{\mathbf{q}',\mathbf{k}',\mathbf{k}}_{\lambda,\mu;\nu,\lambda''}\right)
\end{aligned}
$$

$$
\begin{aligned}
&- \sum_{\nu,\nu'} P^{\lambda,\nu}_{\mathbf{k}} \sum_{\mathbf{k}''} \left(\sum_{\lambda''} V^{\nu'\lambda'\lambda''\nu}_{\mathbf{k},\mathbf{k}''-\mathbf{q},\mathbf{k}''-\mathbf{k}} c^{\mathbf{q},\mathbf{k}',\mathbf{k}''}_{\nu',\mu;\mu',\lambda''} - \sum_{\mu''} V^{\nu'\mu'\mu''\nu}_{\mathbf{k},\mathbf{k}''+\mathbf{j},\mathbf{k}''-\mathbf{k}} c^{-\mathbf{j},\mathbf{k}',\mathbf{k}''}_{\nu',\mu;\lambda',\mu''} \right) \\
&- \sum_{\nu,\nu'} P^{\mu,\nu}_{\mathbf{k}'} \sum_{\mathbf{k}''} \left(\sum_{\mu''} V^{\nu'\mu'\mu''\nu}_{\mathbf{k}',\mathbf{k}''+\mathbf{q},\mathbf{k}''-\mathbf{k}'} c^{\mathbf{q},\mathbf{k}'',\mathbf{k}}_{\lambda,\nu';\mu'',\lambda'} - \sum_{\lambda''} V^{\nu'\lambda'\lambda''\nu}_{\mathbf{k}',\mathbf{k}''-\mathbf{j},\mathbf{k}''-\mathbf{k}'} c^{-\mathbf{j},\mathbf{k}'',\mathbf{k}}_{\lambda,\nu';\lambda'',\mu'} \right) \\
&+ \sum_{\nu,\nu'} P^{\nu',\lambda'}_{\mathbf{k}-\mathbf{q}} \sum_{\mathbf{k}''} \left(\sum_{\lambda''} V^{\lambda''\nu'\nu\lambda}_{\mathbf{k},\mathbf{k}''-\mathbf{q},\mathbf{k}''-\mathbf{k}} c^{\mathbf{q},\mathbf{k}',\mathbf{k}''}_{\lambda'',\mu;\mu',\nu} - \sum_{\mu''} V^{\mu''\nu'\nu\mu}_{\mathbf{k}',\mathbf{k}''-\mathbf{j},\mathbf{k}''-\mathbf{k}'} c^{-\mathbf{j},\mathbf{k}'',\mathbf{k}}_{\lambda,\mu'';\nu,\mu'} \right) \\
&+ \sum_{\nu,\nu'} P^{\nu',\mu'}_{\mathbf{k}'+\mathbf{q}} \sum_{\mathbf{k}''} \left(\sum_{\mu''} V^{\mu''\nu'\nu\mu}_{\mathbf{k}',\mathbf{k}''+\mathbf{q},\mathbf{k}''-\mathbf{k}'} c^{\mathbf{q},\mathbf{k}'',\mathbf{k}}_{\lambda,\mu'';\nu,\lambda'} - \sum_{\lambda''} V^{\lambda''\nu'\nu\lambda}_{\mathbf{k},\mathbf{k}''+\mathbf{j},\mathbf{k}''-\mathbf{k}} c^{-\mathbf{j},\mathbf{k}',\mathbf{k}''}_{\lambda'',\mu;\lambda',\nu} \right). \qquad \text{(A.10)}
\end{aligned}
$$

A.5 Derivation of Anomalous Currents using the Semiconductor Bloch Equations within the First-Order Adiabatic Perturbation

A.5.1 The Abelian Case

Applying the first-order perturbation to the SBE with THz field and assuming that the system already has a population $n_{\mathbf{k}}^{\lambda,(0)}$ which was generated by an optical field, we have

$$\begin{aligned}\frac{\mathrm{d}}{\mathrm{d}t}p_{\mathbf{k}}^{\lambda\mu,(1)} &= \frac{i}{\hbar}\sum_{\nu}\left(\mathrm{H}_{0,\mathbf{k}}^{\lambda\nu}\rho_{\mathbf{k}}^{\nu\mu,(1)} - \rho_{\mathbf{k}}^{\lambda\nu,(1)}\mathrm{H}_{0,\mathbf{k}}^{\nu\mu}\right) - \frac{i}{\hbar}e\mathbf{E}(t)\cdot\sum_{\nu}\left(\xi_{\mathbf{k}}^{\lambda\nu}\rho_{\mathbf{k}}^{\nu\mu,(0)} - \rho_{\mathbf{k}}^{\lambda\nu,(0)}\xi_{\mathbf{k}}^{\nu\mu}\right)\\ &\quad - \gamma_{\mathbf{k}}^{\lambda\mu}p_{\mathbf{k}}^{\lambda\mu,(1)}\\ &= i\left(\omega_{\mathbf{k}}^{\lambda\mu} + i\gamma_{\mathbf{k}}^{\lambda\mu}\right)p_{\mathbf{k}}^{\lambda\mu,(1)} - \frac{i}{\hbar}e\mathbf{E}(t)\cdot\xi_{\mathbf{k}}^{\lambda\mu}\left(n_{\mathbf{k}}^{\mu,(0)} - n_{\mathbf{k}}^{\lambda,(0)}\right).\end{aligned} \tag{A.11}$$

This equation has the form of an inhomogeneous differential equation, so we can write the solution as

$$\begin{aligned}p_{\mathbf{k}}^{\lambda\mu,(1)}(t) &= \int_{-\infty}^{t}\mathrm{d}t' e^{i\left(\omega_{\mathbf{k}}^{\lambda\mu}+i\gamma_{\mathbf{k}}^{\lambda\mu}\right)(t-t')}\frac{-i}{\hbar}e\mathbf{E}(t')\cdot\xi_{\mathbf{k}}^{\lambda\mu}\left(n_{\mathbf{k}}^{\mu,(0)} - n_{\mathbf{k}}^{\lambda,(0)}\right)\\ &= \int_{-\infty}^{t}\mathrm{d}t'\left[\frac{\mathrm{d}}{\mathrm{d}t'}e^{i\left(\omega_{\mathbf{k}}^{\lambda\mu}+i\gamma_{\mathbf{k}}^{\lambda\mu}\right)(t-t')}\right]\frac{1}{\Delta_{\mathbf{k}}^{\lambda\mu} + i\hbar\gamma_{\mathbf{k}}^{\lambda\mu}}e\mathbf{E}(t')\cdot\xi_{\mathbf{k}}^{\lambda\mu}\left(n_{\mathbf{k}}^{\mu,(0)} - n_{\mathbf{k}}^{\lambda,(0)}\right)\\ &= e^{i\left(\omega_{\mathbf{k}}^{\lambda\mu}+i\gamma_{\mathbf{k}}^{\lambda\mu}\right)(t-t')}\frac{1}{\Delta_{\mathbf{k}}^{\lambda\mu} + i\hbar\gamma_{\mathbf{k}}^{\lambda\mu}}e\mathbf{E}(t')\cdot\xi_{\mathbf{k}}^{\lambda\mu}\left(n_{\mathbf{k}}^{\mu,(0)} - n_{\mathbf{k}}^{\lambda,(0)}\right)\Bigg|_{-\infty}^{t}\\ &\quad + \xi_{\mathbf{k}}^{\lambda\mu}\cdot\int_{-\infty}^{t}\mathrm{d}t' e^{i\left(\omega_{\mathbf{k}}^{\lambda\mu}+i\gamma_{\mathbf{k}}^{\lambda\mu}\right)(t-t')}\left[\frac{1}{\Delta_{\mathbf{k}}^{\lambda\mu} + i\hbar\gamma_{\mathbf{k}}^{\lambda\mu}}\frac{\mathrm{d}}{\mathrm{d}t'}e\mathbf{E}(t')\right]\left(n_{\mathbf{k}}^{\mu,(0)} - n_{\mathbf{k}}^{\lambda,(0)}\right)\\ &= \frac{1}{\Delta_{\mathbf{k}}^{\lambda\mu} + i\hbar\gamma_{\mathbf{k}}^{\lambda\mu}}e\mathbf{E}(t')\cdot\xi_{\mathbf{k}}^{\lambda\mu}\left(n_{\mathbf{k}}^{\mu,(0)} - n_{\mathbf{k}}^{\lambda,(0)}\right)\\ &\quad + \xi_{\mathbf{k}}^{\lambda\mu}\cdot\int_{-\infty}^{t}\mathrm{d}t' e^{i\left(\omega_{\mathbf{k}}^{\lambda\mu}+i\gamma_{\mathbf{k}}^{\lambda\mu}\right)(t-t')}\left[\frac{1}{\Delta_{\mathbf{k}}^{\lambda\mu} + i\hbar\gamma_{\mathbf{k}}^{\lambda\mu}}\frac{\mathrm{d}}{\mathrm{d}t'}e\mathbf{E}(t')\right]\left(n_{\mathbf{k}}^{\mu,(0)} - n_{\mathbf{k}}^{\lambda,(0)}\right).\end{aligned} \tag{A.12}$$

Assuming that the electric field varying slowly in time compared to the inverse of the energy gaps between two bands, i.e.,

$$\frac{1}{\Delta_{\mathbf{k}}^{\lambda\mu}}\frac{\mathrm{d}}{\mathrm{d}t'}e\mathbf{E}(t') \to 0, \tag{A.13}$$

we can approximately ignore the second integral term, and thereby obtain

$$p_{\mathbf{k}}^{\lambda\mu,(1)}(t) = \frac{1}{\Delta_{\mathbf{k}}^{\lambda\mu} + i\hbar\gamma_{\mathbf{k}}^{\lambda\mu}} e\mathbf{E}(t') \cdot \xi_{\mathbf{k}}^{\lambda\mu}\left(n_{\mathbf{k}}^{\mu,(0)} - n_{\mathbf{k}}^{\lambda,(0)}\right). \tag{A.14}$$

Taking the expectation value of the velocity operator, we have

$$\begin{aligned}\left\langle \mathbf{v}^{(1)}(t)\right\rangle &= \frac{1}{L^2}\sum_{\lambda,\mu\neq\lambda,\mathbf{k}} \mathbf{v}_{\mathbf{k}}^{\lambda\mu} p_{\mathbf{k}}^{\mu\lambda,(1)}(t) \\ &= \sum_{\lambda,\mu\neq\lambda}\frac{1}{(2\pi)^2}\int \mathrm{d}\mathbf{k}\, \mathbf{v}_{\mathbf{k}}^{\lambda\mu}\frac{1}{\Delta_{\mathbf{k}}^{\mu\lambda} + i\hbar\gamma_{\mathbf{k}}^{\mu\lambda}}\left(e\mathbf{E}(t')\cdot\xi_{\mathbf{k}}^{\mu\lambda}\right)\left(n_{\mathbf{k}}^{\lambda,(0)} - n_{\mathbf{k}}^{\mu,(0)}\right).\end{aligned} \tag{A.15}$$

Next, using the Dirac's identity

$$\frac{1}{\Delta\epsilon + i\gamma} = \mathrm{P}\frac{1}{\Delta\epsilon} - i\pi\delta(\Delta\epsilon), \tag{A.16}$$

we obtain

$$\left\langle \mathbf{v}^{(1)}(t)\right\rangle = \sum_{\lambda,\mu\neq\lambda}\frac{1}{(2\pi)^2}\int \mathrm{d}\mathbf{k}\, \mathbf{v}_{\mathbf{k}}^{\lambda\mu}\left[\mathrm{P}\frac{1}{\Delta_{\mathbf{k}}^{\mu\lambda}} - i\pi\delta(\Delta_{\mathbf{k}}^{\mu\lambda})\right]\left(e\mathbf{E}(t')\cdot\xi_{\mathbf{k}}^{\mu\lambda}\right)\left(n_{\mathbf{k}}^{\lambda,(0)} - n_{\mathbf{k}}^{\mu,(0)}\right). \tag{A.17}$$

Because $\Delta_{\mathbf{k}}^{\lambda\mu}$ is always different from zero when the indices λ, μ belong to disconnected band, we can eliminate the term with the Dirac delta function

$$\left\langle \mathbf{v}^{(1)}(t)\right\rangle = \frac{1}{(2\pi)^2}\int \mathrm{d}\mathbf{k}\sum_{\lambda,\mu\neq\lambda}\mathbf{v}_{\mathbf{k}}^{\lambda\mu}\frac{1}{\Delta_{\mathbf{k}}^{\mu\lambda}}\left(e\mathbf{E}(t')\cdot\xi_{\mathbf{k}}^{\mu\lambda}\right)\left(n_{\mathbf{k}}^{\lambda,(0)} - n_{\mathbf{k}}^{\mu,(0)}\right). \tag{A.18}$$

Using the relation between $\xi_{\mathbf{k}}^{\lambda\mu}$ and $\mathbf{v}_{\mathbf{k}}^{\lambda\mu}$

$$\xi_{\mathbf{k}}^{\lambda\mu} = -i\hbar\frac{\mathbf{v}_{\mathbf{k}}^{\lambda\mu}}{\varepsilon_{\mathbf{k}}^{\lambda} - \varepsilon_{\mathbf{k}}^{\mu}}, \tag{A.19}$$

we obtain

$$\begin{aligned}\left\langle \mathbf{v}^{(1)}(t)\right\rangle &= \frac{1}{(2\pi)^2}\int \mathrm{d}\mathbf{k}\sum_{\lambda,\mu\neq\lambda}\mathbf{v}_{\mathbf{k}}^{\lambda\mu}\frac{-i\hbar}{\left(\Delta_{\mathbf{k}}^{\mu\lambda}\right)^2}\left(e\mathbf{E}(t')\cdot\mathbf{v}_{\mathbf{k}}^{\mu\lambda}\right)\left(n_{\mathbf{k}}^{\lambda,(0)} - n_{\mathbf{k}}^{\mu,(0)}\right) \\ &= \frac{1}{(2\pi)^2}\int \mathrm{d}\mathbf{k}\left\{\sum_{\lambda,\mu\neq\lambda}\mathbf{v}_{\mathbf{k}}^{\lambda\mu}\frac{-i\hbar}{\left(\Delta_{\mathbf{k}}^{\mu\lambda}\right)^2}\left(e\mathbf{E}(t')\cdot\mathbf{v}_{\mathbf{k}}^{\mu\lambda}\right)n_{\mathbf{k}}^{\lambda,(0)}\right. \\ &\qquad \left. - \sum_{\lambda,\mu\neq\lambda}\mathbf{v}_{\mathbf{k}}^{\lambda\mu}\frac{-i\hbar}{\left(\Delta_{\mathbf{k}}^{\mu\lambda}\right)^2}\left(e\mathbf{E}(t')\cdot\mathbf{v}_{\mathbf{k}}^{\mu\lambda}\right)n_{\mathbf{k}}^{\mu,(0)}\right\}.\end{aligned} \tag{A.20}$$

Then, grouping the terms with the same index of $n_{\mathbf{k}}^{\lambda,(0)}$, we get

$$\left\langle \mathbf{v}^{(1)}(t) \right\rangle = \frac{1}{(2\pi)^2} \int \mathrm{d}\mathbf{k} \sum_{\lambda,\mu\neq\lambda} n_{\mathbf{k}}^{\lambda,(0)} \frac{-i\hbar}{\left(\Delta_{\mathbf{k}}^{\mu\lambda}\right)^2} \left[\mathbf{v}_{\mathbf{k}}^{\lambda\mu} \left(e\mathbf{E}(t') \cdot \mathbf{v}_{\mathbf{k}}^{\mu\lambda} \right) - \mathbf{v}_{\mathbf{k}}^{\mu\lambda} \left(e\mathbf{E}(t') \cdot \mathbf{v}_{\mathbf{k}}^{\lambda\mu} \right) \right]. \tag{A.21}$$

Applying the triplet vector identity

$$\mathbf{A}(\mathbf{B}\cdot\mathbf{C}) - \mathbf{C}(\mathbf{B}\cdot\mathbf{A}) = \mathbf{B}\times(\mathbf{A}\times\mathbf{C}), \tag{A.22}$$

and the Kubo-like formula for Abelian Berry curvature

$$\mathbf{\Omega}_{\mathbf{k}}^{\lambda} = i\hbar^2 \sum_{\mu\neq\lambda} \frac{\mathbf{v}_{\mathbf{k}}^{\lambda\mu} \times \mathbf{v}_{\mathbf{k}}^{\mu\lambda}}{\left(\Delta_{\mathbf{k}}^{\mu\lambda}\right)^2}, \tag{A.23}$$

we finally obtain

$$\begin{aligned} \left\langle \mathbf{v}^{(1)}(t) \right\rangle &= \frac{1}{(2\pi)^2} \int \mathrm{d}\mathbf{k} \sum_{\lambda} -\frac{1}{\hbar} e\mathbf{E}(t) \times \left[i\hbar^2 \sum_{\mu\neq\lambda} \frac{\mathbf{v}_{\mathbf{k}}^{\lambda\mu} \times \mathbf{v}_{\mathbf{k}}^{\mu\lambda}}{\left(\Delta_{\mathbf{k}}^{\mu\lambda}\right)^2} \right] n_{\mathbf{k}}^{\lambda,(0)} \\ &= \frac{1}{(2\pi)^2} \int \mathrm{d}\mathbf{k} \sum_{\lambda} -\frac{e}{\hbar} \mathbf{E}(t) \times \mathbf{\Omega}_{\mathbf{k}}^{\lambda} n_{\mathbf{k}}^{\lambda,(0)}. \end{aligned} \tag{A.24}$$

A.5.2 The Non-Abelian Case

Applying the first-order perturbation to the SBE with THz field and assuming that the system has initial population and coherence between degenerate or near-degenerate states $\rho_{\lambda\mu\mathbf{k}}^{(0)}$ ($\lambda,\mu\in\Sigma_\lambda$), we have

$$\begin{aligned} \frac{\mathrm{d}}{\mathrm{d}t} p_{\mathbf{k}}^{\lambda\mu,(1)} &= \frac{i}{\hbar} \sum_{\nu} \left(\mathrm{H}_{0,\mathbf{k}}^{\lambda\nu} \rho_{\mathbf{k}}^{\nu\mu,(1)} - \rho_{\mathbf{k}}^{\lambda\nu,(1)} \mathrm{H}_{0,\mathbf{k}}^{\nu\mu} \right) - \frac{i}{\hbar} e\mathbf{E}(t) \cdot \sum_{\nu} \left(\boldsymbol{\xi}_{\mathbf{k}}^{\lambda\nu} \rho_{\mathbf{k}}^{\nu\mu,(0)} - \rho_{\mathbf{k}}^{\lambda\nu,(0)} \boldsymbol{\xi}_{\mathbf{k}}^{\nu\mu} \right) \\ &\quad - \gamma_{\mathbf{k}}^{\lambda\mu} p_{\mathbf{k}}^{\lambda\mu,(1)} \\ &= i\left(\omega_{\mathbf{k}}^{\lambda\mu} + i\gamma_{\mathbf{k}}^{\lambda\mu} \right) p_{\mathbf{k}}^{\lambda\mu,(1)} - \frac{i}{\hbar} e\mathbf{E}(t) \cdot \left(\sum_{\nu\in\Sigma_\mu} \boldsymbol{\xi}_{\mathbf{k}}^{\lambda\nu} \rho_{\mathbf{k}}^{\nu\mu,(0)} - \sum_{\nu\in\Sigma_\lambda} \rho_{\mathbf{k}}^{\lambda\nu,(0)} \boldsymbol{\xi}_{\mathbf{k}}^{\nu\mu} \right). \end{aligned} \tag{A.25}$$

Here, Σ_λ contains all indices of states which are degenerate with state λ. As in the Abelian case, we also obtain the approximate solution by assuming a slowly varying THz field as

$$p_{\mathbf{k}}^{\lambda\mu,(1)} = \frac{1}{\Delta_{\mathbf{k}}^{\mu\lambda} + i\hbar\gamma_{\mathbf{k}}^{\mu\lambda}} e\mathbf{E}(t) \cdot \left(\sum_{\nu\in\Sigma_\mu} \xi_{\mathbf{k}}^{\lambda\nu} \rho_{\mathbf{k}}^{\nu\mu,(0)} - \sum_{\nu\in\Sigma_\lambda} \rho_{\mathbf{k}}^{\lambda\nu,(0)} \xi_{\mathbf{k}}^{\nu\mu} \right). \tag{A.26}$$

Taking the expectation value of the velocity operator, we have

$$\begin{aligned}
\left\langle \mathbf{v}^{(1)}(t) \right\rangle &= \frac{1}{L^2} \sum_{\lambda,\mu\neq\Sigma_\lambda,\mathbf{k}} \mathbf{v}_{\mathbf{k}}^{\lambda\mu} p_{\mathbf{k}}^{\mu\lambda,(1)}(t) \\
&= \sum_{\lambda,\mu\neq\Sigma_\lambda} \frac{1}{(2\pi)^2} \int \mathrm{d}\mathbf{k}\, \mathbf{v}_{\mathbf{k}}^{\lambda\mu} \frac{1}{\Delta_{\mathbf{k}}^{\mu\lambda} + i\hbar\gamma_{\mathbf{k}}^{\mu\lambda}} e\mathbf{E}(t) \cdot \left(\sum_{\nu\in\Sigma_\mu} \xi_{\mathbf{k}}^{\lambda\nu} \rho_{\mathbf{k}}^{\nu\mu,(0)} - \sum_{\nu\in\Sigma_\lambda} \rho_{\mathbf{k}}^{\lambda\nu,(0)} \xi_{\mathbf{k}}^{\nu\mu} \right) \\
&= \frac{1}{(2\pi)^2} \int \mathrm{d}\mathbf{k} \sum_{\lambda,\mu\neq\Sigma_\lambda} \mathbf{v}_{\mathbf{k}}^{\lambda\mu} \frac{-i\hbar}{\left(\Delta_{\mathbf{k}}^{\mu\lambda}\right)^2} e\mathbf{E}(t) \cdot \left(\sum_{\nu\in\Sigma_\lambda} \mathbf{v}_{\mathbf{k}}^{\mu\nu} \rho_{\mathbf{k}}^{\nu\lambda,(0)} - \sum_{\nu\in\Sigma_\mu} \rho_{\mathbf{k}}^{\mu\nu,(0)} \mathbf{v}_{\mathbf{k}}^{\nu\lambda} \right) \\
&= \frac{1}{(2\pi)^2} \int \mathrm{d}\mathbf{k} \Bigg\{ \sum_{\lambda,\mu\neq\Sigma_\lambda} \mathbf{v}_{\mathbf{k}}^{\lambda\mu} \frac{-i\hbar}{\left(\Delta_{\mathbf{k}}^{\mu\lambda}\right)^2} e\mathbf{E}(t) \cdot \sum_{\nu\in\Sigma_\lambda} \mathbf{v}_{\mathbf{k}}^{\mu\nu} \rho_{\mathbf{k}}^{\nu\lambda,(0)} \\
&\qquad - \sum_{\lambda,\mu\neq\Sigma_\lambda} \mathbf{v}_{\mathbf{k}}^{\lambda\mu} \frac{-i\hbar}{\left(\Delta_{\mathbf{k}}^{\mu\lambda}\right)^2} e\mathbf{E}(t) \cdot \sum_{\nu\in\Sigma_\mu} \rho_{\mathbf{k}}^{\mu\nu,(0)} \mathbf{v}_{\mathbf{k}}^{\nu\lambda} \Bigg\}.
\end{aligned} \tag{A.27}$$

In the same way as for the Abelian case, by grouping the appropriate terms in the summation in the expression above with the note that the energy bands within degenerate or near-degenerate band are approximately the same, we obtain the final expression for the velocity as

$$\begin{aligned}
\left\langle \mathbf{v}^{(1)}(t) \right\rangle &= \frac{1}{(2\pi)^2} \int \mathrm{d}\mathbf{k} \sum_{\lambda,\mu\in\Sigma} -\frac{3}{\hbar} \mathbf{E}(t) \times i\hbar^2 \sum_{\nu\notin\Sigma} \frac{\mathbf{v}_{\mathbf{k}}^{\lambda\nu} \times \mathbf{v}_{\mathbf{k}}^{\nu\mu}}{\Delta_{\mathbf{k}}^{\lambda\nu} \Delta_{\mathbf{k}}^{\mu\nu}} \rho_{\mathbf{k}}^{\mu\lambda,(0)}(t) \\
&= \frac{1}{(2\pi)^2} \int \mathrm{d}\mathbf{k} \sum_{\lambda,\mu\in\Sigma} -\frac{e}{\hbar} \mathbf{E}(t) \times \Omega_{\mathbf{k}}^{\lambda\mu} \rho_{\mathbf{k}}^{\mu\lambda,(0)}(t).
\end{aligned} \tag{A.28}$$

A.6 Optical-Pump Optical-Probe Equations of Motion in the Coherent $\chi^{(3)}$ Limit

In this Appendix, we present the EOM in the coherent $\chi^{(3)}$ limit which are used to simulate the optical-pump optical-probe experiment. In this experiment, the system is excited by the pump and probe pulses. The pump pulse $\mathbf{E}_{\text{pump}}(t)$ induces the carrier occupation $n_{\sigma,\mathbf{k}}$ and interband polarization $p_{\sigma,\mathbf{k}}$. The probe pulse $\mathbf{E}_{\text{probe}}(t)$ induces a small change of the carrier distributions $\delta n_{\sigma,\mathbf{k}}$, of the interband polarization $\delta p_{\sigma,\mathbf{k}}$. The coherent Coulomb correlations are induced only by the probe pulse in the $\chi^{(3)}$ limit. These correlations include polarization and hole correlations δc_{vvvc}, polarization and electron correlations δc_{vccc}, and biexcitonic correlations δc_{BiX}. The differential absorption which is measured in the probe direction, $\mathbf{k}_{\text{probe}} + (\mathbf{k}_{\text{pump}} - \mathbf{k}_{\text{pump}})$, is in the $\chi^{(3)}$ limit proportional to $\mathbf{E}_{\text{probe}}\left|\mathbf{E}_{\text{pump}}\right|^2$. The pump and probe pulses propagating into the direction $\mathbf{k}_i$ have the form

$$\mathbf{E}_i(t) = \mathbf{E}_i^{\text{env}}(t)\left[e^{i(\mathbf{k}_i\cdot\mathbf{r}-\omega_i t)} + \text{c.c.}\right], \tag{A.29}$$

where $\mathbf{E}_i^{\text{env}}(t)$ is the slowly varying amplitude. By applying the rotating wave approximation, we multiply both sides of the above expression for pump and probe pulses with $e^{-i(\mathbf{k}_i\cdot\mathbf{r}-\omega_{\text{pump}}t)}$ and keeping only the resonant terms, we have

$$\mathbf{E}_{\text{pump}}(t)e^{-i(\mathbf{k}_{\text{pump}}\cdot\mathbf{r}-\omega_{\text{pump}}t)} = \mathbf{E}_{\text{pump}}^{\text{env}}(t), \tag{A.30}$$

$$\mathbf{E}_{\text{probe}}(t)e^{-i(\mathbf{k}_{\text{probe}}\cdot\mathbf{r}-\omega_{\text{pump}}t)} = \mathbf{E}_{\text{probe}}^{\text{env}}(t)e^{i(\omega_{\text{pump}}-\omega_{\text{probe}})t} = \mathbf{E}_{\text{probe}}^{\text{env}}(t)e^{i\Delta\omega_{\text{L}}t}. \tag{A.31}$$

In the first order, the pump and probe pulses induce interband coherences due to the linear source term $\mathbf{E}(t)\cdot\mathbf{d}_{\sigma,\mathbf{k}}^{\text{cv}}$ which are given by the following linear optical EOM

$$\begin{aligned} i\hbar\frac{\partial}{\partial t}p_{\sigma,\mathbf{k}}^{(1)(1|0)} &= \left(\varepsilon_{\sigma,\mathbf{k}}^{\text{e}} + \varepsilon_{\sigma,\mathbf{k}}^{\text{h}} - \hbar\omega_{\text{pump}} - i\gamma_2\right)p_{\sigma,\mathbf{k}}^{(1)(1|0)} - \sum_{\mathbf{k}'} V_{\sigma\sigma,\mathbf{k}'-\mathbf{k}}^{\text{vc}} p_{\sigma,\mathbf{k}'}^{(1)(1|0)} \\ &\quad - \mathbf{E}_{\text{pump}}^{\text{env}}(t)\cdot\mathbf{d}_{\sigma,\mathbf{k}}^{\text{cv}}, \end{aligned} \tag{A.32}$$

$$\begin{aligned} i\hbar\frac{\partial}{\partial t}\delta p_{\sigma,\mathbf{k}}^{(1)(0|1)} &= \left(\varepsilon_{\sigma,\mathbf{k}}^{\text{e}} + \varepsilon_{\sigma,\mathbf{k}}^{\text{h}} - \hbar\omega_{\text{pump}} - i\gamma_2\right)\delta p_{\sigma,\mathbf{k}}^{(1)(0|1)} - \sum_{\mathbf{k}'} V_{\sigma\sigma,\mathbf{k}'-\mathbf{k}}^{\text{vc}} \delta p_{\sigma,\mathbf{k}'}^{(1)(0|1)} \\ &\quad - \mathbf{E}_{\text{probe}}^{\text{env}}(t)\cdot\mathbf{d}_{\sigma,\mathbf{k}}^{\text{cv}}\, e^{i\Delta\omega_{\text{L}}t}. \end{aligned} \tag{A.33}$$

Here, the superscript $(l)(m|n)$ denotes the l-th order in the electric fields with a spatial dependence proportional to $e^{i(m\mathbf{k}_{\text{pump}}+n\mathbf{k}_{\text{probe}})\cdot\mathbf{r}}$. In second order, there are three relevant quantities. The first two are the pump-induced and probe-induced occupations, obtained by expanding the EOM (5.7)

$$\begin{aligned} \hbar\frac{\partial}{\partial t}n_{\sigma,\mathbf{k}}^{(2)(0|0)} &= -i\left[\left(\mathbf{E}_{\text{pump}}^{\text{env}}(t)\cdot\mathbf{d}_{\sigma,\mathbf{k}}^{\text{cv}} + \sum_{\mathbf{k}'} V_{\sigma\sigma,\mathbf{k}'-\mathbf{k}}^{\text{vc}} p_{\sigma,\mathbf{k}'}^{(1)(1|0)}\right)^* p_{\sigma,\mathbf{k}}^{(1)(1|0)} - \text{c.c.}\right] \\ &\quad - \gamma_1 n_{\sigma,\mathbf{k}}^{(2)(0|0)}, \end{aligned} \tag{A.34}$$

$$\hbar\frac{\partial}{\partial t}\delta n^{(2)(-1|1)}_{\sigma,\mathbf{k}} = -i\Bigg[\left(\mathbf{E}^{\mathrm{env}}_{\mathrm{pump}}(t)\cdot\mathbf{d}^{\mathrm{cv}}_{\sigma,\mathbf{k}} + \sum_{\mathbf{k}'} V^{\mathrm{vc}}_{\sigma\sigma,\mathbf{k}'-\mathbf{k}} p^{(1)(1|0)}_{\sigma,\mathbf{k}'}\right)^{*}\delta p^{(1)(0|1)}_{\sigma,\mathbf{k}} - \left(\mathbf{E}^{\mathrm{env}}_{\mathrm{probe}}(t)\cdot\mathbf{d}^{\mathrm{cv}}_{\sigma,\mathbf{k}}\, e^{i\Delta\omega_{\mathrm{L}}t} + \sum_{\mathbf{k}'} V^{\mathrm{vc}}_{\sigma\sigma,\mathbf{k}'-\mathbf{k}}\delta p^{(1)(0|1)}_{\sigma,\mathbf{k}'}\right)\left(p^{(1)(1|0)}_{\sigma,\mathbf{k}}\right)^{*}\Bigg] - \gamma_1\delta n^{(2)(-1|1)}_{\sigma,\mathbf{k}}. \tag{A.35}$$

In the above EOM for the correlations, we can see that only the biexcitonic correlations in second order with direction (1|1) are relevant. By expanding the EOM (5.13) and keeping only the relevant terms, we obtain

$$\begin{aligned}
i\hbar\frac{\partial}{\partial t}\delta c^{\mathbf{q},\mathbf{k}',\mathbf{k},(2)(1|1)}_{\mathrm{BX};\sigma\sigma'\sigma'\sigma} &= \left(\varepsilon^{\mathrm{e}}_{\sigma,\mathbf{k}-\mathbf{q}} + \varepsilon^{\mathrm{e}}_{\sigma',\mathbf{k}'+\mathbf{q}} + \varepsilon^{\mathrm{h}}_{\sigma',\mathbf{k}'} + \varepsilon^{\mathrm{h}}_{\sigma,\mathbf{k}} - 2\hbar\omega_{\mathrm{pump}} - i\gamma_T\right)\delta c^{\mathbf{q},\mathbf{k}',\mathbf{k},(2)(1|1)}_{\mathrm{BX};\sigma\sigma'\sigma'\sigma} \\
&+ \sum_{\mathbf{k}''}\Bigg(V^{\mathrm{vv}}_{\sigma'\sigma,\mathbf{k}''}\delta c^{\mathbf{q}-\mathbf{k}'',\mathbf{k}'+\mathbf{k}'',\mathbf{k}-\mathbf{k}'',(2)(1|1)}_{\mathrm{BX};\sigma\sigma'\sigma'\sigma} + V^{\mathrm{cc}}_{\sigma\sigma',\mathbf{k}''-\mathbf{q}}\delta c^{\mathbf{k}'',\mathbf{k}',\mathbf{k},(2)(1|1)}_{\mathrm{BX};\sigma\sigma'\sigma'\sigma} \\
&\quad - V^{\mathrm{vc}}_{\sigma\sigma,\mathbf{k}''-\mathbf{k}}\delta c^{\mathbf{q},\mathbf{k}',\mathbf{k}'',(2)(1|1)}_{\mathrm{BX};\sigma\sigma'\sigma'\sigma} - V^{\mathrm{vc}}_{\sigma\sigma',\mathbf{k}''-\mathbf{k}}\delta c^{\mathbf{k}''+\mathbf{q}-\mathbf{k},\mathbf{k}',\mathbf{k}'',(2)(1|1)}_{\mathrm{BX};\sigma\sigma'\sigma'\sigma} \\
&\quad - V^{\mathrm{vc}}_{\sigma'\sigma',\mathbf{k}''-\mathbf{k}'}\delta c^{\mathbf{q},\mathbf{k}'',\mathbf{k},(2)(1|1)}_{\mathrm{BX};\sigma\sigma'\sigma'\sigma} - V^{\mathrm{vc}}_{\sigma'\sigma,\mathbf{k}''-\mathbf{k}'}\delta c^{\mathbf{k}'+\mathbf{q}-\mathbf{k}'',\mathbf{k}'',\mathbf{k},(2)(1|1)}_{\mathrm{BX};\sigma\sigma'\sigma'\sigma}\Bigg) \\
&+ \left(V^{\mathrm{cc}}_{\sigma'\sigma,\mathbf{q}}\delta p^{(1)(0|1)}_{\sigma',\mathbf{k}'} - V^{\mathrm{vc}}_{\sigma'\sigma,\mathbf{q}}\delta p^{(1)(0|1)}_{\sigma',\mathbf{k}'+\mathbf{q}}\right)p^{(1)(1|0)}_{\sigma,\mathbf{k}} \\
&- \left(V^{\mathrm{cv}}_{\sigma'\sigma,\mathbf{q}}\delta p^{(1)(0|1)}_{\sigma',\mathbf{k}'} - V^{\mathrm{vv}}_{\sigma'\sigma,\mathbf{q}}\delta p^{(1)(0|1)}_{\sigma',\mathbf{k}'+\mathbf{q}}\right)p^{(1)(1|0)}_{\sigma,\mathbf{k}-\mathbf{q}} \\
&+ \left(V^{\mathrm{cc}}_{\sigma'\sigma,\mathbf{q}}p^{(1)(1|0)}_{\sigma',\mathbf{k}'} - V^{\mathrm{vc}}_{\sigma'\sigma,\mathbf{q}}p^{(1)(1|0)}_{\sigma',\mathbf{k}'+\mathbf{q}}\right)\delta p^{(1)(0|1)}_{\sigma,\mathbf{k}} \\
&- \left(V^{\mathrm{cv}}_{\sigma'\sigma,\mathbf{q}}p^{(1)(1|0)}_{\sigma',\mathbf{k}'} - V^{\mathrm{vv}}_{\sigma'\sigma,\mathbf{q}}p^{(1)(1|0)}_{\sigma',\mathbf{k}'+\mathbf{q}}\right)\delta p^{(1)(0|1)}_{\sigma,\mathbf{k}-\mathbf{q}} \\
&+ \delta_{\sigma\sigma'}\Bigg[\left(V^{\mathrm{vc}}_{\sigma\sigma,\mathbf{j}}\delta p^{(1)(0|1)}_{\sigma,\mathbf{k}'} - V^{\mathrm{vv}}_{\sigma\sigma,\mathbf{j}}\delta p^{(1)(0|1)}_{\sigma,\mathbf{k}-\mathbf{q}}\right)p^{(1)(1|0)}_{\sigma,\mathbf{k}'+\mathbf{q}} \\
&\quad - \left(V^{\mathrm{cc}}_{\sigma\sigma,\mathbf{j}}\delta p^{(1)(0|1)}_{\sigma,\mathbf{k}'} - V^{\mathrm{cv}}_{\sigma\sigma,\mathbf{j}}\delta p^{(1)(0|1)}_{\sigma,\mathbf{k}-\mathbf{q}}\right)p^{(1)(1|0)}_{\sigma,\mathbf{k}} \\
&\quad + \left(V^{\mathrm{vc}}_{\sigma\sigma,\mathbf{j}}p^{(1)(1|0)}_{\sigma,\mathbf{k}'} - V^{\mathrm{vv}}_{\sigma\sigma,\mathbf{j}}p^{(1)(1|0)}_{\sigma,\mathbf{k}-\mathbf{q}}\right)\delta p^{(1)(0|1)}_{\sigma,\mathbf{k}'+\mathbf{q}} \\
&\quad - \left(V^{\mathrm{cc}}_{\sigma\sigma,\mathbf{j}}p^{(1)(1|0)}_{\sigma,\mathbf{k}'} - V^{\mathrm{cv}}_{\sigma\sigma,\mathbf{j}}p^{(1)(1|0)}_{\sigma,\mathbf{k}-\mathbf{q}}\right)\delta p^{(1)(0|1)}_{\sigma,\mathbf{k}}\Bigg].
\end{aligned} \tag{A.36}$$

By expanding the EOM (5.8) and including all lower-order source contributions, we obtain the probe-induced coherence in the coherent third-order response along the direction $\mathbf{k}_{\mathrm{probe}}$ as

$$\begin{aligned}
i\hbar\frac{\partial}{\partial t}\delta p^{(3)(0|1)}_{\sigma,\mathbf{k}} &= \left(\varepsilon^{\mathrm{e}}_{\sigma,\mathbf{k}} + \varepsilon^{\mathrm{h}}_{\sigma,\mathbf{k}} - \hbar\omega_{\mathrm{pump}} - i\gamma_2\right)\delta p^{(3)(0|1)}_{\sigma,\mathbf{k}} - \sum_{\mathbf{k}'} V^{\mathrm{vc}}_{\sigma\sigma,\mathbf{k}'-\mathbf{k}}\delta p^{(3)(0|1)}_{\sigma,\mathbf{k}'} \\
&\quad + 2n^{(2)(0|0)}_{\sigma,\mathbf{k}}\mathbf{E}^{\mathrm{env}}_{\mathrm{probe}}(t)\cdot\mathbf{d}^{\mathrm{cv}}_{\sigma,\mathbf{k}}\, e^{i\Delta\omega_{\mathrm{L}}t} + 2\delta n^{(2)(-1|1)}_{\sigma,\mathbf{k}}\mathbf{E}^{\mathrm{env}}_{\mathrm{pump}}(t)\cdot\mathbf{d}^{\mathrm{cv}}_{\sigma,\mathbf{k}}
\end{aligned}$$

$$
\begin{aligned}
&+ 2n^{(2)(0|0)}_{\sigma,\mathbf{k}} \sum_{\mathbf{k}'} V^{\mathrm{vc}}_{\sigma\sigma,\mathbf{k}'-\mathbf{k}} \delta p^{(1)(0|1)}_{\sigma,\mathbf{k}'} + 2\delta n^{(2)(-1|1)}_{\sigma,\mathbf{k}} \sum_{\mathbf{k}'} V^{\mathrm{vc}}_{\sigma\sigma,\mathbf{k}'-\mathbf{k}} p^{(1)(1|0)}_{\sigma,\mathbf{k}'} \\
&- \delta p^{(1)(0|1)}_{\sigma,\mathbf{k}} \sum_{\mathbf{k}'} \left(V^{\mathrm{vv}}_{\sigma\sigma,\mathbf{k}'-\mathbf{k}} + V^{\mathrm{cc}}_{\sigma\sigma,\mathbf{k}'-\mathbf{k}} \right) n^{(2)(0|0)}_{\sigma,\mathbf{k}'} \\
&- p^{(1)(1|0)}_{\sigma,\mathbf{k}} \sum_{\mathbf{k}'} \left(V^{\mathrm{vv}}_{\sigma\sigma,\mathbf{k}'-\mathbf{k}} + V^{\mathrm{cc}}_{\sigma\sigma,\mathbf{k}'-\mathbf{k}} \right) \delta n^{(2)(-1|1)}_{\sigma,\mathbf{k}'} \\
&- \sum_{\sigma} \left(2V^{\mathrm{vc}}_{\sigma\sigma,\mathbf{0}} - V^{\mathrm{vv}}_{\sigma\sigma,\mathbf{0}} - V^{\mathrm{cc}}_{\sigma\sigma,\mathbf{0}} \right) \left(p^{(1)(1|0)}_{\sigma,\mathbf{k}} \sum_{\mathbf{k}'} \delta n^{(2)(-1|1)}_{\sigma,\mathbf{k}'} \right. \\
&\qquad\qquad \left. + \delta p^{(1)(0|1)}_{\sigma,\mathbf{k}} \sum_{\mathbf{k}'} n^{(2)(0|0)}_{\sigma,\mathbf{k}'} \right) \\
&+ \delta\Gamma^{(3)(0|1)}_{\sigma,\mathbf{k}}.
\end{aligned} \tag{A.37}
$$

Here, the last term in the above equation represents the contribution from Coulomb correlations, which is given by

$$
\begin{aligned}
\delta\Gamma^{(3)(0|1)}_{\sigma,\mathbf{k}} = \sum_{\sigma',\mathbf{k}',\mathbf{q}} \Bigg(& V^{\mathrm{cv}}_{\sigma\sigma',\mathbf{q}} \delta c^{\mathbf{q},\mathbf{k}',\mathbf{k},(3)(0|1)}_{\mathrm{ph};\sigma\sigma'\sigma'\sigma} + V^{\mathrm{cc}}_{\sigma\sigma',\mathbf{q}} \delta c^{\mathbf{q},\mathbf{k}',\mathbf{k},(3)(0|1)}_{\mathrm{pe};\sigma\sigma'\sigma'\sigma} \\
& - V^{\mathrm{vv}}_{\sigma\sigma',\mathbf{q}} \delta c^{-\mathbf{q},\mathbf{k}'+\mathbf{q},\mathbf{k}-\mathbf{q},(3)(0|1)}_{\mathrm{ph};\sigma\sigma'\sigma'\sigma} - V^{\mathrm{vc}}_{\sigma\sigma',\mathbf{q}} \delta c^{-\mathbf{q},\mathbf{k}'+\mathbf{q},\mathbf{k}-\mathbf{q},(3)(0|1)}_{\mathrm{pe};\sigma\sigma'\sigma'\sigma} \Bigg).
\end{aligned} \tag{A.38}
$$

For the probe-induced polarization-carrier occupation correlations, we obtain by expanding the EOMs (5.10) and (5.11) to third order and keeping only terms with direction $(0|1)$

$$
\begin{aligned}
i\hbar \frac{\partial}{\partial t} \delta c^{\mathbf{q},\mathbf{k}',\mathbf{k},(3)(0|1)}_{\mathrm{ph};\sigma\sigma'\sigma'\sigma} = & \left(\varepsilon^{\mathrm{e}}_{\sigma,\mathbf{k}-\mathbf{q}} - \varepsilon^{\mathrm{h}}_{\sigma',\mathbf{k}'+\mathbf{q}} + \varepsilon^{\mathrm{h}}_{\sigma',\mathbf{k}'} + \varepsilon^{\mathrm{h}}_{\sigma,\mathbf{k}} - \hbar\omega_{\mathrm{pump}} - i\gamma_T \right) \delta c^{\mathbf{q},\mathbf{k}',\mathbf{k},(3)(0|1)}_{\mathrm{ph};\sigma\sigma'\sigma'\sigma} \\
& + \sum_{\mathbf{k}''} \Bigg(V^{\mathrm{vv}}_{\sigma'\sigma,\mathbf{k}''} \delta c^{\mathbf{q}-\mathbf{k}'',\mathbf{k}'+\mathbf{k}'',\mathbf{k}-\mathbf{k}'',(3)(0|1)}_{\mathrm{ph};\sigma\sigma'\sigma'\sigma} - V^{\mathrm{vc}}_{\sigma\sigma,\mathbf{k}''-\mathbf{k}} \delta c^{\mathbf{q},\mathbf{k}',\mathbf{k}'',(3)(0|1)}_{\mathrm{ph};\sigma\sigma'\sigma'\sigma} \\
& \qquad - V^{\mathrm{vc}}_{\sigma'\sigma,\mathbf{k}''-\mathbf{k}'} \delta c^{\mathbf{k}'+\mathbf{q}-\mathbf{k}'',\mathbf{k}'',\mathbf{k},(3)(0|1)}_{\mathrm{ph};\sigma\sigma'\sigma'\sigma} \Bigg) \\
& + \left(V^{\mathrm{vc}}_{\sigma'\sigma,\mathbf{q}} \delta p^{(1)(0|1)}_{\sigma,\mathbf{k}} - V^{\mathrm{vv}}_{\sigma'\sigma,\mathbf{q}} \delta p^{(1)(0|1)}_{\sigma,\mathbf{k}-\mathbf{q}} \right) n^{(2)(0|0)}_{\sigma',\mathbf{k}'+\mathbf{q}} \\
& - \left(V^{\mathrm{cc}}_{\sigma'\sigma,\mathbf{q}} \delta p^{(1)(0|1)}_{\sigma,\mathbf{k}} - V^{\mathrm{cv}}_{\sigma'\sigma,\mathbf{q}} \delta p^{(1)(0|1)}_{\sigma,\mathbf{k}-\mathbf{q}} \right) \left(p^{(1)(1|0)}_{\sigma',\mathbf{k}'+\mathbf{q}} \right)^* p^{(1)(1|0)}_{\sigma',\mathbf{k}'} \\
& + \left(V^{\mathrm{vc}}_{\sigma'\sigma,\mathbf{q}} p^{(1)(1|0)}_{\sigma,\mathbf{k}} - V^{\mathrm{vv}}_{\sigma'\sigma,\mathbf{q}} p^{(1)(1|0)}_{\sigma,\mathbf{k}-\mathbf{q}} \right) \delta n^{(2)(-1|1)}_{\sigma',\mathbf{k}'+\mathbf{q}} \\
& - \left(V^{\mathrm{cc}}_{\sigma'\sigma,\mathbf{q}} p^{(1)(1|0)}_{\sigma,\mathbf{k}} - V^{\mathrm{cv}}_{\sigma'\sigma,\mathbf{q}} p^{(1)(1|0)}_{\sigma,\mathbf{k}-\mathbf{q}} \right) \left(p^{(1)(1|0)}_{\sigma',\mathbf{k}'+\mathbf{q}} \right)^* \delta p^{(1)(0|1)}_{\sigma',\mathbf{k}'} \\
& + \delta_{\sigma\sigma'} \Bigg[\left(V^{\mathrm{vv}}_{\sigma\sigma,\mathbf{j}} \delta p^{(1)(0|1)}_{\sigma,\mathbf{k}-\mathbf{q}} - V^{\mathrm{vc}}_{\sigma\sigma,\mathbf{j}} \delta p^{(1)(0|1)}_{\sigma,\mathbf{k}'} \right) n^{(2)(0|0)}_{\sigma,\mathbf{k}'+\mathbf{q}} \\
& \qquad - \left(V^{\mathrm{cv}}_{\sigma\sigma,\mathbf{j}} \delta p^{(1)(0|1)}_{\sigma,\mathbf{k}-\mathbf{q}} - V^{\mathrm{cc}}_{\sigma\sigma,\mathbf{j}} \delta p^{(1)(0|1)}_{\sigma,\mathbf{k}'} \right) \left(p^{(1)(1|0)}_{\sigma,\mathbf{k}'+\mathbf{q}} \right)^* p^{(1)(1|0)}_{\sigma,\mathbf{k}}
\end{aligned}
$$

$$
\begin{aligned}
&+\left(V^{\mathrm{vv}}_{\sigma\sigma,\mathbf{j}}p^{(1)(1|0)}_{\sigma,\mathbf{k}-\mathbf{q}}-V^{\mathrm{vc}}_{\sigma\sigma,\mathbf{j}}p^{(1)(1|0)}_{\sigma,\mathbf{k}'}\right)\delta n^{(2)(-1|1)}_{\sigma,\mathbf{k}'+\mathbf{q}}\\
&-\left(V^{\mathrm{cv}}_{\sigma\sigma,\mathbf{j}}p^{(1)(1|0)}_{\sigma,\mathbf{k}-\mathbf{q}}-V^{\mathrm{cc}}_{\sigma\sigma,\mathbf{j}}p^{(1)(1|0)}_{\sigma,\mathbf{k}'}\right)\left(p^{(1)(1|0)}_{\sigma,\mathbf{k}'+\mathbf{q}}\right)^{*}\delta p^{(1)(0|1)}_{\sigma,\mathbf{k}}\Bigg]\\
&-\left(\mathbf{d}^{\mathrm{cv}}_{\sigma',\mathbf{k}'+\mathbf{q}}\cdot\mathbf{E}_{\mathrm{pump}}(t)+\sum_{\mathbf{k}''}V^{\mathrm{vc}}_{\sigma'\sigma',\mathbf{k}''-\mathbf{k}'-\mathbf{q}}p^{(1)(1|0)}_{\sigma',\mathbf{k}''}\right)^{*}\delta c^{\mathbf{q},\mathbf{k}',\mathbf{k},(2)(1|1)}_{\mathrm{BX};\sigma\sigma'\sigma'\sigma}\\
&+\left(p^{(1)(1|0)}_{\sigma',\mathbf{k}'+\mathbf{q}}\right)^{*}\sum_{\mathbf{k}''}\Bigg(V^{\mathrm{vc}}_{\sigma'\sigma',\mathbf{k}''-\mathbf{k}'}\delta c^{\mathbf{q},\mathbf{k}'',\mathbf{k},(2)(1|1)}_{\mathrm{BX};\sigma\sigma'\sigma'\sigma}-V^{\mathrm{cc}}_{\sigma\sigma',\mathbf{k}''-\mathbf{q}}\delta c^{\mathbf{k}'',\mathbf{k}',\mathbf{k},(2)(1|1)}_{\mathrm{BX};\sigma\sigma'\sigma'\sigma}\\
&\qquad+V^{\mathrm{vc}}_{\sigma\sigma',\mathbf{k}''-\mathbf{k}}\delta c^{\mathbf{k}''+\mathbf{q}-\mathbf{k},\mathbf{k}',\mathbf{k}'',(2)(1|1)}_{\mathrm{BX};\sigma\sigma'\sigma'\sigma}\Bigg),
\end{aligned}
\tag{A.39}
$$

and

$$
\begin{aligned}
i\hbar\frac{\partial}{\partial t}\delta c^{\mathbf{q},\mathbf{k}',\mathbf{k},(3)(0|1)}_{\mathrm{pe};\sigma\sigma'\sigma'\sigma}&=\left(\varepsilon^{\mathrm{e}}_{\sigma,\mathbf{k}-\mathbf{q}}+\varepsilon^{\mathrm{e}}_{\sigma',\mathbf{k}'+\mathbf{q}}-\varepsilon^{\mathrm{e}}_{\sigma',\mathbf{k}'}+\varepsilon^{\mathrm{h}}_{\sigma,\mathbf{k}}-\hbar\omega_{\mathrm{pump}}-i\gamma_T\right)\delta c^{\mathbf{q},\mathbf{k}',\mathbf{k},(3)(0|1)}_{\mathrm{pe};\sigma\sigma'\sigma'\sigma}\\
&+\sum_{\mathbf{k}''}\Bigg(V^{\mathrm{cc}}_{\sigma\sigma',\mathbf{k}''-\mathbf{q}}\delta c^{\mathbf{k}'',\mathbf{k}',\mathbf{k},(3)(0|1)}_{\mathrm{pe};\sigma\sigma'\sigma'\sigma}-V^{\mathrm{vc}}_{\sigma\sigma',\mathbf{k}''-\mathbf{k}}\delta c^{\mathbf{k}''+\mathbf{q}-\mathbf{k},\mathbf{k}',\mathbf{k}'',(3)(0|1)}_{\mathrm{pe};\sigma\sigma'\sigma'\sigma}\\
&\qquad-V^{\mathrm{vc}}_{\sigma\sigma,\mathbf{k}''-\mathbf{k}}\delta c^{\mathbf{q},\mathbf{k}',\mathbf{k}'',(3)(0|1)}_{\mathrm{pe};\sigma\sigma'\sigma'\sigma}\Bigg)\\
&+\left(V^{\mathrm{cc}}_{\sigma'\sigma,\mathbf{q}}\delta p^{(1)(0|1)}_{\sigma,\mathbf{k}}-V^{\mathrm{cv}}_{\sigma'\sigma,\mathbf{q}}\delta p^{(1)(0|1)}_{\sigma,\mathbf{k}-\mathbf{q}}\right)n^{(2)(0|0)}_{\sigma',\mathbf{k}'}\\
&-\left(V^{\mathrm{vc}}_{\sigma'\sigma,\mathbf{q}}\delta p^{(1)(0|1)}_{\sigma,\mathbf{k}}-V^{\mathrm{vv}}_{\sigma'\sigma,\mathbf{q}}\delta p^{(1)(0|1)}_{\sigma,\mathbf{k}-\mathbf{q}}\right)\left(p^{(1)(1|0)}_{\sigma',\mathbf{k}'}\right)^{*}p^{(1)(1|0)}_{\sigma',\mathbf{k}'+\mathbf{q}}\\
&+\left(V^{\mathrm{cc}}_{\sigma'\sigma,\mathbf{q}}p^{(1)(1|0)}_{\sigma,\mathbf{k}}-V^{\mathrm{cv}}_{\sigma'\sigma,\mathbf{q}}p^{(1)(1|0)}_{\sigma,\mathbf{k}-\mathbf{q}}\right)\delta n^{(2)(-1|1)}_{\sigma',\mathbf{k}'}\\
&-\left(V^{\mathrm{vc}}_{\sigma'\sigma,\mathbf{q}}p^{(1)(1|0)}_{\sigma,\mathbf{k}}-V^{\mathrm{vv}}_{\sigma'\sigma,\mathbf{q}}p^{(1)(1|0)}_{\sigma,\mathbf{k}-\mathbf{q}}\right)\left(p^{(1)(1|0)}_{\sigma',\mathbf{k}'}\right)^{*}\delta p^{(1)(0|1)}_{\sigma',\mathbf{k}'+\mathbf{q}}\\
&+\delta_{\sigma\sigma'}\Bigg[\left(V^{\mathrm{vc}}_{\sigma\sigma,\mathbf{j}}\delta p^{(1)(0|1)}_{\sigma,\mathbf{k}'+\mathbf{q}}-V^{\mathrm{cc}}_{\sigma\sigma,\mathbf{j}}\delta p^{(1)(0|1)}_{\sigma,\mathbf{k}}\right)n^{(2)(0|0)}_{\sigma,\mathbf{k}'}\\
&\qquad-\left(V^{\mathrm{vv}}_{\sigma\sigma,\mathbf{j}}\delta p^{(1)(0|1)}_{\sigma,\mathbf{k}'+\mathbf{q}}-V^{\mathrm{cv}}_{\sigma\sigma,\mathbf{j}}\delta p^{(1)(0|1)}_{\sigma,\mathbf{k}}\right)\left(p^{(1)(1|0)}_{\sigma,\mathbf{k}'}\right)^{*}p^{(1)(1|0)}_{\sigma,\mathbf{k}-\mathbf{q}}\\
&\qquad+\left(V^{\mathrm{vc}}_{\sigma\sigma,\mathbf{j}}p^{(1)(1|0)}_{\sigma,\mathbf{k}'+\mathbf{q}}-V^{\mathrm{cc}}_{\sigma\sigma,\mathbf{j}}p^{(1)(1|0)}_{\sigma,\mathbf{k}}\right)\delta n^{(2)(-1|1)}_{\sigma,\mathbf{k}'}\\
&\qquad-\left(V^{\mathrm{vv}}_{\sigma\sigma,\mathbf{j}}p^{(1)(1|0)}_{\sigma,\mathbf{k}'+\mathbf{q}}-V^{\mathrm{cv}}_{\sigma\sigma,\mathbf{j}}p^{(1)(1|0)}_{\sigma,\mathbf{k}}\right)\left(p^{(1)(1|0)}_{\sigma,\mathbf{k}'}\right)^{*}\delta p^{(1)(0|1)}_{\sigma,\mathbf{k}-\mathbf{q}}\Bigg]\\
&+\left(\mathbf{d}^{\mathrm{cv}}_{\sigma',\mathbf{k}'}\cdot\mathbf{E}_{\mathrm{pump}}(t)+\sum_{\mathbf{k}''}V^{\mathrm{vc}}_{\sigma'\sigma',\mathbf{k}''-\mathbf{k}'}p^{(1)(1|0)}_{\sigma',\mathbf{k}''}\right)^{*}\delta c^{\mathbf{q},\mathbf{k}',\mathbf{k},(2)(1|1)}_{\mathrm{BX};\sigma\sigma'\sigma'\sigma}\\
&-\left(p^{(1)(1|0)}_{\sigma',\mathbf{k}'}\right)^{*}\sum_{\mathbf{k}''}\Bigg(V^{\mathrm{vc}}_{\sigma'\sigma',\mathbf{k}''-\mathbf{k}'}\delta c^{\mathbf{q},\mathbf{k}'',\mathbf{k},(2)(1|1)}_{\mathrm{BX};\sigma\sigma'\sigma'\sigma}\\
&\qquad+V^{\mathrm{vc}}_{\sigma'\sigma,\mathbf{k}''-\mathbf{k}'}\delta c^{\mathbf{k}'+\mathbf{q}-\mathbf{k}'',\mathbf{k}'',\mathbf{k},(2)(1|1)}_{\mathrm{BX};\sigma\sigma'\sigma'\sigma}
\end{aligned}
$$

$$- V^{\mathrm{vv}}_{\sigma'\sigma,\mathbf{k}''}\delta c^{\mathbf{q}-\mathbf{k}'',\mathbf{k}'+\mathbf{k}'',\mathbf{k}-\mathbf{k}'',(2)(1|1)}_{\mathrm{BX};\sigma\sigma'\sigma'\sigma}\Bigg). \tag{A.40}$$

With the closed set of EOM presented above we can calculate the differential absorption which is determined by the differential polarization $\delta p^{(3)(0|1)}_{\sigma,\mathbf{k}}$. There are three nonlinear source terms contributing to $\delta p^{(3)(0|1)}_{\sigma,\mathbf{k}}$, which are the Pauli-blocking contribution (PB), the first-order Coulomb contribution $\mathrm{CI}_{\mathrm{1st}}$, and higher-order Coulomb correlations ($\mathrm{CI}_{\mathrm{corr}}$). By decomposing Eq. (A.37) into the three nonlinear source terms, we obtain

$$\begin{aligned}
i\hbar\frac{\partial}{\partial t}\delta p^{(3)(0|1),\mathrm{PB}}_{\sigma,\mathbf{k}} &= \Big(\varepsilon^{\mathrm{e}}_{\sigma,\mathbf{k}} + \varepsilon^{\mathrm{h}}_{\sigma,\mathbf{k}} - \hbar\omega_{\mathrm{pump}} - i\gamma_2\Big)\delta p^{(3)(0|1),\mathrm{PB}}_{\sigma,\mathbf{k}} - \sum_{\mathbf{k}'} V^{\mathrm{vc}}_{\sigma\sigma,\mathbf{k}'-\mathbf{k}}\delta p^{(3)(0|1),\mathrm{PB}}_{\sigma,\mathbf{k}'} \\
&\quad + 2n^{(2)(0|0)}_{\sigma,\mathbf{k}}\mathbf{E}^{\mathrm{env}}_{\mathrm{probe}}(t)\cdot\mathbf{d}^{\mathrm{cv}}_{\sigma,\mathbf{k}}\, e^{i\Delta\omega_{\mathrm{L}}t} + 2\delta n^{(2)(-1|1)}_{\sigma,\mathbf{k}}\mathbf{E}^{\mathrm{env}}_{\mathrm{pump}}(t)\cdot\mathbf{d}^{\mathrm{cv}}_{\sigma,\mathbf{k}}, \qquad \text{(A.41)} \\
i\hbar\frac{\partial}{\partial t}\delta p^{(3)(0|1),\mathrm{CI_{1st}}}_{\sigma,\mathbf{k}} &= \Big(\varepsilon^{\mathrm{e}}_{\sigma,\mathbf{k}} + \varepsilon^{\mathrm{h}}_{\sigma,\mathbf{k}} - \hbar\omega_{\mathrm{pump}} - i\gamma_2\Big)\delta p^{(3)(0|1),\mathrm{CI_{1st}}}_{\sigma,\mathbf{k}} - \sum_{\mathbf{k}'} V^{\mathrm{vc}}_{\sigma\sigma,\mathbf{k}'-\mathbf{k}}\delta p^{(3)(0|1),\mathrm{CI_{1st}}}_{\sigma,\mathbf{k}'} \\
&\quad + 2n^{(2)(0|0)}_{\sigma,\mathbf{k}}\sum_{\mathbf{k}'} V^{\mathrm{vc}}_{\sigma\sigma,\mathbf{k}'-\mathbf{k}}\delta p^{(1)(0|1)}_{\sigma,\mathbf{k}'} + 2\delta n^{(2)(-1|1)}_{\sigma,\mathbf{k}}\sum_{\mathbf{k}'} V^{\mathrm{vc}}_{\sigma\sigma,\mathbf{k}'-\mathbf{k}}p^{(1)(1|0)}_{\sigma,\mathbf{k}'} \\
&\quad - \sum_{\mathbf{k}'}\Big(V^{\mathrm{vv}}_{\sigma\sigma,\mathbf{k}'-\mathbf{k}} + V^{\mathrm{cc}}_{\sigma\sigma,\mathbf{k}'-\mathbf{k}}\Big)n^{(2)(0|0)}_{\sigma,\mathbf{k}'}\delta p^{(1)(0|1)}_{\sigma,\mathbf{k}} \\
&\quad - \sum_{\mathbf{k}'}\Big(V^{\mathrm{vv}}_{\sigma\sigma,\mathbf{k}'-\mathbf{k}} + V^{\mathrm{cc}}_{\sigma\sigma,\mathbf{k}'-\mathbf{k}}\Big)\delta n^{(2)(-1|1)}_{\sigma,\mathbf{k}'}p^{(1)(1|0)}_{\sigma,\mathbf{k}} \\
&\quad - \sum_{\sigma}\Big(2V^{\mathrm{vc}}_{\sigma\sigma,\mathbf{0}} - V^{\mathrm{vv}}_{\sigma\sigma,\mathbf{0}} - V^{\mathrm{cc}}_{\sigma\sigma,\mathbf{0}}\Big)\Bigg(p^{(1)(1|0)}_{\sigma,\mathbf{k}}\sum_{\mathbf{k}'}\delta n^{(2)(-1|1)}_{\sigma,\mathbf{k}'} \\
&\qquad\qquad + \delta p^{(1)(0|1)}_{\sigma,\mathbf{k}}\sum_{\mathbf{k}'} n^{(2)(0|0)}_{\sigma,\mathbf{k}'}\Bigg), \qquad \text{(A.42)} \\
i\hbar\frac{\partial}{\partial t}\delta p^{(3)(0|1),\mathrm{corr}}_{\sigma,\mathbf{k}} &= \Big(\varepsilon^{\mathrm{e}}_{\sigma,\mathbf{k}} + \varepsilon^{\mathrm{h}}_{\sigma,\mathbf{k}} - \hbar\omega_{\mathrm{pump}} - i\gamma_2\Big)\delta p^{(3)(0|1),\mathrm{corr}}_{\sigma,\mathbf{k}} - \sum_{\mathbf{k}'} V^{\mathrm{vc}}_{\sigma\sigma,\mathbf{k}'-\mathbf{k}}\delta p^{(3)(0|1),\mathrm{corr}}_{\sigma,\mathbf{k}'} \\
&\quad + \delta\Gamma^{(3)(0|1)}_{\sigma,\mathbf{k}}. \qquad \text{(A.43)}
\end{aligned}$$

Bibliography

[1] P. Harrison and A. Valavanis, *Quantum wells, wires and dots: Theoretical and computational physics of semiconductor nanostructures* (Wiley, Hoboken, 2016).

[2] J. H. Davies, *The physics of low-dimensional semiconductors: an introduction* (Cambridge University Press, Cambridge, 1998).

[3] V. Mitin, V. Kochelap, and M. Stroscio, *Quantum heterostructures: microelectronics and optoelectronics* (Cambridge University Press, Cambridge, 1999).

[4] H. Haug and S. W. Koch, *Quantum theory of the optical and electronic properties of semiconductors*, 4th ed. (World Scientific, Singapore, 2004).

[5] L. Coldren, S. Corzine, and M. Mashanovitch, *Diode lasers and photonic integrated circuits*, Wiley Series in Microwave and Optical Engineering (Wiley, Hoboken, 2012).

[6] U. T. Schwarz, "Physics and technology of AlGaInN-based laser diode", in *Encyclopedia of applied physics* (Wiley, Hoboken, 2021), pp. 1–32.

[7] T.-Y. Seong, J. Han, H. Amano, and H. Morkoc, *III-Nitride based light emitting diodes and applications* (Springer, Singapore, 2017).

[8] A. David and B. Miller, "Optical physics of quantum wells", in *Quantum dynamics of simple systems* (Taylor & Francis, Bristol, 1997), pp. 239–266.

[9] K. K. Choi, *The physics of quantum well infrared photodetectors* (World Scientific, Singapore, 1997).

[10] Y. Zhang, Y.-W. Tan, H. L. Stormer, and P. Kim, Experimental observation of the quantum Hall effect and Berry's phase in graphene, Nature **438**, 201–204 (2005).

[11] C. G. Yale, F. J. Heremans, B. B. Zhou, A. Auer, G. Burkard, and D. D. Awschalom, Optical manipulation of the Berry phase in a solid-state spin qubit, Nat. Photonics **10**, 184–189 (2016).

[12] J. Wang and S.-C. Zhang, Topological states of condensed matter, Nat. Mater. **16**, 1062–1067 (2017).

[13] J. Wang, S. Valligatla, Y. Yin, L. Schwarz, M. Medina-Sánchez, S. Baunack, C. H. Lee, R. Thomale, S. Li, V. M. Fomin, L. Ma, and O. G. Schmidt, Experimental observation of Berry phases in optical Möbius-strip microcavities, Nat. Photonics **17**, 120–125 (2023).

[14] R. Karplus and J. M. Luttinger, Hall effect in ferromagnetics, Phys. Rev. **95**, 1154–1160 (1954).

[15] W. Kohn and J. M. Luttinger, Quantum theory of electrical transport phenomena, Phys. Rev. **108**, 590–611 (1957).

[16] J. M. Luttinger, Theory of the Hall effect in ferromagnetic substances, Phys. Rev. **112**, 739–751 (1958).

[17] E. N. Adams and E. I. Blount, Energy bands in the presence of an external force field—II: Anomalous velocities, J. Phys. Chem. Solids **10**, 286–303 (1959).

[18] E. Blount, "Formalisms of band theory", in *Solid state physics*, edited by F. Seitz and D. Turnbull (Academic Press, New York and London, 1962), pp. 305–373.

[19] M. V. Berry, Quantal phase factors accompanying adiabatic changes, Proc. R. Soc. Lond. **392**, 45–57 (1984).

[20] F. Wilczek and A. Zee, Appearance of gauge structure in simple dynamical systems, Phys. Rev. Lett. **52**, 2111–2114 (1984).

[21] E. Cohen, H. Larocque, F. Bouchard, F. Nejadsattari, Y. Gefen, and E. Karimi, Geometric phase from Aharonov–Bohm to Pancharatnam–Berry and beyond, Nat. Rev. Phys. **1**, 437–449 (2019).

[22] M. C. Chang and Q. Niu, Berry phase, hyperorbits, and the Hofstadter spectrum, Phys. Rev. Lett. **75**, 1348–1351 (1995).

[23] M. C. Chang and Q. Niu, Berry phase, hyperorbits, and the Hofstadter spectrum: Semiclassical dynamics in magnetic Bloch bands, Phys. Rev. B **53**, 7010–7023 (1996).

[24] G. Sundaram and Q. Niu, Wave-packet dynamics in slowly perturbed crystals: gradient corrections and Berry-phase effects, Phys. Rev. B **59**, 14915–14925 (1999).

[25] N. A. Sinitsyn, Semiclassical theories of the anomalous Hall effect, J. Phys. Condens. Matter **20**, 023201 (2008).

[26] V. I. Belinicher, E. L. Ivchenko, and B. I. Sturman, Linear photovoltaic effect in gyrotropic crystals, Sov. Phys. JETP **56**, 359 (1982).

[27] E. M. Hankiewicz and G. Vignale, Spin-Hall effect and spin-Coulomb drag in doped semiconductors, J. Phys. Condens. Matter **21**, 253202 (2009).

[28] J. E. Moore and J. Orenstein, Confinement-induced Berry phase and helicity-dependent photocurrents, Phys. Rev. Lett. **105**, 026805 (2010).

[29] H. Murakawa, M. S. Bahramy, M. Tokunaga, Y. Kohama, C. Bell, Y. Kaneko, N. Nagaosa, H. Y. Hwang, and Y. Tokura, Detection of Berry's phase in a bulk Rashba semiconductor, Science **342**, 1490–1493 (2013).

[30] S. Prabhakar, R. Melnik, and L. L. Bonilla, Gate control of Berry phase in III-V semiconductor quantum dots, Phys. Rev. B **89**, 245310 (2014).

[31] T. Li, L. A. Yeoh, A. Srinivasan, O. Klochan, D. A. Ritchie, M. Y. Simmons, O. P. Sushkov, and A. R. Hamilton, Manifestation of a non-Abelian Berry phase in a p-type semiconductor system, Phys. Rev. B **93**, 205424 (2016).

[32] L. H. Thong, C. Ngo, H. T. Duc, X. Song, and T. Meier, Microscopic analysis of high harmonic generation in semiconductors with degenerate bands, Phys. Rev. B **103**, 085201 (2021).

[33] G. Bae, Y. Kim, and J. D. Lee, Revealing Berry curvature of the unoccupied band in high harmonic generation, Phys. Rev. B **106**, 205422 (2022).

[34] L. Yue and M. B. Gaarde, Characterizing anomalous high-harmonic generation in solids, Phys. Rev. Lett. **130**, 166903 (2023).

[35] W. Sha, T. B. Norris, W. J. Schaff, and K. E. Meyer, Time-resolved ballistic acceleration of electrons in a GaAs quantum-well structure, Phys. Rev. Lett. **67**, 2553–2556 (1991).

[36] E. A. Shaner and S. A. Lyon, Picosecond time-resolved two-dimensional ballistic electron transport, Phys. Rev. Lett. **93**, 037402 (2004).

[37] P. von Allmen, Conduction subbands in a GaAs/Al_xGa_{1-x}As quantum well: Comparing different k·p models, Phys. Rev. B **46**, 15382–15386 (1992).

[38] W. J. Elder, R. M. Ward, and J. Zhang, Double-group formulation of $\mathbf{k} \cdot \mathbf{p}$ theory for cubic crystals, Phys. Rev. B **83**, 165210 (2011).

[39] J. Hübner, S. Kunz, S. Oertel, D. Schuh, M. Pochwała, H. T. Duc, J. Förstner, T. Meier, and M. Oestreich, Electron g-factor anisotropy in symmetric (110)-oriented GaAs quantum wells, Phys. Rev. B **84**, 041301 (2011).

[40] M. El kurdi, G. Fishman, S. Sauvage, and P. Boucaud, Comparison between 6-band and 14-band $\mathbf{k} \cdot \mathbf{p}$ formalisms in SiGe/Si heterostructures, Phys. Rev. B **68**, 165333 (2003).

[41] H. Mayer and U. Rössler, Spin splitting and anisotropy of cyclotron resonance in the conduction band of GaAs, Phys. Rev. B **44**, 9048–9051 (1991).

[42] P. Y. Yu and M. Cardona, *Fundamentals of semiconductors: Physics and materials properties*, Graduate Texts in Physics (Springer, Berlin, Heidelberg, 2010).

[43] G. L. Bir and G. E. Pikus, *Symmetry and strain-induced effects in semiconductors* (Wiley, New York, Jerusalem, 1974).

[44] P. Enders, A. Bärwolff, M. Woerner, and D. Suisky, $k \cdot p$ theory of energy bands, wave functions, and optical selection rules in strained tetrahedral semiconductors, Phys. Rev. B **51**, 16695–16704 (1995).

[45] T. Fujisawa, T. Sato, M. Mitsuhara, T. Kakitsuka, T. Yamanaka, Y. Kondo, and F. Kano, Successful application of the 8-band $k\cdot p$ theory to optical properties of highly strained In(Ga)As/InGaAs quantum wells with strong conduction-valence band coupling, IEEE J. Quantum Electron. **45**, 1183–1191 (2009).

[46] R. Winkler, *Spin-orbit coupling effects in two-dimensional electron and hole systems*, Springer Tracts in Modern Physics (Springer, Berlin, Heidelberg, 2003).

[47] S. Richard, F. Aniel, and G. Fishman, Band diagrams of Si and Ge quantum wells via the 30-band $\mathbf{k} \cdot \mathbf{p}$ method, Phys. Rev. B **72**, 245316 (2005).

[48] H.-R. Trebin, U. Rössler, and R. Ranvaud, Quantum resonances in the valence bands of zinc-blende semiconductors. I. Theoretical aspects, Phys. Rev. B **20**, 686–700 (1979).

[49] C. G. Van de Walle, Band lineups and deformation potentials in the model-solid theory, Phys. Rev. B **39**, 1871–1883 (1989).

[50] H. T. Duc, C. Ngo, and T. Meier, Ballistic photocurrents in semiconductor quantum wells caused by the excitation of asymmetric excitons, Phys. Rev. B **100**, 045308 (2019).

[51] M. Lax, *Symmetry principles in solid state and molecular physics*, Dover Books on Physics (Dover Publications, New York, 2012).

[52] C. Aversa and J. E. Sipe, Nonlinear optical susceptibilities of semiconductors: Results with a length-gauge analysis, Phys. Rev. B **52**, 14636–14645 (1995).

[53] K. S. Virk and J. E. Sipe, Semiconductor optics in length gauge: A general numerical approach, Phys. Rev. B **76**, 035213 (2007).

[54] H. T. Duc, J. Förstner, and T. Meier, Microscopic analysis of charge and spin photocurrents injected by circularly polarized one-color laser pulses in GaAs quantum wells, Phys. Rev. B **82**, 115316 (2010).

[55] W. Hoyer, M. Kira, and S. W. Koch, Influence of Coulomb and phonon interaction on the exciton formation dynamics in semiconductor heterostructures, Phys. Rev. B **67**, 155113 (2003).

[56] F. Rossi and T. Kuhn, Theory of ultrafast phenomena in photoexcited semiconductors, Rev. Mod. Phys. **74**, 895–950 (2002).

[57] G. D. Mahan, *Many-particle physics*, 2nd ed., Physics of Solids and Liquids (Springer, New York, 2011).

[58] M. Kira and S. W. Koch, Many-body correlations and excitonic effects in semiconductor spectroscopy, Prog. Quantum Electron. **30**, 155–296 (2006).

[59] I. Vurgaftman, J. R. Meyer, and L. R. Ram-Mohan, Band parameters for III–V compound semiconductors and their alloys, J. Appl. Phys. **89**, 5815–5875 (2001).

[60] V. M. Axt and A. Stahl, A dynamics-controlled truncation scheme for the hierarchy of density matrices in semiconductor optics, Z. Phys. B **93**, 195–204 (1994).

[61] M. Lindberg, Y. Z. Hu, R. Binder, and S. W. Koch, $\chi^{(3)}$ formalism in optically excited semiconductors and its applications in four-wave-mixing spectroscopy, Phys. Rev. B **50**, 18060–18072 (1994).

[62] T. Meier, P. Thomas, and S. W. Koch, *Coherent semiconductor optics: From basic concepts to nanostructure applications* (Springer, Berlin, Heidelberg, 2007).

[63] C. Sieh, T. Meier, F. Jahnke, A. Knorr, S. W. Koch, P. Brick, M. Hübner, C. Ell, J. Prineas, G. Khitrova, and H. M. Gibbs, Coulomb memory signatures in the excitonic optical Stark effect, Phys. Rev. Lett. **82**, 3112–3115 (1999).

[64] C. Sieh, T. Meier, A. Knorr, F. Jahnke, P. Thomas, and S. W. Koch, Influence of carrier correlations on the excitonic optical response including disorder and microcavity effects, Eur. Phys. J. B **11**, 407–421 (1999).

[65] S. Weiser, T. Meier, J. Möbius, A. Euteneuer, E. J. Mayer, W. Stolz, M. Hofmann, W. W. Rühle, P. Thomas, and S. W. Koch, Disorder-induced dephasing in semiconductors, Phys. Rev. B **61**, 13088–13098 (2000).

[66] W. Schäfer, D. S. Kim, J. Shah, T. C. Damen, J. E. Cunningham, K. W. Goossen, L. N. Pfeiffer, and K. Köhler, Femtosecond coherent fields induced by many-particle correlations in transient four-wave mixing, Phys. Rev. B **53**, 16429–16443 (1996).

[67] F. Schäfer, A. Trautmann, C. Ngo, J. T. Steiner, C. Fuchs, K. Volz, F. Dobener, M. Stein, T. Meier, and S. Chatterjee, Optical Stark effect in type-II semiconductor heterostructures, Phys. Rev. B **109**, 075301 (2024).

[68] F. Jahnke, M. Kira, S. W. Koch, G. Khitrova, E. K. Lindmark, T. R. Nelson Jr., D. V. Wick, J. D. Berger, O. Lyngnes, H. M. Gibbs, and K. Tai, Excitonic nonlinearities of semiconductor microcavities in the nonperturbative regime, Phys. Rev. Lett. **77**, 5257–5260 (1996).

[69] F. Jahnke, M. Kira, and S. W. Koch, Linear and nonlinear optical properties of excitons in semiconductor quantum wells and microcavities, Z. Phys. B **104**, 559–572 (1997).

[70] J. Hader, D. Bossert, J. Stohs, W. W. Chow, S. W. Koch, and J. V. Moloney, Clamping of the linewidth enhancement factor in narrow quantum-well semiconductor lasers, Appl. Phys. Lett. **74**, 2277–2279 (1999).

[71] H. Haug and A. Jauho, *Quantum kinetics in transport and optics of semiconductors*, 2nd ed., Springer Series in Solid-State Sciences (Springer, Berlin, Heidelberg, 2008).

[72] K. Baumann and G. C. Hegerfeldt, A noncommutative Marcinkiewicz theorem, Publications of the Research Institute for Mathematical Sciences **21**, 191–204 (1985).

[73] H. Wyld and B. D. Fried, Quantum mechanical kinetic equations, Ann. Phys. **23**, 374–389 (1963).

[74] J. Fricke, Transport equations including many-particle correlations for an arbitrary quantum system: A general formalism, Ann. Phys. **252**, 479–498 (1996).

[75] J. Fricke, V. Meden, C. Wöhler, and K. Schönhammer, Improved transport equations including correlations for electron–phonon systems: Comparison with exact solutions in one dimension, Ann. Phys. **253**, 177–197 (1997).

[76] H. Schoeller, A new transport equation for single-time Green's functions in an arbitrary quantum system. General formalism, Ann. Phys. **229**, 273–319 (1994).

[77] W. Hoyer, M. Kira, and S. W. Koch, "Cluster expansion in semiconductor quantum optics", in *Nonequilibrium physics at short time scales: formation of correlations*, edited by K. Morawetz (Springer, Berlin, Heidelberg, 2004), pp. 309–335.

[78] M. Kira, W. Hoyer, and S. W. Koch, Terahertz signatures of the exciton formation dynamics in non-resonantly excited semiconductors, Solid State Commun. **129**, 733–736 (2004).

[79] M. Kira and S. W. Koch, Exciton-population inversion and terahertz gain in semiconductors excited to resonance, Phys. Rev. Lett. **93**, 076402 (2004).

[80] M. Kira, W. Hoyer, T. Stroucken, and S. W. Koch, Exciton formation in semiconductors and the influence of a photonic environment, Phys. Rev. Lett. **87**, 176401 (2001).

[81] M. Kira, F. Jahnke, W. Hoyer, and S. W. Koch, Quantum theory of spontaneous emission and coherent effects in semiconductor microstructures, Prog. Quantum Electron. **23**, 189–279 (1999).

[82] M. Kira and S. W. Koch, *Semiconductor quantum optics* (Cambridge University Press, Cambridge, 2011).

[83] D. J. Griffiths and D. F. Schroeter, *Introduction to quantum mechanics*, 3rd ed. (Cambridge University Press, Cambridge, 2018).

[84] J. J. Sakurai, *Modern quantum mechanics* (Addison-Wesley, Reading, 1994).

[85] D. Vanderbilt, *Berry phases in electronic structure theory* (Cambridge University Press, Cambridge, 2018).

[86] D. Xiao, M.-C. Chang, and Q. Niu, Berry phase effects on electronic properties, Rev. Mod. Phys. **82**, 1959–2007 (2010).

[87] L. B. Madsen, Different forms of laser–matter interaction operators and expansion in adiabatic states, Eur. Phys. J. Spec. Top. **230**, 4141–4150 (2021).

[88] R. Resta, Macroscopic polarization in crystalline dielectrics: the geometric phase approach, Rev. Mod. Phys. **66**, 899–915 (1994).

[89] R. D. King-Smith and D. Vanderbilt, Theory of polarization of crystalline solids, Phys. Rev. B **47**, 1651–1654 (1993).

[90] M. Gradhand, D. V. Fedorov, F. Pientka, P. Zahn, I. Mertig, and B. L. Györffy, First-principle calculations of the Berry curvature of Bloch states for charge and spin transport of electrons, J. Phys. Condens. Matter **24**, 213202 (2012).

[91] M.-C. Chang and Q. Niu, Berry curvature, orbital moment, and effective quantum theory of electrons in electromagnetic fields, J. Phys. Condens. Matter **20**, 193202 (2008).

[92] A. A. Soluyanov and D. Vanderbilt, Smooth gauge for topological insulators, Phys. Rev. B **85**, 115415 (2012).

[93] L. Yue and M. B. Gaarde, Structure gauges and laser gauges for the semiconductor Bloch equations in high-order harmonic generation in solids, Phys. Rev. A **101**, 053411 (2020).

[94] H. T. Duc, R. Podzimski, S. Priyadarshi, M. Bieler, and T. Meier, Ultrafast shift and rectification photocurrents in GaAs quantum wells: Excitation intensity dependence and the importance of band mixing, Phys. Rev. B **94**, 085305 (2016).

[95] P. Földi, Gauge invariance and interpretation of interband and intraband processes in high-order harmonic generation from bulk solids, Phys. Rev. B **96**, 035112 (2017).

[96] C. Ngo, S. Priyadarshi, H. T. Duc, M. Bieler, and T. Meier, Excitonic anomalous currents in semiconductor quantum wells, Phys. Rev. B **108**, 165302 (2023).

[97] B. I. Sturman and V. M. Fridkin, *Photovoltaic and photo-refractive effects in noncentrosymmetric materials* (Gordon and Breach, Philadelphia, 1992).

[98] X.-C. Zhang, Y. Jin, and X. F. Ma, Coherent measurement of THz optical rectification from electro-optic crystals, Appl. Phys. Lett. **61**, 2764–2766 (1992).

[99] R. Podzimski, H. T. Duc, and T. Meier, Anisotropic excitons and their contributions to shift current transients in bulk GaAs, Phys. Rev. B **96**, 205201 (2017).

[100] J. E. Sipe and A. I. Shkrebtii, Second-order optical response in semiconductors, Phys. Rev. B **61**, 5337–5352 (2000).

[101] F. Nastos and J. E. Sipe, Optical rectification and shift currents in GaAs and GaP response: Below and above the band gap, Phys. Rev. B **74**, 035201 (2006).

[102] F. Nastos and J. E. Sipe, Optical rectification and current injection in unbiased semiconductors, Phys. Rev. B **82**, 235204 (2010).

[103] M. Bieler, K. Pierz, U. Siegner, and P. Dawson, Quantum interference currents by excitation of heavy- and light-hole excitons in $GaAsAl_{0.3}Ga_{0.7}As$ quantum wells, Phys. Rev. B **73**, 241312 (2006).

[104] M. Bieler, K. Pierz, U. Siegner, and P. Dawson, Shift currents from symmetry reduction and Coulomb effects in (110)-orientated $GaAsAl_{0.3}Ga_{0.7}As$ quantum wells, Phys. Rev. B **76**, 161304 (2007).

[105] S. Priyadarshi, A. M. Racu, K. Pierz, U. Siegner, M. Bieler, H. T. Duc, J. Förstner, and T. Meier, Reversal of coherently controlled ultrafast photocurrents by band mixing in undoped GaAs quantum wells, Phys. Rev. Lett. **104**, 217401 (2010).

[106] R. D. R. Bhat and J. E. Sipe, Optically injected spin currents in semiconductors, Phys. Rev. Lett. **85**, 5432–5435 (2000).

[107] R. D. R. Bhat, F. Nastos, A. Najmaie, and J. E. Sipe, Pure spin current from one-photon absorption of linearly polarized light in noncentrosymmetric semiconductors, Phys. Rev. Lett. **94**, 096603 (2005).

[108] S. D. Ganichev, E. L. Ivchenko, S. N. Danilov, J. Eroms, W. Wegscheider, D. Weiss, and W. Prettl, Conversion of spin into directed electric current in quantum wells, Phys. Rev. Lett. **86**, 4358–4361 (2001).

[109] S. D. Ganichev, U. Rössler, W. Prettl, E. L. Ivchenko, V. V. Bel'kov, R. Neumann, K. Brunner, and G. Abstreiter, Removal of spin degeneracy in p-SiGe quantum wells demonstrated by spin photocurrents, Phys. Rev. B **66**, 075328 (2002).

[110] L. E. Golub, Spin-splitting-induced photogalvanic effect in quantum wells, Phys. Rev. B **67**, 235320 (2003).

[111] K. S. Virk and J. E. Sipe, Optical injection and terahertz detection of the macroscopic Berry curvature, Phys. Rev. Lett. **107**, 120403 (2011).

[112] S. Priyadarshi, K. Pierz, and M. Bieler, Detection of the anomalous velocity with subpicosecond time resolution in semiconductor nanostructures, Phys. Rev. Lett. **115**, 257401 (2015).

[113] S. Priyadarshi, M. Leidinger, K. Pierz, A. M. Racu, U. Siegner, M. Bieler, and P. Dawson, Terahertz spectroscopy of shift currents resulting from asymmetric (110)-oriented GaAs/AlGaAs quantum wells, Appl. Phys. Lett. **95**, 151110 (2009).

[114] Y. Varshni, Temperature dependence of the energy gap in semiconductors, Physica **34**, 149–154 (1967).

[115] W. Press, *Numerical recipes 3rd edition: The art of scientific computing*, Numerical Recipes: The Art of Scientific Computing (Cambridge University Press, Cambridge, 2007).

[116] J. Feldmann, T. Meier, von Plessen G, M. Koch, E. O. Göbel, P. Thomas, G. Bacher, C. Hartmann, H. Schweizer, W. Schäfer, and H. Nickel, Coherent dynamics of excitonic wave packets, Phys. Rev. Lett. **70**, 3027–3030 (1993).

[117] W. Yao and Q. Niu, Berry phase effect on the exciton transport and on the exciton Bose-Einstein condensate, Phys. Rev. Lett. **101**, 106401 (2008).

[118] J. Zhou, W.-Y. Shan, W. Yao, and D. Xiao, Berry phase modification to the energy spectrum of excitons, Phys. Rev. Lett. **115**, 166803 (2015).

[119] J. B. Krieger and G. J. Iafrate, Time evolution of Bloch electrons in a homogeneous electric field, Phys. Rev. B **33**, 5494–5500 (1986).

[120] T. Meier, G. von Plessen, P. Thomas, and S. W. Koch, Coherent electric-field effects in semiconductors, Phys. Rev. Lett. **73**, 902–905 (1994).

[121] H. T. Duc, Q. T. Vu, T. Meier, H. Haug, and S. W. Koch, Temporal decay of coherently optically injected charge and spin currents due to carrier–LO-phonon and carrier-carrier scattering, Phys. Rev. B **74**, 165328 (2006).

[122] O. Schubert, M. Hohenleutner, F. Langer, B. Urbanek, C. Lange, U. Huttner, D. Golde, T. Meier, M. Kira, S. W. Koch, and R. Huber, Sub-cycle control of terahertz high-harmonic generation by dynamical Bloch oscillations, Nat. Photonics **8**, 119–123 (2014).

[123] K. F. Mak and J. Shan, Opportunities and challenges of interlayer exciton control and manipulation, Nat. Nanotechnol. **13**, 974–976 (2018).

[124] P. Rivera, H. Yu, K. L. Seyler, N. P. Wilson, W. Yao, and X. Xu, Interlayer valley excitons in heterobilayers of transition metal dichalcogenides, Nat. Nanotechnol. **13**, 1004–1015 (2018).

[125] A. Usman, M. A. Aly, H. Masenda, J. J. Thompson, S. M. Gunasekera, M. Mucha-Kruczyński, S. Brem, E. Malic, and M. Koch, Enhanced excitonic features in an anisotropic ReS_2/WSe_2 heterostructure, Nanoscale **14**, 10851–10861 (2022).

[126] E. Barré, O. Karni, E. Liu, A. L. O'Beirne, X. Chen, H. B. Ribeiro, L. Yu, B. Kim, K. Watanabe, T. Taniguchi, et al., Optical absorption of interlayer excitons in transition-metal dichalcogenide heterostructures, Science **376**, 406–410 (2022).

[127] V. M. Axt and A. Stahl, The role of the biexciton in a dynamic density matrix theory of the semiconductor band edge, Z. Phys. B **93**, 205–211 (1994).

[128] S. Weiss, M.-A. Mycek, J.-Y. Bigot, S. Schmitt-Rink, and D. S. Chemla, Collective effects in excitonic free induction decay: Do semiconductors and atoms emit coherent light in different ways?, Phys. Rev. Lett. **69**, 2685–2688 (1992).

[129] H. Wang, K. Ferrio, D. G. Steel, Y. Z. Hu, R. Binder, and S. W. Koch, Transient nonlinear optical response from excitation induced dephasing in GaAs, Phys. Rev. Lett. **71**, 1261–1264 (1993).

[130] T. Östreich, K. Schönhammer, and L. J. Sham, Exciton-exciton correlation in the nonlinear optical regime, Phys. Rev. Lett. **74**, 4698–4701 (1995).

[131] H. Wang, K. B. Ferrio, D. G. Steel, P. R. Berman, Y. Z. Hu, R. Binder, and S. W. Koch, Transient four-wave-mixing line shapes: Effects of excitation-induced dephasing, Phys. Rev. A **49**, R1551–R1554 (1994).

[132] K. Bott, O. Heller, D. Bennhardt, S. T. Cundiff, P. Thomas, E. J. Mayer, G. O. Smith, R. Eccleston, J. Kuhl, and K. Ploog, Influence of exciton-exciton interactions on the coherent optical response in GaAs quantum wells, Phys. Rev. B **48**, 17418–17426 (1993).

[133] Y. Z. Hu, R. Binder, S. W. Koch, S. T. Cundiff, H. Wang, and D. G. Steel, Excitation and polarization effects in semiconductor four-wave-mixing spectroscopy, Phys. Rev. B **49**, 14382–14386 (1994).

[134] P. Kner, W. Schäfer, R. Lövenich, and D. S. Chemla, Coherence of four-particle correlations in semiconductors, Phys. Rev. Lett. **81**, 5386–5389 (1998).

[135] C. Sieh, T. Meier, F. Jahnke, A. Knorr, S. W. Koch, P. Brick, M. Hübner, C. Ell, J. Prineas, G. Khitrova, and H. M. Gibbs, Coulomb memory signatures in the excitonic optical Stark effect, Phys. Rev. Lett. **82**, 3112–3115 (1999).

[136] E. J. Mayer, G. O. Smith, V. Heuckeroth, J. Kuhl, K. Bott, A. Schulze, T. Meier, D. Bennhardt, S. W. Koch, P. Thomas, R. Hey, and K. Ploog, Evidence of biexcitonic contributions to four-wave mixing in GaAs quantum wells, Phys. Rev. B **50**, 14730–14733 (1994).

[137] E. J. Mayer, G. O. Smith, V. Heuckeroth, J. Kuhl, K. Bott, A. Schulze, T. Meier, S. W. Koch, P. Thomas, R. Hey, and K. Ploog, Polarization dependence of beating phenomena at the energetically lowest exciton transition in GaAs quantum wells, Phys. Rev. B **51**, 10909–10914 (1995).

[138] T. F. Albrecht, K. Bott, T. Meier, A. Schulze, M. Koch, S. T. Cundiff, J. Feldmann, W. Stolz, P. Thomas, S. W. Koch, and E. O. Göbel, Disorder mediated biexcitonic beats in semiconductor quantum wells, Phys. Rev. B **54**, 4436–4439 (1996).

[139] B. F. Feuerbacher, J. Kuhl, and K. Ploog, Biexcitonic contribution to the degenerate-four-wave-mixing signal from a GaAs/$Al_xGa_{1-x}As$ quantum well, Phys. Rev. B **43**, 2439–2441 (1991).

[140] D. J. Lovering, R. T. Phillips, G. J. Denton, and G. W. Smith, Resonant generation of biexcitons in a GaAs quantum well, Phys. Rev. Lett. **68**, 1880–1883 (1992).

[141] K.-H. Pantke, D. Oberhauser, V. G. Lyssenko, J. M. Hvam, and G. Weimann, Coherent generation and interference of excitons and biexcitons in GaAs/$Al_xGa_{1-x}As$ quantum wells, Phys. Rev. B **47**, 2413–2416 (1993).

[142] D. Hulin and M. Joffre, Excitonic optical Stark redshift: The biexciton signature, Phys. Rev. Lett. **65**, 3425–3428 (1990).

[143] M. Stein, C. Lammers, P.-H. Richter, C. Fuchs, W. Stolz, M. Koch, O. Vänskä, M. J. Weseloh, M. Kira, and S. W. Koch, Dynamics of charge-transfer excitons in type-II semiconductor heterostructures, Phys. Rev. B **97**, 125306 (2018).

[144] M. Fey, M. Stein, C. Fuchs, W. Stolz, K. Volz, and S. Chatterjee, Phase relaxation control in heterostructures featuring charge-transfer excitons, Phys. Rev. B **106**, 165303 (2022).

[145] F. Guo, M. Chandross, and S. Mazumdar, Stable biexcitons in conjugated polymers, Phys. Rev. Lett. **74**, 2086–2089 (1995).

[146] G. Fuchs, J. Hörer, A. Hangleiter, V. Härle, F. Scholz, R. Glew, and L. Goldstein, Intervalence band absorption in strained and unstrained InGaAs multiple quantum well structures, Appl. Phys. Lett. **60**, 231–233 (1992).

[147] K. J. Moore, G. Duggan, K. Woodbridge, and C. Roberts, Observations and calculations of the exciton binding energy in (In,Ga)As/GaAs strained-quantum-well heterostructures, Phys. Rev. B **41**, 1090–1094 (1990).

[148] M. Schlierkamp, R. Wille, K. Greipel, U. Rössler, W. Schlapp, and G. Weimann, Quantum-well states under biaxial compression and tension, Phys. Rev. B **40**, 3077–3080 (1989).

[149] J. Röder, M. Gerhard, C. Fuchs, W. Stolz, W. Heimbrodt, M. Koch, C. Ngo, J. T. Steiner, and T. Meier, Charge transfer magnetoexcitons in magnetoabsorption spectra of asymmetric type-II double quantum wells, Phys. Rev. B **110**, 195306 (2024).

[150] C. Gros and R. Valentí, Cluster expansion for the self-energy: A simple many-body method for interpreting the photoemission spectra of correlated Fermi systems, Phys. Rev. B **48**, 418–425 (1993).

[151] S. Das Sarma and W.-Y. Lai, Screening and elementary excitations in narrow-channel semiconductor microstructures, Phys. Rev. B **32**, 1401–1404 (1985).

[152] J. Lee and H. N. Spector, Dielectric response function for a quasi-one-dimensional semiconducting system, J. Appl. Phys. **57**, 366–372 (1985).

[153] S. S. Kubakaddi, Electron-phonon interaction in a quantum wire in the Bloch-Gruneisen regime, Phys. Rev. B **75**, 075309 (2007).

[154] W. Schäfer, D. S. Kim, J. Shah, T. C. Damen, J. E. Cunningham, K. W. Goossen, L. N. Pfeiffer, and K. Köhler, Femtosecond coherent fields induced by many-particle correlations in transient four-wave mixing, Phys. Rev. B **53**, 16429–16443 (1996).

[155] M. Wegener, D. S. Chemla, S. Schmitt-Rink, and W. Schäfer, Line shape of time-resolved four-wave mixing, Phys. Rev. A **42**, 5675–5683 (1990).

[156] L. Wissinger, U. Rössler, R. Winkler, B. Jusserand, and D. Richards, Spin splitting in the electron subband of asymmetric GaAs/Al_xGa_{1-x}As quantum wells: The multiband envelope function approach, Phys. Rev. B **58**, 15375–15377 (1998).

Danksagung

I would like to express my deepest gratitude to Prof. Dr. Torsten Meier for giving me the opportunity to join his Computational Optoelectronics and Photonics research group. This opportunity allowed me to participate in many exciting research projects and attend physics conferences and various workshops, where I had the chance to interact with outstanding researchers and explore many new places. Throughout this time, Prof. Dr. Torsten Meier has consistently supported me in tackling complex physics problems. His guidance and patience have been invaluable, and without them, completing this dissertation would not have been possible.

Since the beginning of my doctoral studies, I have been fortunate to receive dedicated guidance from Dr. Johannes Steiner. He has always been willing to discuss and assist me in understanding and applying the cluster expansion method and programming related to complex physics problems. I would like to express my deep gratitude to him for his invaluable support.

I would like to sincerely thank the scientific committee for accepting my request, and especially Dr. Xuekai Ma for dedicating his time to reviewing my dissertation and thoroughly providing a report.

I extend my heartfelt thanks to Dr. Huynh Thanh Duc for his valuable advice, sincere encouragement, and dedicated guidance in the field of photocurrents.

Additionally, I want to thank my colleagues in the research group for their enthusiastic collaboration and the friendly working environment. In particular, I am deeply grateful to Dr. Matthias Reichelt for his insightful ideas, valuable advice, and dedicated support, which greatly facilitated my research work. I also thank a former colleague, Dr. Alexander Trautmann, for his effective collaboration on joint projects.

Furthermore, I wish to thank Ms. Simone Lange, the group's secretary, for her kindness and tireless support with administrative tasks, which enabled me to better focus on my research.

Lastly, I want to express my heartfelt gratitude to my parents, wife, and little daughter. Their love, encouragement, and unwavering support have been a tremendous source of motivation, helping me overcome all challenges on this journey.